Development and optimization of analytical methods for identifying and quantifying organic compounds in biological and paleontological specimens

Dissertation

zur

Erlangung des Doktorgrades (Dr. rer. nat.)

der

Mathematisch-Naturwissenschaftlichen Fakultät

der

Rheinischen Friedrich-Wilhelms-Universität Bonn

vorgelegt von

Mariam Gamal Mohamed Elsaid TAHOUN

aus

Giza, Ägypten

Bonn 2023

Angefertigt mit Genehmigung der Mathematisch-Naturwissenschaftlichen Fakultät

der Rheinischen Friedrich-Wilhelms-Universität Bonn

1. Gutachterin: Prof. Dr. Christa E. Müller
2. Gutachterin: PD Dr. Marianne Engeser

Tag der Promotion: 30.10.2023
Erscheinungsjahr: 2023

Table of Contents

1. Abstract

Preservation of soft tissues is a rare phenomenon which leads to the formation of fossils that survive for millions of years and are then subject to investigations by paleontologists. Several classes of chemical compounds have been reported to be preserved in fossils, including lipids, fatty acids, and porphyrins. However, the process of fossilization is not fully understood, which prompted investigations into the molecular aspects of decay, known as molecular taphonomy studies. The advancements of analytical techniques in recent decades have enabled progress in the field of molecular paleontology dedicated to the search for organic compounds in fossils and to understanding the changes that occur after death. Here, analytical methods are developed for the identification and quantification of organic compounds from biological, taphonomic, and fossil samples, applying various analytical techniques, including high performance liquid chromatography coupled to mass spectrometry and diode array ultraviolet/visible light detection, infrared spectroscopy, nuclear magnetic resonance spectroscopy, and atomic absorption spectrophotometry. First, since this dissertation deals largely with the chemical class of porphyrins, a review article is presented that provides a detailed overview on the chemistry of porphyrins in fossils (Chapter 3). This is followed by a review on the chemistry of the major compounds detected in dinosaurs and the analytical techniques used for their identification (Chapter 4). A major part of the studies described in this dissertation aimed to establish and optimize an extraction protocol for heme, the prosthetic group of hemoglobin, from bone, with a high recovery rate, in order to be applied to analyses on fossil dinosaur bone (Chapter 6). Moreover, a molecular taphonomy study on heme was performed, elucidating the chemical degradation products of heme formed under conditions favorable to fossilization (Chapter 5). Furthermore, analytical methods were established for the quantification of two naturally occurring depsipeptides, FR900959 and YM-254890, from mouse organs after intratracheal and intraperitoneal administration, as well as the determination of their chemical stability in simulated gastrointestinal fluids (Chapter 7). Additionally, an analytical method was developed to detect fatty acid constituents of the plant polymer suberin, which is unique to bark, and the results were used to identify preserved bark in a 45-million-year-old fossil tree known as "monkeyhair" collected in the Geiseltal Lagerstätte near Halle (Saale), East Germany (Chapter 8). Finally, several collaborative projects were completed, in which different analytical techniques were used to determine calcium concentrations, identify degradation products of fats in samples of the decaying crayfish *Cambarellus diminitus*, and to identify components of lignin in a fossil wood sample (Chapters 9-11). In summary, the findings of this

dissertation demonstrate the power of analytical chemistry for analyzing a variety of compounds originating from diverse matrices, and contributes to the growing field of molecular paleontology. It provides novel findings and contributions to the fossil record, and presents analytical methods that may be applied in the future to study further specimens.

2. Introduction

2.1. Processes of taphonomy and fossilization

Fossils are preserved parts of organisms that have survived the process of decay for at least 10,000 years [1]. Fossilization is rare, because when organisms die, chemical and microbial degradation usually lead to complete decomposition of organic material and soft parts, leaving behind the hard mineralized skeleton. Minerals in the groundwater are redeposited in the interstitial spaces, slowly transforming vertebrate bones and teeth into inorganic rock. This is known as permineralization [2]. If this process is exceptionally slowed down or paused early on, certain microstructures and associated organic compounds can get preserved because they are isolated, cemented and protected by an inorganic environment, and are not completely permineralized, forming fossils as a result [3]. Millions of years later, fossils are excavated by paleontologists from sedimentary deposits (Konservat-Lagerstätten) around the world [4], such as the Miocene Clarkia (Idaho, USA) [5], the Morrison Formation (Utah, USA) [6], and Geiseltal (Germany) [7]. Fossils have always drawn a lot of attention not only because of their rarity, but also because of the potential for retrieval of valuable biological and evolutionary information that is generally not available from the permineralized hard skeletons which make up the bulk of fossilized vertebrates [2,8].

Examples of soft tissue reported to survive for millions of years include osteocytes, bone collagen fibers, blood vessels, skin structures, claws, feathers, hair, nerves, nerve tissues, digestive organs, eggshells, muscles, and chondrocytes ([9–11] and references therein). Fossilized soft tissues are described and characterized using a combination of analytical methods. As analytical instruments became more advanced and sensitive, a specialty of paleontology known as molecular paleontology came to light and focused on the extraction and identification of the organic content in those preserved tissues, in addition to understanding the process of tissue and molecular preservation [12].

The process of fossilization is not yet fully understood. There have been attempts to simulate decay and fossilization in extant tissues in the form of experimental taphonomy studies, which investigate the morphological changes that occur after death [13,14]. This type of study was also extended to the molecular level, known as molecular taphonomy studies, which investigate the molecular aspects of fossilization and the diagenetic changes that occur to biomolecules (e.g., nucleic acids, lipids, proteins, and carbohydrates) and their constituents over time [3]. These studies aid in establishing the environmental conditions surrounding the fossil at the time

of burial (paleoenvironment), and in answering evolutionary questions [15]. Figure 2.1 illustrates these processes and how they are interconnected and give feedback to each other.
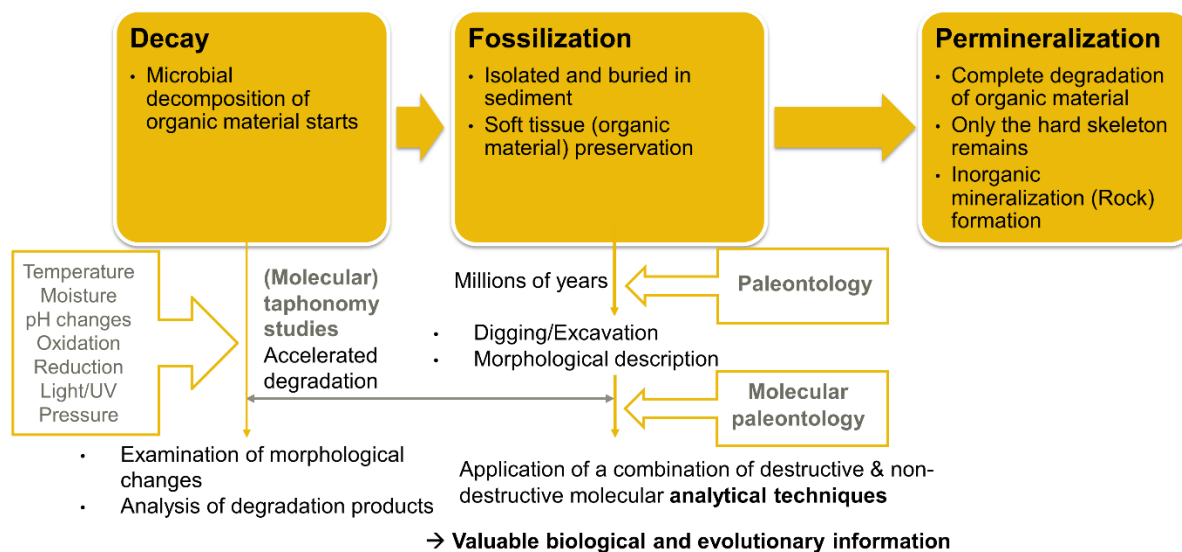
Figure 2.1. An overview of processes that take place immediately after death of an organism (decay) until complete degradation of organic material (permineralization) or fossilization under exceptional conditions.

To understand how preservation occurs and what compounds or derivatives are expected to survive millions of years, experimental or molecular taphonomy studies can be performed on the compounds alone or along with the decaying tissue of interest, aiming to determine the environmental or chemical parameters that affect their fossilization [14,16,17]. Generally, selected studied parameters are temperature changes (thermal decomposition), moisture (hydrolysis), light exposure (photochemical reactions), differences in pH (e.g., due to bacterial decay), tissue-specific biological properties, and geochemical and environmental properties of sediment (compaction, low moisture, oxidizing/reducing conditions) [2–4,18]. The results of molecular taphonomy studies are usually put into context along with the location of the molecules within the decaying environment of the fossil, the microbiome community in the surrounding sediment, and other necessary chemical and biochemical data [3].

The fate of many biomolecules during fossilization is still not fully understood from the chemical perspective because molecular taphonomy studies have not been done on every type of biomolecule. This illustrates the need for more studies, in which the molecular aspects that permit the persistence of these molecules both on the short- and long-term scale are to be investigated [3]. There is a combination of factors that influence the preservation of biomolecules, such as their chemistry, the environment in which the fossils are buried, and the

processes that possibly occur during decay [2,3]. Temperature generally speeds up a chemical reaction [2]. However, too high temperatures can degrade thermolabile compounds [19]. The source of moisture in a fossil could be groundwater entering the fossil by diffusion through openings or pores in the decaying organism. Moisture may generally lead to hydrolysis of labile bonds such as peptide, sugar, and ester bonds. Exposure to light may lead to photo-oxidative reactions and degradation. Differences in pH may lead to degradation; for example, acidic environments may induce hydrolysis [3,4].

2.2. Molecular mechanisms for preservation of organic compounds

Biomolecules have diverse physicochemical properties and therefore not all of them can be preserved under the same conditions. Generally, lipids and biopolymers (e.g., lignin) are poorly or not soluble in water and are more likely to be detected in fossils than labile water-soluble biomolecules [20,21]. Within the class of lipids, fatty acids are more likely to be degraded by decarboxylation or microbial decomposition than sterols and hydrocarbons [22]. In addition to these aspects, the chemical environment within the organism, such as being surrounded by more persistent molecules (e.g., cellulose is surrounded by lignin in the plant cell wall), can protect labile constituents [3].

Microbes are very crucial determinants for molecular degradation and in dictating the conditions of the surrounding environment (e.g., pH value) [23]. The type of microbes available at the burial site depends on the pH (e.g., some bacteria cannot survive in extreme acidic conditions), ionic environment, and whether the microorganism can find what it needs to be nourished [24]. Microbes generally cannot exert their effects in dry environments, when the temperatures are very low or very high, when the pH is not in their ideal working range, and in the presence of high salt concentrations ([3,23] and references therein).

Availability of oxygen is also a determining factor for preservation and needs to be considered along with the location of the fossil within the sediment, because oxygen will be usually present only in the first few meters of the sediment, while the environment deeper down is considered anoxic [3,25,26]. Nevertheless, in the latter condition, degradation can still occur by anaerobic bacteria, but is slower than in aerobic conditions [27]. For fossils buried under water, the depth of the water can determine its susceptibility for degradation, where sulfate reduction is more predominant in shallower than in deeper lakes [3,28].

A decaying organism is exposed to two stages of diagenesis: early and late diagenesis [3]. For the molecules, the most important process is the early diagenetic phase because it determines whether the soft parts can survive at all [4]. The preservation of a molecule throughout early diagenesis is mainly determined by its physicochemical properties, the nature of the organism (whether it has mineralized tissues, for example), and external processes (microbial and enzymatic decomposition) [3,24,29].

Late stages of diagenesis mainly determine the survival of molecules over a longer period of time [3,30]. Late diagenetic processes include the joining of molecules and formation of larger molecules with new bonds, probably through loss of water (e.g., through condensation), loss of functional groups, isomerization, racemization, and hydrolysis [3,31].

In addition to properties related to the molecule itself, the surrounding sediment may play a role in preservation [3,32]. For example, sometimes antioxidative and radical scavenging compounds (e.g., tocopherol) may be present in the sediment originating from other decaying organisms [3]. Furthermore, pressure and compaction of the organism during burial limit access to microbes, water, and enzymes, and may play a larger role during late diagenesis due to facilitating the chemical changes that occur during late diagenesis (e.g., cross-linking) [2,3,17,32]. As a result of all of these simultaneous processes, the organism remains in a closed system for millions of years and is fossilized.

2.3. Chemistry and preservation potential of selected biomolecules and small organic compounds

2.3.1. Lipids and free fatty acids

Lipids are organic compounds comprising different chemical classes. The simplest lipid constituents are fatty acids, which range in chain length and degree of unsaturation, and can associate with other atoms besides hydrocarbons, each having diverse biological functions. Other lipids include mono-, di-, and triglycerides, phospholipids, and sterols [33]. Lipids are found in fat stores of animals, such as storage of triglycerides as lipid droplets in adipose tissue [34], and in plant cell walls, e.g., in polymers such as suberin (in the outer bark) and cutin (in cuticles) [35].

Lipids are hydrophobic and not soluble in water, which is an important factor affecting their preservation in decaying environments and making them resistant to degradation [36]. Lipids are therefore among the most widely studied class of organic compounds from sediments and

in the fossil record ([37,38] and references therein). The preservation of free fatty acids is multifactorial and depends on their physicochemical properties. Among the diagenetic pathways that can modify the structure of fatty acids are the conversion of unsaturated linkages to saturated bonds, the formation of aromatic bonds in ring structures, and the removal of functional groups such as the carboxyl function by decarboxylation [3,36]. The chain length of the fatty acid can affect preservation, with longer chain fatty acids being more likely preserved than shorter chain fatty acids. In addition, the presence of unsaturation makes unsaturated fatty acids less likely to survive than saturated fatty acids [20,39]. In case of moisturized environments, fatty polymers typically undergo ester hydrolysis releasing free fatty acids [3].

In addition to chemical degradation, microbial decomposition of triglycerides during early diagenesis leads to the formation of adipocere (grave wax), which is a waxy mixture of the calcium salts of free saturated and unsaturated fatty acids, mainly palmitic, stearic, myristic and oleic acids, and their hydroxy derivatives [40]. This reaction occurs in wet environments because water is needed for hydrolysis of the triglycerides, but also anaerobic conditions are required [41]. Once it is formed, however, adipocere is resistant to further decay, its waxy consistence isolating it from its surrounding environment [42].

Suberin is a polymeric organic compound located specifically in the cell walls of the phellem (cork) in the outer bark, that offers a protective layer to the tree, for example against microbes, fungi, and water loss. In bark, the phellem is composed of dead compacted hollow cells that contain suberin in their cell walls, whereas the phelloderm is composed of living cells which do not contain suberin [43]. The outer bark of *Quercus suber* (cork-oak tree) has a thick layer of cork and is an economically important source of cork [44]. Its cork layer contains about 40-50% suberin (w/w) [45]. Suberin consists of esters of α,ω-hydroxy diacids and ω-hydroxy acids with glycerol or ferulic acid [46]. Its high potential for preservation has been demonstrated [47]. In addition to hydrolysis to its free fatty acid components, the diagenetic changes that may occur to suberin include decarboxylation to non-hydrolyzable alkane and alkene derivatives, known as suberan [48].

2.3.2. Proteins and peptides

Proteins are macromolecules consisting of amino acids which are connected by peptide bonds. Proteins have many biological functions as receptors, hormones, enzymes, for transport, storage, and structural functions, e.g., being part of the cytoskeleton and the extracellular matrix [49]. Proteins and their fragments have been claimed to survive for millions of years,

despite having a relatively lower preservation potential than lipids [47]. The sub-field of paleontology known as paleoproteomics is mainly focused on the extraction and detection of proteins in the fossil record [50]. Among the diagenetic changes that may occur to proteins are hydrolysis of the peptide bonds, attacks on side chain substituents (e.g., amino, carboxyl, hydroxyl, and thiol groups), and changes in stereochemistry [3,50]. Among the environmental conditions that deter preservation of proteins are moisture because it leads to protein hydrolysis. Some conditions are in favor of protein preservation, such as dry environments, immobilization and protection of the tissue (which prevents access of enzymes and microbes), and having a tightly folded tertiary structure (protecting the interior of the protein) [3].

Examples of proteins preserved in the fossil record are collagen and non-collagenous proteins such as albumin [51], osteocalcin [52,53], and keratins [54–56], mainly from dinosaurs and other fossil vertebrates ([19,57] and references therein).

2.3.3. Porphyrins

Porphyrins are macrocyclic molecules consisting of a tetrapyrrole ring connected by methine bridges. They often form a complex with transition metal ions such as iron, zinc, copper, cobalt, nickel and oxovanadium. The metal ion coordinates with each nitrogen atom of the pyrrole rings, forming compounds that are known as metalloporphyrins [58]. Porphyrins and metalloporphyrins exert various biological functions and are present in diverse communities of organisms. Biologically relevant porphyrins include heme (**1**, Figure 2.2), the metalloporphyrin that is the prosthetic group of hemoglobin, its precursor protoporphyrin IX (**2**, Figure 2.2), and its degradation product biliverdin (**3**, Figure 2.2). Elevated levels of urinary and fecal porphyrins such as uroporphyrins and coproporphyrins are indicative of porphyrias, disorders affecting the synthesis and metabolism of porphyrins especially heme [59].
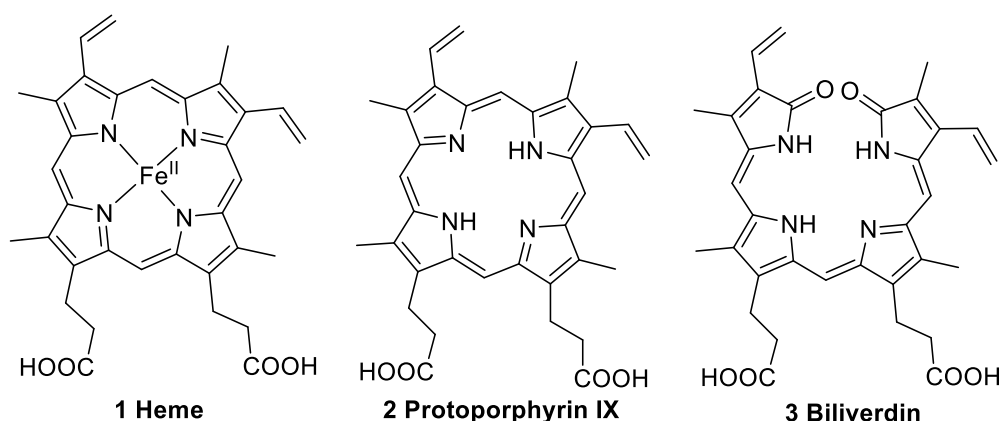
Figure 2.2. Selected structures belonging to the chemical class of porphyrins.

Closely related structures belonging to the chemical class of porphyrins are the chlorophylls, which have an extra five-membered isocyclic ring attached to one of the pyrrole rings of the porphyrin scaffold. Chlorophylls are classified into several types according to the organism in which they are prominent: chlorophylls, bacteriochlorophylls and *Chlorobium* chlorophylls (Figure 2.3). Chlorophylls are present in higher plants and the major members are chlorophyll *a* (**4**, Figure 2.3) and chlorophyll *b* (**5**, Figure 2.3) [60]. Bacteriochlorophylls are present in cyanobacteria and some algae (e.g., **6**, Figure 2.3) [61,62]. *Chlorobium* chlorophylls (e.g., **7**, Figure 2.3) are present in algae [63].

Figure 2.3. Selected structures of chlorophylls, bacteriochlorophylls and *Chlorobium* chlorophylls [64].

Porphyrins, metalloporphyrins and their derivatives have been often reported to be preserved for millions of years in sediments [65], and were detected in various fossils ranging from plant leaves [66,67] to dinosaur bones [68] to fossil mosquitoes [69] and sea turtles [70]. As for the conditions that may deter their fossilization, porphyrins are susceptible to oxidation [71].

In attempts to understand the fossilization of heme and chlorophyll *a*, the diagenetic changes that occur to heme and chlorophyll *a* have been proposed by the organic chemist Alfred Treibs in the 1930s and are based on the previously introduced general late diagenetic pathways in

Section 2.2 [72,73]. A combination of demetallation, reduction, loss of functional groups, and trans-metalation takes place. Two diagenetic pathways of heme were proposed, in which its iron atom is first oxidized to form hemin (**8**, Figure 2.4) and then removed, forming protoporphyrin IX (**2**, Figure 2.4). Afterwards, the vinyl groups are either only reduced to ethyl groups (**9**, Figure 2.4) or completely cleaved off (**10**, Figure 2.4), followed by the decarboxylation of both of the carboxylic acid groups, forming mesoetioporphyrin (**11**, Figure 2.4) or deuteroetioporphyrin (**12**, Figure 2.4), respectively [73]. This is followed by forming complexes with nickel or oxovanadium (**13** and **14**, Figure 2.4) [74].
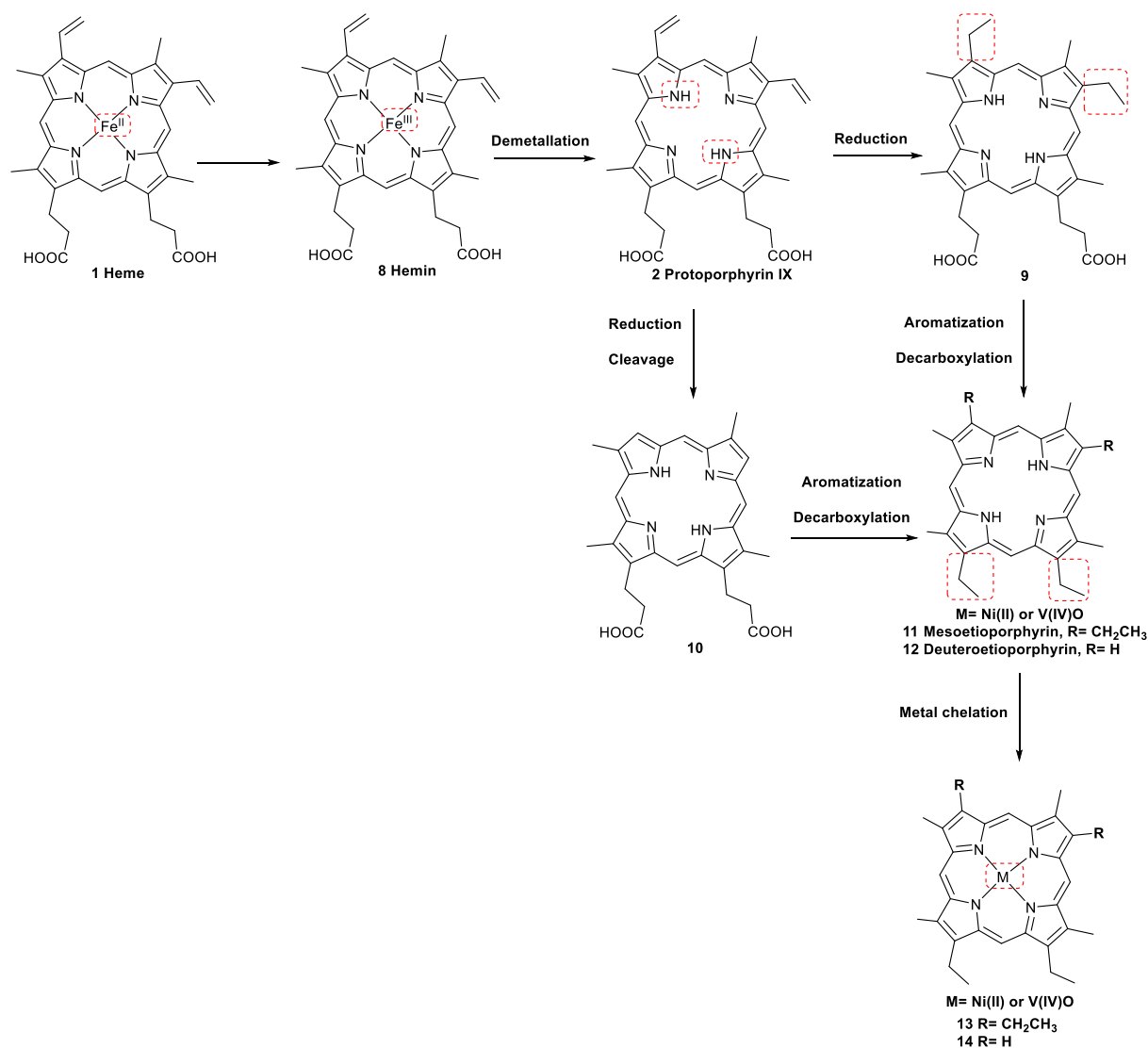
Figure 2.4. The proposed diagenetic changes that occur to heme according to A. E. Treibs [72–74], adapted from [64].

As for chlorophyll *a*, magnesium is first to be removed, forming **15** (Figure 2.5), followed by the hydrolysis of the ester groups (**16**, Figure 2.5). The vinyl groups are then reduced to ethyl

groups and the carboxyl group on the isocyclic ring is completely removed (**17**, Figure 2.5). Aromatization occurs to form the classic conjugated pattern of porphyrins (**18**, Figure 2.5). The oxygen of the carbonyl group on the isocyclic ring are reduced and replaced by hydrogens, forming desoxophylloerythrin (**19**, Figure 2.5). This is followed by removal of the carboxylic group of the propionic acid substituents on the tetrapyrrole ring to form deoxyphylloerythroetioporphyrin (**20**, DPEP, Figure 2.5). Finally, complexation occurs with other metal ions (**21**, Figure 2.5) [73].

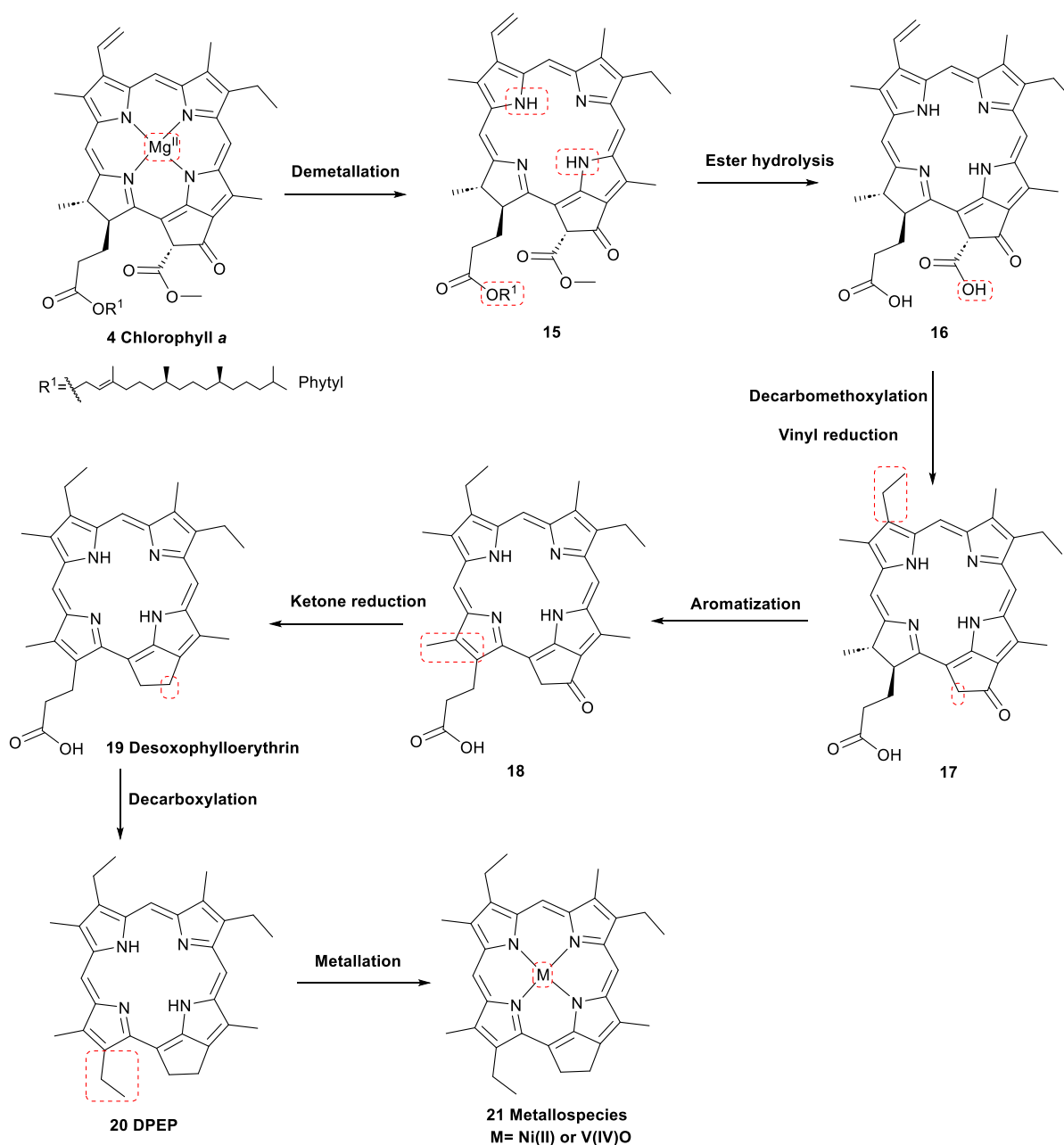**Figure 2.5.** The proposed diagenetic changes that occur to chlorophyll *a* according to A. E. Treibs [72–74], adapted from [64].

Reported evidence for this diagenetic process was provided by 1.1 billion-year-old porphyrins detected from marine sediments of the Taoudeni Basin in Mauritania [65], which, based on structural similarity, were assumed to be derived from chlorophylls and bacteriochlorophylls. In addition, several porphyrins of unknown age were extracted and detected from Moroccan oil shales and could originate from chlorophylls *b/c* and/or bacteriochlorophyll *d* [75]. Selected structures of the oldest porphyrins, **21-26**, are shown in Figure 2.6.
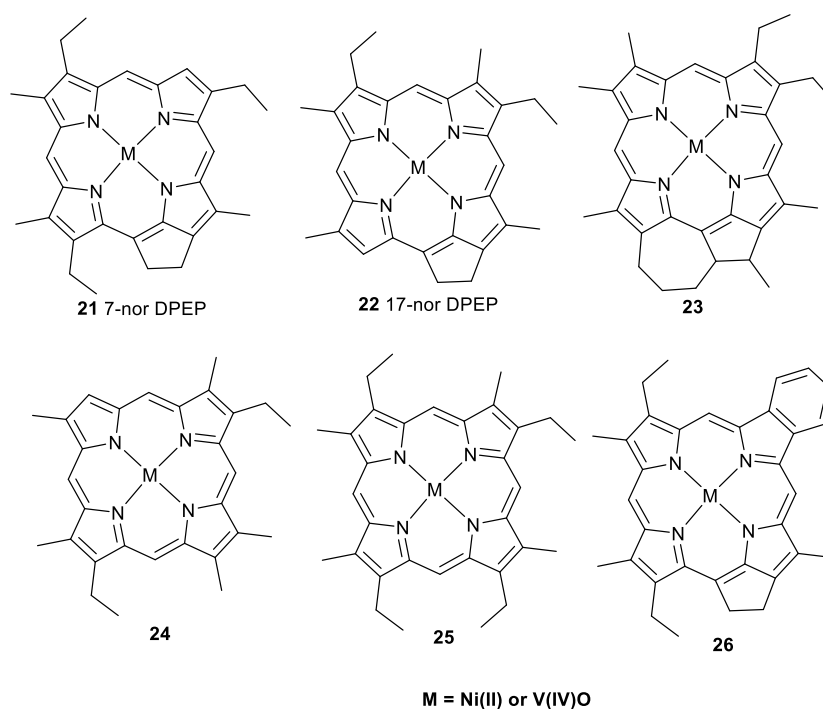
Figure 2.6. Selected structures of 1.1 billion-year-old porphyrins detected from marine sediments of the Taoudeni Basin in Mauritania [65], adapted from [64].

2.4 An overview of organic preservation in dinosaurs

Reports on soft tissue preservation from dinosaurs started in the 1960s and have been increasing since the 1990s [76]. Specifically focusing on dinosaurs, preserved soft tissues are commonly detected from bone e.g., osteocytes [11,77–79], blood vessels [11,80–82], skin structures (claws, feathers, and hairs) [83–88], and eggshells [10,89–94]. Figure 2.7 shows histological cross-section slides of the bones of selected sauropod dinosaurs *Neusticosaurus pusillus* (ca. 200-245 million years old), *Plateosaurus engelhardti* (ca. 204-214 million years old), and a diplodocid dinosaur sp. (ca. 145-155 million years old), illustrating their preserved bone compact internal structures, including osteocytes and vascular canals.
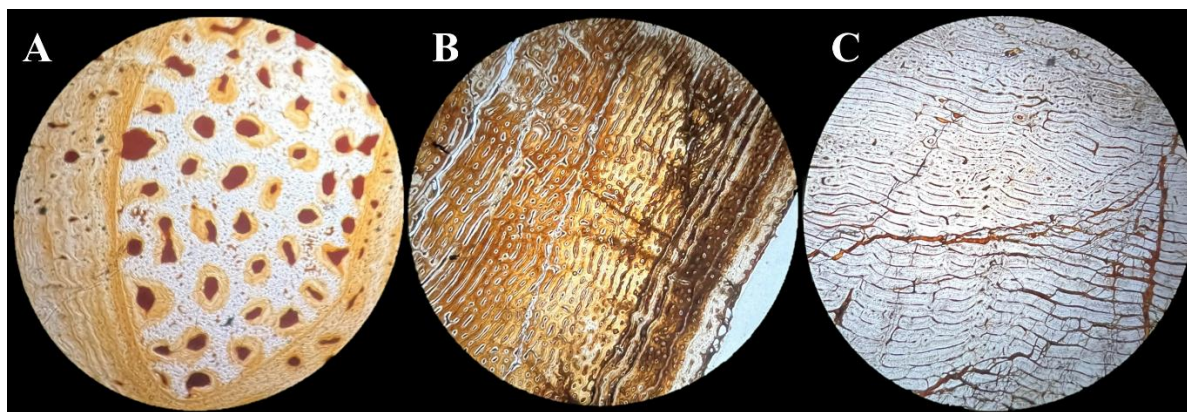
Figure 2.7. Histological slides of fossil bone thin sections viewed under the light microscope under normal transmitted light (10x magnification), from A) *Neusticosaurus pusillus* (ca. 200-245 million years old, cross section of humerus), B) the basal sauropodomorph *Plateosaurus engelhardti* (ca. 204-214 million years old, cross section of tibia), and C) an indeterminate diplodocid dinosaur sp. (ca. 145-155 million years old, cross section of a femur). Photos were taken by Mariam Tahoun. Slides were provided by Prof. Dr. P. Martin Sander during a histology course at the University of Bonn.

With advancements in developing sensitive analytical techniques, new directions of research have been to search for organic compounds that are preserved in the analyzed fossils. Organic compounds detected in non-avian dinosaurs so far belong to two classes: pigments and proteins (recently reviewed in [95]). The pigments described are melanin [85,87,96,97] and porphyrins [68,91,98], whereas the proteins are mainly collagen type I [80,99–103], but also collagen type II [104] and β-keratin [55,105] have been reported.

Porphyrins

Several porphyrin derivatives have been detected in dinosaurs. the prosthetic group of hemoglobin, heme (**1**, Figure 2.2), was detected from extracts of trabecular bone of a 66-million-year-old *Tyrannosaurus rex* [68]. The iron-free derivative of heme, protoporphyrin IX (**2**, Figure 2.2) and its long-chain tetrapyrrole derivative biliverdin (**3**, Figure 2.2) were detected in eggshells of the oviraptorid dinosaur *Heyuannia huangi* [91,98].

Melanin

Melanin is a pigment widely spread in many body parts, such as skin, eyes, and hair, and is synthesized by melanosomes [106]. Melanin is divided into two chemically distinct classes, pheomelanin and eumelanin, having the same biological precursors, tyrosine and dopaquinone,

but different biosynthetic pathways. Pheomelanin (**27**, Figure 2.8) is a red pigment derived from 1,4-benzothiazine [107]. Eumelanin (**28**, Figure 2.8) is a black pigment derived from 2,4-dihydroxyindole and 5,6-dihydroxyindole-2-carboxylic acid. Melanin generally functions as a free radical scavenger providing protection from harmful ultraviolet light rays [108]. Despite extensive investigations into melanin's biosynthetic pathways, some of the chemical aspects of melanin, especially its polymerization, are still unknown [106]. Melanin has been reported in fossils, and in dinosaurs. Both pheomelanin and eumelanin were detected from skin epidermal layers and scales of a 112-million-year-old *Borealopelta markmitchelli* [87], and eumelanin was detected in feather-like structures of a 150-million-year-old *Anchiornis huxleyi* [96].
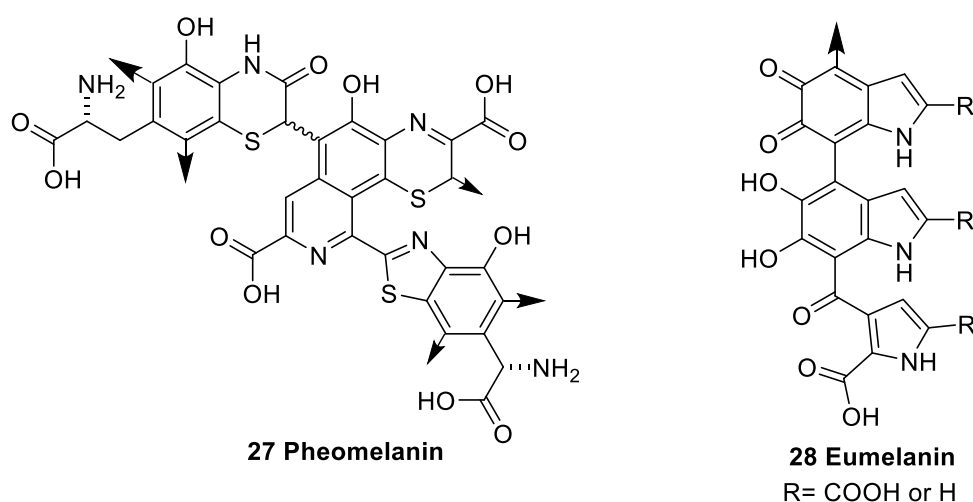
Figure 2.8. Structures of two types of the pigment melanin: pheomelanin and eumelanin.

Collagen

Collagen comprises a large family of proteins consisting of 28 types. It is the major protein present in vertebrate animals [109]. The most unique feature of collagen is its peptide backbone, which consists of a repeating tripeptide pattern of glycine-X-Y, which is commonly occupied as glycine – proline – 4-hydroxyproline (Figure 2.9(a)), although the X and Y positions can be any amino acid except tryptophan, tyrosine and cysteine [110]. The presence of glycine as every third residue is crucial for the stability of the triple helix, because sterically speaking, any other amino acid cannot fit there [109,111], and this was proven by mutational studies in which glycine was substituted, leading to a disruption in the structure of collagen [112]. The proline content of collagen is also important for the structure of the triple helix [111]. The presence of 4-hydroxyproline makes collagen stable to high temperatures [111,113]. Collagen

is stabilized by the high number of hydrogen bonds between the different alpha-chains constituting the triple helix [110,111].

(a)

Repeating peptide sequence of collagens
Glycine - Proline - 4-hydroxyproline

(b)

Type-I collagen
2 α1 and
1 α2 chains

Type-II collagen
3 α1 chains

~1.5 nm   ~300 nm   Telopeptide
(non-spiral part)
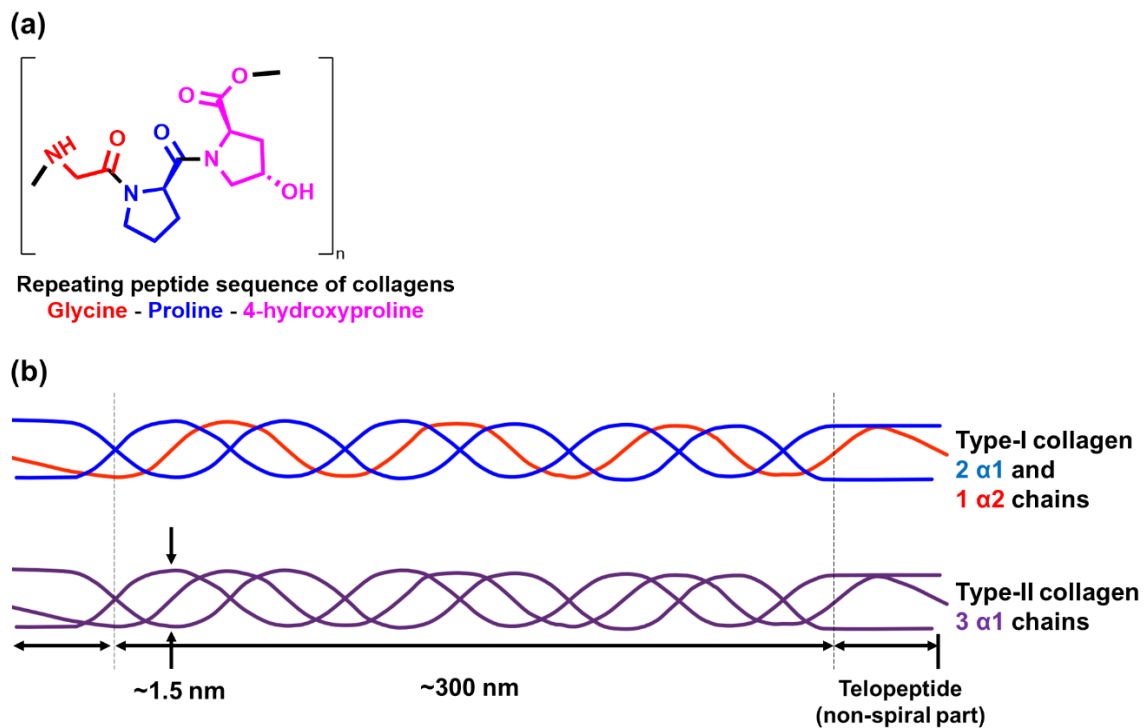
Figure 2.9. (a) Structure of the repeating peptide sequence of collagens: glycine – proline – 4-hydroxyproline. (b) the secondary structure of collagen type I and collagen type II, showing the difference between them with respect to the type of alpha-chains present. Adapted from [95].

Collagen is made up of three α-helices tightly folded in a compact structure, known as α-chains (Figure 2.9(b)). The two types of collagens detected in non-avian dinosaurs are collagen type I and type II. Collagen type I is present in many types of body parts such as bone, ligaments, tendons, and skin dermal layers, and its triple helix consists of two types of α-chains: two of the type α1(I) polypeptide chains and one of the type α2(I) chain (Figure 2.9(b)) [109].

Peptide fragments and partial sequences of collagen type I were detected from trabecular bone of a 68-million-year-old *Tyrannosaurus rex* [11,101], femur bones of an 80-million-year-old *Brachylophosaurus canadensis* [102,103], and from various bones of 75-million-year-old dinosaurs [80]. Characteristic infrared absorption bands for collagen type I were detected from the rib bone of a 195-million-year-old *Lufengosaurus* species [99]. Collagen type II is present in cartilage and the vitreous body of the eyes, and its triple helix consists of only one type of α-chain: three α1(II) polypeptide chains (Figure 2.9(b)) [109]. Type II collagen was detected

15

in the skull structure of a 75-million-year-old *Hypacrosaurus stebingeri* by immunohistochemical techniques [104].

Keratin

Keratin is an insoluble protein which is a major component of the outermost skin layer of reptiles and birds [114]. Keratin is a component of hair, nails, horns, beaks, claws and feathers [115]. The characteristic hard structure of keratin is attributed to its high number of cysteine residues (Figure 2.10(a)) that form stabilizing intramolecular and intermolecular disulfide bonds [115]. Other amino acids that are abundant in keratin are proline, serine and glycine, and minor amino acid constituents are methionine, lysine, and histidine (Figure 2.3(a)) [116,117]. Keratin is classified into two types exhibiting distinct physicochemical and structural properties: alpha-keratin and beta-keratin [114]. Alpha-keratin is predominant in hair, nails, and horns, whereas beta-keratin is found in feathers, beaks, and claws [115]. Alpha-keratins are composed of large molecular weight peptides (40-68 kDa), with an α-helical secondary structure (Figure 2.10(b)) which forms intermediate filaments with a diameter of 7 nm (Figure 2.10(c)) [114,115]. Beta-keratins are made up of small molecular weight peptides (10-20 kDa), having a pleated β-sheet secondary structure (Figure 2.10(b)) which forms filaments with a diameter of 3 nm (Figure 2.10(c)) [114,115]. In dinosaurs, beta-keratin was found to be preserved in feather-like structures from a 100-million-year old *Shuvuuia deserti* [55], and from claws of a 75-million-year old *Citipati osmolskae* [105].
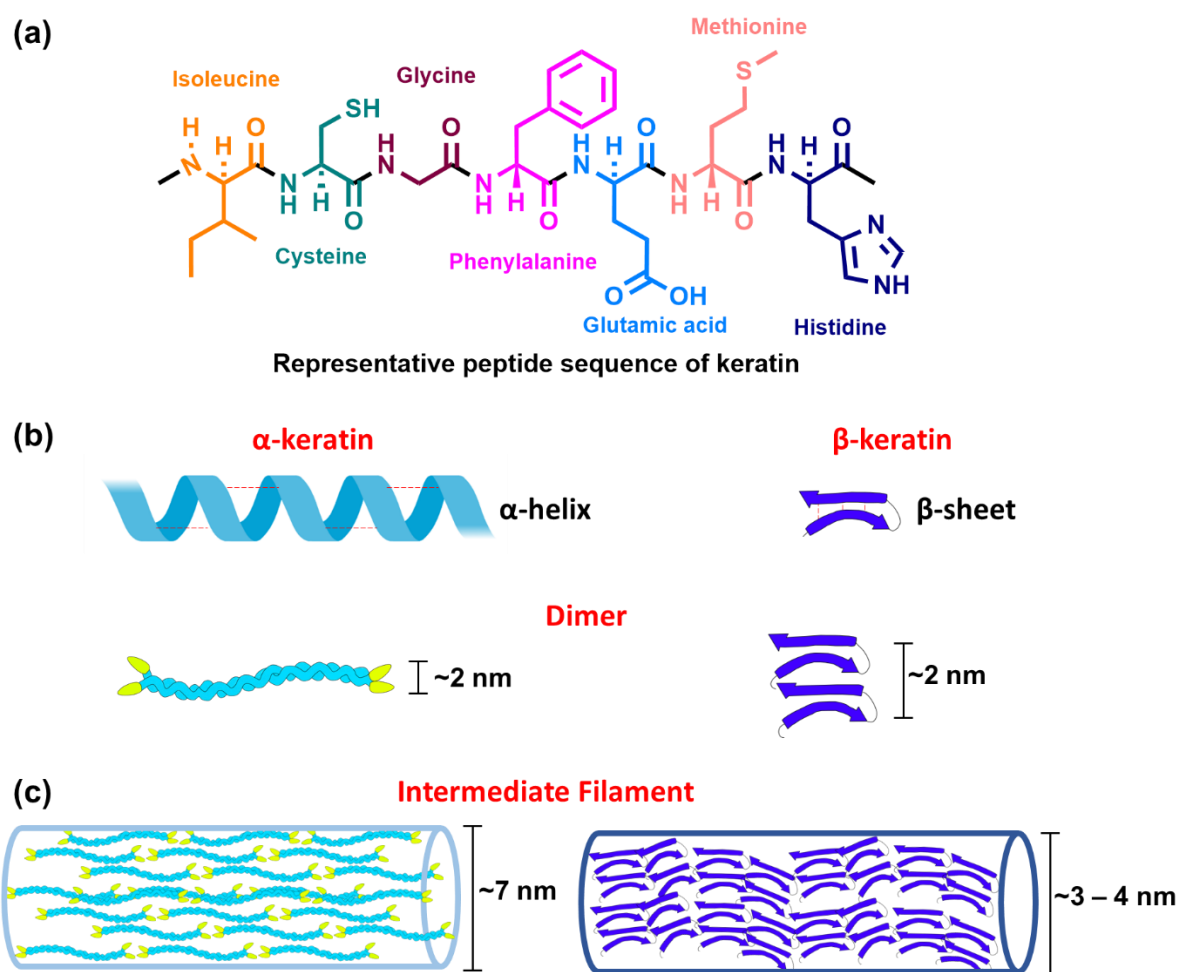
Figure 2.10. (a) Representative peptide sequence of keratin, (b) the secondary structure, and (c) the intermediate filaments of α- and β-keratin, showing their diameters. Adapted from [95].

2.5 An overview of selected analytical techniques used to study fossils

Fossils are usually analyzed using a combination of techniques which characterize the fossil descriptively or chemically [95,118,119]. The descriptive techniques include microscopy, which is divided into light microscopy, scanning electron microscopy, and transmission electron microscopy [119], and imaging techniques [118]. The techniques used for chemical characterization of fossils are spectroscopic and spectrometric methods, such as ultraviolet/visible light spectroscopy, Raman spectroscopy, infrared spectroscopy, and mass spectrometry (coupled to liquid or gas chromatography) [95,118,120]. This subsection will discuss principles of those analytical techniques that have been applied in the work of this dissertation: mass spectrometry, atomic absorption spectrometry, infrared spectroscopy, and ultraviolet/visible light spectroscopy.

17

2.5.1 Spectrometric methods

Mass spectrometry (in combination with high performance liquid chromatography or gas chromatography)

Mass spectrometry (MS) is a technique used for qualitative and quantitative analysis of gaseous and liquid samples. The main structural information gathered from mass spectrometric analysis is the determination of the molecular mass of an analyte of interest, and ideally the molecular formula can be predicted. A mass spectrometer can be used alone in case of pure analytes, or in combination with liquid (LC-MS) or gas chromatography (GC-MS) for separation of sample components from mixtures prior to identification. A mass spectrometer usually operates under vacuum and consists of a sample inlet, ionization source, mass analyzer, detector, and finally a computer needed for data generation and analysis. The sample inlet is used for direct injection of the sample gas or solution into the mass spectrometer if pure enough. Alternatively, a liquid or gas chromatography column connected to a mass spectrometer is used. Mass spectrometry relies on converting the sample molecules to ions, which depends on an ionization source in the instrument. Different types of ionization sources exist depending on the application, including electrospray ionization (ESI), chemical ionization, atmospheric pressure ionization, electron impact ionization, fast atom bombardment, and matrix-assisted laser desorption/ionization. ESI is among the most used ionization sources. The sample is ionized by means of an atomizer which generates very small droplets that easily evaporate the solvent and ionize the molecules by means of charge repulsions. The sample is carried forward to the mass analyzer by a carrier gas and changes in voltage. In the mass analyzer, the component ions of the sample will be passed on a path and separated according to mass. Preset parameters often will focus on certain masses and thus only a selected mass will make it to the detector. Various mass analyzers are available, such as quadrupole, time-of-flight, quadrupole-ion trap, magnetic sector, and ion cyclotron resonance devices. Some of these mass analyzers, such as the magnetic sector technique, offer a high resolution of masses up to several decimal points and enable the determination of exact or accurate masses, which is useful to distinguish compounds having the same nominal mass but slight changes in the exact mass. Detectors rely on sensing the ionic charge, amplifying the signal by passing ions through photomultipliers, and finally generating an electronic signal and a mass spectrum [121–123].

Mass spectra are a plot of the relative abundance of ions versus the mass-to-charge ratio (*m/z*) of the ions, from which the molecular mass can be deduced. As for the interpretation, in

addition to the molecular mass and the chemical formula, isotopic patterns can be seen. Moreover, a fragmentation pattern is generated for the compound, which can help in identifying unknown structures based on the mass of their fragments or the difference in mass between the original molecule and the fragment [122].

A variant of mass spectrometry, known as tandem mass spectrometry (MS/MS), utilizes two mass analyzers in series with an extra chamber in between known as collision chamber, in which parent compounds of a certain mass selectively enter and are fragmented to daughter ions. Both parent and daughter ions reach the detector, which offers increased selectivity and more information about a structure, as fragment ions are characteristic for compounds [123].

Atomic absorption spectrometry

Atomic absorption spectrometry (AAS) is a technique used for quantitative analysis of specific elements in a liquid sample. Therefore, the prerequisite is that one knows which element is to be analyzed. The principle of AAS relies on the fact that the outermost electrons of an atom get easily excited and emit photons as they absorb ultraviolet or visible light [124]. The sample's components are transferred into the gaseous phase and are detected as free atoms [125]. The elements that can be analyzed by AAS are usually metals because their valence electron can be easily excited, whereas non-metals are harder to be converted to free atoms [125].

Components of an atomic absorption spectrometric instrument are a source of radiation, monochromator, nebulizer assembly, atomizer, and detector. The source of radiation is specific to each element and emits only the wavelengths that would be specific for the element of interest. Different lamps are in use depending on the element being studied, which make this technique very selective, but usually a hollow cathode lamp is used [125]. The monochromator is the most crucial part of the instrument, because it allows only the wavelengths that are absorbed by the element to be transmitted to the detector and not the ones absorbed by the undesired elements. Thus, the monochromators contribute to the high selectivity and sensitivity of AAS. The nebulizer assembly is where the vaporization of the sample and the conversion to free atoms takes place. Liquid droplets of the sample are mixed with an oxidant gas and a fuel gas and are passed through an atomizer to be converted into very small droplets [125]. With the aid of a flame, the droplets are ignited, which leads to removal of solvent, evaporation to gas, and dissociation of sample components to free atoms [124]. The light energy transmitted

to the detector, which is made up of a photomultiplier tube, is converted to electrical signals proportional to the concentration of the sample, and is amplified using dynodes. Blank samples and standards are measured in the same manner as the samples, and subsequently a calibration curve is established, from which the quantity of an element can be calculated. AAS is typically applied in trace metal analysis (e.g., lead, silver, mercury, arsenic, or iron) in biological and environmental samples [124,125].

2.5.2 Spectroscopic methods

Infrared spectroscopy

Infrared (IR) spectroscopy is a technique mostly used for preliminary structural elucidation of a compound based on identifying characteristic chemical bonds and functional groups (qualitative analysis); it is less frequently used for quantitative analysis [126]. The IR region covers a wide range of 10,000 to 100 cm^{-1}; however, the near-IR region (4000-400 cm^{-1}) is the one typically relevant for the identification of compounds [127]. IR spectroscopy can be applied to organic and inorganic compounds present in the gaseous, liquid, and solid states [127]. Molecules which absorb IR radiation undergo a change of the dipole moment and their bonds perform molecular vibrations in the form of stretching or bending, but do not get excited beyond the ground energy level [126]. Every functional group absorbs IR radiation at a specific frequency, which is visualized as peaks in an IR spectrum. A special region of the spectrum, known as the fingerprint region (between 1200-700 cm^{-1}), is usually unique to a given compound. The IR spectrum, combined with structural information from mass spectrometry (molecular mass) and nuclear magnetic resonance spectroscopy (positional information), can help to identify a compound's structure. Usually, a comparison of the IR spectrum to that of a known compound is needed to be sure [126].

Regarding instrumentation, an IR spectrophotometer is composed of an IR radiation source, a monochromator, a sample holding compartment, and a detector [126]. The IR radiation source is a rod made of silicon carbide or a mixture of rare-earth metal oxides. The monochromator uses an optical device (known as diffraction grating) to filter out the light beams except for a certain wavelength. The sample holding compartment is used to place the sample and is made of transparent materials such as ionic salts (e.g., potassium bromide) or less soluble salts (e.g., silver chloride). Finally, the detector senses the heat from the IR radiation and converts this heat energy into an electric voltage. The main disadvantage of using IR is that atmospheric moisture and carbon dioxide interfere with analyses because they also absorb IR, requiring a

background measurement prior to sample analysis. A variant of IR spectroscopy known as Fourier-transform IR spectroscopy (FTIR) differs only in that it uses an interferometer instead of a monochromator, which enables the simultaneous measurement of absorption at several wavelengths, and therefore many fast measurements can be performed. FTIR requires a special software to convert raw data into IR spectra [127].

Ultraviolet-visible light spectroscopy

Ultraviolet-visible light spectroscopy (UV-VIS spectroscopy) is a technique used for qualitative and quantitative analysis of compounds which absorb light in the range of 185-760 nm. As absorbance is proportional to concentration, the amount of an analyte can be calculated based on an established calibration curve. UV-VIS active compounds have a chromophore showing characteristic wavelengths at which maximum absorption occurs, and this is used for their identification. The instrumental setup of a UV-VIS spectrophotometer is like that of an IR spectrometer, having a light source, a monochromator, a sample holding compartment, and a light-sensing detector. The light source consists of two lamps: a hydrogen or deuterium lamp (source of UV radiation) and a tungsten lamp (for visible light). The detector can either be a photomultiplier or a silicon photodiode. The concept of the photomultiplier is similar to that of AAS, using dynodes to amplify the signal and convert light energy to electrical signals, whereas the silicon photodiode uses a semiconductor instead of dynodes to generate an electrical response. In addition, the silicon photodiode is compact in size and can be arranged sequentially in an array to simultaneously detect absorption at wide wavelength ranges, which is advantageous. It is then known as a photodiode array detector (DAD) and is commonly used with high-performance liquid chromatography. The advantage is that both types of detectors are sensitive and can be used for low concentrations of analytes. UV-VIS spectrophotometers can be used independently or in conjunction with other techniques such as high-performance liquid chromatography [128].

2.6 Aims of this dissertation

Following this introduction to the basics needed to understand the background of the research performed and published in this dissertation, the aim of this work is to develop analytical methods for extracting and detecting various compounds from different types of specimens: biological (Chapters 6 and 7), taphonomic (Chapters 5, 9.1, and 9.2), and fossilized (Chapters 8 and 9.3) samples. Firstly, a comprehensive literature research was performed resulting in

detailed overview on the chemistry of porphyrins in fossils, presented in Chapter 3 as a published review article in the peer-reviewed journal *RSC Advances* (2021). An in-depth review on the organic compounds preserved and detected in non-avian dinosaurs and the analytical techniques used for this purpose is given in Chapter 4 as a published review article in the peer-reviewed journal *Biology (MDPI)* (2022). In Chapter 5, a molecular taphonomy study was performed on heme in order to understand its degradation behavior under a combination of simulated fossilization conditions, in which heme and its degradation products are analyzed by high performance liquid chromatography coupled to electrospray ionization mass spectrometry and a diode array detector (HPLC-(DAD)-ESI-MS). An article describing these results manuscript was recently published in a peer-reviewed journal. In Chapter 6, the development of a method for the extraction of heme from bones is presented, including challenges in obtaining high recovery rates for heme. An established and optimized extraction protocol is provided, using HPLC-(DAD)-ESI-MS as the method of detection. In Chapter 7, the extraction of two naturally occurring depsipeptides, FR900959 and YM-254890, used as selective $G\alpha_q$ inhibitors, from various murine organs, using HPLC-MS/MS, and their quantitative analysis is described after intratracheal and intraperitoneal administration for *in vivo* characterization. In addition, their stability in simulated gastric fluid and alkaline intestinal fluids was to be investigated for further *in vitro* characterization. This study was published in the peer-reviewed journal *ACS Pharmacology and Translational Science* (2021). In Chapter 8, evidence for the unique bark constituent suberin in a fossilized tree trunk is described using HPLC-(DAD)-ESI-MS analysis. The results provide evidence that the outermost layer of the fossil was bark. In Chapters 9-11, several collaboration projects are discussed, in which calcium concentrations are quantified from the crayfish *Cambarellus diminitus* using AAS (Chapter 9), adipocere components are extracted and identified from the same decaying crayfish species using HPLC-(DAD)-ESI-MS (Chapter 10), and IR spectra providing evidence of lignin constituents in a sample of silicified fossil wood (Chapter 11). Two of these studies have been already published in peer-reviewed journals, while the third publication is in preparation.

3. Chemistry of porphyrins in fossil plants and animals

Mariam Tahoun, Carole T. Gee, Victoria E. McCoy, P. Martin Sander, and Christa E. Müller

RSC Adv., **2021**, 11(13), 7552-7563, doi: 10.1039/d0ra10688g

Introduction

Porphyrins are natural pigments found in a broad selection of plants and animals, generally having a tetrapyrrolic ring structure connected with methine bridges. Often, they are complexed with a central metal ion such as Fe^{2+}, Mg^{2+}, Cu^{2+}, and Zn^{2+}, yielding metalloporphyrins [129]. Many exceptionally well-preserved fossilized hard and soft tissues, such as digestive organs, eggshells, red blood cells, bone osteocytes, and muscle cells, have been described. However, very few fossils have been chemically analyzed for their content of small organic molecules [9]. The field of molecular paleontology investigates small organic molecules in fossils or their diagenetic products in decaying organisms using a combination of analytical techniques [3]. Due to their physicochemical properties, porphyrins can resist decay. For instance, heme, the prosthetic group of the blood protein hemoglobin, was detected in several samples in the fossil record. The first report was from trabecular bone extracts of a 66-million-year-old tyrannosaur *Tyrannosaurus rex*, detected by high performance liquid chromatography coupled to ultraviolet-visible light detection [68]. The second report of heme was from the abdomen of a 46-million-year-old female fossil mosquito (*Culiseta spp.*), and was detected using time-of-flight secondary ion mass spectrometry [69]. Fragments of heme were found in a 54-million-year-old fossil sea turtle (*Tasbacka danica*) after time-of-flight secondary ion mass spectrometric analysis [56]. Moreover, biliverdin, a degradation product of heme with a linear tetrapyrrole chain, and protoporphyrin IX, the iron-free derivative of heme, have been detected in extracts of eggshells from the 66-million-year-old oviraptorid dinosaur *Heyuannia huangi* using high-performance liquid chromatography coupled to electrospray ionization time-of-flight mass spectrometry [89].

Chlorophylls are closely related natural pigments to porphyrins. Different classes of chlorophylls are found in higher plants (chlorophylls), photosynthetic algae (*Chlorobium* chlorophylls), and cyanobacteria (bacteriochlorophylls) [130,131]. Selected chlorophyll metabolites – pheophytin *a* and pheophorbide *a* – have been detected in fossil leaves located in Geiseltal (Halle, Germany) [66] and Clarkia Flora deposits (Idaho, USA) [132].

The oldest porphyrin reported was from 1.1 billion-year-old sediments and its structure was assumed to be derived from chlorophyll *a* [65]. This was in agreement with the chemical changes that occur during fossilization, proposed by Alfred Treibs, who suggested that a combination of processes occur during the fossilization of heme and chlorophyll *a*: demetallation (of iron or magnesium), reduction, aromatization, ester hydrolysis, decarboxylation, and trans-metalation (formation of a coordination complex with nickel or vanadium oxide) [72,73].

This review aims to compile all the chemical aspects and relevant evidence of porphyrins in the fossil record.

Summary and outlook

The article starts out with an introduction into the chemistry of porphyrins, with a focus on the nomenclature, structures, and physicochemical properties of representative compounds (heme, biliverdin, bilirubin and protoporphyrin IX, chlorophylls, bacteriochlorophylls and their degradation products), including the characteristic Soret band in the UV-visible light region which is used for their identification. This is followed by a detailed overview of porphyrins discovered in the fossil record, with brief mention of porphyrins found in sediments. For each of the compounds, the identified structures are shown and the analytical technique used for their detection is described with reference to the original literature. In addition, a suggested pathway for the structural changes that occur during fossilization is proposed for heme and chlorophyll *a*.

Several of the compounds listed – for example heme, and chlorophyll metabolites such as pheophytin *a* and pheophorbide *a* – have been detected using preliminary analytical methods (UV spectra) and the findings have since then never been confirmed and reported in more recent publications. This emphasizes the need for future discoveries of porphyrins in fossils, especially considering the latest advancements in highly sensitive analytical techniques and instrumentation.

Author contribution

The doctoral student prepared all figures in the manuscript (except Fig. 4, 5, and 13), analyzed the literature, and wrote the main text under supervision of and with contributions by Prof. Dr. Christa E. Müller and the co-authors.

4. Chemistry and analysis of organic compounds in dinosaurs

Mariam Tahoun, Marianne Engeser, Vigneshwaran Namasivayam, P. Martin Sander, and Christa E. Müller

Introduction

The process of decay after an organism's death can exceptionally be halted if exposed to favorable conditions, under which a fossil forms. Some organic compounds may thus be preserved for millions of years. Reports on the preservation of soft tissues and their associated organic compounds in many plants and animals have been increasing over the past decades [9]. This is mainly due to the development of sensitive analytical techniques that allow trace analysis. Molecular paleontology is the field concerned with the extraction, analysis, and detection of organic compounds found in fossils [12]. The analytical techniques used in this field are usually a combination of destructive and non-destructive methods [118–120,133]. The sample is not recoverable after using destructive methods, which include liquid chromatography coupled to tandem mass spectrometry (LC-MS/MS), time-of-flight secondary ion mass spectrometry (ToF-SIMS), and immunological techniques such as Western blot analysis, enzyme-linked immunosorbent assays (ELISA), and immunohistochemistry. In contrast, non-destructive methods preserve the sample for re-analysis and are usually favored by paleontologists because fossil material is rare and precious. The non-destructive methods include light microscopy, scanning electron microscopy (SEM), transmission electron microscopy (TEM), spectroscopic methods such as Fourier-transform infrared spectroscopy (FTIR) and Raman spectroscopy.

Turning the attention to dinosaur fossils, soft tissue preservation has gained interest since the 1960s when the first microstructures were reported by Pawlicki [134]. With the advent of the above-mentioned analytical techniques around the late 1990s, reports on preserved organic compounds started to appear at an increasing rate (e.g., [9,11]). These organic compounds belong to two main chemical classes: Pigments and proteins. The pigments detected include porphyrins (heme, protoporphyrin IX, and biliverdin) and melanins (pheomelanin and eumelanin). Porphyrins are biologically relevant pigments that are present in many organisms and consist of a tetrapyrrole ring connected by methine bridges and often complexed with a

metal ion in the center [64]. Melanins are skin pigments that consist of five different classes depending on the precursor and type of tissue: eumelanin, pheomelanin, pyomelanin, allomelanin, and neuromelanin [135].

The proteins detected comprise collagen type I, collagen type II, and β-keratin. Collagen types I and II consist of three alpha-chains usually consisting of the repetitive pattern of glycine - proline - hydroxyproline. Collagen type I has two different types of α-chains (α1 and α2), whereas type II only has type α1 [136]. Keratin is a protein with many functions that usually contains a high amount of cysteine, glycine, proline, and serine in its sequences, and rarely contain lysine, histidine, and methionine. According to its secondary structure, it is classified into α-keratin and β-keratin [137].

Proteins are especially subject to debates about their true origins when detected in fossils, because, from a chemical perspective, amino acids can easily be degraded and therefore protein sequences are not expected to be detected in fossils [120,138]. The organic compounds that have been found in non-avian dinosaurs and information on their detailed chemistry and analytical techniques used for their identification had not been compiled to date. This review aims to collect all this information and to provide insights into future molecular paleontological research.

Summary and outlook

The article starts out with an introduction into preservation of organic compounds in fossils and then provides a detailed overview of the analytical techniques that are used for the detection of organic compounds in dinosaur fossils. The principles and applications of each destructive and non-destructive analytical technique are discussed. Techniques applied so far for analyses of dinosaur fossils are high-performance liquid chromatography coupled to ultraviolet-visible light detection (HPLC-UV/VIS) or to quadrupole/time-of-flight mass spectrometry, ToF-SIMS, Raman spectroscopy, SEM, infrared spectroscopy, Western blot, ELISA, and immunohistochemistry.

This part is followed by presenting the organic compounds found in non-avian dinosaurs, namely pigments and proteins, focusing on their detailed structures and chemical classes, locality of the fossils and type of tissue in which they were detected, and methods of analysis. Non-avian dinosaur fossils of varying ages and associated preserved organic compounds (pigments and proteins) have been detected in Canada, China, Mongolia, and USA from different tissues. Pigments were detected from trabecular bone of *Tyrannosaurus rex* [68],

eggshells of *Heyuannia huangi* [91,98], tail filaments of *Sinosauropteryx* and *Sinonithosaurus* [85], outer scales of *Psittacosaurus* [97], feather-like structures of *Anchiornis huxleyi* [96], and outer skin layers of *Borealopelta markmitchelli* [87]. Proteins were identified from trabecular bone of *T. rex* [11,101], rib bone of *Lufengosaurus sp.* [8], hind limb femur bone of *Brachylophosaurus canadensis* [102], skull cartilage of *Hypacrosaurus stebingeri* [104], feather-like structures of *Shuvuuia deserti* [55], and claws of *Citipati osmolskae* [105].

This list of analyzed dinosaur fossils is expected to grow in number over the coming years, as more sensitive analytical techniques are continuously developed.

Author contribution

The doctoral student prepared all figures in the manuscript, analyzed the literature, and wrote main text under supervision of and with contributions by Prof. Dr. Christa E. Müller and the co-authors.

5. Molecular taphonomy of heme: Chemical degradation of hemin under presumed fossilization conditions

Mariam Tahoun, Marianne Engeser, Luca Svolacchia, P. Martin Sander, and Christa E. Müller.

Introduction

Heme is the molecule responsible for the oxygen-carrying functions of the blood protein hemoglobin. Structurally, it is a metalloporphyrin consisting of a tetrapyrrole ring with a central iron atom. In addition to the four pyrrolic nitrogen atoms, iron can form coordinate bonds with oxygen, water, and other ligands [64,139]. Several degradation pathways for heme have been described. The enzymatic degradation by heme oxygenase is by far the most studied pathway, in which heme is oxidatively cleaved to the linear tetrapyrrole derivative biliverdin; this constitutes the *in vivo* pathway of degradation [140]. There are other degradation pathways, e.g., the enzyme nicotinamide adenine dinucleotide phosphate (NADPH)-cytochrome P450 reductase and chemical degradation by oxidative agents such as chromic acid and hydrogen peroxide, that do not produce biliverdin but degrade the tetrapyrrole ring further to monopyrrolic (hematinic acid and methylvinylmaleimide) and dipyrrolic structures (propentdyopents) [141–143].

Heme and its structurally related derivatives protoporphyrin IX and biliverdin have been reported to survive for millions of years in various types of fossils such as mosquitoes [69], sea turtles [56], the trabecular bones of the tyrannosaur *Tyrannosaurus rex* [68], and dinosaur eggshells [89]. However, the mechanism and processes by which heme is preserved have not yet been fully elucidated. To understand the fossilization of heme and study its degradation, molecular taphonomy studies, in which a molecule is studied under controlled conditions related to fossilization, and by which a degradation profile is established, can help in understanding the selective persistence of certain classes of compounds in the fossil record [3]. This type of study has not been performed on heme. Accordingly, the following manuscript aims to study and elucidate the degradation of heme under a variety of conditions presumed to occur during fossilization, such as altering pH values between neutral and alkaline pH,

reductive conditions, oxidation, aerobic and anaerobic conditions. Heating was used for accelerated degradation. Hemin, the Fe(III) derivative and analytical standard of heme, was used for the experiments. The following manuscript was published in the peer-reviewed journal *Molecules* in June 2023.

Summary and outlook

Hemin was exposed to a combination of conditions presumed to occur during decay and fossilization, and resulting degradation products were elucidated to understand its degradation profile. At least four major degradation products were identified and elucidated by high performance liquid chromatography coupled to tandem mass spectrometry (HPLC-MS/MS). Hemin was found to be most unstable under oxidative conditions after using hydrogen peroxide, by which hemin is rapidly and completely degraded to the monopyrrole hematinic acid, as isolated and confirmed by nuclear resonance spectroscopy (NMR) and high-resolution tandem mass spectrometry. Hemin was more stable while heating in the absence of air (half-life 5.5 days) than in the presence of air (half-life 2.6 days). In addition to the effect of air, the observed higher stability may also be attributed to the differences in pH values (8 vs. 7.4, respectively) or to the slight change in temperatures (70ºC vs 75ºC, respectively). In both cases, a common degradation product termed DP-1 was produced. Only under anaerobic conditions, at least two further degradation products (DP-2 and DP-3) were formed.

Structural characterization of DP-1 (618 *m/z*), DP-2 (620 *m/z*) and DP-3 (636 *m/z*) by HPLC-MS/MS led to the assumption that hemin's vinyl groups are the main reason for its degradation under these conditions. This was confirmed by testing a related synthetic derivative of hemin, known as mesohemin, which has ethyl groups instead of vinyl groups, under the same conditions, under which no degradation occurred. Thus, DP-1 and DP-2 were determined to be derivatives of hemin in which one or both vinyl groups are oxidatively cleaved to formyl groups, respectively, and DP-3 is likely formed as a result of further oxidation of one of the formyl groups to carboxylic acid. This is the first evidence of these degradation products obtained by mass spectrometry.

Under anaerobic reductive conditions, hemin was most stable (half-life 9.5 days). In this case, DP-1 was a minor degradation product, and a compound with a mass of 650 *m/z* was the major degradation product. The latter could not be further characterized but our results suggest that the increased stability under anaerobic reductive conditions are associated with a different

degradation pathway than the observed cleavage of the vinyl group to a formyl group in the presence of oxygen.

Furthermore, testing of protoporphyrin IX proved that iron is crucial for the degradation because the iron-free compound remained moderately stable throughout the experiment under anaerobic conditions. This is in support of previous reports that high-valent iron complexes are essential for the degradation of heme [141,142,144].

These results show that in principle heme is stable enough to be detected in fossils, and more reports can be expected in the future. This calls for further studies on the analysis of heme in fossils.

Author contribution

The doctoral student performed all experiments with exception of the high-resolution tandem mass spectrometry measurements, prepared all figures in the manuscript and the Supplementary Information with the exception of Figure 7 and Figures S3-S4, and wrote the main text together with Prof. Dr. Christa E. Müller and PD Dr. Marianne Engeser with contributions by the other co-authors.

5. Molecular taphonomy of heme: Chemical degradation of hemin under presumed fossilization conditions

6. Establishment and optimization of protocols for heme extraction from recent bones

6.1. Introduction and preliminary work

Bone composition

Bones are hard tissues that protect the organs, forming the basic skeleton of an organism. In addition, bone is the site of formation of blood cells (bone marrow), and the site of storage of minerals (especially Ca^{2+}) in the body [145]. Bone is composed of an organic phase (30% by volume, also known as the extracellular matrix) and an inorganic phase (70% by volume). The organic phase is mainly composed of collagen type I protein (90%), minor non-collagenous proteins (5%, e.g., osteocalcin) and lipids (2%) [146]. Cells and blood vessels are part of the organic phase [147]. The cells present are osteocytes, osteoclasts, and osteoblasts. Osteoblasts build up bone, whereas osteoclasts break down bone for re-modelling and repair [145]. The inorganic phase of bone consists predominantly (90%) of calcium phosphate $(Ca_{10}(PO_4)_6(OH)_2)$ crystals, known as hydroxyapatite, which fill up the spaces between the organic phase components and are responsible for the rigidity of bone [148].

Soft-tissue preservation in bones

The organic phase of bone in dinosaur fossils has been analyzed since the 1960s when the first reports of preserved soft tissues and bone proteins in fossil dinosaur bone were published [134,149]. However, due to the primitive techniques and few follow-up studies to back this up at that time, details of the preserved structures did not become very clear. Since 2005, as more advanced techniques were developed, there have been a number of reports mainly by the workgroup of Mary Schweitzer and colleagues who isolated and detected osteocytes, blood vessels, cartilage, and collagen type I fragments after digestion of mineralized fossil dinosaur bone [11,82,103,104,150–152].

Despite the reports of preserved soft tissues in fossil bones, the source of these detected structures is still debatable, as some groups claim that the identified structures originate from biofilms produced by micro-organisms during bone decay [24,81,153,154], which became co-crystallized among the mineral deposits during later stages of fossilization [153]. Current evidence indicates that the soft tissues were originally belonging to the fossil; nevertheless, proving that these structures belong to the fossil bone requires further analysis using a

33

combination of analytical techniques (e.g., immunohistochemistry, microscopy, and mass spectrometry) [81,151,152,155].

Additionally, most recent work on fossil bones seems to suggest that iron compounds play an important role in the preservation of soft tissues in bone, especially through complexation. The source of iron is thought to be from heme in hemoglobin, presumably originating from the blood vessels of the bone, as it is expected to have been rapidly incorporated during the early stages of fossilization [80,81,99,151]. However, heme was only reported once in the fossil record of bone [68]. We hypothesize that heme might be more frequently preserved fossilized bones.

Preliminary work

As part of the DFG research unit FOR 2685 "Fossilization," preserved organic compounds in fossil dinosaur bone were to be analyzed. Special interest has been focused on the extraction and detection of heme as a degradation product of hemoglobin, and the question whether heme or its degradation products are preserved in fossil bones. This is because the early evidence for the presence of heme in fossil bone has not been confirmed since it was reported to have been found in trabecular bone of *Tyrannosaurus rex* in 1997 [68]. Moreover, heme was only detected using its characteristic UV band, which, although it is specific for porphyrin compounds, constitutes a preliminary method of detection. In our group, we aim trace analysis of heme in fossil dinosaur bone using highly sensitive mass spectrometry. However, first, we needed to develop and optimize an extraction method for heme with a high recovery rate.

Previous work in our group to address the extraction of heme from fossil bones was to develop a protocol using recent bones first, with the aim that the optimized extraction method would be applied to fossil bone afterwards. The sensitive analysis of heme and related compounds out of biological matrices turned out to be demanding due to heme's chemical properties, despite using a sensitive quadrupole-time-of-flight mass spectrometer (q-TOF-MS). A published protocol used for extraction of heme from dinosaur trabecular bone was tested [68]. The solution consisted of 0.3 M NaCl, 5% glycerol, 5 mM dithiothreitol (DTT, to reduce the disulfide bonds of proteins), 2 mM ethylenediaminetetraacetic acid (EDTA, for metal chelation and demineralization), 1% 3-[(3-cholamidopropyl)dimethylammonio]-1-propanesulfonate (CHAPS, detergent for solubilizing membrane proteins and breaking protein-protein interactions), 6 M guanidine hydrochloride (unfolds proteins, decreases enzymatic activity, increases solubility of hydrophobic molecules) and 100 mM

tris(hydroxymethyl)aminomethane hydrochloride (TRIS-HCl, buffer to keep pH between 7.0-9.0). Fossil bone powder is incubated for a period of time and then centrifuged. The supernatant is then dialyzed to remove the ions. The extract is subsequently concentrated by lyophilization. However, this procedure revealed a poor recovery rate of heme due to its poor solubility in the buffer.

Another method was studied, in which recent deer bones were ground in a mill, and the resulting powder was incubated with methanol containing 1% of NH_3 followed by centrifugation. The supernatant was analyzed for heme after reducing the volume of the solvent. For comparison, samples spiked with heme and hematin were subjected to the same procedure. The recovery rate using methanol/1% NH_3 was around 7% and needed to be improved.

Overall, there are several challenges while extracting heme. Heme, due to its lipophilic property, tends to adsorb to surfaces, and the poor recovery was the result of a combination of different factors: Limited solubility in the extraction buffer, adsorption onto beads used for homogenizing the bone tissue, adsorption onto the inner surface of the Eppendorf tubes, adsorption to the bone tissue itself, and the extraction power of the buffer in recovering heme. In addition, certain buffer components were not compatible with mass spectrometric detection, which complicated the workup of this method of extraction. As a result, a new method had to be developed.

In literature, described bone extraction protocols included prior demineralization of bone using weak organic acids (e.g., acetic acid or citric acid) or dilute strong acids (such as HCl) or the complex-forming ligand EDTA [156,157]. However, the focus on those published protocols was on protein extraction, especially of collagen type I. Therefore, they cannot be directly applied to the extraction of heme. In addition, the acids may possibly degrade organic compounds, such as heme, in an uncontrollable manner, if the bones are incubated for a long period of time with the bone.

This chapter aims to present efforts to develop and optimize a protocol for the extraction of heme from bones, and to provide an overview of the challenges that had to be overcome. Here we apply extraction protocols for heme from different biological matrices, such as plants [158], micro-organisms [159], and animal bone. This includes the calculation of the resulting recovery rates, aiming to improve the recovery of heme from bone matrices. We use cow (*Bos taurus*) bone as a recent bone control sample for developing the extraction protocol. High-performance liquid chromatography coupled to electrospray ionization mass spectrometry and diode

array/UV detection [HPLC-(DAD/UV)-ESI-MS] is employed to compare the efficiency of different extraction reagents and calculate the recovery rate. As this is a different device than the one used in the previous studies, a new analytical method for heme detection was first optimized. Finally, throughout this chapter, the commercially available ferric iron form of heme, known as hemin, will be used as a standard for heme, and therefore the terms "heme" and "hemin" will thus be used interchangeably.

6.2. Materials and Methods

Chemicals and Reagents

Hemin chloride was purchased from Sigma Aldrich (Darmstadt, Germany). Millipore water was used for LC-MS analysis (from an in-house Millipore water purification system, Darmstadt, Germany). LC-MS grade methanol was purchased from Honeywell (Offenbach/Main, Germany). Acetonitrile (LC-MS grade), formic acid (LC-MS grade) and hydrochloric acid (37%) were purchased from VWR Chemicals (Darmstadt, Germany). Analytical grade ammonia solution (25% in water) was purchased from Chemsolute (Renningen, Germany). Ammonium acetate (LC-MS grade) and acetone (p.a.) were purchased from Merck (Darmstadt, Germany). Protein LoBind Eppendorf tubes were purchased from Eppendorf SE (Hamburg, Germany).

Sample preparation

Cow bone was cut into thin sections (ca. 2.5 x 1 cm, L x W) using a diamond mill (done by Olaf Dülfer, Paleontology Department, University of Bonn). This was followed by milling in a Retsch MM400 ball mill, for around 2-3 min at 30 Hz after freezing the samples in liquid nitrogen to make them more brittle and to avoid exposing the bone to the increasing heat within the milling chamber.

6.3. Extraction methods and calculation of recovery rate

Extraction reagents

The following reagents were tested for extraction of heme from bones (Table 6.1).

Table 6.1. Extraction reagents tested for extraction of heme from bones.

Designation	Solvent mixture	Preparation
A	Methanol/1% NH_3	192 ml methanol + 8 ml of 25% aq. NH_3 solution
B	Acetone/10mM NH_4OH (8:2, v/v)	8 ml acetone + 2 ml of a 10 mM solution of NH_4OH
C	Acetone/Water (8:2, v/v)	8 ml acetone + 2 ml of Millipore water
D	Acetone/1.6 M HCl (8:2, v/v)	8 ml acetone + 2 ml of a 1.6 M HCl solution
E	Acetonitrile/1.6 M HCl (8:2, v/v)	8 ml acetonitrile + 2 ml of a 1.6 M HCl solution

Method for determining the recovery rate

For the employed solid-liquid extraction, a recovery rate must be calculated to evaluate the efficiency of extraction. The recovery rate is specific for each compound and matrix. For the quantification of samples containing unknown amounts of analyte, the recovery rate is considered as a correction factor to compensate for the loss of analyte during extraction. Extraction methods were established and optimized, and the recovery rate for the extraction of hemin from bone was calculated. For this purpose, bone powder (25 mg) was spiked with various amounts of hemin. Them the mixtures were incubated with extraction reagent, homogenized, centrifuged, and the hemin was quantified by the optimized HPLC-(DAD/UV)-ESI-MS method.

For this purpose, a preliminary extraction protocol was used, and subsequently modified.

Addressing previous challenges of hemin extraction from bone

The poor recovery rate of hemin by our previously used extraction method may be attributed to several reasons, which were addressed separately in a stepwise manner. These were (1) adsorption of hemin to the surfaces of the tubes, (2) adsorption to the beads of the TissueLyzer device used for homogenization, and (3) poor suitability of the solvents used for extraction.

First, to address the problem of adsorption of hemin onto the surfaces of the standard polypropylene sample tubes, a different type of Eppendorf tubes, known as LoBind Eppendorf tubes was employed. The recovery rate was calculated using methanol/1% NH_3 for extraction, with and without using the stainless steel or zirconium oxide beads for homogenization. Bone powder (25 mg) was weighed into each tube and the following samples were prepared: 3 controls (to which only methanol/1% NH_3 is added), and 3 samples (final concentration 25 µM hemin). Different beads were tested for homogenization and for their effect on recovery. Each combination of sample and control was tested after adding 2 beads of stainless steel, zirconium oxide, or no beads at all. The tubes were incubated with extraction buffers, and the bone was homogenized using a TissueLyzer LT (Qiagen, Venlo, Netherlands) for 10 min at 50 Hz. This step was followed by centrifugation (20,000g, 10 min, 4°C). The supernatant was transferred into HPLC vials, and analyzed by HPLC-(DAD/UV)-ESI-MS. Standard solutions of hemin (0.05-50 µM) were also measured in the same run. Negligible adsorption to the surface of the Eppendorf tube was confirmed using a calibration curve. Thus, these Eppendorf tubes were suitable for handling heme solutions.

To address the second issue regarding adsorption of hemin to the beads used in the TissueLyzer, the recovery rate of hemin was calculated using methanol/1% NH_3 and was found to be 14% using stainless steel beads, and 19% using zirconium oxide beads. Since the use of zirconium oxide-coated beads led to a slightly better recovery rate for heme than employing stainless steel beads, they were selected for further homogenization experiments.

Finally, after addressing the problems due to adsorption of heme to tubing and beads, it was clear that the main issue responsible for the low recovery of hemin was the poor extraction using methanol/1% NH_3 as a solvent. This was due to precipitation of hemin in the pellet after extraction, showing that methanol/1% NH_3 was not optimal for extraction. As this precipitation occurs during the homogenization step, this step is the determining factor for the recovery of heme from bone. This same issue was observed when the following extraction buffers were considered: Acetonitrile/0.1% HCO_2H; acetonitrile/1% HCO_2H; acetonitrile/HCO_2H (8:2,

v/v); methanol/2 mM NH_4OAc/0.1% HCO_2H; and water/2 mM NH_4OAc/0.1% HCO_2H. Hemin was insoluble, and co-precipitated with the pellet after homogenization and centrifugation, rendering the procedure without any significant recovery rate.

Influence of bone matrix on extraction and recovery rate of heme: Matrix effect

Furthermore, the bone matrix itself may negatively affect the detection of hemin and thus the recovery rate. To test this hypothesis, a parameter known as matrix effect was determined. The matrix effect is a measure of the influence of the sample matrix on detection. A matrix effect below 100 means that a signal suppression occurs, a value close to 100 means the absence of a matrix effect, while a value above 100 means that the matrix enhances the signal [160]. The matrix effect is specific for each solvent and matrix, and is calculated according to Eq. (1), using the peak area of the same solution of hemin in solvent without adding bone tissue or beads (i.e., matrix-free) [160].

$$Matrix\ effect\ (\%) = \frac{Peak\ area\ of\ spiked\ sample\ in\ matrix}{Peak\ area\ of\ standard\ in\ matrix-free\ solvent} \times 100 \qquad \text{Eq. (1)}$$

Table 6.2 summarizes the values of the matrix effects for selected extraction reagents. The greatest signal suppression due to the matrix occurs after using methanol/1% NH_3 (23.5% matrix effect), followed by moderate signal suppression (84%) when using acetone/water (8:2, v/v) (84%). Only a minimal matrix effect (95%) was observed upon using acetone/10 mM NH_4OH or acetone/1.6 M HCl (8:2, v/v) (Table 6.2). Note that these are only preliminary data and would need to be repeated for confirmation if needed.

Table 6.2. Matrix effect determined for different extraction reagents in a preliminary study.

Extraction reagent	Matrix effect
Methanol/1% NH_3	23.5%
Acetone/10 mM NH_4OH (8:2, v/v)	95%
Acetone/Water (8:2, v/v)	84%
Acetone/1.6 M HCl (8:2, v/v)	95%
Acetonitrile/1.6 M HCl (8:2, v/v)	n.d.

Therefore, in order to compensate for the suppressive effects of the matrix, the idea was to use a standard having the same matrix as the sample (known as a matrix-equaled sample), and this standard is set at 100% recovery. This was achieved by spiking known concentrations of hemin into bone matrix which was exposed to all the extraction steps (post-extraction spiking), just

before measurement, and comparing it to a sample spiked with the same concentration of hemin at the beginning of the extraction procedure (pre-extraction spike). Matrix-equaled standards were then used for the calculation of recovery rates using peak areas [161,162].

Final optimized extraction method

This optimized extraction protocol was used for the extraction of heme from powdered bone samples. Extraction reagents applied to this method were acetone/1.6 M HCl (8:2, v/v) [158] and acetonitrile/1.6 M HCl, 8:2, v/v) [159].

The final extraction protocol of heme from bones and the recovery rate calculation are as follows (see Figures 6.1 and 6.2 for illustrations on the steps):

1. Ground bone samples (25 mg) were weighed into Eppendorf tubes.
2. Extraction buffer was added to bone samples: for zero control and post-extraction spiked samples, 1 ml; for pre-extraction spiked samples, 0.9 ml extraction buffer and 0.1 ml of a 100 µM hemin solution (dissolved in water/0.1% ammonia). The final concentration is 10 µM hemin. Samples (pre- and post-extraction spiked) were prepared in replicates of 2 to 3, and the zero control was only one sample.
3. The bone samples were incubated in a freezer (-20°C) for 30 min to facilitate protein precipitation.
4. All samples were homogenized in the TissueLyzer LT (Qiagen, Venlo, Netherlands) for 15 min at 50 Hz, with the aid of 2 zirconium oxide beads added to each tube prior to homogenization.
5. The samples were directly centrifuged (20,000g, 20 min, 4°C). Supernatant was transferred to a new Eppendorf tube. For post-extraction spiked samples and 10 µM standard solutions, 0.9 ml of supernatant was mixed with 0.1 ml of a 100 µM hemin solution, and vigorously mixed (to give a final concentration of 10 µM hemin). For the other calibration standard solutions, the amount of supernatant transferred depended on the concentration.
6. The new tubes were centrifuged (20,000g, 45 min, 4°C) to ensure clarity of the solution before injecting them into the instrument. Supernatants (0.2 ml) were transferred into an HPLC vial with a glass-insert and measured using the developed HPLC-(DAD/UV)-MS method.

1 | Bone (25 mg)

Pre-extraction spiking solution added

2 | 1 ml extraction reagent   Control

3 | Incubation at -20ºC, 30 min

2 beads of zirconium oxide added to each tube

4 | Homogenization in TissueLyzer, 15 min, 50Hz

5 | Centrifugation (20,000*g*, 20 min, 4°C)

Supernatant transferred to new tube; Post-extraction spiking solution added

6 | Centrifugation (20,000*g*, 45 min, 4°C)

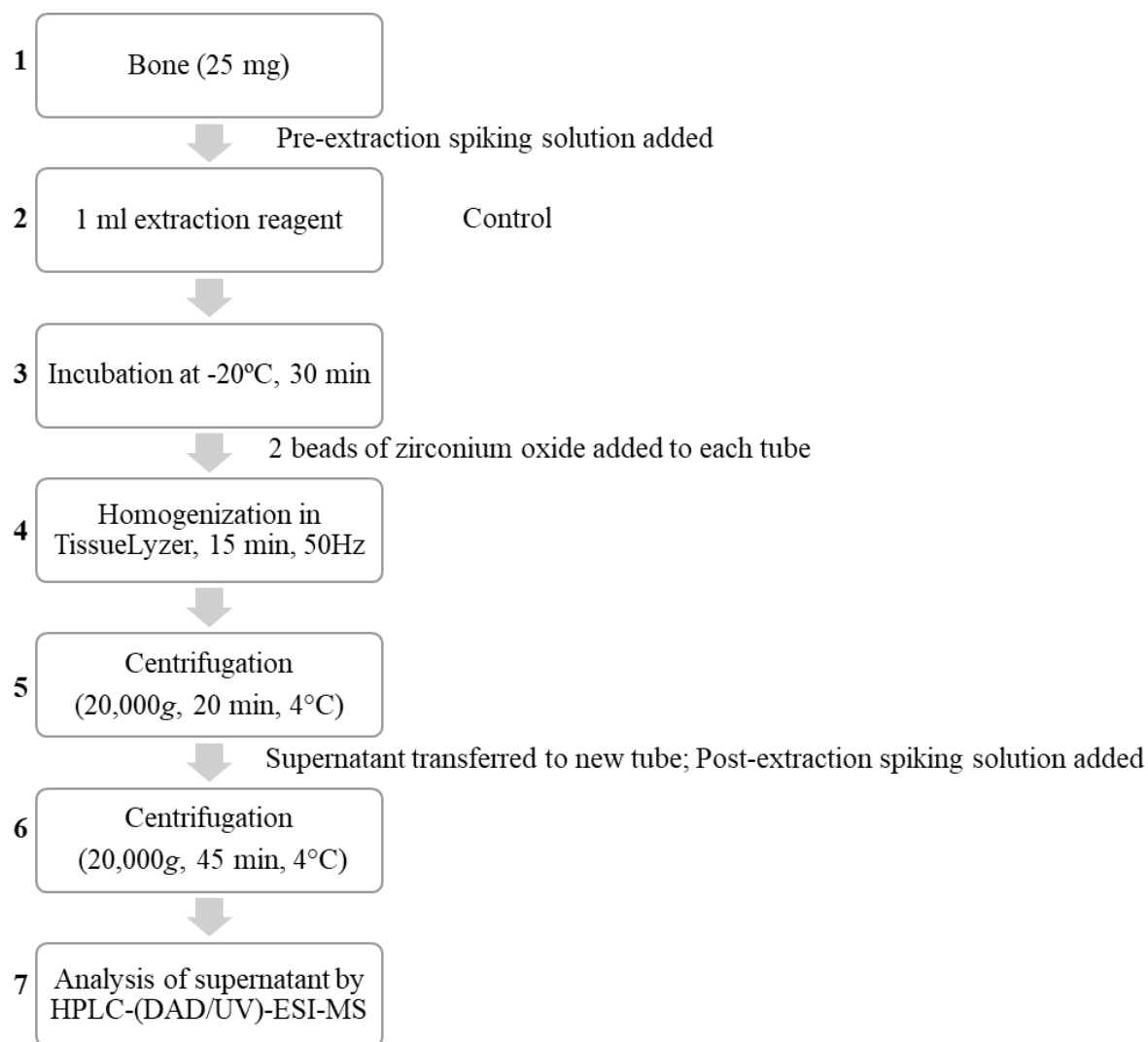**7** | Analysis of supernatant by HPLC-(DAD/UV)-ESI-MS

Figure 6.1. Schematic representation of the steps of the optimized extraction protocol for heme in bones, also indicating when the post-extraction spiking solution of heme was added. Extraction reagents tested were acetone/1.6 M HCl (8:2, v/v) [158] and acetonitrile/1.6 M HCl, 8:2, v/v) [159].
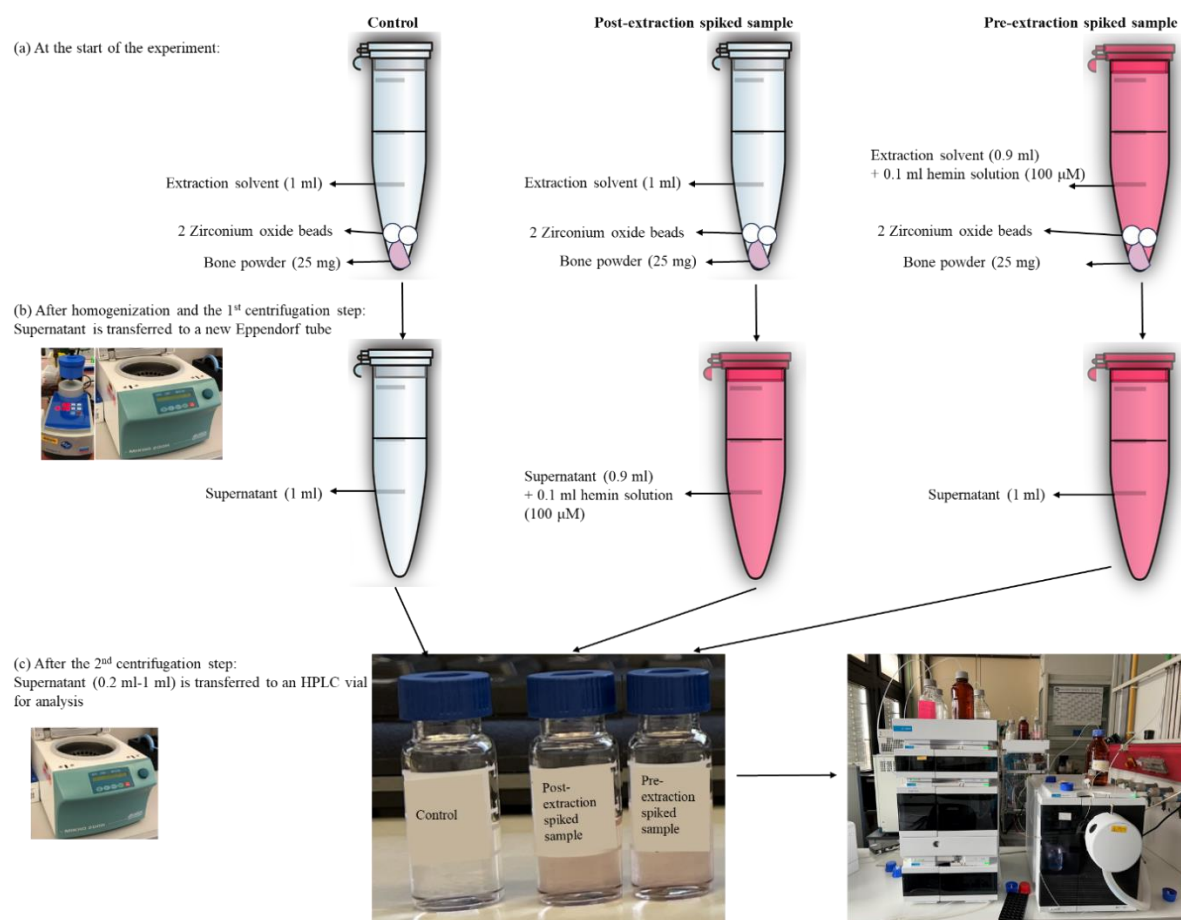
Figure 6.2. Illustration of the prepared solutions during determination of the recovery rate of hemin from bone (a) at the start of the experiment (see steps 1-3 in Figure 6.1), (b) after homogenization and the first centrifugation step (20,000*g*, 20 min, 4°C, see steps 4-5 in Figure 6.1), and (c) after the second centrifugation step (20,000*g*, 45 min, 4°C, see step 6 in Figure 6.1) and prior to HPLC-MS analysis. The clip art of Eppendorf tubes was obtained from the Open Clipart public domain (https://openclipart.org/) which allows re-use according to the Creative Commons Zero 1.0 Public Domain License CC0 1.0 (https://creativecommons.org/publicdomain/zero/1.0/). The rest of the pictures were taken by Mariam Tahoun.

The recovery rates for hemin after applying the various extraction solvents were calculated as shown in Eq. (2) and compared. Hemin may be present in the control due to extraction of hemin from the bone in the control. Therefore, the peak areas of the control sample were subtracted from the peak areas of spiked samples before calculation. The amounts in the control sample usually contributed a maximum of 1% to the value of the recovery rate or 10% of the total peak area, which corresponds to a concentration of 0.1 μM. For validation, the recovery rate was also calculated from the concentrations computed from the calibration curve (prepared in the

same way as the post-extraction spiked samples) compared to the expected concentrations, using Eq. (3).

$$Recovery\ rate\ (\%) = \frac{Peak\ area\ of\ sample\ spiked\ before\ homogenization}{Peak\ area\ of\ sample\ spiked\ after\ homogenization} \times 100 \qquad Eq.\ (2)$$

$$Recovery\ rate\ (\%) = \frac{Calculated\ concentration\ of\ spiked\ sample}{Expected\ concentration} \times 100 \qquad Eq.\ (3)$$

As shown in Table 6.3 and Figure 6.3, the recovery rate of hemin in bone ranges from 19% to 99.7% with the various extraction reagents tested (Table 6.1). In basic solvents, hemin precipitated with the pellet after centrifugation and therefore, a large proportion was unrecoverable, with recovery rates between 19% (for methanol/1% NH_3) and 39% (for acetone/10 mM NH_4OH (8:2, v/v)). In the neutral solvent acetone/water (8:2, v/v), the recovery rate was 41%.

Table 6.3. Recovery rates of hemin after extraction from bone using various extraction reagents.

Extraction reagent	Recovery rate (%) ± SEM	Recovery rate (%) ± SD	Number of replicates (n)
Methanol/1% ammonia	19.0%	19.0%	1
Acetone/Water (8:2, v/v)	39.1%	39.1%	1
Acetone/10 mM NH₄OH (8:2, v/v)	41.1%	41.1%	1
Acetone/1.6 M HCl (8:2, v/v)	96.9 ± 0.2%	96.9 ± 0.7%	9
Acetonitrile/1.6 M HCl (8:2, v/v)	99.7 ± 0.9%	99.7 ± 2.1%	6

In acidic solvents, the recovery rate strongly improved. In this case, the experiments were repeated several times for confirmation of the findings. The standard deviation and standard errors of the mean were low, showing that the extraction protocol and the recovery rates are reproducible, repeatable, and precise. For acetone/HCl, the recovery rate was 96.9±0.2% (9 replicates), and for acetonitrile/HCl, the recovery rate was 99.7±0.9% (6 replicates).
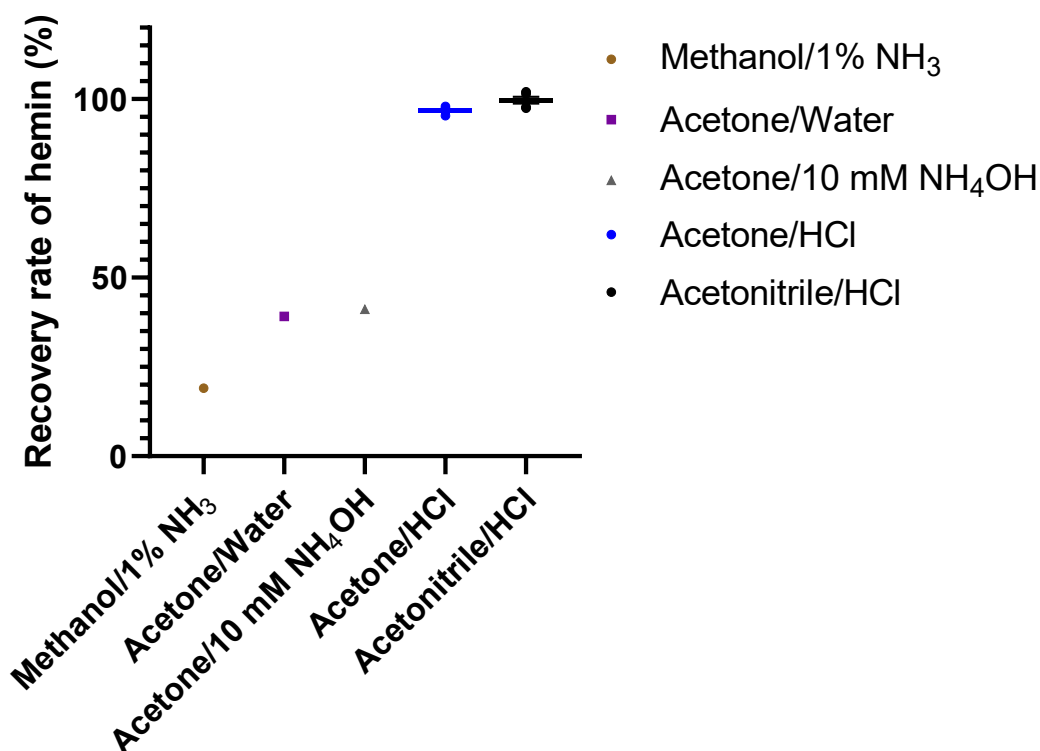
Figure 6.3. Recovery rates of hemin after extraction from bone using various extraction reagents (methanol/1% ammonia; acetone/10 mM NH$_4$OH (8:2, v/v); acetone/water (8:2, v/v); acetone/HCl = acetone/1.6 M HCl (8:2, v/v); acetonitrile/HCl = acetonitrile/1.6 M HCl (8:2, v/v).

6.4. HPLC-(DAD/UV)-MS method and validation

Instrumental conditions for HPLC(DAD/UV)-MS analysis

Measurements were performed on an Agilent 1260 Infinity HPLC coupled to an Agilent Infinity Lab LC/MSD single quadrupole mass spectrometer with an electrospray ion source and a DAD-UV detector (200-600 nm) (Agilent Technologies Germany GmbH & Co. KG, Waldbronn, Germany). Chromatographic separation was performed on an EC 50/3 Nucleodur C18 Gravity, 3 μm (Macherey-Nagel, Dueren, Germany) column. Mobile phase A consisted of methanol with 2 mmol/l ammonium acetate, and mobile phase B consisting of water with 0.1% formic acid. The run started with 10% A and 90% B, followed by a gradient that reached 100% of eluent A after 20 min. Then, the column was flushed for 5 min with 100% of mobile phase A followed by 10% A and 90% B for 5 min before starting the next run. Positive and negative full scan MS was obtained from 100 to 1000 *m/z*. The column temperature was set at

40°C, the injection volume was 4 μl, and the flow rate was adjusted to 0.5 ml/min. Data were collected and processed using the Data Analysis program of OpenLab CDS 2.6 software (Agilent Technologies Germany GmbH & Co. KG, Waldbronn, Germany). The extracted ion chromatogram (EIC) was used to identify and quantify hemin using its exact mass (616.2 ± 0.7 *m/z*), and the diode array detector (DAD) wavelength chromatogram at 400 nm was additionally used to determine the absorbance of hemin (its characteristic absorption wavelength, "Soret band"). The recovery rate was determined from the peak area of hemin's EIC. The calibration curve was automatically computed from the integrated peaks on the EIC by OpenLab CDS 2.6 Data Analysis software. Calculations of matrix effect, recovery rate, population standard deviation (SD), and standard error of the mean (SEM) were performed on Microsoft Excel 2019. Graphs were drawn using GraphPad Prism 8.0.1.

Evaluation of method performance

To validate the method performance, certain parameters were determined according to specifications by the International Conference on Harmonization (2005) "Validation of analytical procedure: Text and Methodology (Q2-R1)," which are summarized and defined in Table 6.4: Linearity, limit of detection (LOD), limit of quantification (LOQ), precision (repeatability and intermediate precision) and selectivity.

Table 6.4. Definitions of analytical parameters [163].

Term	Definition
Linearity	The range of concentrations in the calibration curve that maintain a linear response of the peak area to the increase in concentration, above which a plateau occurs and the response is no longer linear. Linearity is assessed by the coefficient of determination (R^2) value of the linear regression of the calibration curve, in which the maximum value is 1.
Signal-to-noise ratio	The ratio of the peak signal to the background noise of the detector in the instrument.
Limit of detection (LOD)	The concentration at which peak signal-to-noise ratio is greater than 3.
Limit of quantification (LOQ)	The concentration at which peak signal-to-noise ratio is greater than 10.
Precision	The extent by which the results from multiple measurements (on the same day or different days) differ from each other, usually expressed as a percent relative standard deviation (RSD%) of the results to each other. Precision on measurements taking place on the same day is expressed as repeatability, whereas that for measurements on different days but within the same laboratory and instrument is expressed as intermediate precision. Precision on measurements taking place in different laboratories and instruments is expressed as reproducibility. In our case, only repeatability and intermediate precision are relevant.
Repeatability	Also known as intra-day precision, this is a measure of relative standard deviations (RSD%) of samples measured on the same day and same run as an indicator for variation of the instrument.
Intermediate precision	Also known as inter-day precision, this is a measure of relative standard deviations (RSD%) of samples measured on different days within the same laboratory and instrument as an indicator for variation of the instrument.
Selectivity	A measure of the variation of the retention time of a compound in presence of a biological matrix, while measuring samples in which impurities (e.g., buffer components, degradation products, metabolites) are likely to interfere with the retention of the substance of interest. In this case, the analytical method is selective if the retention time of the compound remains unaffected.

Linearity, limit of detection (LOD) and limit of quantification (LOQ)

Linearity, limit of detection (LOD) and limit of quantification (LOQ) were determined after establishing a calibration curve in the concentration range of 0.05 µM to 50 µM in methanol/1% NH$_3$ without bone matrix (Figure 6.4). The limit of detection (LOD) of hemin was 0.1-0.25 µM. The limit of quantitation (LOQ) of hemin was 0.5-1 µM.

In the presence of bone matrix, calibration curves gave a good fit ($R^2 > 0.98$ at least), over the established concentration range from the LOQ to 15 µM, after extraction with acetone/1.6 M

HCl (8:2, v/v) and acetonitrile/1.6 M HCl (8:2, v/v) (Figure 6.4). However, at 25 µM and higher, the response was no longer linear, and these values were therefore excluded from the final curve. In fact, the peak signals after extraction with acetone/1.6 M HCl (8:2, v/v) and acetonitrile/1.6 M HCl (8:2, v/v) were significantly higher than that of methanol/1% NH$_3$ (Figure 6.4), which is in agreement with the preliminary studies on the matrix effect shown in Table 6.2.
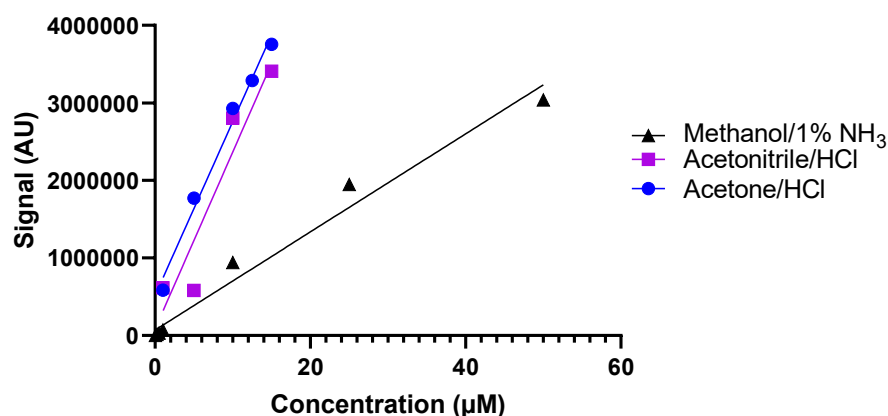

Figure 6.4. Calibration curves of hemin after extraction of bone with acetone/1.6 M HCl (8:2, v/v), acetonitrile/1.6 M HCl (8:2, v/v), and methanol containing 1% NH$_3$ (without bone), respectively.

Repeatability and intermediate precision

Repeatability and intermediate precision were investigated using replicate samples measured on the same day and on different days, respectively. Repeatability of the method was demonstrated by a low relative standard deviation (RSD%) between replicates measured on the same day (0.18-0.36% for acetonitrile/1.6 M HCl, 8:2 v/v; 0.12-1.06% for acetone/1.6 M HCl, 8:2, v/v).

Intermediate precision of the method was also expressed by a low relative standard deviation (RSD%) between replicates measured on different days (2.37% for acetonitrile/1.6 M HCl, 8:2 v/v; 0.71% for acetone/1.6 M HCl, 8:2, v/v).

Selectivity

Selectivity was determined by evaluating if hemin's retention time remains the same even when bone matrix is present in both pre- and post-extraction spiked samples. The retention time for hemin did not change significantly during the analyses (varied from 0.1-0.2% up to a maximum

of 1% in the presence of matrix, Figures 6.5-6.7). Thus, the method remained selective for hemin despite the presence of the bone matrix, as required.

Figure 6.5. Extracted-ion chromatograms (EIC) of hemin (616.2 ± 0.70, positive ion mode) of the bone extracts: (**A**) control, (**B**) pre-extraction spiked samples, and (**C**) post-extraction spiked samples, after extraction of bone with acetone/1.6 M HCl (8:2, v/v).

Figure 6.6. Extracted-ion chromatograms (EIC) of hemin (616.2 ± 0.70, positive ion mode) of the bone extracts: (**A**) control, (**B**) pre-extraction spiked samples, and (**C**) post-extraction spiked samples, after extraction of bone with acetonitrile/1.6 M HCl (8:2, v/v).
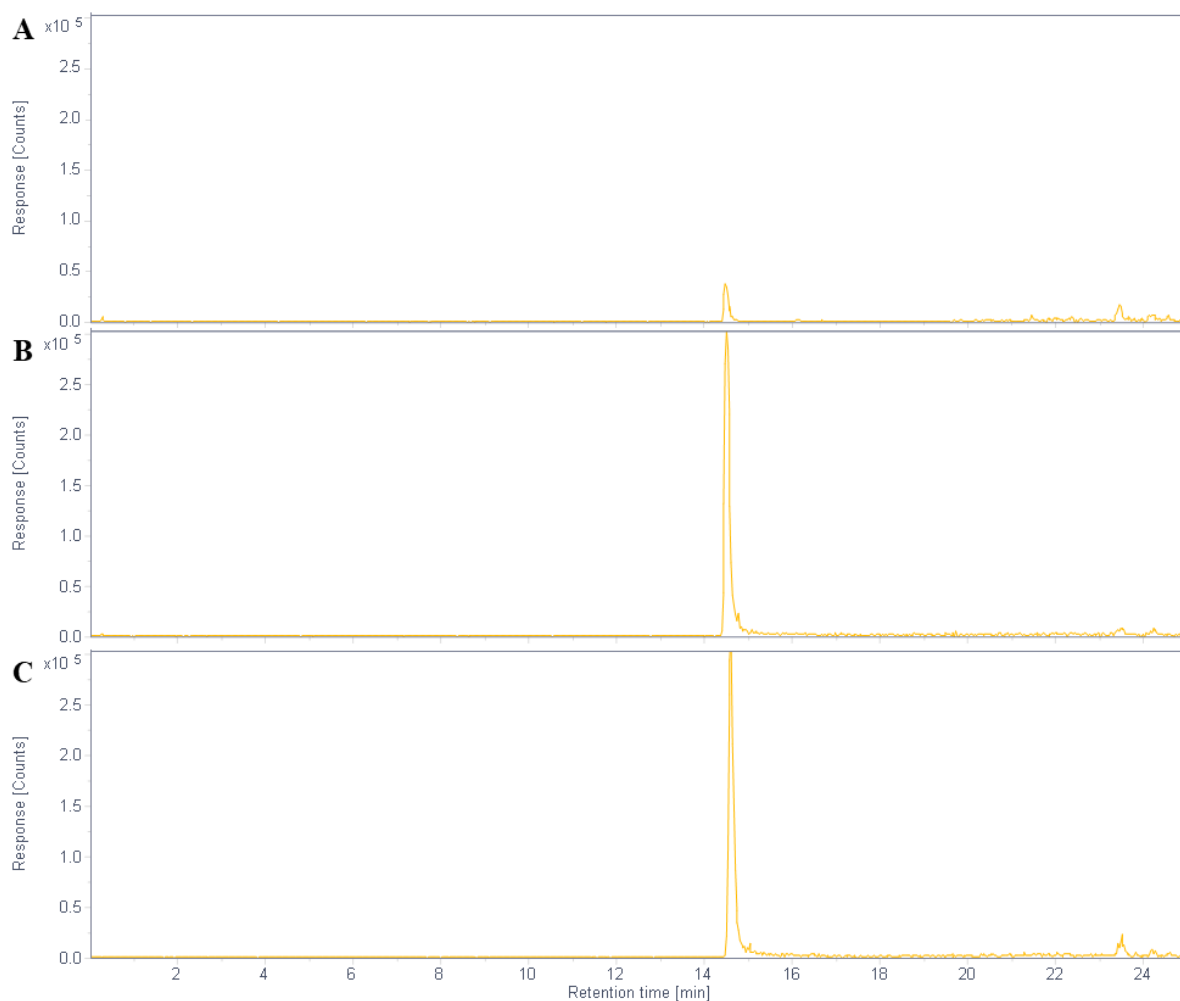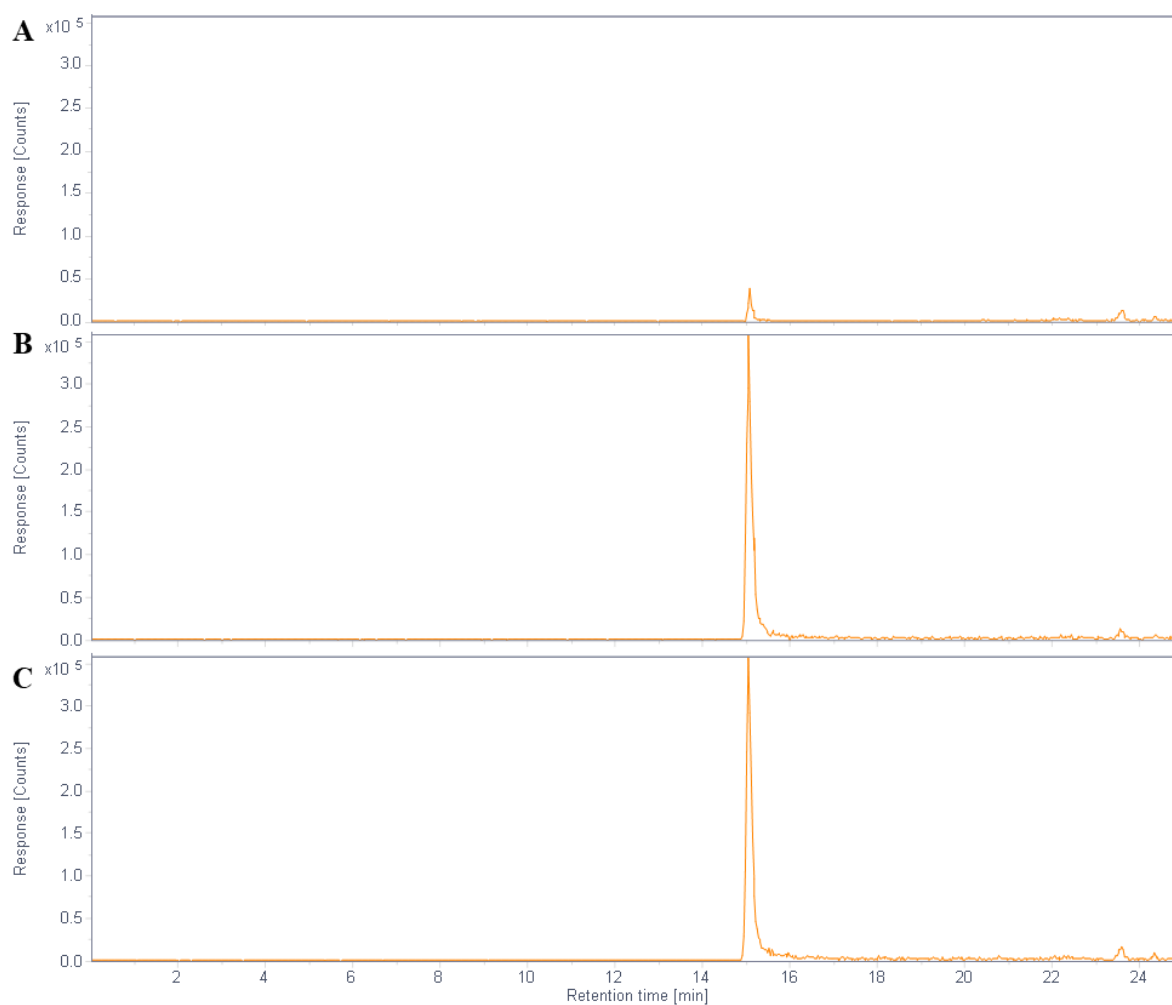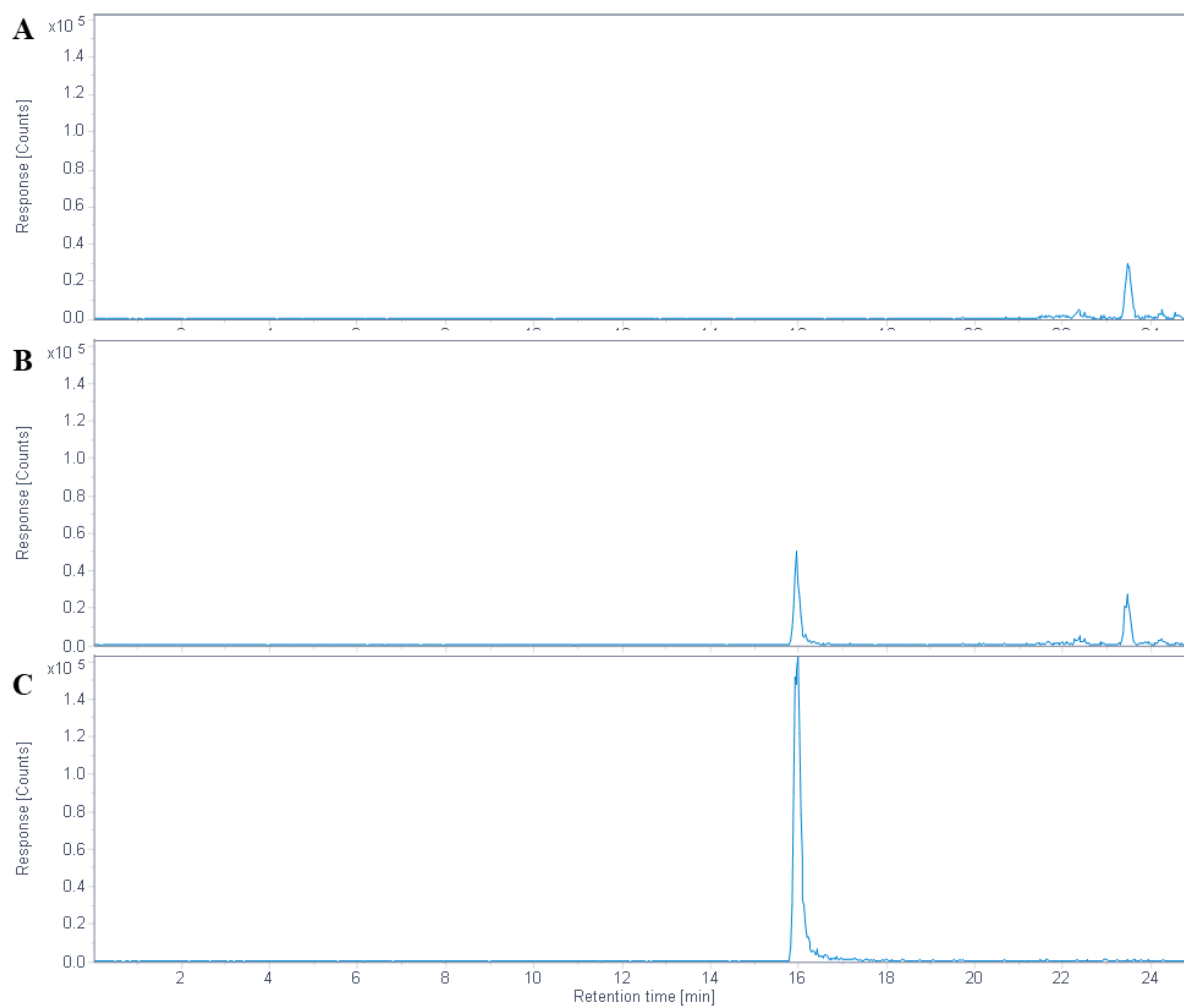
Figure 6.7. Extracted-ion chromatograms (EIC) of hemin (616.2 ± 0.70, positive ion mode) of the bone extracts: (**A**) control, (**B**) pre-extraction spiked samples, and (**C**) post-extraction spiked samples, after extraction of bone with methanol containing 1% NH_3.

6.5. Summary and outlook

This study proposes an optimized protocol for the extraction of heme from bones using two different extraction reagents: acetone/1.6 M HCl, 8:2, v/v, and acetonitrile/1.6 M HCl (8:2, v/v). High recovery rates were achieved (96.9%, and 99.7%, respectively), with low variations between samples. Other extraction buffers were considered, but they resulted in co-precipitation of hemin with the pellet after homogenization and centrifugation. In contrast, the finally selected solvent mixtures were able to keep hemin in solution and recovery was almost quantitative. The extraction method using acetone/HCl and acetonitrile/HCl shows that hemin can be selectively and precisely detected, and that quantitative analysis should be possible in biological and fossil bone samples. As blood vessels are frequently detected in fossil dinosaur bone, heme is expected to be present, at least in trace amounts. The limit of detection (LOD) was 0.1-0.25 µM, and the limit of quantification was 0.5-1 µM on the employed single quadrupole mass spectrometer. The LOD is quite high, but for future studies, measurements will be performed on our much more sensitive Sciex triple-quadrupole-Q-Trap instrument to continue the search for trace amounts of heme in fossilized dinosaur bone samples. Different bone extracts will be analyzed and compared with zero control samples and recent bone control samples. The challenge in this case would be to prove the endogeneity of heme, if indeed detected, to the fossil bone, and not as a carryover contamination. Compared to the HPLC-(DAD/UV)-ESI-MS device used here for optimization, the Sciex instrument offers both higher sensitivity and selectivity, due to a feature known as multiple reaction monitoring (MRM), which analyzes both parent compound (heme) and its most intense fragment daughter ion. MRM is also useful in tuning down background noise from sample matrices. In special cases, an extra fragmentation step can be performed to offer even higher selectivity (known as MRM3/MS3).

7. Macrocyclic Gq protein inhibitors FR900359 and/or YM-254890 – fit for translation?

Jonathan G. Schlegel*, Mariam Tahoun*, Alexander Seidinger, Jan H. Voss, Markus Kuschak, Stefan Kehraus, Marion Schneider, Michaela Matthey, Bernd K. Fleischmann, Gabriele M. König, Daniela Wenzel, and Christa E. Müller.

* The doctoral student is a joint first-author of this publication with Jonathan Schlegel.

Introduction

G-protein coupled receptors (GPCRs) are transmembrane receptors that translate extracellular signals into the cells mediated by intracellular guanine nucleotide-binding proteins (G proteins) [164]. GPCRs have many biological functions, are involved in the pathogenesis of diseases, and are therefore targeted by approximately 34% of all current marketed drugs [165].

The G proteins that are activated by GPCRs are known as heterotrimeric G protein complexes, which are membrane-bound and consist of three subunits: $G\alpha$, $G\beta$, and $G\gamma$ [166]. The heterotrimeric G proteins are grouped into four main families into G_i, G_s, G_q, and $G_{12/13}$, which modulate various downstream signaling events by interacting with different effectors [167]. G_q activates phospholipase C (PLC), which cleaves phosphatidylinositol 4,5-bisphosphate (PIP_2) into diacylglycerol (DAG) and inositol trisphosphate (IP_3). The latter binds to calcium channels in the endoplasmic or sarcoplasmic reticulum, releasing Ca^{2+} and raising its concentration inside the cell [168].

The most important selective inhibitors of G_q are YM-254890 (YM) and FR900359 (FR). YM is a cyclic depsipeptide first extracted from the broth of the bacterial species *Chromobacterium spp.* during a screening campaign for platelet aggregation inhibitors, where it was found to inhibit ADP-induced platelet aggregation *in vitro* [169]. FR is a natural cyclic depsipeptide produced by the bacterium *Candidatus Burkholderia crenata* [170], which is in a symbiotic relationship with the plant *Ardisia crenata*, residing on its leaves [171]. Despite FR's structure closely resembling that of YM except for two residues, their inhibitory kinetics are different [172]. YM and FR have been used to understand G_q protein signaling pathways (e.g., [168,173,174]) and have been investigated as potential lead structures and drug candidates [168,175–179].

For further preclinical development of FR and YM, the inhibitors need to be further characterized with respect to their pharmacokinetic and physicochemical properties. This study aims to gather information about FR and YM by applying a combination of biological assays such as Caco-2 cell permeation assays, determination of chemical and metabolic stability, and determination of *in vivo* bioavailability and tissue distribution after administration by intratracheal and intraperitoneal routes, as well as the consequences of these properties for the observed pharmacological effects.

Summary and outlook

In this study, a characterization of two natural products, YM and FR, which are cyclic depsipeptides and potent selective inhibitors of the G_q subfamily of G proteins, was performed. Their chemical stability (at 37°C) in simulated gastric fluid (pH 1), in weakly basic (pH 9), and in more strongly basic conditions (pH 11) was determined, and their pharmacokinetic profiles and distribution in various organs of mice after intratracheal and intraperitoneal injection was investigated. Qualitative and quantitative analyses were performed using high-performance liquid chromatography–mass spectrometry (HPLC-MS), including high-resolution quadrupole-time-of-flight (qTOF) mass spectrometry, and quantitative analysis was performed using the extract ion chromatograms (EICs) of both compounds.

In simulated gastric fluid (pH 1) and mild alkaline aqueous solution (pH 9) FR and YM were relatively stable, FR being more stable than YM. However, under harsher alkaline conditions (pH 11), FR and YM degraded, but YM degraded more rapidly than FR.

Furthermore, after *in vivo* intratracheal application of FR or YM (5 μg) in mice on 7 consecutive days, their concentrations were determined in all organs using high-resolution LC-qTOF-MS/MS. The highest accumulation was found in lungs and kidneys, and the lowest concentrations were found in the brain and in plasma. Furthermore, after intraperitoneal application of FR to mice over 3 weeks in an additional *in vivo* study, it was found to accumulate mostly in the lung. Minor amounts were found in liver, eyes and intestine, and the lowest concentrations were detected in the brain. Thus, FR showed almost the same organ distribution after application by both routes.

In conclusion, two *in vivo* studies showed that FR and YM could barely cross the blood-brain barrier, and are detected in vital peripheral organs (liver, kidney) in addition to lungs and eyes. This information is useful with regard to their therapeutic application.

Author contribution

The doctoral student performed the experiments for analyzing the chemical stability, determining the recovery rates, and performed the quantitative analysis of the concentrations of FR900359 and YM-254890 by LC-MS/MS in samples of mouse tissues. Furthermore, the doctoral student created figures on her results, and wrote the methodology (Quantitative Analysis of FR and YM by LC-MS/MS for in Vitro Stability Studies and Quantification of FR and YM in Mouse Tissues), results, and discussion section on her contributions in the manuscript in cooperation with Christa E. Müller, Jonathan Schlegel, and all co-authors.

7. Macrocyclic Gq protein inhibitors FR900359 and/or YM-254890 – fit for translation?

8. Suberin, a unique constituent of bark, identified in a 45-million-year-old tree

8.1. Introduction

Soft tissues originating from plants and animals have been described to be preserved in fossil material, mostly based on morphological similarities to recent material. At first this was met with controversy, as it was believed that after an organism's death, only the hard tissues are preserved, and organic material is destroyed. However, more recently, the development of highly sensitive analytical techniques has led to research breakthroughs in this field, paving the way for molecular paleontology, that is focused on the chemical characterization of organic compounds in fossils [9,12].

In the fossil record of plants, intact tree trunks are rare, because the most exposed parts of the fossils, bark and wood, usually dry out and detach from the rest of the fossil. As a result, they are either degraded or cannot be detected at all. This is particularly true for the outer bark, which is the outermost layer of the tree, and is therefore the first target for bacteria and fungi during early stages of degradation and fossilization [180].

Reports on fossil bark are primarily descriptive studies, and the few specimens that have been described are usually not well-preserved. Nonetheless, it is interesting to note that bark in the fossil record dates over a wide range of periods (48 to 382.7 million years old) [181], genera and species (e.g., *Mesoxylon spp., Araucarioxylon spp., Vectia spp., Parsacupressinoxylon spp., Cedroxylon spp., Aphloioxylon spp., Taxodioxylon spp., Cordaixylon spp., Callixylon spp., Pityoxylon spp, Cedroxylon spp, Amyelon spp.,* and *Cheirolepis spp.*) [181], and worldwide locations (Canada, USA (Arizona, Kansas, Ohio, New York), England, Wales, and Greenland). A unique component of bark as well as roots is suberin (Figure 8.1), a polymeric organic compound present in the cell walls of the phellem (cork) located in the outer layer of the trees. Suberin offers a protective layer to the tree, e.g., against microbes, fungi, and water loss. The outer bark of *Quercus suber* (cork-oak tree) has a thick layer of cork and is an economically important source of suberin [44], its cork layer containing about 40-50% of suberin [45]. Major constituents of suberin comprise esters of mainly long-chain (C_{16}-C_{24}) α,ω-hydroxy diacids (e.g., 1,18-octadec-9-enedioic acid (*cis*-, **29** and *trans*-configurated, **30**) and 1,20-eicosanedioic acid (**31**)) and ω-hydroxy acids (e.g., 22-hydroxydocosanoic acid) with glycerol or ferulic acid (*cis*-, **32** and *trans*-configurated, **33**). Minor components of suberin include 1-alkanols (e.g., 1-

tetracosanol) and 1-alkanoic acids (e.g., docosanoic acid) [45,46]. Reports on suberin in the fossil record are rare. The only report that mentioned suberin was from an estimated 41,000-year-old fossil tree trunk, in which only assumptions were made about the presence of suberin rather than providing concrete chemical evidence. This was due to poor preservation because the environment surrounding the fossil was high in moisture that probably led to degradation of suberin into its constituents [180].
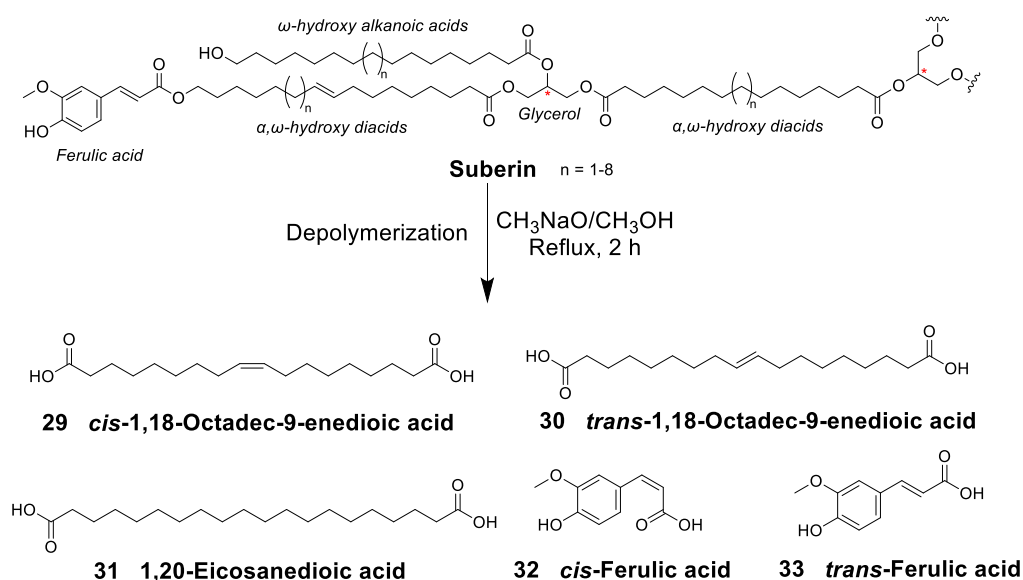

Figure 8.1. Suberin and selected monomeric constituents. Partial structure of the polymer suberin and selected monomers **29-33** which are obtained by depolymerization of suberin using sodium methanolate in methanol.

In the present study, we investigated a well-preserved 45-million-year-old specimen known as "monkey hair," (Figure 8.2), originating from the Geiseltal Lagerstätte near Halle, Eastern Germany, used for coal mining, which was stored in the Geiseltal Collections of the Martin Luther University Halle-Wittenberg (inventory number GHM Y74). It was recently analyzed by microcomputer tomography (micro-CT), and described to have the appearance of a flattened tree trunk, containing an outermost layer appearing like bark (**I**, Figure 8.2), a middle layer of degraded organic material thought to represent wood (**II**, Figure 8.2), and an innermost layer of laticifers containing *in situ* vulcanized rubber (**III**, Figure 8.2) [182]. Although "monkey hair" has been studied for more than 100 years aiming to understand its composition and fossilization, most of the chemical analyses have focused on the hair-like laticifers [182–186]. Until now, the organic matter to which some specimens of "monkey hair" are attached were assumed to be remains of bark or wood solely based on anatomy, but have not been chemically studied and characterized.
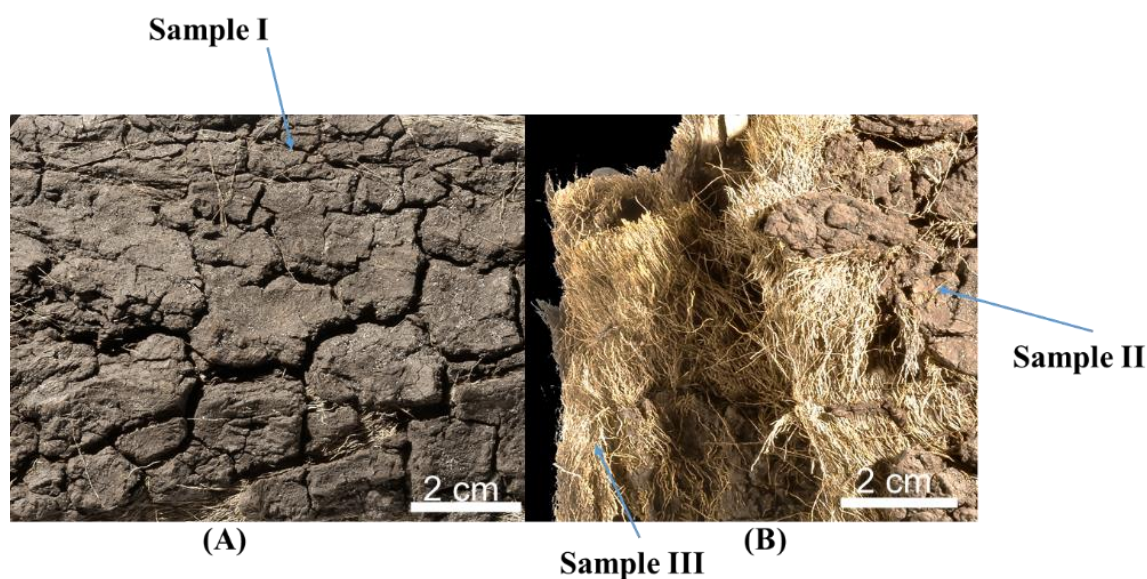
Figure 8.2. Studied "monkey hair" specimen GHM Y74. (**A**) Outermost layer (sample **I**) of the "monkey hair" specimen GHM Y74 [182]. (**B**) The middle layer (sample **II**), and the innermost layer (fossil laticifers, sample **III**) of GHM Y74. Photos were taken by Victoria E. McCoy.

Here we use high-performance liquid chromatography coupled to electrospray ionization mass spectrometry (HPLC-ESI-MS) to assess whether the outermost layer of the specimen GHM Y74 represents preserved bark. The polymeric constituent suberin is only present in bark, but neither in wood nor in laticifers. Thus, detection of suberin constituents would unambiguously allow the identification of the outermost layer as bark. 1,18-Octadec-9-enedioic acid, 1,20-eicosanedioic acid, and ferulic acid were chosen as typical suberin constituents for analysis after alkaline hydrolysis of the polymer. The preservation of suberin in its intact polymeric form was indirectly confirmed by analyzing the samples before and after depolymerization.

8.2. Results

A chemical approach was chosen to investigate whether the outermost layer of the well-preserved "monkey hair" fossil specimen GHM Y74 might stem from bark. For this purpose, samples of the outer bark of recent *Quercus suber* (cork) were employed to optimize an extraction method for determining suberin constituents. A recent cork sample was also used as positive control, while a cellulose thimble used for the Soxhlet extraction served as negative control. Standard solutions of selected constituents were used to develop a suitable analytical method for HPLC-ESI-MS analysis.

Development and validation of an analytical HPLC-ESI-MS method

For the analysis of carboxylic acid derivatives, three typical suberin constituents were chosen and used as standards: the fatty acids 1,18-octadec-9-enedioic acid (as a mixture of *cis*-, **29**, and *trans*-isomers, **30**) and 1,20-eicosanedioic acid (**31**), *cis*-ferulic acid (**32**) (for structures see Figure 8.1) and *trans*-ferulic acid (**33**). Two HPLC-ESI-MS methods were developed and optimized for the analysis of **29**, **30**, **31**, **32,** and **33**, employing different mobile phases (for details see Experimental Section): methanol/water (1:1), both containing 2 mmol/l ammonium acetate, with a linear gradient reaching 100% methanol/2 mmol/l ammonium acetate (method A, for compounds **1** and **2**), and 10% methanol/90% water containing 0.5% acetic acid (method B, for compounds **3** and **4**), with a stepwise gradient that reaches 100% methanol. The methods were validated by evaluating linearity, limit of detection (LOD), limit of quantification (LOQ) and selectivity according to the International Council for Harmonization (ICH) guidelines. Linearity was determined in a wide concentration range of 0.01-1 µmol/L compounds **29/30**, 0.0125-1 µmol/L compound **31**, and 0.1-100 µmol/L compound **33**. The correlation coefficient was found to be > 0.99 in all cases, indicating linearity (Table 8.1). LOD and LOQ were determined and indicating the minimum concentration that can be confidently detected and quantified, respectively. The method was found to be sufficiently sensitive (see Table 8.1).

Table 8.1. Method validation parameters for HPLC-ESI-MS determination of standard compounds.

Compound	Concentration range	Linear regression and correlation coefficient (r^2)	Limit of detection (pg/µl)	Limit of quantification (pg/µl)
(*cis/trans*)-1,18-Octadec-9-enedioic acid	0.01-1 µmol/l	$y = 13216x + 220.7$ ($r^2 = 0.9997$)	73.4-78.1	223
1,20-Eicosanedioic acid	0.0125-1 µmol/l	$y = 36927x - 480.2$ ($r^2 = 0.9913$)	41.1-65.4	124
trans-Ferulic acid	0.1-100 µmol/l	$y = 3952x + 8380$ ($r^2 = 0.9937$)	517-583	1460 – 1940

Optimization of methanolate-induced cleavage of suberin using recent bark

A previously published method for the determination of suberin constituents from *Quercus suber* [45] was adapted to small amounts of sample material (ca. 100-250 mg). In a first step, extractives containing waxes, non-polar constituents, phenolic and polyphenolic compounds were removed by applying sequential Soxhlet extraction with dichloromethane followed by methanol [45]. The extracted amount corresponded to 6% (w/w) of the original material. The samples of recent *Quercus suber* were subsequently treated with sodium methanolate in methanol to cleave the ester groups of suberin, followed by acidification to pH 6 and extraction with dichloromethane [45,187]. Then, the extracts were dried and taken up in a mixture of dichloromethane/methanol (3:1 v/v) for subsequent analysis. After methanolate-induced cleavage and extraction, the *Quercus suber* sample (250 mg) yielded 41.9% (w/w) of the original mass, containing the hydrolysis products of suberin (Table 8.2). This result was comparable to that of published studies (40-50%) [45], indicating that the extraction method was suitable for application to the fossil material.

Methanolate-induced cleavage of the fossil samples

As a next step, the optimized extraction procedure and the validated HPLC-ESI-MS methods were applied to the fossil specimen GHM Y74. Samples were taken from the outermost (**I**), the middle (**II**), and the innermost layers (**III**) of the "monkey hair" specimen GHM Y74 (see Figure 8.2). The appearances of the samples and the various extracts are depicted in Supplementary Figure 8.3. A general overview of the procedure is shown in Figure 8.4, including the weights of the samples used for each step.
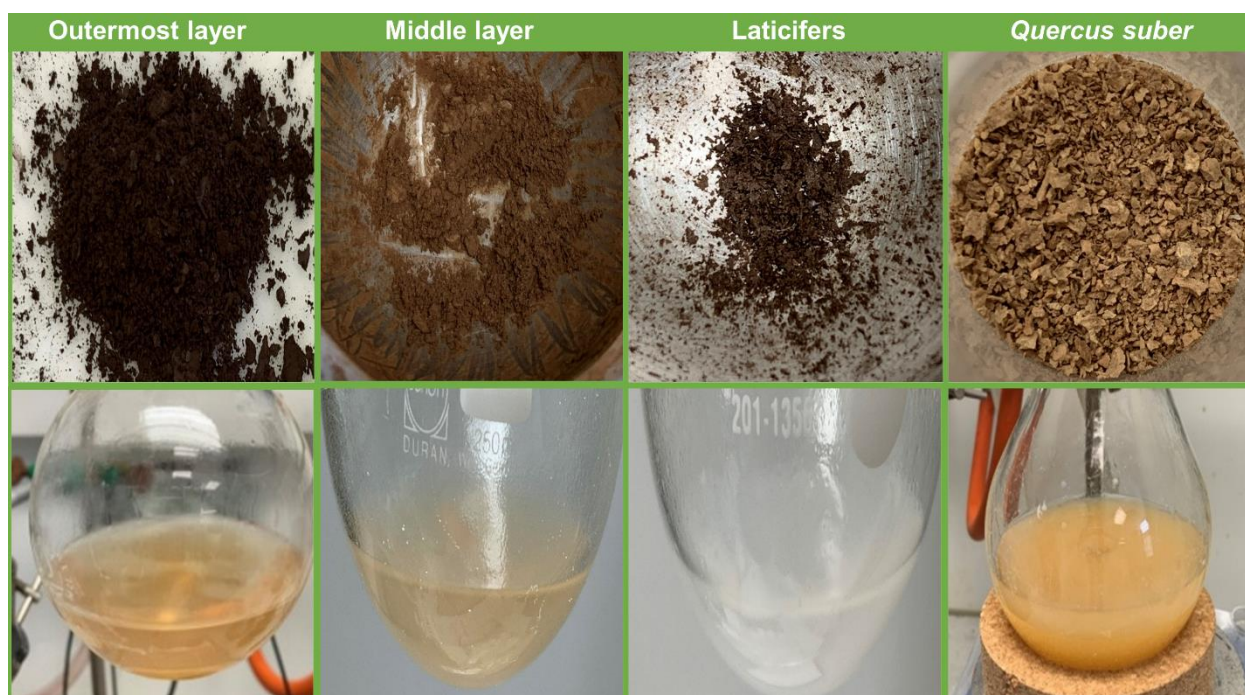

Figure 8.3. Comparison of the appearance of the samples and their extracts (a) powdered samples (b) Mixture obtained after methanolysis and acidification to pH 6.

I Outermost layer	**II** Middle layer	**III** Inner layer	*Quercus suber* (positive control)	Cellulose (negative control)

| Weight of starting material | 183 mg | 187 mg | 12.5 mg | 1.58 g | 1.93 g |

Soxhlet extraction 1. with dichloromethane, and 2. with methanol

| Weight after Soxhlet extraction | 109 mg | 51 mg | 2.4 mg | 0.25 g * | 1.9 g |

Methanolate-induced cleavage

| Weight of residue | 28.7 mg | 2.5 mg | 1.6 mg | 104 mg | 77 mg |

HPLC-MS analysis of:
1. Soxhlet extracts 2. The residue after induced cleavage

*Only a portion of the sample was subjected to methanolate-induced cleavage

Figure 8.4. Workflow of the Soxhlet extraction and methanolate-induced cleavage of the fossil samples, *Quercus suber* (positive control), and cellulose (negative control). A detailed overview of the procedure employed in this study to extract and analyze suberin constituents from the (**I**) outermost, (**II**) middle, and (**III**) innermost layer of the "monkey hair" fossil GHM Y74, *Quercus suber* (positive control), and cellulose (negative control) is shown. The weight of the starting material of the samples and the weight obtained after each step is given.

For evaluation, the following two parameters were calculated: (1) Percentage (w/w) of extractives obtained after Soxhlet extraction (based on weight of starting material) and (2) percentage (w/w) of residue obtained after methanolate-induced cleavage (based on weight of starting material and on weight after Soxhlet extraction). These were calculated according to Eq. (1) and Eq. (2) and are collected in Table 8.2 for each sample.

Eq. (1): $Percentage\ (w/w)\ of\ extractives = \dfrac{Weight\ after\ Soxhlet\ extraction}{Weight\ of\ starting\ material} \times 100$

Eq. (2):

$Percentage\ (w/w)\ of\ residue = \dfrac{Weight\ after\ methanolate-induced\ cleavage}{Weight\ of\ starting\ material\ or\ after\ Soxhlet\ extraction} \times 100$

Afterwards, to normalize the data for comparison, the amounts of the compounds detected were calculated in mg per gram of residue obtained after methanolate-induced cleavage or per gram of starting material (Table 8.2).

Table 8.2. Amounts of suberin monomers 1,18-octadec-9-enedioic acid (detected as a mixture of *cis*-, **29**, and *trans*-isomers, **30**) and 1,20-eicosanedioic acid (**31**), represented as milligrams of compound per gram of starting material before methanolysis, and gram of residue obtained after methanolysis, respectively. In addition, percentage (w/w) of residues obtained after methanolysis and extraction of outermost, middle, and innermost layers of the fossil specimen GHM Y74**,** a sample of *Quercus suber*, and a sample of cellulose (negative control), compared to the starting weight before sample preparation, and sample weight after Soxhlet extraction, is calculated. In addition, the percentage (w/w) of extractives obtained after Soxhlet extraction compared to the starting weight of all samples is shown.

Sample	Percentage (w/w) of extractives obtained after Soxhlet extraction, based on weight of starting material	Percentage (w/w) of residue obtained after methanolate-induced cleavage, based on weight a) of starting material b) after Soxhlet extraction	Amount of compound a) mg per g of starting material b) mg per g of residue after methanolate-induced cleavage	
			Compounds 29 & 30	Compound 31
Cellulose thimble (negative control)	1.6%	a) 3.9% b) 4.1%	< LOD	< LOD
Quercus suber bark	6%	a) 33.5% b) 41.9%	a) 0.318 b) 0.764	a) 0.146 b) 0.353
I Outermost layer	40%	a) 15.7% b) 26.3%	a) 0.148 b) 0.941	a) 0.0777 b) 0.493
II Middle layer	73%	a) 1.3% b) 4.9%	< LOD	< LOD
III Innermost layer	81%	a) 12.8% b) 66.7%	< LOD	< LOD

Sample **I** (109 mg), the outermost layer, resulted in 40% (w/w) of extractives related the initial sample weight (Table 8.2 and Figure 8.4). This is significantly higher than the percentage observed for recent *Quercus suber* (6%, Table 8.2 and Figure 8.4), probably due to chemical changes that had occurred during fossilization leading to an alteration of the chemical composition. After hydrolysis of the residue, 26.3% (w/w), compared to the weight of the original material, were obtained, which is only 1.6-fold less than the amount from the recent *Quercus suber* control sample in this step (see Table 8.2).

Extracts of the middle layer (187 mg) showed a higher percentage of extractives (74%, Table 8.2). After methanolate-induced cleavage of the sample (51 mg), only a low percentage of

residue was obtained (4.9%, Table 8.2 and Figure 8.4). This suggests that this layer does not contain many hydrolyzable polymers.

The innermost layer (12.5 mg) showed the highest percentage of extractives in the fossil, constituting 81% of the sample (Table 8.2). After methanolate-induced cleavage of the extractive-free material (2.4 mg), a very low amount of residue was obtained (1.6 mg), accounting to 66.7% (w/w) compared to the weight after Soxhlet extraction, or to 12.8% (w/w) of the weight of dry starting material (Table 8.2 and Figure 8.4). The high proportion of extractives present in the fossil is likely due to the presence of various hydrocarbon derivatives e.g., terpenoid, phenolic and polycyclic hydrocarbon derivatives, as a result of diagenesis [182–186].

Qualitative and quantitative analysis of suberin constituents in the fossil specimen

Regarding the fatty acid composition, only in extracts of the outermost layer of GHM Y74, the three characteristic monomers of suberin, selected for analysis within this study, were present after methanolate-induced cleavage: 1,18-Octadec-9-enedioic acid (detected as a mixture of *cis*-, **29**, and *trans*-isomers, **30**, Figure 8.5), 1,20-eicosanedioic acid (**31**, Figure 8.6), and *cis*-ferulic acid (**32**, Figure 8.7) (for structures see Figure 8.1). To confirm the identity of the compounds, the extracted ion chromatograms (EIC, Figure 8.5A4, Figure 8.6A4, and Figure 8.7A3) and electrospray ion negative mode mass spectra (ESI-MS) of GHM Y74's outermost layer (Figure 8.5B2, 8.6B2, and 8.7B2) were compared to and matched those of solutions of 1,18-octadec-9-enedioic acid (mixture of *cis*- and *trans*-isomers, Figure 8.5A1 and 8.5B1), 1,20-eicosanedioic acid (Figure 8.6A1 and 8.6B1), and *cis*-ferulic acid (Figure 8.7A1 and 8.7B1) used as standards for comparison, and to those obtained from *Q. suber* extracts (positive control, Figure 8.5A8, Figure 8.6A8, and Figure 8.7A6). In a negative control utilizing the same extraction procedure employing a Soxhlet sleeve consisting of cellulose, these compounds were not detected (Figure 8.5A2, Figure 8.6A2 and Figure 8.7A2). These results further confirm that the peaks observed in the outermost layer were true signals from the "monkey hair" fossil, and excludes their presence in the utilized reagents or as residues in the instrument. Furthermore, these compounds were neither detected in the middle layer (Figure 8.5A5, Figure 8.6A5, and Figure 8.7A4) nor in the innermost layer (Figure 8.5A6, Figure 8.6A6, and Figure 8.7A5) of GHM Y74.

Moreover, prior to depolymerization induced by methanolate, the constituents 1,18-octadec-9-enedioic acid (mixture of *cis*- and *trans*-isomers, Figure 8.5A3) and 1,20-eicosanedioic acid (Figure 8.6A3) were not detected in methanolic extracts, indicating that these carboxylic acids had been bound to the polymeric suberin structure and were released upon depolymerization. This provides at least indirect evidence for the presence of suberin in the outermost layer of the fossil.

Only in extracts of *Q. suber* and in the outermost layer of GHM Y74, the amounts of the mixture of compounds **29** and **30**, and amount of compound **31** were above the LOQ (Table 8.1) with a signal-to-noise ratio of above 10, permitting quantification of a compound according to International Council for Harmonization (ICH) guidelines with high confidence. This was not the case for the extracts of the middle and innermost layers of GHM Y74, in which the analytes were below the limits of detection and quantification with a signal-to-noise ratio below 3. The compound amounts found in the extracts are listed in Table 8.2.

Detection and quantification of cis-/trans-1,18-octadec-9-enedioic acid using HPLC-ESI-MS

Compared to recent *Q. suber*, the amount of 1,18-octadec-9-enedioic acid (detected as a mixture of *cis*-, **29**, and *trans*-isomers, **30**) in the outermost layer was approximately 50% of the amount found in *Q. suber* per gram of starting material.
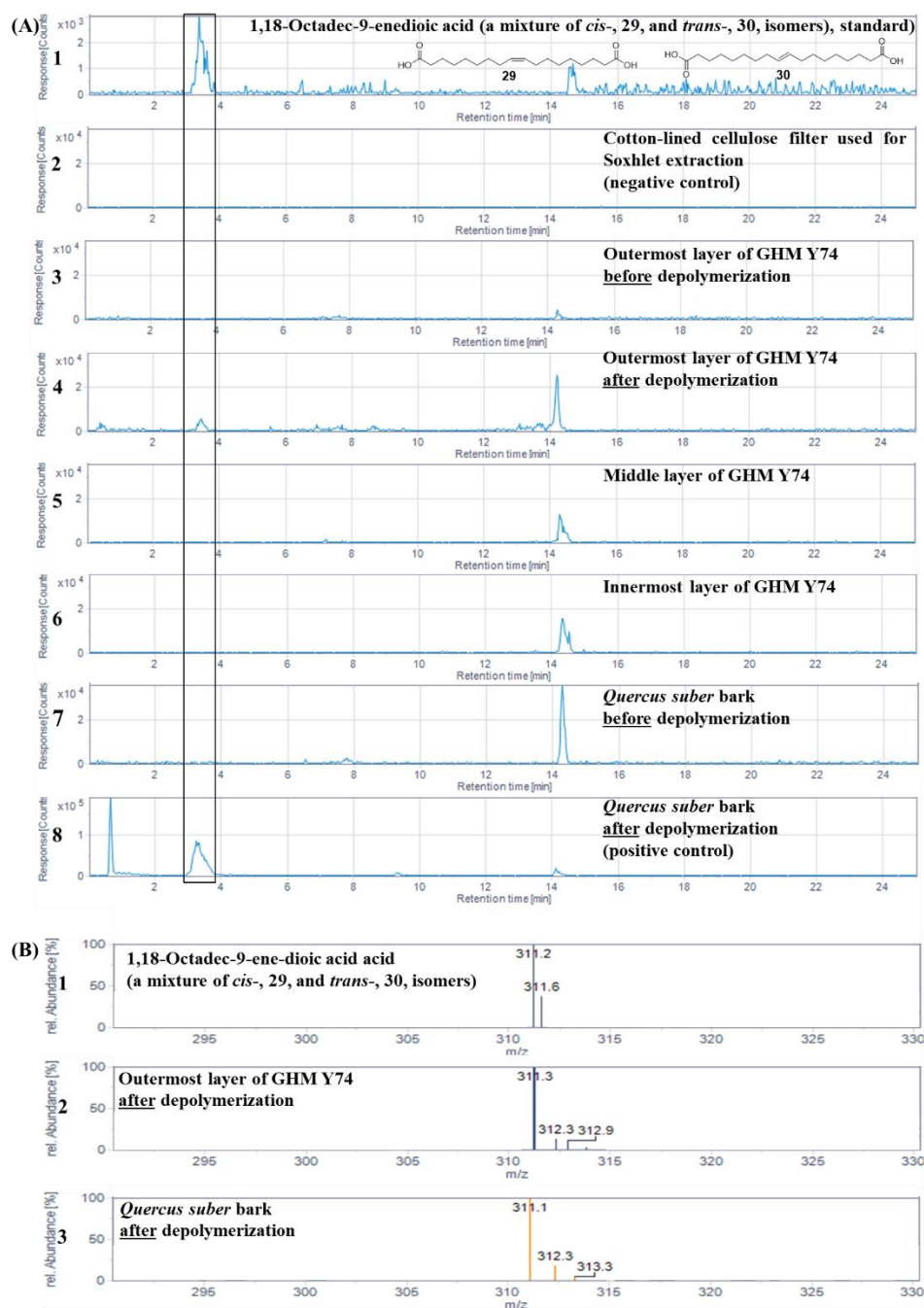

Figure 8.5. Presence of the suberin monomer 1,18-octadec-9-enedioic acid (detected as a mixture of *cis*- and *trans*-isomers) in the outermost layer of GHM Y74 after depolymerization and extraction detected by HPLC-ESI-MS. (A). Extracted-ion

chromatograms of 1,18-octadec-9-enedioic acid (detected as a mixture of *cis-*, **29**, and *trans-*isomers, **30**, 311.23 ± 0.70 m/z, negative ion mode) of (**1**) a standard solution of 1,18-octadec-9-enedioic acid (a mixture of *cis-* and *trans-*isomers), from the extracts of (**2**) the cotton-lined cellulose filter used for Soxhlet extraction (negative control), (**3**) outermost (before depolymerization) (**4**) outermost (after depolymerization), (**5**) middle and (**6**) innermost layers of the "monkeyhair" fossil GHM Y74, (**7**) *Quercus suber* bark (positive reference for suberin, before depolymerization), and (**8**) *Quercus suber* bark (after depolymerization). A mixture of compounds **29** and **30** was detected with confidence in samples from *Quercus suber* and the outermost layer of GHM Y74. The compound was not detected in Soxhlet methanolic extracts of (**3**) the outermost layer of GHM Y74 or (**7**) in recent *Quercus suber* bark before depolymerization, indicating that it was released from the suberin upon ester cleavage induced by methanolate. (**B**). Electrospray ionization mass spectra of (**1**) standard 1,18-octadec-9-enedioic acid (a mixture of *cis-* and *trans-*isomers), (**2**) extracts of *Quercus suber* bark after depolymerization, and (**3**) the peak in extracts of outermost layer of GHM Y74 after depolymerization, showing the deprotonated $[M-H]^-$ ion (311.2 ± 0.3 m/z in the negative ion mode).

Detection and quantification of 1,20-eicosanedioic acid using HPLC-ESI-MS

Similarly, the amount of 1,20-eicosanedioic acid (**31**) was approximately 50% of the amount found in *Q. suber* per gram of starting material (Table 8.2).
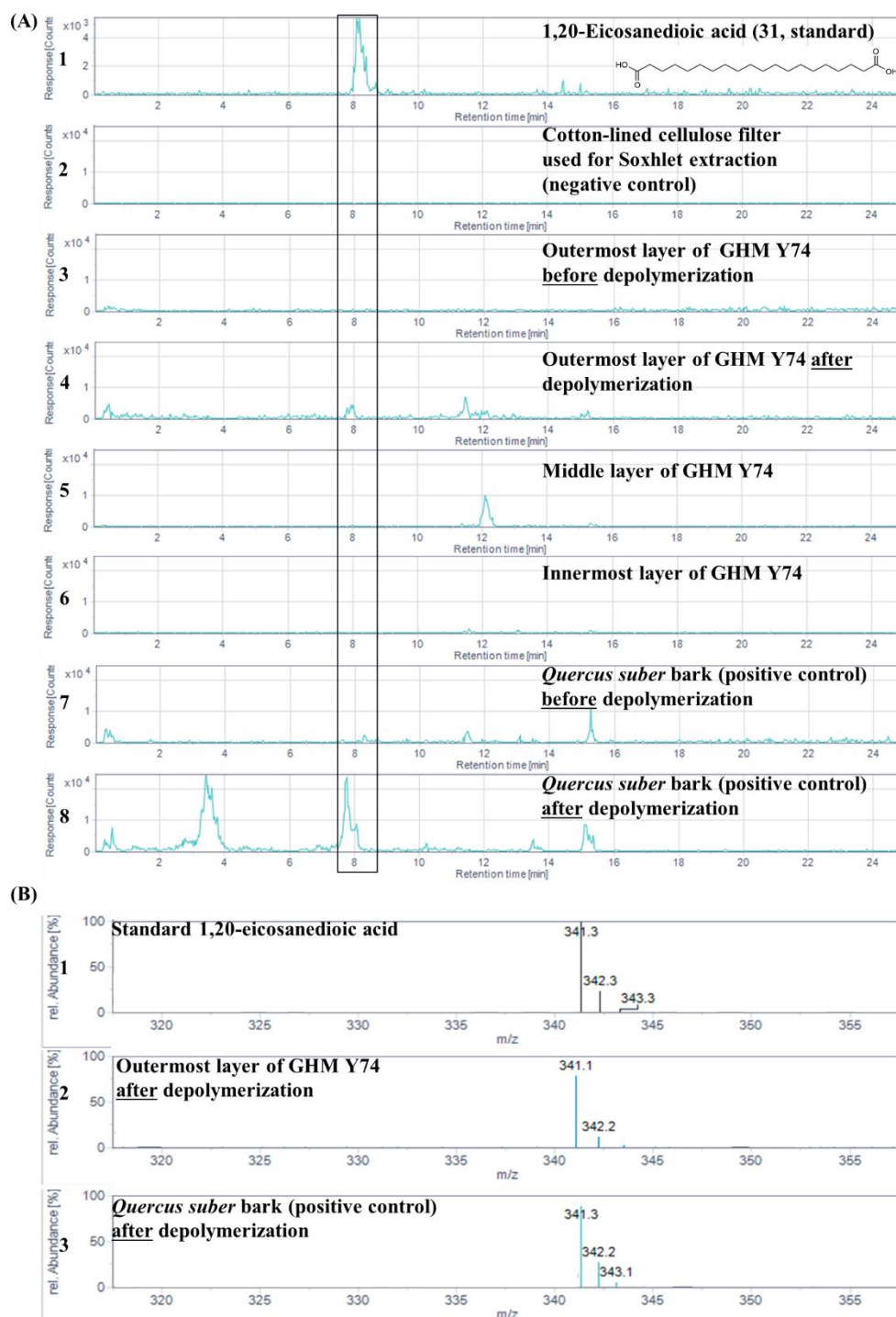

Figure 8.6. Presence of the suberin monomer 1,20-eicosanedioic acid in the outermost layer of GHM Y74 after depolymerization and extraction detected by HPLC-ESI-MS. (**A**). Extracted-ion chromatograms of 1,20-eicosanedioic acid (341.23 ± 0.70 m/z, negative ion

mode) of (**1**) a standard solution of 1,20-eicosanedioic acid, from the extracts of (**2**) the cotton-lined cellulose filter used for Soxhlet extraction (negative control), (**3**) outermost (before depolymerization) (**4**) outermost (after depolymerization), (**5**) middle and (**6**) innermost layers of the "monkeyhair" fossil GHM Y74, (**7**) *Quercus suber* bark (positive reference for suberin, before depolymerization), and (**8**) *Quercus suber* bark (after depolymerization). Compound **31** was detected with confidence in samples from *Quercus suber* and the outermost layer of GHM Y74. The compound was not detected in Soxhlet methanolic extracts of (**3**) the outermost layer of GHM Y74 or (**7**) in recent *Quercus suber* bark before depolymerization, indicating that it was released from the suberin upon ester cleavage induced by methanolate. (**B**). Electrospray ionization mass spectra of (**1**) standard 1,20-eicosanedioic acid, (**2**) the outermost layer of GHM Y74 after depolymerization and (**3**) extracts of *Quercus suber* bark after depolymerization, showing the deprotonated [M-H]$^-$ ion (341.2 ± 0.3 m/z in the negative ion mode).

Detection of cis-ferulic acid using HPLC-ESI-MS

As can be seen in Figure 8.7, the *trans-* isomer of ferulic acid, the natural isomer of ferulic acid present in many plants [188], was not present in the outermost layer of the fossil. This may explain the reversed trend of compound amounts observed in the fossil compared to modern bark, considering that compounds **29**, **30** and **31** were found to be higher in the fossil relative to the weight obtained after methanolysis.
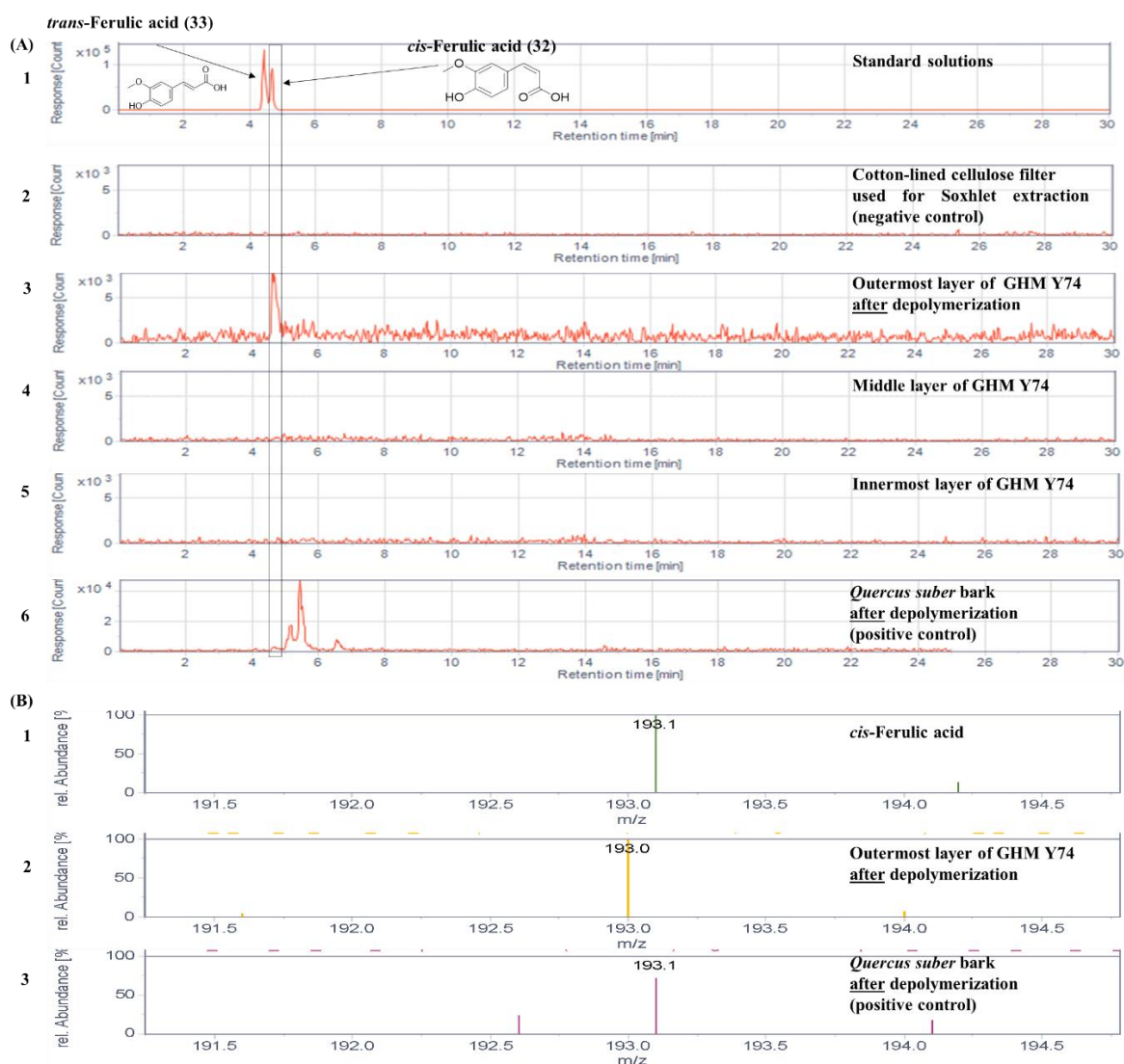
Figure 8.7. Presence of the suberin monomer *cis*-ferulic acid in the outermost layer of GHM Y74 after depolymerization and extraction detected by HPLC-ESI-MS. (A). Extracted-ion chromatograms of *cis*-ferulic acid (193.06 ± 0.70, negative ion mode) of (**1**) a standard solution of *cis*-ferulic acid, from the extracts of (**2**) the cotton-lined cellulose filter used for Soxhlet extraction (negative control), (**3**) outermost (after depolymerization), (**4**) middle and (**5**) innermost layers of the "monkeyhair" fossil GHM Y74, and (**6**) *Quercus suber*

71

bark (positive reference for suberin, after depolymerization). Compound **32** was detected with confidence in samples from the outermost layer of GHM Y74. (**B**). Electrospray ionization mass spectra of (**1**) standard *cis*-ferulic acid, (**2**) extracts of the outermost layer of GHM Y74 after depolymerization, and (**3**) extracts of *Quercus suber* bark after depolymerization showing the deprotonated [M-H]$^-$ ion (193.0 ± 0.3 m/z in the negative ion mode).

8.3. Discussion

In our study, compounds **29**, **30**, **31**, **32** and **33** had been selected as abundant constituents of suberin found, e.g., in the bark of *Quercus suber*. They were analyzed to answer the question whether suberin was present in the outermost layer of the well-preserved "monkey hair" specimen GHM Y74. Interestingly, the outermost layer of GHM Y74 (sample **I**) contained all of the analyzed constituents of suberin, except for *trans*-ferulic acid, but relatively large amounts of *cis*-ferulic acid instead. In hydrolysates of the middle and innermost layers of GHM Y74, these compounds were below the limit of detection (Table 8.2). Thus, based on chemical evidence, only the outermost layer can be characterized as preserved bark. In addition, detection of these acids only after the depolymerization process implies that intact, polymeric suberin was preserved in the "monkey hair" fossil.

The percentage of residue obtained as suberin constituents in the outermost layer of GHM Y74 (26.3% w/w) was quite high and comparable to that of *Q. suber* (40-50% w/w). Since limited data is available on the suberin content of a living "monkey hair" tree, we cannot calculate exactly how much of the original suberin present in the tree was preserved. Nevertheless, it is possible that the suberin content of the then living "monkey hair" tree was originally less than that of *Q. suber*, since the amount is species-specific, and it is well known that the cork tree *Q. suber* has particularly high amounts of suberin (40-50% w/w) compared to other trees [44].

Nevertheless, partial degradation of suberin present in the once-living "monkey hair" tree due to diagenesis is not excluded, as indicated by the high percentage of extractives we found in the outermost layer of the fossil GHM Y74 (Table 8.2). Fatty acid constituents of suberin released after degradation can undergo decarboxylation to aliphatic alkanes or alkenes, which might explain why we did not detect the fatty acids **29**, **30** and **31** before methanolate-induced cleavage of the fossil material [180,189]. After hydrolysis of suberin to release its fatty acid constituents, decarboxylation may have occurred, converting the constituents to straight-chain alkanes and alkenes, which are insoluble in typical organic solvents used for extraction (e.g., dichloromethane), as observed for the fossil *Diaphorodenron sp.* bark (estimated to be 298-

358 million years old) following analysis by pyrolysis GC/MS [48,190]. These studies, although they do not provide any direct chemical evidence for the presence of suberin, seem to suggest that suberin might be preserved in bark when given favorable low-moisture conditions. Such conditions have likely enabled the preservation of the "monkeyhair" specimen GHM Y74.

So far, no study has been published on the chemical composition of the organic material surrounding the laticifers of "monkey hair." Most of the results had been descriptive; although the samples had an appearance like bark and wood, chemical evidence for preserved chemical constituents has been lacking. Thus, we believe that we present the first chemical evidence of preserved bark in "monkey hair" using HPLC-ESI-MS. Elsewhere in the plant fossil record, limited reports on the chemical composition of fossil bark applying various methods and analytical techniques only provided speculations that suberin might have been present, but had been extensively degraded. Comparing bark extracts of a fossil *Sequoiadendron giganteum* tree trunk (at least 41,000 years old) to modern *Sequoia* bark, before alkaline hydrolysis, a high content of free carboxylic acids was found in the fossil in contrast to the control. This means that suberin had been mostly degraded in the fossil bark [180]. In an older example, a 45-million-year-old unidentified isolated piece of bark found in the litter of a forest in Canada, not associated with a fossil trunk, was chemically analyzed by GC-MS after extraction with dichloromethane without any prior depolymerization. As no fatty acids could be detected in the extractives, it was implied that suberin may have been preserved, but this was not further investigated to prove it [189]. Thus, to our knowledge, we have provided unequivocal chemical evidence for the preservation of suberin a 45-million year old bark sample associated with a fossil tree trunk, using HPLC-ESI-MS, and this is the oldest sample, in which suberin has been clearly identified.

Finally, detection of *cis*-ferulic acid (**32**) in the outermost layer of GHM Y74 (sample **I**) is noteworthy (see Figure 8.7). Ferulic acid is not only a phenolic component of suberin, but due to its carboxylic acid and hydroxyl groups, it is also a component of lignin, in which it forms covalent bonds with lignin constituents (monolignols) [191] and can cross-link lignin to polysaccharides and suberin in the cell wall [192]. Failing to detect ferulic acid in the middle layer of GHM Y74 (sample **II**) which was assumed to be wood-like, could imply that wood, especially lignin, had been largely degraded. This finding supports previous hypotheses that the "monkey hair" fossil underwent differential degradation which led to greater destruction of wood as compared to bark [182]. It is also interesting to note that ferulic acid was present as a *cis*-isomer and not in its naturally abundant *trans*-isomer [188]. This isomerization could not

have happened due to the ester hydrolysis since we could not find the *cis*-isomer with a similar abundance in the control cork sample, hinting that these changes might have happened during the fossilization process. UV irradiation during fossilization could have led to the isomerization reaction.

This study demonstrates the power of liquid chromatography coupled to mass spectrometry for chemical analyses in the field of paleobotany. Although there are many reports of specimens in the fossil record that show anatomical resemblance to modern bark, chemical analysis of such samples is still limited. Further studies will broaden our understanding of the chemical composition of fossil plants and allow us to gain novel insights, e.g., into the paleoenvironment at the respective time period, and the conditions under which fossilization occurred.

8.4. Conclusions

Unambiguous indirect evidence for the presence of intact suberin, a hallmark constituent of bark, in the outermost layer of a "monkey hair" specimen (GHM Y74) has been provided. This is the first time that compelling chemical evidence for the presence of intact suberin in fossil trunks has been obtained, since in other investigated specimens, only degradation products were detected. Thus, fossilization conditions in the Geiseltal Lagerstätte appear to have been mild, and probably due to low moisture, the ester bonds of suberin were not hydrolyzed. This information will help paleontologists to understand the mechanisms of fossilization and how the sedimentary environment present in the Geiseltal Lagerstätte contributed to the preservation of organic compounds. In addition, it is the first time that bark from a "monkey hair" tree has been chemically characterized for the presence of suberin. These findings further complement a series of publications aiming to characterize the exceptionally preserved "monkey hair" specimen GHM Y74 using various analytical methods, such as microcomputer tomography, pyrolysis GC/MS [182], and most recently Raman spectroscopy [193].

8.5. Materials and Methods

Materials

The following compounds were purchased: *trans*-ferulic acid (Sigma Aldrich Chemie GmbH, Taufkirchen, Germany), 1,20-eicosanedioic acid (Apollo Scientific, Bredbury, England), and a mixture of *cis*- and *trans*-1,18-octadec-9-enedioic acid (abcr GmbH, Karlsruhe, Germany). The compound *cis*-ferulic acid was synthesized from its *cis*-isomer by UV irradiation for 90 min. All HPLC solvents and mobile phase additives (formic acid, acetic acid, and ammonium acetate) used for analysis were of LC-MS grade. Water was used from the in-house Millipore milliQ water purification system.

Sample description

The studied specimen of "monkeyhair" originating from the brown coal mines of Geiseltal fossil Lagerstätte near Halle (Saale), Eastern Germany, is thought to have been collected during mining in the period of 1920 to the early 2000 and has been stored in the Geiseltal Collections of the Martin Luther University Halle-Wittenberg, under the inventory number GHM Y74. Samples from the GHM Y74 specimen consisted of an outer layer (sample **I**), middle layer (sample **II**), and an innermost layer (laticifers, sample **III**). For method development and as a positive control, recent bark of *Quercus suber* was used. As a negative control, the cellulose sleeve used for Soxhlet extraction (Cytiva Europe GmbH/GE Healthcare, Freiburg im Breisgau, Germany) was employed without samples.

Methods

Sample preparation. *Q. suber* (1.58 g) was cut into pieces, frozen in liquid nitrogen, then ground using a Retsch MM40 mixer mill (Retsch GmbH, Haan, Germany). The material was subjected to Soxhlet extraction (size 29/32, Lenz Laborglas GmbH, Wertheim, Germany) using 150 ml of dichloromethane for 6 h followed by 150 ml of methanol for 6 h. Then, the remaining solid material was left to dry under a hood for 24 h. Samples **I** (183 mg), **II** (187 mg), **III** (12.5 mg), and negative control (1.93 g) were prepared using this procedure.

Methanolate-induced cleavage and extraction of suberin constituents. This method was adapted from Pereira (1988) [45]. Dry material (0.25 g, *Q. suber*) obtained after extraction was refluxed with 3% sodium methoxide in dry methanol (25 ml) for 2 h with stirring under an argon atmosphere. The resulting mixture was filtered, and the resulting filtrate was

subsequently acidified to pH 6 using 2 mol/l sulfuric acid in methanol (ca. 2 ml, accurately determined by a pH meter). Then, the filtrate was evaporated to dryness using a rotary evaporator at about 40°C under reduced pressure. The residue was suspended in 50 ml of distilled water and extracted three times with 50 ml of dichloromethane each. The combined organic extracts were dried over anhydrous magnesium sulfate (ca. 5 g), filtered, and evaporated to dryness. The residue was weighed, and aliquots were taken for LC-MS analysis. Methanolysis and extraction was similarly performed using samples **I** (109 mg), **II** (51.0 mg), **III** (2.40 mg) and the cellulose sleeve used for Soxhlet extraction (negative control, 1.9 g).

HPLC-(DAD-UV)-ESI-MS analysis. Aliquots from the residues obtained after methanolysis were dissolved in a 3:1 (v/v) mixture of methanol/dichloromethane and subsequently analyzed by HPLC-(DAD-UV)-ESI-MS. Measurements were performed on an Agilent 1260 Infinity HPLC instrument coupled to an Agilent Infinity Lab LC/MSD Single Quadrupole mass spectrometer with an electrospray ion source and a DAD-UV detector (200-600 nm). Chromatographic separation was performed on an EC 50/3 Nucleodur C18 Gravity, 3 μm (Macherey-Nagel, Dueren, Germany).

HPLC Method A. Mobile phase A consisted of methanol with 2 mmol/l ammonium acetate, and mobile phase B consisted of water with 2 mmol/l ammonium acetate. The run started with 50% A and 50% B for 1 min, followed by a gradient that reached 100% of eluent A after 15 min. Then, the column was flushed for 10 min with 100% of mobile phase A, then with 50% A and 50% B for 5 min before starting the next run. Positive and negative full scan MS was obtained from 100 to 1000 m/z. The column temperature was set at 40°C, the injection volume was 5 μl, and the flow rate was adjusted to 0.5 ml/min. Using this method, the expected retention time of 1,18-octadec-9-enedioic acid (detected as a mixture of its cis-, **29**, and *trans*-, **30**, isomers) was 3.33 min and of 1,20-eicosanedioic acid (**31**) was 7.89 min.

HPLC Method B. Mobile phase A consisted of methanol, and mobile phase B consisted of water with 0.5% acetic acid. The run started with 10% A and 90% B and a gradient started that reached 45% A and 55% B (0-4 min). This was maintained for a further 5 min (4-9 min), followed by another gradient that reached 80% A and 20% B (9-12 min). Then, another gradient started that reached 100% of eluent A (12-25 min). The column was flushed for 5 min with 100% of mobile phase A, then with 10% A and 90% B for 5 min before starting the next run. Positive and negative full scan MS was obtained from 100 to 1000 m/z. The column temperature was set at 40°C, the injection volume was 5 μl, and the flow rate was adjusted to

0.5 ml/min. Using this method, the expected retention time of *trans*-ferulic acid (**33**) was 4.64 min, and that of *cis*-ferulic acid (**32**) was 4.69 min.

Qualitative and quantitative analysis. Identification of the peaks was performed using the Data Analysis program on OpenLab CDS 2.4 software (Agilent Technologies Germany GmbH & Co. KG, Waldbronn, Germany). The extracted ion chromatogram (EIC) was used to evaluate peak areas and provide a quantitative estimate of the detected compounds according to the following parameters: 1,18-Octadec-9-enedioic acid (mixture of *cis*-, **29**, and *trans*-, **30**, isomers, 311.23 ± 0.70 m/z), 1,20-eicosanedioic acid (**31**, 341.23 ± 0.70 m/z), and ferulic acid (*cis*-, **32** and *trans*-, **33**, isomers, 193.06 ± 0.70 m/z).

Limit of detection (LOD) and limit of quantitation (LOQ) were determined experimentally by residual standard deviation of regression, and resulting signal-to-noise ratios from the calibration curve (6-sigma method) in accordance with International Council for Harmonization (ICH) guidelines: *trans*-Ferulic acid (LOD: 517 – 583 pg/µl; LOQ: 1460 – 1940 pg/µl), 1,20-eicosanedioic acid (LOD: 41.1 – 65.4 pg/µl; LOQ: 124 pg/µl) and 1,18-octadec-9-enedioic acid (mixture of *cis*- and *trans*- isomers, LOD: 73.4 – 78.1 pg/µl; LOQ: 223 pg/µl).

9. Quantitative analysis of calcium in the decaying crayfish (*Cambarellus diminitus*) using atomic absorption spectrophotometry

This is part of a collaboration study which was published as: "Calcite precipitation forms crystal clusters and muscle mineralization during the decomposition of *Cambarellus diminutus* (Decapoda: *Cambaridae*) in freshwater."

Bastian Mähler, Kathrin Janssen, Martina Menneken, Mariam Tahoun, Markus Lagos, Gabriele Bierbaum, Christa E. Müller, & Jes Rust

Introduction

In the framework of an experimental taphonomy study performed by Dr. Bastian Mähler (Paleontology Department, University of Bonn), twenty specimens of the crayfish *Cambarellus diminitus*, that were living in a laboratory-scale water tank at his department and were given a specific source of nutrition for crayfish, were chosen. The specimens were sacrificed, dried, placed in sterile tubes, ten of which containing tank water and the other ten containing distilled water. The decay of the crayfish was monitored over eleven days in an incubator at 30°C. Six of those specimens were provided to the doctoral student by Dr. Bastian Mähler. The aim here was to determine the calcium content in the crayfish using atomic absorption spectrophotometry (AAS) with and without previous ashing in a muffle oven at 450°C. The given specimens were divided into two groups of three crayfish each, and the criteria was for each group was based on the presence or absence of a gastrolith. Briefly, weighed amounts of the six powdered dry crayfish samples were dissolved with 2 mL of 0.5 N aqueous hydrochloric acid solution, filtered and diluted to 100 mL with deionized water. A 1:10 dilution was made and the samples were analyzed. Calcium chloride solutions in a concentration range of 0.01-0.03 g/L were used for constructing a calibration curve. The measurements were repeated for six different powdered dry crayfish samples but with prior ashing in a porcelain dish in a muffle oven for 1 h at 450°C. All measurements were performed on a Shimadzu AA-7000 Atomic Absorption Spectrophotometer (Shimadzu Deutschland GmbH). Evaluation was performed using the WizAArd Software (Shimadzu Deutschland GmbH). The concentration of calcium in µmol/mg of dry weight of two groups of six crayfish each were calculated, and samples with and without prior ashing were compared. In addition, this AAS study complemented other techniques tested on the rest of the specimens of *Cambarellus diminitus*, including micro

computed tomography (micro-CT), inductively coupled plasma mass spectrometry, scanning electron microscopy (SEM), and confocal Raman spectroscopy.

Summary and outlook

The calcium concentrations of six specimens of *Cambarellus diminutus*, three of which having gastroliths, and three of which not having gastroliths, were measured and determined by atomic absorption spectrophotometry (AAS). The quantitative analysis revealed that the gastrolith-free specimens possessed more calcium than the crayfish specimens containing gastroliths. In addition, the gastrolith volumes played a role in the amount of calcium present. Specimens having large gastrolith volumes (2.12 mm^3 and 7.72 mm^3) contained an amount of calcium approximately in the range of 1.9 µmol/mg, whereas specimens having smaller volumes of gastroliths (0.2 mm^3) contained more calcium (approximately 2.82 µmol/mg). The amount of calcium in the three gastrolith-free specimens was approximately 2.94 µmol/mg, 3.94 µmol/mg and 3.12 µmol/mg. Precipitated crystal structures consistent in composition with calcite (calcium carbonate) were visible on the decaying exoskeletal structure of the crayfish, which were confirmed and visualized by micro-CT, scanning electron microscopy, and confocal Raman spectroscopy. Based on the quantification of the calcium content in the crayfish by atomic absorption spectrophotometry, the source of calcium for precipitation in samples incubated in distilled water, to which no external calcium was added, was confirmed to originate from the crayfish itself. The results indicate that precipitation of calcite is an early-stage diagenetic process. As this experimental taphonomy study was performed on a few crayfish specimens, a larger-scale study is a plan for future experiments for the purpose of validating this observed precipitation.

Author contribution

The doctoral student performed the experiments for the determination of the calcium concentrations in the crayfish. Furthermore, the doctoral student created tables on her results (Appendix 11), and wrote the methodology (section: Atomic Absorption Spectrophotometry), and incorporated the results and discussion section with her contributions in the manuscript in cooperation with Christa E. Müller and all co-authors.

10. Extraction and analysis of adipocere in decaying crayfish *Cambarellus diminitus*

This is part of a collaboration study which was published as: "Adipocere formation in biofilms as a first step in soft tissue preservation."

Bastian Mähler, Kathrin Janssen, Mariam Tahoun, Frank Tomaschek, Rico Schellhorn, Christa E. Müller, Gabriele Bierbaum, & Jes Rust

Sci. Rep., **2022**, 12(1), 10122.

Introduction

Adipocere is a wax-like organic substance formed by the anaerobic bacterial hydrolysis of tissue fat in a decaying organism. It has a grayish-white appearance and is crumbly and insoluble in water. It is formed in the presence of high moisture, the absence of oxygen and in warm weather. Adipocere is the product of the hydrolysis of triglycerides in adipose tissues which contains mainly the free fatty acids. The saturated fatty acids are the major components present and usually contain an even number of carbons. Palmitic acid is the most abundant of them, followed by stearic acid and then myristic acid. The most common unsaturated fatty acids present are oleic acid, linoleic acid and palmitoleic acid.

The aim was to extract and analyze a sample from a nine-day post-mortem decaying crayfish *Cambarellus diminutus*, provided by Dr. Bastian Mähler (Paleontology Department, University of Bonn), hypothesized to be adipocere, by HPLC-ESI-MS, and to identify the different fatty acid components of adipocere from the resulting chromatographic peaks and mass spectra.

Physiologically, in the crayfish *Cambarellus diminutus*, the major saturated fatty acid present is palmitic acid, and the major unsaturated fatty acid present is oleic acid. In addition, triglycerides can be composed purely of one fatty acid or a mixture of fatty acids. But their composition depends on the nutrition sources of the crayfish. Measurements were performed on an Agilent 1260 Infinity HPLC coupled to an Agilent Infinity Lab LC/MSD single quadrupole mass spectrometer with an electrospray ion source and a DAD-UV detector (200-600 nm) (Agilent Technologies Germany GmbH & Co. KG, Waldbronn, Germany). Chromatographic separation was performed on an EC 50/3 Nucleodur C18 Gravity, 3 μm (Macherey-Nagel, Dueren, Germany) column.

In addition to HPLC-(DAD-UV)-ESI-MS analysis, several techniques were performed on the sample, including micro-computed tomography (micro-CT), microbiological assays, and confocal Raman spectroscopy.

Summary and outlook

The sample was extracted with dichloromethane to obtain the lipophilic constituents present without chemical modification. Then, aliquots were taken and diluted 1:1 with acetonitrile (final concentration of dichloromethane = 50%) and subsequently analyzed by HPLC-(DAD-UV)-ESI-MS. Equal volumes of sample were measured with and without adding a known concentration of palmitic acid, stearic acid, and oleic acid (final concentration of all acids was 1 µmol/l) as reference compounds. The chromatograms showed peaks corresponding to each of the free fatty acid expected to be present in adipocere. To confirm the presence of the free fatty acids, the standard addition method, also known as spiking, was used for unambiguously identifying oleic acid, palmitic acid, and stearic acid in the sample.

After extraction of the sample with dichloromethane and subsequent analysis by HPLC-ESI-MS, the following conclusions were drawn. The sample is indeed adipocere. It contains a mixture of saturated (palmitic, stearic and myristic acids) and unsaturated (oleic, linoleic and palmitoleic acids) fatty acids. The unsaturated oleic acid remained intact in the sample. Oleic acid was the most abundant free fatty acid in the sample comprising approximately 50% of the total peak area. Palmitic acid was the second most abundant fatty acid, representing approximately 25% of the total peak area. The rest of the fatty acids analyzed showed individual peak areas below 10% of the total peak areas.

The results from confocal Raman spectroscopy and HPLC-(DAD-UV)-ESI-MS analysis showed unambiguous chemical evidence that most of the triglycerides had degraded in the crayfish within nine days, forming adipocere. Therefore, it was concluded that adipocere is among the first diagenetic changes to occur after death, and that this process is dependent on the microbial community present in the decaying environment.

Author contribution

The doctoral student performed the experiments for the determination of adipocere components in the crayfish sample. Furthermore, the doctoral student created figures (Figure 6, Figure 7, Supplementary Figures S5 and S6) and tables (Supplementary Table S2) on her results and wrote the methodology (section: high performance liquid chromatography coupled to ultraviolet and mass spectrometry detection (HPLC-UV/MS), results, and discussion section on her contributions in the manuscript in cooperation with Christa E. Müller and all co-authors.

11. Development of infrared spectra of a silicified fossil wood sample and search for characteristic bands of lignin

Introduction and contribution of doctoral student

An infrared (IR) spectrum of a silicified fossil wood sample, provided by Dr. Moritz Liesegang (at that time affiliated with the Paleontology Department, University of Bonn), was to be determined, aiming to identify bands specific for organic components of lignin. Samples from recent wood (wood shavings, wood dust, wood litter and small animal bedding) were also analyzed in the same manner to support the identification of characteristic bands belonging to lignin, a major organic component of wood. The IR spectrum of the fossil wood sample was corrected for atmospheric contributions of ambient water and carbon dioxide, by determining a reference spectrum of potassium bromide (KBr) which was subtracted.

In comparison with data obtained from pure lignin as reported in literature, many bands indicating the presence of organic signals could be identified: OH-stretching, C-H stretching, aromatic skeletal vibration, C-H deformation (methyl and methylene groups), C-H in-plane deformation with aromatic ring stretching, C-O stretching, in-plane deformation, C-H vibration, and carboxyl groups. In addition, there were unidentified bands present in the fingerprint region of all spectra that could bear more evidence that the sample contains organic signals. Based on the obtained results, it can be concluded that there are organic compounds present in the fossil silicified wood sample.

Preliminary manuscript

This contribution is being finalized as a manuscript and currently in the process of submission. Liesegang, M., Schnell, A., Xie, A., Tahoun, M., Engeser, M., Gee, C. T., & Müller, C. E. Silicification cycles, trace cation gradients, and organic compounds in Upper Jurassic wood as revealed by EPMA, Raman spectroscopy, and MALDI-ToF-MS. The doctoral student performed the experiments for the determination of the IR spectrum of the silicified fossil wood sample. Furthermore, the doctoral student created figures on her results, and wrote the methodology, results, and discussion section on her contributions to the manuscript in cooperation with Christa E. Müller and all co-authors.

11. Development of infrared spectra of a silicified fossil wood sample and search for characteristic bands of lignin

12. Summary

This thesis presents research results from research projects that focus on the development and optimization of analytical methods for identifying and quantifying organic compounds in biological, taphonomic, and fossil samples. The central research objectives for this thesis were:

- Investigation of the chemical degradation of heme, the prosthetic group of the blood protein hemoglobin, under presumed fossilization conditions (Chapter 5)

- Establishment and optimization of protocols for heme extraction from bones (Chapter 6)

- Extraction and quantitative analyses of the cyclic depsipeptides FR and YM from various mouse organs for further *in vitro* and *in vivo* characterization (Chapter 7)

- Extraction, identification, and quantification of compounds from fossils, namely suberin, the polymer unique to bark in plants, from a "monkey hair" fossil tree specimen (Chapter 8)

Additionally, we published two review articles, one containing a detailed overview of the chemistry of porphyrins in fossil plants and animals in general (Chapter 3), published in the peer-reviewed journal *RSC Advances* in 2021, and one containing a detailed overview of organic compounds detected in non-avian dinosaurs, along with the employed analytical techniques (Chapter 4), published in the peer-reviewed journal *Biology (MDPI)* in 2022.

Moreover, several projects were completed in collaboration with members of the Deutsche Forschungsgemeinschaft (DFG) research unit FOR 2685, including determination of the calcium concentrations in the crayfish *Cambarellus diminitus* by atomic absorption spectrophotometry (Chapter 9), and the identification of components of the waxy degradation products of triglycerides, called adipocere, in the same crayfish species (Chapter 10). In addition, characteristic infrared absorption bands of lignin were identified in a silicified fossil wood sample measured by infrared spectroscopy (Chapter 11).

Overall, for the work in this thesis many analytical techniques were employed, namely high-performance liquid chromatography coupled to mass spectrometry with diode array detection (HPLC-(DAD)-MS) or coupled to tandem mass spectrometry (HPLC-MS/MS), atomic absorption spectrophotometry (AAS), infrared (IR) spectroscopy, and nuclear magnetic resonance (NMR) spectroscopy. We found that it is of great importance to develop a variety of analytical methods for the detection of organic compounds in fossils. The following paragraphs

provide a detailed summary and discussion of the obtained data addressing each of the tackled research questions, and, where applicable, providing an outlook towards future research.

12.1. Development and optimization of a method for extraction of heme from bones using HPLC-(DAD)-MS (Chapter 6)

A suitable extraction method of heme (Figure 12.1) from bone was developed (Chapter 6), with the aim to apply this method to dinosaur bone specimens.
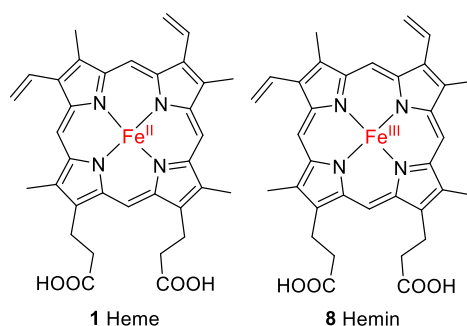

Figure 12.1. Structures of heme and its commercially available form, hemin, used as a standard compound.

Previous attempts to extract heme from recent bones for optimizing a suitable protocol had been limited by the poor recovery rate of heme in the utilized extraction buffers and by the relatively high detection limit of the applied instrument. In this study, we systematically investigated various extraction buffers on recent cow bone and determined the recovery rates of heme obtained by each method. For the experiments, the Fe(III) derivative of heme, hemin chloride (**8**, Figure 12.1), was employed as a standard compound, since it constitutes the stable form of the molecule. The highest recovery rates were observed upon the extraction of hemin using acetone/1.6 M HCl (8:2, v/v) and acetonitrile/1.6 M HCl (8:2, v/v), whereas low to moderate recovery rates were obtained after using methanol/1% ammonia, acetone/10 mM NH$_4$OH (8:2, v/v), or acetone/water (8:2, v/v), see Table 12.1. Moreover, the matrix effect was determined for each extraction solvent to establish whether the signal might be affected by the bone matrix or the extraction buffer (Table 12.1). A matrix effect of 95% means that the sample matrix has a negligible influence on the detection of the compound.

Table 12.1. Recovery rates of hemin after extraction from bone using various extraction reagents, and the matrix effect determined for each reagent.

Extraction reagent	Recovery rate (%) ± SEM	Matrix effect
Acetone/1.6 M HCl (8:2, v/v)	96.9 ± 0.2%	95%
Acetonitrile/1.6 M HCl (8:2, v/v)	99.7 ± 0.9%	n.d.

The developed analytical HPLC-(DAD)-MS method was validated with respect to linearity, limit of detection (LOD), limit of quantification (LOQ), selectivity, repeatability, and intermediate precision, in accordance with the specifications of the International Conference on Harmonization (2005) "Validation of analytical procedure: Text and Methodology (Q2-R1)." The LOD was 0.1-0.25 µM and the LOQ was 0.5-1 µM. The response remained linear up to a concentration of 25 µM, and calibration curves gave a good fit in the range of 0.5-15 µM. The retention time varied only a little (0.1-1%) in the presence of bone matrix and was found to be repeatable possessing high intermediate precision with a low relative standard deviation between replicate sample measurements on the same day and on different days.

With these results, we have now established and optimized an extraction protocol for heme with high recovery that is ready to be applied for the extraction of heme from fossil dinosaur bones. Since the analyses in this study were performed on a single-quadrupole mass spectrometer that is not suitable for trace analysis, re-evaluating the method validation parameters on the more sensitive new hybrid triple-quadrupole ion trap instrument (SCIEX QTRAP 6500+ LC-MS/MS system) can be expected to substantially improve the limits of detection and quantification.

12.2. Molecular taphonomy of heme: Degradation products under presumed fossilization conditions characterized by HPLC-MS/MS (Chapter 5)

Another major part of the work presented in this thesis focused on the elucidation of degradation products of heme (**1**, Figure 12.1) that are produced under presumed fossilization conditions (Chapter 5).

Thus, a molecular taphonomy study was performed, which will help to understand the preservation of compounds over millions of years [3]. Hemin chloride (**8**, Figure 12.1) was exposed to a combination of conditions: oxidation (using hydrogen peroxide), heating in the absence of air, heating in the presence of air, heating in the presence of anaerobic reductive conditions (using sodium dithionite as the reducing agent), and changes in pH value (physiological pH of 7.4, slightly alkaline pH of 8.0, and strongly alkaline pH of 11). The highest stability of hemin was observed upon heating in the absence of air under reductive conditions and a slightly alkaline pH of 8.0, whereas the lowest stability of hemin was seen upon oxidation using hydrogen peroxide. The detailed reaction conditions and half-lives of hemin, and the major degradation products are listed in Table 12.2.

Table 12.2. Experimental conditions employed for studying the degradation of hemin, its observed half-life, and major degradation products detected under each condition.

Type of condition	Conditions, duration and temperature	Major degradation product(s)	Half-life of hemin
Oxidation under alkaline conditions	1% NH_3 in methanol (pH 11.5) + 1% aq. H_2O_2 (v/v) Room temperature (7 h)	Hematinic acid	≤1 min
	1% NH_3 in water (pH 10.5) + 5% aq. H_2O_2 (v/v) 60°C (only for initial 30 min)		≤1 min
Oxidation at physiological pH	Phosphate buffered saline (PBS) (pH 7.4) + 3% aq. H_2O_2 (v/v) Room temperature (8 h)		≤1 min
Heating at physiological pH	PBS (pH 7.4) under aerated conditions 75°C (7 days)	• Hematinic acid • DP-1[a]	2.6 days
	PBS (pH 7.4) under aerated conditions 95°C		0.73 days
	PBS (pH 7.4) under an argon atmosphere 75°C		n.d.
Heating under alkaline conditions	0.1 N aq. NaOH (pH 8) under an argon atmosphere 70°C	• DP-1[a] • DP-2[a] • DP-3[a]	5.5 days
	0.1 N aq. NaOH (pH 8) 0.9% sodium dithionite under an argon atmosphere 70°C	Unknown degradation product with a mass of 650 m/z	9.5 days

[a] DP-1 = degradation product-1; For structures, see Figure 12.2

Analysis by HPLC-MS/MS led to the identification and structural elucidation of at least four degradation products (for structures see Figure 12.2): hematinic acid (**33**, mass-to-charge-ratio (m/z) of 183), degradation product (DP)-1 (**34**, 618 m/z), DP-2 (**35**, 620 m/z), DP-3 (636 m/z), and an unidentified degradation product (650 m/z). Hematinic acid was isolated from the reaction mixture treated under oxidative conditions by preparative HPLC, and its structure was confirmed by nuclear magnetic resonance spectroscopy. The results revealed that the main site of degradation are the vinyl groups of hemin, which was confirmed by lacking degradation in a derivative of hemin, mesohemin chloride (**36**, Figure 12.2), in which the vinyl groups are replaced by ethyl residues. Our results indicated that iron was a key factor contributing to the degradation of heme, which we confirmed by the moderate stability of protoporphyrin IX (**2**, Figure 12.2), its iron-free derivative.
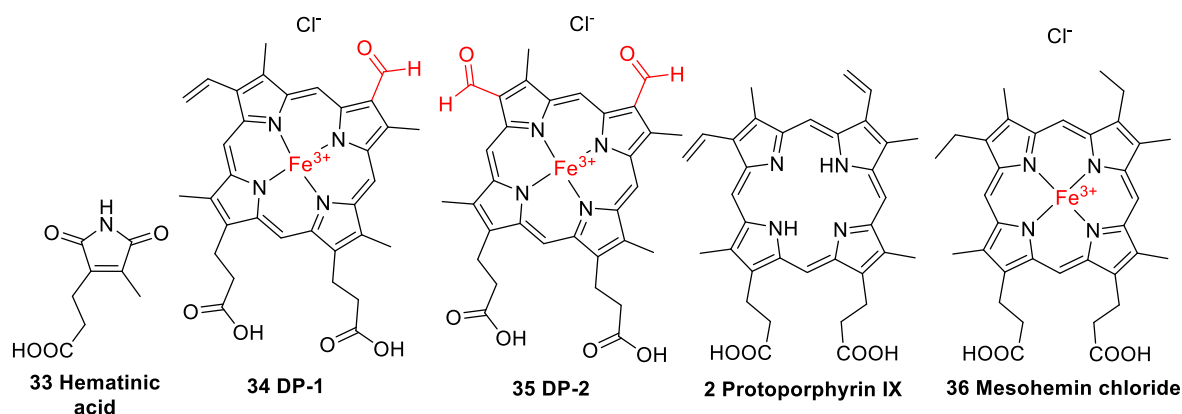
Figure 12.2. Structures of the elucidated degradation products (DP) hematinic acid, DP-1, and DP-2. In addition, the structures of protoporphyrin IX and mesohemin chloride employed as reference compounds in this study are shown.

On the basis of these experiments and the predicted molecular formulae, we could for the first time provide evidence for these degradation products by mass spectrometry: DP-1 is a heme derivative with one vinyl group oxidized to formyl (probably present as two isomers: ferric 2-formyl-8-vinyldeuteroporphyrin IX or ferric 8-formyl-2-vinyldeuteroporphyrin IX), DP-2 is a derivative in which both vinyl groups are oxidized to formyl (ferric 2,8-diformylporphyrin IX), and DP-3 is likely produced by the oxidation of one of the formyl groups of DP-2 to a carboxylic acid (ferric 2-formylporphyrin IX-8-carboxylic acid). Overall, these results indicated that heme might be preserved in some fossils, especially because of the long half-life observed under anaerobic reductive conditions and at a slightly alkaline pH value, which are favorable conditions for fossilization [18]. These findings are useful for understanding the fossilization of heme. The results of this study were published in the peer-reviewed journal *Molecules* in June 2023.

12.3. *In vivo* and *in vitro* characterization of the cyclic depsipeptides FR and YM using HPLC-MS (Chapter 7)

YM and FR are natural cyclic depsipeptides used as tool compounds for studying the signaling pathways of $G\alpha_q$ protein-coupled receptors. YM, FR, and their derivatives have potential for the treatment of asthma, heart and eye diseases. In this study, the compounds were characterized pre-clinically. Chemical stability was evaluated in simulated gastric fluid (pH 1), weakly basic (pH 9), and more strongly basic conditions (pH 11)), and the *in vivo* tissue and organ distribution after intratracheal and intraperitoneal injection were investigated. For sample measurements, qualitative and quantitative analyses were performed using HPLC coupled to tandem mass spectrometry (MS/MS), including high-resolution quadrupole-time-of-flight (qTOF) tandem mass spectrometry, and quantitative analysis was performed using the extract ion chromatograms (EICs) of both compounds.

In simulated gastric fluid (pH 1) and mild alkaline aqueous solution (pH 9), FR and YM were relatively stable, FR was being even more stable than YM. However, under harsher alkaline conditions (pH 11), both FR and YM degraded, FR displaying a slower degradation rate.

After intratracheal application of FR or YM (5 µg) in mice for 7 consecutive days, their concentrations were determined in all organs using high-resolution HPLC-qTOF-MS/MS, with prior determination of the recovery rates. Lungs and kidney contained the highest quantities of FR and YM, whereas in the brain and plasma very low concentrations were found. In a longer *in vivo* study with intraperitoneal application of FR to mice for 3 weeks, the compound was mainly found in the lung, along with lower amounts in liver, eyes and intestine, and negligible amounts in the brain. Thus, regardless of the route of administration, the organ distribution of FR was similar.

The results showed that FR and YM are detected in vital organs (liver, kidney) in addition to the lungs and eyes; however, only negligible amounts are able to cross the blood-brain barrier. These results are of great importance for future pharmacological studies. The results of this study were published in the peer-reviewed journal *ACS Pharmacology and Translational Science* in 2021.

12.4. Identification of the bark constituent suberin from a 45-million-year-old fossilized "monkey hair" tree using HPLC-MS (Chapter 8)

"Monkey hair" is an approximately 45-million-year-old fossil made up of mats of preserved laticifers, occasionally surrounded by partially elucidated organic matter, believed to be parts of a tree, found in the former coal mine in Geiseltal (Eastern Germany). An exceptionally preserved fossil "monkeyhair" specimen, GHM Y74, was studied with the aim to chemically characterize the outermost layer for suberin, the unique component of bark (Figure 12.3), to be able to confirm that this layer is indeed preserved bark. Using HPLC-(DAD)-MS, samples from each layer, recent *Quercus suber* (as a positive control) and cellulose (negative control) were depolymerized and extracted to search for hydrolysis products of suberin. Only after depolymerization, the compounds 1,18-octadec-9-enedioic acid (detected as a mixture of its *cis*-, **29**, and *trans*-, **30**, isomers, Figure 12.3), 1,20-eicosanedioic acid (**31**, Figure 12.3), and *cis*-ferulic acid (**32**, Figure 12.3) were identified and quantified in the outermost layer, but not in the other layers. Our results indicate that the outermost layer indeed represents preserved bark containing suberin.
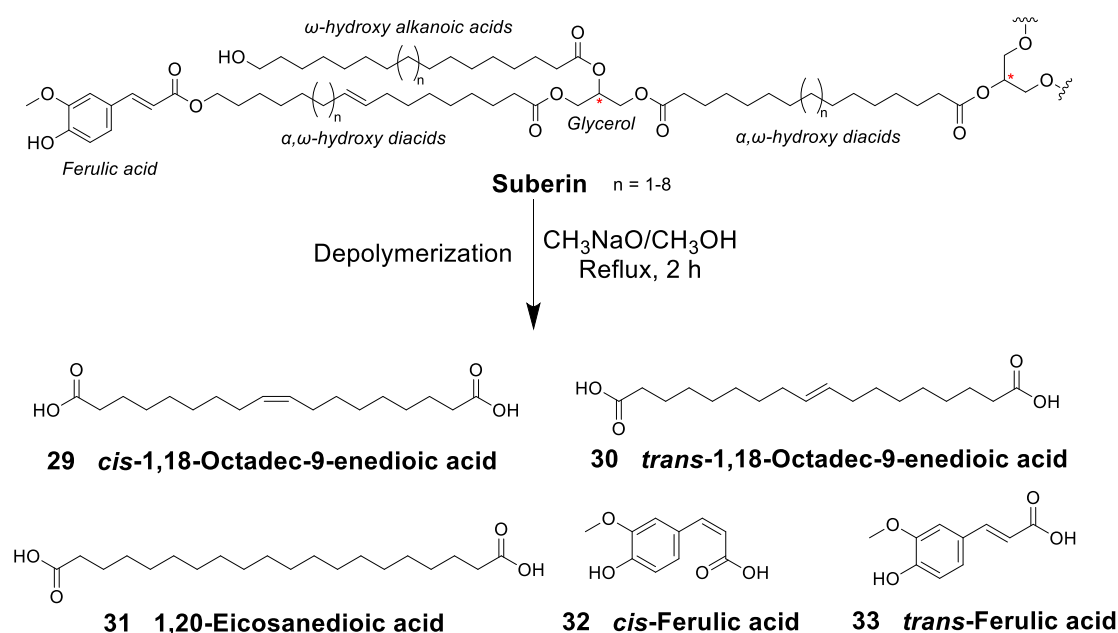

Figure 12.3. Partial structure of suberin and selected monomeric constituents detected in this study.

It is interesting to note that ferulic acid was present as a *cis*-isomer (**32**, Figure 12.3) and not in its natural *trans*-configuration (**33**, Figure 12.3), suggesting changes to the stereochemistry during the fossilization process.

This is the first time that compelling chemical evidence for the presence of suberin in fossilized tree trunks has been obtained. Thus, in the "monkeyhair" fossil, fossilization conditions appear to have been mild, and probably due to low moisture, the ester bonds were not hydrolyzed. This information could help paleontologists in understanding the mechanisms of fossilization and how the sedimentary environment present in the Geiseltal Lagerstätte contributed to the preservation of organic compounds and soft tissues. The results of this study are planned to be incorporated in a manuscript to be submitted to a peer-reviewed journal.

12.5. Collaboration projects (Chapters 9-11)

In a collaboration study with Dr. Bastian Mähler (Department of Paleontology, University of Bonn), the calcium concentrations in decaying crayfish of the species *Cambarellus diminitus* were determined and quantified using AAS (published in *Palaeontologia Electronica*, 2020).

In another collaboration study with Dr. Bastian Mähler, constituents of adipocere in decaying crayfish of the species *Cambarellus diminitus* were extracted and analyzed using HPLC-(DAD)-MS (published in *Scientific Reports*, 2022).

In a collaboration study with Dr. Moritz Liesegang (who was then affiliated with the Department of Paleontology, University of Bonn), constituents of lignin, a structural component present in the cell walls of plants as a component of wood, were identified in a silicified fossil wood sample using IR spectroscopy (manuscript in preparation).

12.6. Conclusions

In conclusion, the results presented in this thesis demonstrate the power of modern analytical techniques for characterizing recent biological samples (e.g., cow bones or mouse organs), taphonomic animal samples (e.g., decaying crayfish), taphonomic samples of molecules (heme), and fossil samples (fossilized tree specimens).

13. References

1.   Brett, C.E.; Thomka, J.R. Fossils and fossilisation. In *Encyclopedia of Life Sciences*; John Wiley & Sons, Ltd, Chichester, UK, 2013; pp. 1–12, ISBN 9780470015902.

2.   Briggs, D.E.G. The role of decay and mineralization in the preservation of soft-bodied fossils. *Annu. Rev. Earth Planet. Sci.* **2003**, *31*, 275–301, doi:10.1146/annurev.earth.31.100901.144746.

3.   Eglinton, G.; Logan, G.A. Molecular preservation. *Philos. Trans. R. Soc. Lond. B Biol. Sci.* **1991**, *333*, 315–328, doi:10.1098/rstb.1991.0081.

4.   Allison, P.A. Konservat-Lagerstätten: Cause and classification. *Paleobiology* **1988**, *14*, 331–344.

5.   Smiley, C.J.; Rember, W.C. Physical setting of the Miocene Clarkia fossil beds, northern Idaho. In *Late Cenozoic History of the Pacific Northwest*; Smiley, C.J., Ed.; American Association for the Advancement of Science: San Francisco, CA, USA, 1985; pp. 11–31.

6.   Chure, D.J.; Litwin, R.; Hasiotis, S.T.; Evanoff, E.; Carpenter, K. The fauna and flora of the Morrison Formation. In *Paleontology and Geology of the Upper Jurassic Morrison Formation. New Mexico Museum of Natural History and Science Bulletin 36*; Foster, J.R., Lucas, S.G., Eds.; New Mexico Museum of Natural History and Science: Albuquerque, NM, USA, 2006; Vol. 36, pp. 233–249.

7.   Hellmund, M. The former Geiseltal Museum (1934-2011), the Eocene Geiseltal Fossilagerstätte (Germany) and the scientific meaning of Ben Barnes as a pioneer of systematic quantitative vertebrate excavations in the Geiseltal lignites. *Anuário Do Inst. Geociências - UFRJ* **2018**, *41*, 108–119, doi:10.11137/2018_1_108_119.

8.   Lee, Y.C.; Chiang, C.C.; Huang, P.Y.; Chung, C.Y.; Huang, T.D.; Wang, C.C.; Chen, C.I.; Chang, R.S.; Liao, C.H.; Reisz, R.R. Evidence of preserved collagen in an early Jurassic sauropodomorph dinosaur revealed by synchrotron FTIR microspectroscopy. *Nat. Commun.* **2017**, *8*, 14220, doi:10.1038/ncomms14220.

9.   Schweitzer, M.H. Soft tissue preservation in terrestrial Mesozoic vertebrates. *Annu. Rev. Earth Planet. Sci.* **2011**, *39*, 187–216, doi:10.1146/annurev-earth-040610-133502.

10.   Senter, P.J. Cells and soft tissues in fossil bone: A review of preservation mechanisms, with corrections of misconceptions. *Palaeontol. Electron.* **2022**, *25*, a34, doi:https://doi.org/10.26879/1248.

11.   Schweitzer, M.H.; Wittmeyer, J.L.; Horner, J.R. Soft tissue and cellular preservation in vertebrate skeletal elements from the Cretaceous to the present. *Proc. R. Soc. B Biol. Sci.* **2007**, *274*, 183–197, doi:10.1098/rspb.2006.3705.

12.   Schweitzer, M.H. Molecular paleontology: Some current advances and problems. *Ann. Paléontol.* **2004**, *90*, 81–102, doi:10.1016/j.annpal.2004.02.001.

13.   Behrensmeyer, A.K.; Kidwell, S.M.; Gastaldo, R.A. Taphonomy and paleobiology. *Paleobiology* **2000**, *26*, 103–147, doi:10.1017/S0094837300026907.

14.   Briggs, D.E.G. Experimental taphonomy. *Palaios* **1995**, *10*, 539–550, doi:10.2307/3515093.

15.   Behrensmeyer, A.K.; Kidwell, S.M. Taphonomy's contributions to paleobiology. *Paleobiology* **1985**, *11*, 105–119, doi:10.1017/S009483730001143X.

16.   Briggs, D.E.G. Molecular taphonomy of animal and plant cuticles: Selective preservation and diagenesis. *Philos. Trans. R. Soc. Lond. B Biol. Sci.* **1999**, *354*, 7–17, doi:10.1098/rstb.1999.0356.

17.   Parry, L.A.; Smithwick, F.; Nordén, K.K.; Saitta, E.T.; Lozano-Fernandez, J.; Tanner, A.R.; Caron, J.-B.; Edgecombe, G.D.; Briggs, D.E.G.; Vinther, J. Soft-bodied fossils are not simply rotten carcasses - Toward a holistic understanding of exceptional fossil preservation. *BioEssays* **2018**, *40*, 1700167, doi:10.1002/bies.201700167.

18.   Pfretzschner, H.-U. Fossilization of Haversian bone in aquatic environments. *Comptes Rendus Palevol* **2004**, *3*, 605–616, doi:10.1016/j.crpv.2004.07.006.

19.   Collins, M.J.; Nielsen-Marsh, C.M.; Hiller, J.; Smith, C.I.; Roberts, J.P.; Prigodich, R. V.; Wess, T.J.; Csapò, J.; Millard, A.R.; Turner-Walker, G. The survival of organic matter in bone: A review. *Archaeometry* **2002**, *44*, 383–394, doi:10.1111/1475-4754.t01-1-00071.

20.   Meyers, P.A.; Leenheer, M.J.; Erstfeld, K.M.; Bourbonniere, R.A. Changes in spruce composition following burial in lake sediments for 10,000 yr. *Nature* **1980**, *287*, 534–536, doi:10.1038/287534a0.

21. Hedges, J.I.; Cowie, G.L.; Ertel, J.R.; James Barbour, R.; Hatcher, P.G. Degradation of carbohydrates and lignins in buried woods. *Geochim. Cosmochim. Acta* **1985**, *49*, 701–711, doi:10.1016/0016-7037(85)90165-6.

22. Cranwell, P.A. Diagenesis of free and bound lipids in terrestrial detritus deposited in a lacustrine sediment. *Org. Geochem.* **1981**, *3*, 79–89, doi:10.1016/0146-6380(81)90002-4.

23. Janssen, K.; Mähler, B.; Rust, J.; Bierbaum, G.; McCoy, V.E. The complex role of microbial metabolic activity in fossilization. *Biol. Rev.* **2022**, *97*, 449–465, doi:10.1111/brv.12806.

24. Briggs, D.E.G.; McMahon, S. The role of experiments in investigating the taphonomy of exceptional preservation. *Palaeontology* **2016**, *59*, 1–11, doi:10.1111/pala.12219.

25. Reimers, C.E.; Fischer, K.M.; Merewether, R.; Smith, K.L.; Jahnke, R.A. Oxygen microprofiles measured *in situ* in deep ocean sediments. *Nature* **1986**, *320*, 741–744, doi:10.1038/320741a0.

26. Revsbech, N.P.; Sorensen, J.; Blackburn, T.H.; Lomholt, J.P. Distribution of oxygen in marine sediments measured with microelectrodes. *Limnol. Oceanogr.* **1980**, *25*, 403–411, doi:10.4319/lo.1980.25.3.0403.

27. Harvey, H.R.; Fallon, R.D.; Patton, J.S. The effect of organic matter and oxygen on the degradation of bacterial membrane lipids in marine sediments. *Geochim. Cosmochim. Acta.* **1986**, *50*, 795–804, doi:10.1016/0016-7037(86)90355-8.

28. Jørgensen, B.B. Mineralization of organic matter in the sea bed—the role of sulphate reduction. *Nature* **1982**, *296*, 643–645, doi:10.1038/296643a0.

29. Butterfield, N.J. Organic preservation of non-mineralizing organisms and the taphonomy of the Burgess Shale. *Paleobiology* **1990**, *16*, 272–286.

30. Saitta, E.T.; Kaye, T.G.; Vinther, J. Sediment-encased maturation: A novel method for simulating diagenesis in organic fossil preservation. *Palaeontology* **2019**, *62*, 135–150, doi:10.1111/pala.12386.

31. Collins, M.; Riley, M.S. Amino acid racemization in biominerals: the impact of protein degradation and loss. In *Perspectives in Amino Acid and Protein Geochemistry*; Goodfriend, G.A., Collins, M.J., Fogel, M.L., Macko, S.A., Wehmiller, J.F., Eds.;

Oxford University Press: Oxford, UK, 2000; pp. 120–142.

32. Zonneveld, K.A.F.; Versteegh, G.J.M.; Kasten, S.; Eglinton, T.I.; Emeis, K.-C.; Huguet, C.; Koch, B.P.; de Lange, G.J.; de Leeuw, J.W.; Middelburg, J.J.; et al. Selective preservation of organic matter in marine environments; processes and impact on the sedimentary record. *Biogeosciences* **2010**, *7*, 483–511, doi:10.5194/bg-7-483-2010.

33. Ratnayake, W.M.N.; Galli, C. Fat and fatty acid terminology, methods of analysis and fat digestion and metabolism. *Ann. Nutr. Metab.* **2009**, *55*, 8–43.

34. Konige, M.; Wang, H.; Sztalryd, C. Role of adipose specific lipid droplet proteins in maintaining whole body energy homeostasis. *Biochim. Biophys. Acta.* **2014**, *1842*, 393–401, doi:10.1016/j.bbadis.2013.05.007.

35. Kolattukudy, P.E. Polyesters in higher plants. In *Biopolyesters. Advances in Biochemical Engineering/Biotechnology*; Babel, W., Steinbüchel, A., Eds.; Springer-Verlag: Berlin, Germany, 2001; Vol. 71, pp. 1–49, ISBN 978-3-540-40021-9.

36. Evershed, R.P. Biomolecular archaeology and lipids. *World Archaeol.* **1993**, *25*, 74–93, doi:10.1080/00438243.1993.9980229.

37. Finkel, P.L.; Carrizo, D.; Parro, V.; Sánchez-García, L. An overview of lipid biomarkers in terrestrial extreme environments with relevance for Mars exploration. *Astrobiology* **2023**, *23*, 563–604, doi:10.1089/ast.2022.0083.

38. Summons, R.E.; Welander, P. V.; Gold, D.A. Lipid biomarkers: Molecular tools for illuminating the history of microbial life. *Nat. Rev. Microbiol.* **2022**, *20*, 174–185, doi:10.1038/s41579-021-00636-2.

39. Meyers, P.A.; Leenheer, M.J.; Bourbonniere, R.A. Diagenesis of vascular plant organic matter components during burial in lake sediments. *Aquat. Geochem.* **1995**, *1*, 35–52, doi:10.1007/BF01025230.

40. Ubelaker, D.H.; Zarenko, K.M. Adipocere: What is known after over two centuries of research. *Forensic Sci. Int.* **2011**, *208*, 167–172, doi:10.1016/j.forsciint.2010.11.024.

41. Schoenen, D.; Schoenen, H. Adipocere formation—The result of insufficient microbial degradation. *Forensic Sci. Int.* **2013**, *226*, 301.e1-301.e6, doi:10.1016/j.forsciint.2013.01.023.

42. Moses, R.J. Experimental adipocere formation: Implications for adipocere formation on buried bone. *J. Forensic Sci.* **2012**, *57*, 589–595, doi:10.1111/j.1556-4029.2011.02032.x.

43. Giannotas, G.; Kamperidou, V.; Barboutis, I. Tree bark utilization in insulating bio-aggregates: A review. *Biofuels Bioprod. Biorefin.* **2021**, *15*, 1989–1999, doi:10.1002/bbb.2291.

44. Leite, C.; Pereira, H. Cork-containing barks—A review. *Front. Mater.* **2017**, *3*, 63.

45. Pereira, H. Chemical composition and variability of cork from *Quercus suber* L. *Wood Sci. Technol.* **1988**, *22*, 211–218.

46. Graça, J.; Santos, S. Glycerol-derived ester oligomers from cork suberin. *Chem. Phys. Lipids* **2006**, *144*, 96–107.

47. Tegelaar, E.W.; de Leeuw, J.W.; Derenne, S.; Largeau, C. A reappraisal of kerogen formation. *Geochim. Cosmochim. Acta* **1989**, *53*, 3103–3106, doi:10.1016/0016-7037(89)90191-9.

48. Tegelaar, E.W.; Hollman, G.; Van Der Vegt, P.; De Leeuw, J.W.; Holloway, P.J. Chemical characterization of the periderm tissue of some angiosperm species: Recognition of an insoluble, non-hydrolyzable, aliphatic biomacromolecule (Suberan). *Org. Geochem.* **1995**, *23*, 239–251, doi:10.1016/0146-6380(94)00123-I.

49. Cooper, G.M. The molecular composition of cells. In *The Cell: A Molecular Approach*; Sinauer Associates: Sunderland, MA, USA, 2000; pp. 43–72, ISBN 0-87893-106-6.

50. Warinner, C.; Korzow Richter, K.; Collins, M.J. Paleoproteomics. *Chem. Rev.* **2022**, *122*, 13401–13446, doi:10.1021/acs.chemrev.1c00703.

51. Montgelard, C. Albumin preservation in fossil bones and systematics of *Malpaisomys insularis* (Muridae, Rodentia), an extinct rodent of the Canary Islands. *Hist. Biol.* **1992**, *6*, 293–302, doi:10.1080/10292389209380437.

52. Ajie, H.O.; Hauschka, P.V.; Kaplan, I.R.; Sobel, H. Comparison of bone collagen and osteocalcin for determination of radiocarbon ages and paleodietary reconstruction. *Earth Planet. Sci. Lett.* **1991**, *107*, 380–388, doi:10.1016/0012-821X(91)90084-U.

53. Muyzer, G.; Sandberg, P.; Knapen, M.H.J.; Vermeer, C.; Collins, M.; Westbroek, P. Preservation of the bone protein osteocalcin in dinosaurs. *Geology* **1992**, *20*, 871–874, doi:10.1130/0091-7613(1992)020<0871:POTBPO>2.3.CO;2.

54. Schweitzer, M.H.; Zheng, W.; Moyer, A.E.; Sjövall, P.; Lindgren, J. Preservation potential of keratin in deep time. *PLOS ONE* **2018**, *13*, e0206569, doi:10.1371/journal.pone.0206569.

55. Schweitzer, M.H.; Watt, J.A.; Avci, R.; Knapp, L.; Chiappe, L.; Norell, M.; Marshall, M. Beta-keratin specific immunological reactivity in feather-like structures of the Cretaceous Alvarezsaurid, *Shuvuuia deserti*. *J. Exp. Zool.* **1999**, *285*, 146–157, doi:10.1002/(SICI)1097-010X(19990815)285:2<146::AID-JEZ7>3.0.CO;2-A.

56. Lindgren, J.; Kuriyama, T.; Madsen, H.; Sjövall, P.; Zheng, W.; Uvdal, P.; Engdahl, A.; Moyer, A.E.; Gren, J.A.; Kamezaki, N.; et al. Biochemistry and adaptive colouration of an exceptionally preserved juvenile fossil sea turtle. *Sci. Rep.* **2017**, *7*, 13324, doi:10.1038/s41598-017-13187-5.

57. Wadsworth, C.; Buckley, M. Proteome degradation in fossils: Investigating the longevity of protein survival in ancient bone. *Rapid Commun. Mass Spectrom.* **2014**, *28*, 605–615, doi:10.1002/rcm.6821.

58. Smith, K.M. General features of the structure and chemistry of porphyrin compounds. In *Porphyrins and Metalloporphyrins: A New Edition Based on the Original Volume by J. E. Falk*; Smith, K.M., Ed.; Elsevier Scientific Publishing Company: Amsterdam, The Netherlands, 1975; pp. 3–28, ISBN 9780444415370.

59. Phillips, J.D. Heme biosynthesis and the porphyrias. *Mol. Genet. Metab.* **2019**, *128*, 164–177, doi:10.1016/j.ymgme.2019.04.008.

60. Roca, M.; Chen, K.; Perez-Galvez, A. Chlorophylls. In *Handbook on Natural Pigments in Food and Beverages: Industrial Applications for Improving Food Color*; Carle, R., Schweiggert, R., Eds.; Woodhead Publishing: Cambridge, UK, 2016; pp. 125–158, ISBN 978-0-08-100371-8.

61. Melkozernov, A.N.; Blankenship, R.E. Photosynthetic functions of chlorophylls. In *Chlorophylls and Bacteriochlorophylls*; Springer: Dordrecht, The Netherlands, 2006; Volume 25, pp. 397–412.

62. Scheer, H. An overview of chlorophylls and bacteriochlorophylls: Biochemistry, biophysics, functions and applications. In *Chlorophylls and Bacteriochlorophylls*; Grimm, B; Porra, R.; Rüdiger, W; Scheer. H., Eds.; Springer: Dordrecht, The Netherlands, 2006; pp. 1–26.

63. Wallace, K.G.; Rimmer, J.; Manley, S.K.; Unsworth, J.F.; Jackson, A.H.; Albert, N. Studies on the biosynthesis of the *Chlorobium* chlorophylls. *Philos. Trans. R. Soc. Lond. B Biol. Sci.* **1976**, *273*, 255–276, doi:10.1098/rstb.1976.0012.

64. Tahoun, M.; Gee, C.T.; McCoy, V.E.; Sander, P.M.; Müller, C.E. Chemistry of porphyrins in fossil plants and animals. *RSC Adv.* **2021**, *11*, 7552–7563, doi:10.1039/D0RA10688G.

65. Gueneli, N.; Mckenna, A.M.; Ohkouchi, N.; Boreham, C.J.; Beghin, J.; Javaux, E.J.; Brocks, J.J. 1.1-billion-year-old porphyrins establish a marine ecosystem dominated by bacterial primary producers. *Proc. Natl. Acad. Sci.* **2018**, *115*, E6978–E6986, doi:10.1073/pnas.1803866115.

66. Dilcher, D.L.; Pavlick, R.J.; Mitchell, J. Chlorophyll derivatives in Middle Eocene sediments. *Science* **1970**, *168*, 1447–1449, doi:10.1126/science.168.3938.1447.

67. Giannasi, D.E.; Niklas, K.J. Flavonoid and other chemical constituents of fossil Miocene *Celtis* and *Ulmus* (Succor Creek Flora). *Science* **1977**, *197*, 765–767, doi:10.1126/science.197.4305.765.

68. Schweitzer, M.H.; Marshall, M.; Carron, K.; Bohle, D.S.; Busse, S.C.; Arnold, E. V.; Barnard, D.; Horner, J.R.; Starkey, J.R. Heme compounds in dinosaur trabecular bone. *Proc. Natl. Acad. Sci. USA* **1997**, *94*, 6291–6296, doi:10.1073/pnas.94.12.6291.

69. Greenwalt, D.E.; Goreva, Y.S.; Siljeström, S.M.; Rose, T.; Harbach, R.E. Hemoglobin-derived porphyrins preserved in a Middle Eocene blood-engorged mosquito. *Proc. Natl. Acad. Sci. USA* **2013**, *110*, 18496–18500, doi:10.1073/pnas.1310885110.

70. Lindgren, J.; Kuriyama, T.; Madsen, H.; Sjövall, P.; Zheng, W.; Uvdal, P.; Engdahl, A.; Moyer, A.E.; Gren, J.A.; Kamezaki, N.; et al. Biochemistry and adaptive colouration of an exceptionally preserved juvenile fossil sea turtle. *Sci. Rep.* **2017**, *7*, 13324, doi:10.1038/s41598-017-13187-5.

71. Yen, T.F. The role of metal-heteroatom complexes in fossil fuel production. In *Environmental Speciation and Monitoring Needs for Trace Metal-containing Substances from Energy-related Processes: Proceedings of the DoE/NBS Workshop Held at the National Bureau of Standards, Gaithersburg, MD, May 18-20, 1981*; Brinckman, F.E., Fish, R.H., Eds.; National Bureau of Standards, US Department of Commerce: Washington, D.C., USA, 1981; Vol. 618, pp. 9–20.

72. Treibs, A. Chlorophyll-und Häminderivate in bituminösen Gesteinen, Erdölen, Erdwachsen und Asphalten. Ein Beitrag zur Entstehung des Erdöls. *Justus Liebigs Ann. Der Chem.* **1934**, *510*, 42–62.

73. Treibs, A. Chlorophyll- und Häminderivate in organischen Mineralstoffen. *Angew. Chem.* **1936**, *49*, 682–686, doi:10.1002/ange.19360493803.

74. Falk, H.; Wolkenstein, K. Natural product molecular fossils. *Prog. Chem. Org. Nat. Prod.* **2017**, *104*, 1–126. doi: 10.1007/978-3-319-45618-8_1

75. Verne-Mismer, J.; Ocampo, R.; Callot, H.J.; Albrecht, P. New chlorophyll fossils from moroccan oil shales. Porphyrins derived from chlorophyll c_3 or a related pigment? *Tetrahedron Lett.* **1990**, *31*, 1751–1754, doi:10.1016/S0040-4039(00)88872-3.

76. Currie, P.J. Celebrating dinosaurs: Their behaviour, evolution, growth, and physiology. *Can. J. Earth Sci.* **2023**, *60*, 263–293, doi:10.1139/cjes-2022-0131.

77. Armitage, M.H.; Solliday, J. UV autofluorescence microscopy of dinosaur bone reveals encapsulation of blood clots within vessel canals. *Micros. Today* **2020**, *28*, 30–38, doi:10.1017/s1551929520001340.

78. Schweitzer, M.H.; Zheng, W.; Cleland, T.P.; Bern, M. Molecular analyses of dinosaur osteocytes support the presence of endogenous molecules. *Bone* **2013**, *52*, 414–423, doi:10.1016/j.bone.2012.10.010.

79. Armitage, M.H.; Anderson, K.L. Soft sheets of fibrillar bone from a fossil of the supraorbital horn of the dinosaur *Triceratops horridus*. *Acta Histochem.* **2013**, *115*, 603–608, doi:10.1016/j.acthis.2013.01.001.

80. Bertazzo, S.; Maidment, S.C.R.; Kallepitis, C.; Fearn, S.; Stevens, M.M.; Xie, H.N. Fibres and cellular structures preserved in 75-million-year-old dinosaur specimens. *Nat. Commun.* **2015**, *6*, 7352, doi:10.1038/ncomms8352.

81. Surmik, D.; Boczarowski, A.; Balin, K.; Dulski, M.; Szade, J.; Kremer, B.; Pawlicki, R. Spectroscopic studies on organic matter from Triassic reptile bones, Upper Silesia, Poland. *PLOS ONE* **2016**, *11*, e0151143, doi:10.1371/journal.pone.0151143.

82. Schweitzer, M.H.; Wittmeyer, J.L.; Horner, J.R.; Toporski, J.K. Soft-tissue vessels and cellular preservation in *Tyrannosaurus rex*. *Science* **2005**, *307*, 1952–1955, doi:10.1126/science.1108397.

83. Vinther, J. Reconstructing vertebrate paleocolor. *Annu. Rev. Earth Planet. Sci.* **2020**, *48*, 345–375, doi:10.1146/annurev-earth-073019-045641.

84. Li, Q.; Gao, K.Q.; Vintner, J.; Shawkey, M.D.; Clarke, J.A.; D'Alba, L.; Meng, Q.; Briggs, D.E.G.; Prum, R.O. Plumage color patterns of an extinct dinosaur. *Science.* **2010**, *327*, 1369–1372, doi:10.1126/science.1186290.

85. Zhang, F.; Kearns, S.L.; Orr, P.J.; Benton, M.J.; Zhou, Z.; Johnson, D.; Xu, X.; Wang, X. Fossilized melanosomes and the colour of Cretaceous dinosaurs and birds. *Nature* **2010**, *463*, 1075–1078, doi:10.1038/nature08740.

86. Pan, Y.; Zheng, W.; Sawyer, R.H.; Pennington, M.W.; Zheng, X.; Wang, X.; Wang, M.; Hu, L.; O'Connor, J.; Zhao, T.; et al. The molecular evolution of feathers with direct evidence from fossils. *Proc. Natl. Acad. Sci. USA* **2019**, *116*, 3018–3023, doi:10.1073/pnas.1815703116.

87. Brown, C.M.; Henderson, D.M.; Vinther, J.; Fletcher, I.; Sistiaga, A.; Herrera, J.; Summons, R.E. An exceptionally preserved three-dimensional armored dinosaur reveals insights into coloration and Cretaceous predator-prey dynamics. *Curr. Biol.* **2017**, *27*, 2514-2521.e3, doi:10.1016/j.cub.2017.06.071.

88. Christiansen, N.A.; Tschopp, E. Exceptional stegosaur integument impressions from the Upper Jurassic Morrison Formation of Wyoming. *Swiss J. Geosci.* **2010**, *103*, 163–171, doi:10.1007/s00015-010-0026-0.

89. Wiemann, J.; Yang, T.R.; Sander, P.N.; Schneider, M.; Engeser, M.; Kath-Schorr, S.; Müller, C.E.; Sander, P.M. Dinosaur origin of egg color: Oviraptors laid blue-green eggs. *PeerJ* **2017**, *5*, e3706, doi:10.7717/peerj.3706.

90. Reisz, R.R.; Huang, T.D.; Roberts, E.M.; Peng, S.; Sullivan, C.; Stein, K.; Leblanc, A.R.H.; Shieh, D.; Chang, R.; Chiang, C.; et al. Embryology of Early Jurassic dinosaur

from China with evidence of preserved organic remains. *Nature* **2013**, *496*, 210–214, doi:10.1038/nature11978.

91.   Wiemann, J.; Yang, T.R.; Norell, M.A. Dinosaur egg colour had a single evolutionary origin. *Nature* **2018**, *563*, 555–558, doi:10.1038/s41586-018-0646-5.

92.   Norell, M.A.; Wiemann, J.; Fabbri, M.; Yu, C.; Marsicano, C.A.; Moore-Nall, A.; Varricchio, D.J.; Pol, D.; Zelenitsky, D.K. The first dinosaur egg was soft. *Nature* **2020**, *583*, 406–410, doi:10.1038/s41586-020-2412-8.

93.   Schweitzer, M.H.; Chiappe, L.; Garrido, A.C.; Lowenstein, J.M.; Pincus, S.H. Molecular preservation in Late Cretaceous sauropod dinosaur eggshells. *Proc. R. Soc. B Biol. Sci.* **2005**, *272*, 775–784, doi:10.1098/rspb.2004.2876.

94.   Dhiman, H.; Dutta, S.; Kumar, S.; Verma, V.; Prasad, G.V.R. Discovery of proteinaceous moieties in Late Cretaceous dinosaur eggshell. *Palaeontology* **2021**, *64*, 585–595, doi:10.1111/pala.12565.

95.   Tahoun, M.; Engeser, M.; Namasivayam, V.; Sander, P.M.; Müller, C.E. Chemistry and analysis of organic compounds in dinosaurs. *Biology* **2022**, *11*, 670, doi:10.3390/biology11050670.

96.   Lindgren, J.; Sjövall, P.; Carney, R.M.; Cincotta, A.; Uvdal, P.; Hutcheson, S.W.; Gustafsson, O.; Lefèvre, U.; Escuillié, F.; Heimdal, J.; et al. Molecular composition and ultrastructure of Jurassic paravian feathers. *Sci. Rep.* **2015**, *5*, 13520, doi:10.1038/srep13520.

97.   Lingham-Soliar, T.; Plodowski, G. The integument of *Psittacosaurus* from Liaoning Province, China: Taphonomy, epidermal patterns and color of a ceratopsian dinosaur. *Naturwissenschaften* **2010**, *97*, 479–486, doi:10.1007/s00114-010-0661-3.

98.   Wiemann, J.; Yang, T.R.; Sander, P.N.; Schneider, M.; Engeser, M.; Kath-Schorr, S.; Müller, C.E.; Martin Sander, P. Dinosaur origin of egg color: Oviraptors laid blue-green eggs. *PeerJ* **2017**, *5*, e3706, doi:10.7717/peerj.3706.

99.   Lee, Y.C.; Chiang, C.C.; Huang, P.Y.; Chung, C.Y.; Huang, T.D.; Wang, C.C.; Chen, C.I.; Chang, R.S.; Liao, C.H.; Reisz, R.R. Evidence of preserved collagen in an Early Jurassic sauropodomorph dinosaur revealed by synchrotron FTIR microspectroscopy. *Nat. Commun.* **2017**, *8*, 14220, doi:10.1038/ncomms14220.

100. Schweitzer, M.H.; Suo, Z.; Avci, R.; Asara, J.M.; Allen, M.A.; Arce, F.T.; Horner, J.R. Analyses of soft tissue from *Tyrannosaurus rex* suggest the presence of protein. *Science.* **2007**, *316*, 277–280, doi:10.1126/science.1138709.

101. Asara, J.M.; Schweitzer, M.H.; Freimark, L.M.; Phillips, M.; Cantley, L.C. Protein sequences from mastodon and *Tyrannosaurus rex* revealed by mass spectrometry. *Science* **2007**, *316*, 280–285, doi:10.1126/science.1137614.

102. Schweitzer, M.H.; Zheng, W.; Organ, C.L.; Avci, R.; Suo, Z.; Freimark, L.M.; Lebleu, V.S.; Duncan, M.B.; Heiden, M.G.V.; Neveu, J.M.; et al. Biomolecular characterization and protein sequences of the Campanian hadrosaur *B. canadensis*. *Science* **2009**, *324*, 626–631, doi:10.1126/science.1165069.

103. Schroeter, E.R.; Dehart, C.J.; Cleland, T.P.; Zheng, W.; Thomas, P.M.; Kelleher, N.L.; Bern, M.; Schweitzer, M.H. Expansion for the *Brachylophosaurus canadensis* collagen I sequence and additional evidence of the preservation of Cretaceous protein. *J. Proteome Res.* **2017**, *16*, 920–932, doi:10.1021/acs.jproteome.6b00873.

104. Bailleul, A.M.; Zheng, W.; Horner, J.R.; Hall, B.K.; Holliday, C.M.; Schweitzer, M.H. Evidence of proteins, chromosomes and chemical markers of DNA in exceptionally preserved dinosaur cartilage. *Natl. Sci. Rev.* **2020**, *7*, 815–822, doi:10.1093/NSR/NWZ206.

105. Moyer, A.E.; Zheng, W.; Schweitzer, M.H. Microscopic and immunohistochemical analyses of the claw of the nesting dinosaur, *Citipati osmolskae. Proc. R. Soc. B Biol. Sci.* **2016**, *283*, 20161997, doi:10.1098/rspb.2016.1997.

106. Simon, J.D.; Peles, D.N. The red and the black. *Acc. Chem. Res.* **2010**, *43*, 1452–1460, doi:10.1021/ar100079y.

107. Ito, S.; Wakamatsu, K. Quantitative analysis of eumelanin and pheomelanin in humans, mice, and other animals: A comparative review. *Pigment Cell Res.* **2003**, *16*, 523–531, doi:10.1034/j.1600-0749.2003.00072.x.

108. Meredith, P.; Sarna, T. The physical and chemical properties of eumelanin. *Pigment Cell Res.* **2006**, *19*, 572–594, doi:10.1111/j.1600-0749.2006.00345.x.

109. Shoulders, M.D.; Raines, R.T. Collagen structure and stability. *Annu. Rev. Biochem.* **2009**, *78*, 929–958, doi:10.1146/annurev.biochem.77.032207.120833.

110. Persikov, A. V.; Ramshaw, J.A.M.; Kirkpatrick, A.; Brodsky, B. Amino acid propensities for the collagen triple-helix. *Biochemistry* **2000**, *39*, 14960–14967, doi:10.1021/bi001560d.

111. Li, X.; Zhang, Q.; Yu, S.M.; Li, Y. The chemistry and biology of collagen hybridization. *J. Am. Chem. Soc.* **2023**, *145*, 10901-10916, doi:10.1021/jacs.3c00713.

112. Beck, K.; Chan, V.C.; Shenoy, N.; Kirkpatrick, A.; Ramshaw, J.A.M.; Brodsky, B. Destabilization of osteogenesis imperfecta collagen-like model peptides correlates with the identity of the residue replacing glycine. *Proc. Natl. Acad. Sci. USA* **2000**, *97*, 4273–4278, doi:10.1073/pnas.070050097.

113. Berg, R.A.; Prockop, D.J. The thermal transition of a non-hydroxylated form of collagen. Evidence for a role for hydroxyproline in stabilizing the triple-helix of collagen. *Biochem. Biophys. Res. Commun.* **1973**, *52*, 115–120, doi:10.1016/0006-291X(73)90961-3.

114. Toni, M.; Dalla Valle, L.; Alibardi, L. Hard (beta-)keratins in the epidermis of reptiles: Composition, sequence, and molecular organization. *J. Proteome Res.* **2007**, *6*, 3377–3392, doi:10.1021/pr0702619.

115. Wang, B.; Yang, W.; McKittrick, J.; Meyers, M.A. Keratin: Structure, mechanical properties, occurrence in biological organisms, and efforts at bioinspiration. *Prog. Mater. Sci.* **2016**, *76*, 229–318, doi:10.1016/j.pmatsci.2015.06.001.

116. Korniłłowicz-Kowalska, T.; Bohacz, J. Biodegradation of keratin waste: Theory and practical aspects. *Waste Manag.* **2011**, *31*, 1689–1701, doi:10.1016/j.wasman.2011.03.024.

117. Shavandi, A.; Silva, T.H.; Bekhit, A.A.; Bekhit, A.E.-D.A. Keratin: Dissolution, extraction and biomedical application. *Biomater. Sci.* **2017**, *5*, 1699–1735, doi:10.1039/C7BM00411G.

118. Pan, Y.; Hu, L.; Zhao, T. Applications of chemical imaging techniques in paleontology. *Natl. Sci. Rev.* **2019**, *6*, 1040–1053, doi:10.1093/nsr/nwy107.

119. Schweitzer, M.H.; Avci, R.; Collier, T.; Goodwin, M.B. Microscopic, chemical and molecular methods for examining fossil preservation. *Comptes Rendus Palevol* **2008**, *7*, 159–184, doi:10.1016/j.crpv.2008.02.005.

120. Schweitzer, M.H.; Schroeter, E.R.; Cleland, T.P.; Zheng, W. Paleoproteomics of Mesozoic dinosaurs and other Mesozoic fossils. *Proteomics* **2019**, *19*, 1800251, doi:10.1002/pmic.201800251.

121. van Bramer, S.E. An introduction to mass spectrometry. Available online: https://science.widener.edu/svb/massspec/massspec.pdf (accessed on 19 May 2023).

122. Kang, J.-S. Principles and applications of LC-MS/MS for the quantitative bioanalysis of analytes in various biological samples. In *Tandem Mass Spectrometry–Applications and Principles*; Prasain, J.K., Ed.; InTech: Rijeka, Croatia, 2012; Vol. 29, pp. 441–492.

123. Madeira, P.J.A.; Florêncio, M.H. Applications of tandem mass spectrometry: From structural analysis to fundamental studies. In *Tandem Mass Spectrometry—Applications and Principles*; Prasain, J.K., Ed.; Intech: Rijeka, Croatia, 2012; pp. 3–32.

124. García, R.; Báez, A.P. Atomic absorption spectrometry (AAS). In *Atomic Absorption Spectroscopy*; Farrukh, M.A., Ed.; IntechOpen: Rijeka, Croatia, 2012; Vol. 1, pp. 1–13.

125. Marshall, W.D. Atomic absorption, emission and fluorescence spectrometry: principles and applications. In *Techniques and Instrumentation in Analytical Chemistry*; Paré, J.R.J., Bélanger, J.M.R., Eds.; Elsevier Science B.V.: Amsterdam, The Netherlands, 1997; pp. 141–178.

126. Ismail, A.A.; van de Voort, F.R.; Sedman, J. Fourier transform infrared spectroscopy: Principles and applications. In *Instrumental Methods in Food Analysis*; Paré, J.R.J., Bélanger, J.M.R., Eds.; Elsevier Science B.V.: Amsterdam, The Netherlands, 1997; Vol. 18, pp. 93–139 ISBN 0167-9244.

127. Kafle, B.P. Infrared (IR) spectroscopy. In *Chemical Analysis and Material Characterization by Spectrophotometry*; Elsevier: Amsterdam, The Netherlands, 2020; pp. 199–243.

128. Akash, M.S.H.; Rehman, K. Ultraviolet-visible (uv-vis) spectroscopy. In *Essentials of Pharmaceutical Analysis*; Springer Nature Singapore Pte Ltd.: Singapore, Singapore, 2020; pp. 29–56, ISBN 978-981-15-1547-7.

129. Buchler, J.W. Static coordination chemistry of metalloporphyrins. In *Porphyrins and Metalloporphyrins: A New Edition Based on the Original Volume by J. E. Falk*; Smith, K.M., Ed.; Elsevier Scientific Publishing Company: Amsterdam, 1975; pp. 157–231 ISBN 9780444415370.

130. Seely, G.R. The structure and chemistry of functional groups. In *The Chlorophylls*; Vernon, L.P., Seely, G.R., Eds.; Academic Press: New York, NY, USA, 1966; pp. 67–109.

131. Gossauer, A.; Engel, N. Chlorophyll catabolism—Structures, mechanisms, conversions. *J. Photochem. Photobiol. B: Biol* **1996**, *32*, 141–151.

132. Niklas, K.J.; Brown, R.M. Ultrastructural and paleobiochemical correlations among fossil leaf tissues from the St. Maries River (Clarkia) area, northern Idaho, USA. *Am. J. Bot.* **1981**, *68*, 332–341, doi:10.2307/2442769.

133. Cleland, T.P.; Schroeter, E.R. A comparison of common mass spectrometry approaches for paleoproteomics. *J. Proteome Res.* **2018**, *17*, 936–945, doi:10.1021/acs.jproteome.7b00703.

134. Pawlicki, R.; Korbel, A.; Kubiak, H. Cells, collagen fibrils and vessels in dinosaur bone. *Nature* **1966**, *211*, 655–657, doi:10.1038/211655a0.

135. Lindgren, J.; Moyer, A.; Schweitzer, M.H.; Sjövall, P.; Uvdal, P.; Nilsson, D.E.; Heimdal, J.; Engdahl, A.; Gren, J.A.; Schultz, B.P.; et al. Interpreting melanin-based coloration through deep time: A critical review. *Proc. R. Soc. B Biol. Sci.* **2015**, *282*, 20150614, doi:10.1098/rspb.2015.0614.

136. Sorushanova, A.; Delgado, L.M.; Wu, Z.; Shologu, N.; Kshirsagar, A.; Raghunath, R.; Mullen, A.M.; Bayon, Y.; Pandit, A.; Raghunath, M.; et al. The collagen suprafamily: From biosynthesis to advanced biomaterial development. *Adv. Mater.* **2019**, *31*, 1801651, doi:10.1002/adma.201801651.

137. Bragulla, H.H.; Homberger, D.G. Structure and functions of keratin proteins in simple, stratified, keratinized and cornified epithelia. *J. Anat.* **2009**, *214*, 516–559, doi:10.1111/j.1469-7580.2009.01066.x.

138. Buckley, M.; Warwood, S.; van Dongen, B.; Kitchener, A.C.; Manning, P.L. A fossil protein chimera; Difficulties in discriminating dinosaur peptide sequences from

modern cross-contamination. *Proc. R. Soc. B Biol. Sci.* **2017**, *284*, 20170544, doi:10.1098/rspb.2017.0544.

139. Kundu, S.; Trent, J.T.; Hargrove, M.S. Plants, humans and hemoglobins. *Trends Plant Sci.* **2003**, *8*, 387–393, doi:10.1016/S1360-1385(03)00163-8.

140. Yoshida, T.; Migita, C.T. Mechanism of heme degradation by heme oxygenase. *J. Inorg. Biochem.* **2000**, *82*, 33–41, doi:10.1016/S0162-0134(00)00156-2.

141. Schaefer, W.H.; Harris, T.M.; Guengerich, F.P. Characterization of the enzymic and nonenzymic peroxidative degradation of iron porphyrins and cytochrome P-450 heme. *Biochemistry* **1985**, *24*, 3254–3263, doi:10.1021/bi00334a027.

142. Guengerich, F.P. Destruction of heme and hemoproteins mediated by liver microsomal reduced nicotinamide adenine dinucleotide phosphate-cytochrome P-450 reductase. *Biochemistry* **1978**, *17*, 3633–3639, doi:10.1021/bi00610a033.

143. Ouellet, Y.H.; Ndiaye, C.T.; Gagné, S.M.; Sebilo, A.; Suits, M.D.L.; Jubinville, É.; Jia, Z.; Ivancich, A.; Couture, M. An alternative reaction for heme degradation catalyzed by the *Escherichia coli* O157:H7 ChuS protein: Release of hematinic acid, tripyrrole and Fe(III). *J. Inorg. Biochem.* **2016**, *154*, 103–113, doi:https://doi.org/10.1016/j.jinorgbio.2015.11.002.

144. Takahashi, A.; Kurahashi, T.; Fujii, H. Redox potentials of oxoiron(IV) porphyrin π-cation radical complexes: Participation of electron transfer process in oxygenation reactions. *Inorg. Chem.* **2011**, *50*, 6922–6928, doi:10.1021/ic102564e.

145. Kini, U.; Nandeesh, B.N. Physiology of bone formation, remodeling, and metabolism. In *Radionuclide and Hybrid Bone Imaging*; Springer Berlin/Heidelberg, Germany, 2012; pp. 29–57.

146. Boskey, A.L. Bone composition: Relationship to bone fragility and antiosteoporotic drug effects. *Bonekey Rep.* **2013**, *2*, 447, doi:10.1038/bonekey.2013.181.

147. Francillon-Vieillot, H.; de Buffrénil, V.; Castanet, J.; Géraudie, J.; Meunier, F.J.; Sire, J.Y.; Zylberberg, L.; de Ricqlès, A. Microstructure and mineralization of vertebrate skeletal tissues. In *Skeletal Biomineralization: Patterns, Processes and Evolutionary Trends*; Carter, J.G., Ed.; Van Nostrand Reinhold: New York, NY, USA, 1990; pp. 471–530.

148. Luo, Y.; Amromanoh, O. Bone organic-inorganic phase ratio is a fundamental determinant of bone material quality. *Appl. Bionics Biomech.* **2021**, *2021*, 4928396, doi:10.1155/2021/4928396.

149. Miller, M.F.; Wyckoff, R.W. Proteins in dinosaur bones. *Proc. Natl. Acad. Sci. USA* **1968**, *60*, 176–178, doi:10.1073/pnas.60.1.176.

150. Cleland, T.P.; Schroeter, E.R.; Zamdborg, L.; Zheng, W.; Lee, J.E.; Tran, J.C.; Bern, M.; Duncan, M.B.; Lebleu, V.S.; Ahlf, D.R.; et al. Mass spectrometry and antibody-based characterization of blood vessels from *Brachylophosaurus canadensis*. *J. Proteome Res.* **2015**, *14*, 5252–5262, doi:10.1021/acs.jproteome.5b00675.

151. Schweitzer, M.H.; Zheng, W.; Cleland, T.P.; Bern, M. Molecular analyses of dinosaur osteocytes support the presence of endogenous molecules. *Bone* **2013**, 414–423, doi:10.1016/j.bone.2012.10.010.

152. Schweitzer, M.H.; Zheng, W.; Zanno, L.; Werning, S.; Sugiyama, T. Chemistry supports the identification of gender-specific reproductive tissue in *Tyrannosaurus rex*. *Sci. Rep.* **2016**, *6*, 23099, doi:10.1038/srep23099.

153. Kaye, T.G.; Gaugler, G.; Sawlowicz, Z. Dinosaurian soft tissues interpreted as bacterial biofilms. *PLoS ONE* **2008**, *3*, e2808, doi:10.1371/journal.pone.0002808.

154. Saitta, E.T.; Liang, R.; Lau, M.C.; Brown, C.M.; Longrich, N.R.; Kaye, T.G.; Novak, B.J.; Salzberg, S.L.; Norell, M.A.; Abbott, G.D.; et al. Cretaceous dinosaur bone contains recent organic material and provides an environment conducive to microbial communities. *eLife* **2019**, *8*, e46205, doi:10.7554/eLife.46205.

155. Wiersma, K.; Läbe, S.; Sander, P.M. Organic phase preservation in fossil dinosaur and other tetrapod bone from deep time. In *Fossilization: Understanding the Material Nature of Ancient Plants and Animals*; Gee, C.T., McCoy, V.E., Sander, P.M., Eds.; Johns Hopkins University Press: Baltimore, MD, USA, 2021; pp. 16–45, ISBN 9781421440217.

156. Cleland, T.P.; Voegele, K.; Schweitzer, M.H. Empirical evaluation of bone extraction protocols. *PLoS ONE* **2012**, *7*, e31443, doi:10.1371/journal.pone.0031443.

157. Schroeter, E.R.; DeHart, C.J.; Schweitzer, M.H.; Thomas, P.M.; Kelleher, N.L. Bone protein "extractomics": comparing the efficiency of bone protein extractions of gallus

gallus in tandem mass spectrometry, with an eye towards paleoproteomics. *PeerJ* **2016**, *4*, e2603, doi:10.7717/peerj.2603.

158. Espinas, N.A.; Kobayashi, K.; Takahashi, S.; Mochizuki, N.; Masuda, T. Evaluation of unbound free heme in plant cells by differential acetone extraction. *Plant Cell Physiol.* **2012**, *53*, 1344–1354, doi:10.1093/pcp/pcs067.

159. Fyrestam, J.; Östman, C. Determination of heme in microorganisms using HPLC-MS/MS and cobalt(III) protoporphyrin IX inhibition of heme acquisition in *Escherichia coli*. *Anal. Bioanal. Chem.* **2017**, *409*, 6999–7010, doi:10.1007/s00216-017-0610-5.

160. Trufelli, H.; Palma, P.; Famiglini, G.; Cappiello, A. An overview of matrix effects in liquid chromatography-mass spectrometry. *Mass Spectrom. Rev.* **2011**, *30*, 491–509, doi:10.1002/mas.20298.

161. Matuszewski, B.K.; Constanzer, M.L.; Chavez-Eng, C.M. Strategies for the assessment of matrix effect in quantitative bioanalytical methods based on HPLC−MS/MS. *Anal. Chem.* **2003**, *75*, 3019–3030, doi:10.1021/ac020361s.

162. Cortese, M.; Gigliobianco, M.R.; Magnoni, F.; Censi, R.; Di Martino, P. Compensate for or minimize matrix effects? Strategies for overcoming matrix effects in liquid chromatography-mass spectrometry technique: A tutorial review. *Molecules* **2020**, *25*, 3047, doi:10.3390/molecules25133047.

163. Peters, F.T.; Drummer, O.H.; Musshoff, F. Validation of new methods. *Forensic Sci. Int.* **2007**, *165*, 216–224, doi:10.1016/j.forsciint.2006.05.021.

164. Ulloa-Aguirre, A.; Stanislaus, D.; Janovick, J.A.; Conn, P.M. Structure-activity relationships of G protein-coupled receptors. *Arch. Med. Res.* **1999**, *30*, 420–435, doi:10.1016/S0188-0128(99)00041-X.

165. Hauser, A.S.; Attwood, M.M.; Rask-Andersen, M.; Schiöth, H.B.; Gloriam, D.E. Trends in GPCR drug discovery: New agents, targets and indications. *Nat. Rev. Drug Discov.* **2017**, *16*, 829–842, doi:10.1038/nrd.2017.178.

166. Oldham, W.M.; Hamm, H.E. Heterotrimeric G protein activation by G-protein-coupled receptors. *Nat. Rev. Mol. Cell Biol.* **2008**, *9*, 60–71, doi:10.1038/nrm2299.

167. Simon, M.I.; Strathmann, M.P.; Gautam, N. Diversity of G proteins in signal

transduction. *Science* **1991**, *252*, 802–808, doi:10.1126/science.1902986.

168.   Zhang, H.; Nielsen, A.L.; Strømgaard, K. Recent achievements in developing selective G$_q$ inhibitors. *Med. Res. Rev.* **2020**, *40*, 135–157, doi:10.1002/med.21598.

169.   Taniguchi, M.; Nagai, K.; Arao, N.; Kawasaki, T.; Saito, T.; Moritani, Y.; Takasaki, J.; Hayashi, K.; Fujita, S.; Suzuki, K.I.; et al. YM-254890, a novel platelet aggregation inhibitor produced by *Chromobacterium* sp. QS3666. *J. Antibiot. (Tokyo)* **2003**, *56*, 358–363, doi:10.7164/antibiotics.56.358.

170.   Carlier, A.; Fehr, L.; Pinto-Carbó, M.; Schäberle, T.; Reher, R.; Dessein, S.; König, G.; Eberl, L. The genome analysis of *Candidatus* Burkholderia crenata reveals that secondary metabolism may be a key function of the *Ardisia crenata* leaf nodule symbiosis. *Environ. Microbiol.* **2016**, *18*, 2507–2522, doi:10.1111/1462-2920.13184.

171.   Fujioka, M.; Koda, S.; Morimoto, Y.; Biemann, K. Structure of FR900359, a cyclic depsipeptide from *Ardisia crenata sims*. *J. Org. Chem.* **1988**, *53*, 2820–2825, doi:10.1021/jo00247a030.

172.   Kuschak, M.; Namasivayam, V.; Rafehi, M.; Voss, J.H.; Garg, J.; Schlegel, J.G.; Abdelrahman, A.; Kehraus, S.; Reher, R.; Küppers, J.; et al. Cell-permeable high-affinity tracers for G$_q$ proteins provide structural insights, reveal distinct binding kinetics, and identify small molecule inhibitors. *Br. J. Pharmacol.* **2019**, *177*, 1898–1916. doi: 10.1111/bph.14960

173.   Pfeil, E.M.; Brands, J.; Merten, N.; Vögtle, T.; Vescovo, M.; Rick, U.; Albrecht, I.-M.; Heycke, N.; Kawakami, K.; Ono, Y.; et al. Heterotrimeric G protein subunit Gαq is a master switch for Gβγ-mediated calcium mobilization by Gi-coupled GPCRs. *Mol. Cell* **2020**, *80*, 940-954.e6, doi:10.1016/j.molcel.2020.10.027.

174.   Schrage, R.; Schmitz, A.L.; Gaffal, E.; Annala, S.; Kehraus, S.; Wenzel, D.; Büllesbach, K.M.; Bald, T.; Inoue, A.; Shinjo, Y.; et al. The experimental power of FR900359 to study Gq-regulated biological processes. *Nat. Commun.* **2015**, *6*, 10156, doi:10.1038/ncomms10156.

175.   Taniguchi, M.; Suzumura, K.I.; Nagai, K.; Kawasaki, T.; Takasaki, J.; Sekiguchi, M.; Moritani, Y.; Saito, T.; Hayashi, K.; Fujita, S.; et al. YM-254890 analogues, novel cyclic depsipeptides with Gαq/11 inhibitory activity from *Chromobacterium* sp.

QS3666. *Bioorganic Med. Chem.* **2004**, *12*, 3125–3133, doi:10.1016/j.bmc.2004.04.006.

176. Xiong, X.F.; Zhang, H.; Boesgaard, M.W.; Underwood, C.R.; Bräuner-Osborne, H.; Strømgaard, K. Structure–activity relationship studies of the natural product G$_{q/11}$ protein inhibitor YM-254890. *ChemMedChem* **2019**, *14*, 865–870, doi:10.1002/cmdc.201900018.

177. Reher, R.; Kuschak, M.; Heycke, N.; Annala, S.; Kehraus, S.; Dai, H.-F.; Müller, C.E.; Kostenis, E.; König, G.M.; Crüsemann, M. Applying molecular networking for the detection of natural sources and analogues of the selective Gq protein inhibitor FR900359. *J. Nat. Prod.* **2018**, *81*, 1628–1635, doi:10.1021/acs.jnatprod.8b00222.

178. Xiong, X.-F.; Zhang, H.; Underwood, C.R.; Harpsøe, K.; Gardella, T.J.; Wöldike, M.F.; Mannstadt, M.; Gloriam, D.E.; Bräuner-Osborne, H.; Strømgaard, K. Total synthesis and structure–activity relationship studies of a series of selective G protein inhibitors. *Nat. Chem.* **2016**, *8*, 1035–1041, doi:10.1038/nchem.2577.

179. Hermes, C.; Richarz, R.; Wirtz, D.A.; Patt, J.; Hanke, W.; Kehraus, S.; Voß, J.H.; Küppers, J.; Ohbayashi, T.; Namasivayam, V.; et al. Thioesterase-mediated side chain transesterification generates potent Gq signaling inhibitor FR900359. *Nat. Commun.* **2021**, *12*, 144, doi:10.1038/s41467-020-20418-3.

180. Staccioli, G.; Uçar, G.; Bartolini, G.; Coppi, C.; Mochi, M. Investigation on a fossil *Sequoia* bark from Turkey. *Holz Roh Werkst.* **1998**, *56*, 426–429, doi:10.1007/s001070050346.

181. Ash, S.R.; Savidge, R.A. The bark of the Late Triassic *Araucarioxylon arizonicum* tree from Petrified Forest National Park, Arizona. *IAWA J.* **2004**, *25*, 349–368, doi:10.1163/22941932-90000371.

182. McCoy, V.E.; Boom, A.; Wings, O.; Wappler, T.; Labandeira, C.C.; Gee, C.T. Fossilization of the Eocene "monkeyhair" laticifer tree from Geiseltal, Germany: A deeper understanding using micro-CT and pyrolysis GC/MS. *Palaios* **2021**, *36*, 1–14.

183. Wilde, V.; Riegel, W. "Affenhaar" revisited—Facies context of *in situ* preserved latex from the Middle Eocene of Central Germany. *Int. J. Coal Geol.* **2010**, *83*, 182–194.

184. Simoneit, B.R.T.; Otto, A.; Wilde, V. Novel phenolic biomarker triterpenoids of fossil

laticifers in Eocene brown coal from Geiseltal, Germany. *Org. Geochem.* **2003**, *34*, 121–129.

185. Collins, L.W.; Rohar, P.C.; Veloski, G.A.; Mahlberg, P.G.; Haubold, H.; White, C.M. Identification of polycyclic hydrocarbons in fossilized latex from brown coal. *Polycycl. Aromat. Compd.* **1995**, *7*, 223–230.

186. Mahlberg, P.G.; Field, D.W.; Frye, J.S. Fossil laticifers from Eocene brown coal deposits of the Geiseltal. *Am. J. Bot.* **1984**, *71*, 1192–1200, doi:10.1002/j.1537-2197.1984.tb11974.x.

187. Marques, A.V.; Pereira, H. On the determination of suberin and other structural components in cork from *Quercus suber* L. *An. Inst. Sup. Agron.* **1987**, *42*, 321–335.

188. Kumar, N.; Pruthi, V. Potential applications of ferulic acid from natural sources. *Biotechnol. Reports (Amst.)* **2014**, *4*, 86–93, doi:10.1016/j.btre.2014.09.002.

189. Staccioli, G.; McMillan, N.J.; Meli, A.; Bartolini, G. Chemical characterisation of a 45 million year bark from Geodetic Hills fossil forest, Axel Heiberg Island, Canada. *Wood Sci. Technol.* **2002**, *36*, 419–427, doi:10.1007/s00226-002-0144-6.

190. Collinson, M.E.; Van Bergen, P.F.; Scott, A.C.; De Leeuw, J.W. The oil-generating potential of plants from coal and coal-bearing strata through time: A review with new evidence from Carboniferous plants. *Geol. Soc. Spec. Publ.* **1994**, *77*, 31–70, doi:10.1144/GSL.SP.1994.077.01.03.

191. Grabber, J.H.; Ralph, J.; Hatfield, R.D. Cross-linking of maize walls by ferulate dimerization and incorporation into lignin. *J. Agric. Food Chem.* **2000**, *48*, 6106–6113.

192. Ralph, J.; Helm, R.F. Lignin/hydroxycinnamic acid/polysaccharide complexes: Synthetic models for regiochemical characterization. In *Forage Cell Wall Structure and Digestibility*; American Society of Agronomy, Crop Science Society of America, Soil Science Society of America: Madison, WI, USA, 1993; pp. 201–246.

193. Lönartz, M.I.; McCoy, V.E.; Gee, C.T.; Geisler, T. Palaeoenvironmental conditions for the natural vulcanization of the Eocene "monkeyhair" laticifers from Geiseltal, Germany, as elucidated by Raman spectroscopy. *Paleobiodivers. Paleoenviron.* **2023**, doi:10.1007/s12549-022-00566-8.

14. Acknowledgements

I would like to thank Prof. Dr. Christa E. Müller for the opportunity of doing my Ph.D. in her working group. I am deeply grateful for the help and guidance I have received during my studies. Thank you for the useful discussions that allowed me to grow as a scientist.

I am grateful to the members of my doctoral committee PD Dr. Marianne Engeser, Prof. Dr. Gerd Bendas, and Prof. Dr. Hanns Häberlein for accepting to be in my committee and for reviewing this thesis.

I am grateful for the Deutsche Forschungsgemeinschaft (DFG) for financially supporting our project FOR 2685. I would also like to thank all the members of the DFG FOR 2685 "Fossilization Research Unit" for the fruitful collaborations we had, especially the ones I worked with directly: PD Dr. Marianne Engeser, PD Dr. Carole T. Gee, Dr. Bastian Mähler, Dr. Victoria E. McCoy, Prof. Dr. Jes Rust, and Prof. Dr. P. Martin Sander.

I would like to thank all the members of AK Müller for providing a nice and supportive working atmosphere in the labs and in the office, especially Christiane Bous, Dr. Jörg Hockemeyer, Marion Schneider, Angelo Oneto, Caro Pikullik, Eugen Potaptschuk, and Luca Svolacchia.

I would like to thank the heads of the 4th semester practical course "Instrumentelle Analytik" Prof. Dr. Finn Hansen, PD Dr. Martin Schlesinger and Dr. Ali El-Tayeb, and all my colleagues there, especially Dr. Kathrin Tan and Sophie Wittenberg for the helpful advice received when I was a teaching assistant.

I would like to thank the Bonn International Graduate School of Drug Sciences (BIGS-DrugS) for awarding me a travel grant to present part of this work in a conference poster in the 11th European Paleobotany and Palynology Conference, and for allowing me to be a graduate student in the doctoral program. I would also like to thank the coordinators Dorothee Müssemeier and Dr. Amelie Fiene for all their efforts.

I am grateful to my family back in Egypt, especially my parents Gamal and Hoda, brother Ahmed, and sister Hana for their never-ending support and unconditional love through this long and challenging path. They always wish me the best and help me in achieving my dreams. I feel blessed and glad to have you all in my life.

I would like to thank my mentors Prof. Dr. Ashraf Abadi and Assoc. Prof. Dr. Mohammad Abdel-Halim for always being there throughout my academic journey.

15. List of non-standard abbreviations

AAS   Atomic absorption spectrometry (or spectrophotometry)

ATR-IR   Attenuated-total reflection infrared spectroscopy

BN-PAGE   Blue native-polyacrylamide gel electrophoresis

CHAPS   3-[(3-Cholamidopropyl)-dimethylammonio]-1-propanesulfonate

DAD-UV   Diode array detector with ultraviolet detection

DP   Degradation product

DPEP   Deoxyphylloerythroetioporphyrin

DTT   Dithiothreitol

EIC   Extracted ion chromatogram

EDS   Energy-dispersive X-ray spectrometry

EDTA   Ethylenediaminetetraacetic acid

ELISA   Enzyme linked immunosorbent assay

ESI-MS   Electrospray ionization mass spectrometry

FR   FR900359

FT-ICR-MS   Fourier transform ion cyclotron resonance mass spectrometry

FTIR   Fourier transform infrared spectroscopy

GC-MS   Gas chromatography coupled to mass spectrometry

GPCR   G protein-coupled receptor

HPLC-(DAD)-ESI-MS High performance liquid chromatography coupled to diode array detection and electrospray ionization mass spectrometry

HPLC-(DAD/UV)-ESI-MS HPLC coupled to diode array/ultraviolet light detection and electrospray ionization mass spectrometry

HPLC-ESI-MS HPLC coupled to electrospray ionization mass spectrometry

HPLC-MS   HPLC coupled to mass spectrometry

HPLC-MS/MS HPLC coupled to tandem mass spectrometry

HPLC-UV/VIS HPLC coupled to ultraviolet-visible light detection

ICH — International Council for Harmonization

IP_3 — Inositol trisphosphate

IR — Infrared spectroscopy

LC-MS — Liquid chromatography coupled to mass spectrometry

LC-MS/MS — Liquid chromatography coupled to tandem mass spectrometry

LOD — Limit of detection

LOQ — Limit of quantitation

Micro-CT — High-resolution X-ray microcomputed tomography

MRM — Multiple reaction monitoring

MS — Mass spectrometry

MS/MS — Tandem mass spectrometry

m/z — Mass-to-charge ratio

NADPH — Nicotinamide adenine dinucleotide phosphate

NMR — Nuclear magnetic resonance

PIP_2 — Phosphatidylinositol 4,5-bisphosphate

PLC — Phospholipase C

Py-GC-MS — Pyrolysis gas-chromatography mass spectrometry

q/TOF-MS — Quadrupole time-of-flight mass spectrometry

RSD% — Relative standard deviation

SDS-PAGE — Sodium dodecyl sulfate-polyacrylamide gel electrophoresis

SD — Standard deviation

SEM — Scanning electron microscopy (Chapters 4 and 10) or standard error of the mean (Chapter 6)

S/N	Signal-to-noise
SR-FTIR	Synchrotron-radiation Fourier transform infrared spectroscopy
TEM	Transmission electron microscopy
ToF-SIMS	Time-of-flight secondary-ion mass spectrometry
TRIS-HCl	Tris(hydroxymethyl)aminomethane hydrochloride
UV-VIS	Ultraviolet-visible light
YM	YM-254890

15. List of non-standard abbreviations

16. Appendix

This section includes the full-length papers, including the supporting information, published during the doctoral studies. The respective introductions to the papers are found within chapters 3, 4, 5, 7, 9.1 and 9.2. In this appendix, the publications are attached in order of appearance in the dissertation, starting with appendix A "Chemistry of porphyrins in fossil plants and animals", followed by appendix B "Chemistry and analysis of organic compounds in dinosaurs", appendix C "Molecular taphonomy of heme: Chemical degradation of hemin under presumed fossilization conditions," appendix D "Macrocyclic Gq Protein Inhibitors FR900359 and/or YM-254890–Fit for Translation?", appendix E "Calcite precipitation forms crystal clusters and muscle mineralization during the decomposition of *Cambarellus diminutus* (Decapoda: Cambaridae) in freshwater", and appendix F "Adipocere formation in biofilms as a first step in soft tissue preservation". The copyright of the papers belongs to the respective publishers of the journals, as indicated by copyright statements displayed before each paper.

16.1. Appendix A – Chemistry of porphyrins in fossil plants and animals

This section contains the review article "Chemistry of porphyrins in fossil plants and animals" as it appears in the journal *RSC Advances* by Royal Society of Chemistry. Reprinted from *RSC Adv.*, 2021, **11**, 7552-7563, Copyright (2021), with permission from Royal Society of Chemistry. This work is licensed under the Creative Commons Attribution-NonCommercial 3.0 Unported License (CC BY-NC 3.0), http://creativecommons.org/licenses/by-nc/3.0/. As guaranteed by the author rights policy of Royal Society of Chemistry, re-use of the article is allowed without permission or payment, as long as the thesis is not published commercially and with full acknowledgement of the original article.

RSC Advances

REVIEW

Check for updates

Chemistry of porphyrins in fossil plants and animals

Mariam Tahoun, [a] Carole T. Gee, [bc] Victoria E. McCoy, [d] P. Martin Sander [b] and Christa E. Müller [*a]

Porphyrins are macrocyclic tetrapyrrole derivatives that are widely distributed in nature. They are often complexed with a metal ion located in the center of the ring system and may be modified by various substituents including additional rings, or by ring opening, which leads to a plethora of different functions. Due to their extended conjugated aromatic ring system, porphyrins absorb light in the visible range and therefore show characteristic colors. Well-known natural porphyrins include the red-colored heme present in hemoglobin, which is responsible for blood oxygen transport, and the chlorophylls in some bacteria and in plants which are utilized for photosynthesis. Porphyrins are mostly lipophilic pigments that display relatively high chemical stability. Therefore, they can even survive hundreds of millions of years. The present review article provides an overview of natural porphyrins, their chemical structures, and properties. A special focus is put on porphyrins discovered in the fossil record. Examples will be highlighted, and information on their chemical analysis will be provided. We anticipate that the development of novel analytical methods with increased sensitivity will prompt new discoveries of porphyrins in fossils.

Introduction

Porphyrins are natural pigments that can be bound to proteins such as cytochromes and hemoglobin and are found in a huge variety of organisms. Their major structural features have remained detectable for up to 1.1 billion years.[1] For these reasons, they are considered important indicators of life and have been studied from the remains of extinct organisms to understand the principles of evolution.[2,3] Porphyrins are found either isolated in sediments, oil shales, and petroleum,[4] or bound to a fossil tissue. While the findings and structural features of sedimentary porphyrins have been extensively discussed,[5–11] reviews on porphyrins extracted from fossil tissues are lacking. This review article aims to describe the major porphyrins found in fossil plants and animals, and to compare them to natural porphyrins well-known in the present-day world such as heme, chlorophylls, and bacteriochlorophylls.

General structure of porphyrins and their derivatives

Porphyrins are conjugated tetrapyrrole macrocycles linked together by methine (=CH–) bridges. The basic, unsubstituted structure is called porphin (1) shown in Fig. 1 along with the current numbering system for porphyrins.[4,12] The pyrrole rings are lettered from A to D.[1] Common side chains attached to porphyrins include methyl, ethyl, vinyl, acetic acid, and propionic acid. The carbon bridges connecting the pyrrole rings are called *meso*-positions and are sometimes designated α-, β-, δ-, and γ-positions. Isomers frequently occur and are identified by adding Roman numerals at the end of the name. Porphyrins readily form complexes with metal cations such as iron(II/III), magnesium(II), copper(II), and zinc(II) to yield metalloporphyrins.[13] Compounds related to porphyrins with saturated bonds and/or extra rings exist that include chlorin (2), phorbin (3), bacteriochlorin (4), and their derivatives (Fig. 1).[4,14] Chlorin (2) is 17,18-dihydroporphin[1] while phorbin (3) is a chlorin derivative containing an extra isocyclic ring between ring C and D. Bacteriochlorin (4) represents a 7,8,17,18-tetrahydroporphin derivative. If a methine bridge between ring A and ring D is cleaved, open-chain tetrapyrroles (bilanes, 5, Fig. 1) are formed.[4] Their numbering is similar to that of porphins with the *meso*-positions lettered a, b, and c. If there are one, two or three double bonds at the *meso*-positions, the corresponding derivatives are named bilenes, biladienes or bilatrienes, respectively.

Physicochemical properties of selected porphyrins

Porphyrins are aromatic and have a square planar geometry. There are 22 π-electrons present, 18 of which are involved in delocalization, while two electron pairs of nitrogen atoms are sterically hindered when bound to hydrogen, in accordance with Hückel's rule.[4,15] The conjugated double bonds of

[a] *Pharmaceutical Institute, Pharmaceutical & Medicinal Chemistry, University of Bonn, An der Immenburg 4, 53121 Bonn, Germany. E-mail: christa.mueller@uni-bonn.de*

[b] *Institute of Geosciences, Division of Paleontology, University of Bonn, Nussallee 8, 53115 Bonn, Germany*

[c] *Huntington Botanical Gardens, 1151 Oxford Road, San Marino, California 91108, USA*

[d] *Department of Geosciences, University of Wisconsin-Milwaukee, 3209 N Maryland Ave, Milwaukee, WI, 53211, USA*
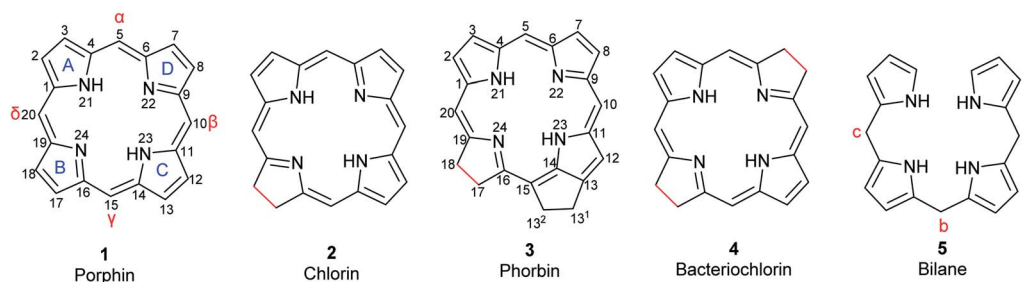
16. Appendix

Fig. 1 Basic structures of tetrapyrrole macrocycles from which the natural pigments are derived. Differences in bond saturation are highlighted in red. The current numbering system for porphin and phorbin are shown.

Table 1 Physicochemical properties of selected porphyrin-based pigments[12,16,17,19–21]

Pigment[a]	Molecular formula	Molecular weight (g mol^{-1})	UV-vis absorption maxima (nm)		Color in solution
			Soret	Q-bands	
Heme	$C_{34}H_{32}FeN_4O_4$	616.5	416[b]	520, 550[b]	Red
Hemin	$C_{34}H_{34}ClFeN_4O_4$	654.0	363, 385[c]	550, 570[c]	Olive-green
Hematin	$C_{34}H_{34}FeN_4O_5$	634.5	364, 383[c]	613[c]	Dark blue-brown
Biliverdin	$C_{33}H_{34}N_4O_6$	582.7	376[c]	671[c]	Blue-green
Bilirubin	$C_{33}H_{36}N_4O_6$	584.7	452[c]	—	Yellow-orange
Protoporphyrin IX	$C_{34}H_{34}N_4O_4$	562.7	400[d]	506, 532, 580, 630[d]	Red-brown
Chlorophyll a	$C_{55}H_{72}MgN_4O_5$	893.5	430[e]	662[e]	Yellow-green
Chlorophyll b	$C_{55}H_{70}MgN_4O_6$	907.5	453[e]	642[e]	Blue-green
Chlorophyll c_1	$C_{35}H_{30}MgN_4O_5$	611.0	444[e]	577, 626[e]	Blue-green
Chlorophyll c_2	$C_{35}H_{28}MgN_4O_5$	609.0	447[e]	580, 627[e]	Blue-green
Chlorophyll c_3	$C_{36}H_{28}MgN_4O_6$	637.0	452[e]	585, 627[e]	Blue-green
Bacteriochlorophyll a	$C_{55}H_{74}MgN_4O_6$	911.5	388	805, 870	Blue-green

[a] For structures, see Fig. 2, 3, 6, and 7. [b] Measured in extracts of mitochondrial cytochrome c from a horse's heart. [c] Measured in 1 M phosphate-buffered saline (PBS) containing 30 mM NaOH (hemin), 7.2 mM KOH (bilirubin) or 5 mM KOH (biliverdin). [d] Measured in a mixture of acetonitrile and DMSO (3 : 1, v/v). [e] Measured in diethyl ether.
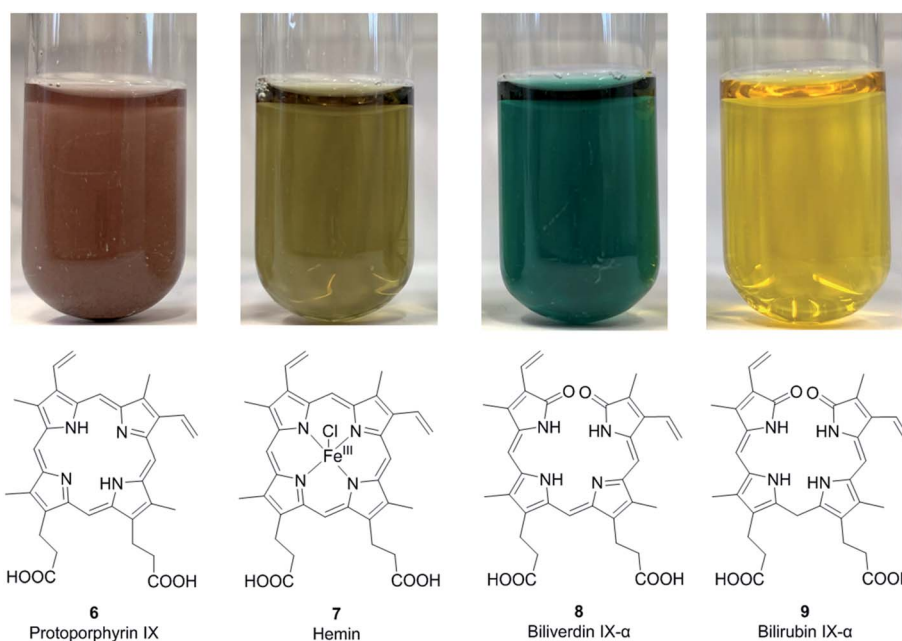

Fig. 2 Structures and colors of protoporphyrin IX (**6**), the metalloporphyrin hemin (**7**), and the open-chain tetrapyrrole derivatives biliverdin IX-α (**8**) and bilirubin IX-α (**9**) in aqueous solution (100 μM concentration).
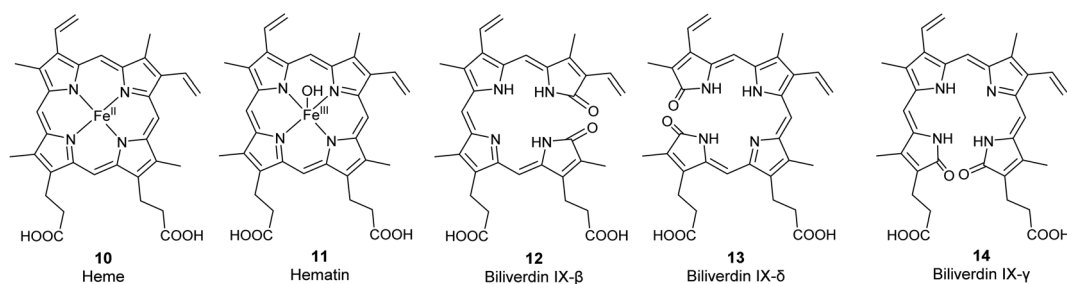
126

RSC Advances

Fig. 3 Structures of the metalloporphyrins heme (**10**) and hematin (**11**) and of the less common biliverdin isomers β, δ, and γ (**12–14**).

porphyrins make them absorb light at defined wavelengths, resulting in a colorful appearance.[4] The electronic absorption spectra of porphyrins are characterized by two prominent bands in the UV region and the visible region. The major band around 400 nm, called the Soret band, appears due to $\pi–\pi^*$ transitions of the delocalized electrons. This band is characteristic for porphyrins and used for quantification using UV-vis spectrophotometry.[4,16] The Soret band becomes less intense if conjugation is lost and/or the ring is cleaved. In the visible region, there are Q-bands that arise from $\pi–\pi^*$ transitions of the conjugation between unsaturated carbons and the pyrrole nitrogens.[4,17] Even in the presence of saturation in ring B, chlorin, phorbin, and bacteriochlorin derivatives still possess the 18 π-electrons necessary for delocalization. They have similar spectra as porphyrins and are green in color. Their Soret bands occur in the region from 380–420 nm due to macrocyclic conjugation, while their Q-bands in the range of 500–800 nm are responsible for their vibrant verdant color (Table 1).[18]

macromolecules, mostly occurring as structural proteins. However, very few have been chemically analyzed for small organic molecular components.[22] The field of "molecular paleontology" investigates fossil organisms for small organic molecules or their diagenetic products using a combination of analytical techniques.[23] Macromolecules are often investigated by microscopic and immunological techniques. Small organic molecules in fossils are usually extracted using suitable techniques, then analyzed using gas chromatography (GC) or high-performance liquid chromatography (HPLC) and quantified by UV-vis spectroscopy or mass spectrometry. If these molecules are not extractable, non-destructive techniques such as Raman or infrared spectroscopy are used to identify specific chemical signals.

Organic molecules that resist decay are either inherently stable in their surrounding environment or are shielded from degradation by embedding within the core of the preserved macromolecules through various chemical mechanisms. Highly hydrophobic molecules such as sterols and porphyrins have a higher chance of being preserved than more polar compounds. Minimal alterations

Porphyrins identified in fossil tissues

Many exceptionally well-preserved fossil hard and soft tissues, such as digestive organs, eggshells, red blood cells, bone osteocytes, and muscle cells, have been morphologically described with major

Fig. 4 The oldest female fossil mosquito (*Culiseta* species, 46 million years old) from the middle Eocene Kishenehn Formation in northwest Montana with blood in its abdomen. Heme (**10**) was identified in the abdomen by time-of-flight secondary-ion mass spectrometry and elemental analysis using energy-dispersive X-ray spectroscopy. Scale bar: 5 mm. Image reproduced with permission from D. E. Greenwalt.[28]

Fig. 5 Clutch of fossil oviraptorid dinosaur eggs from Upper Cretaceous sediments of southern China. Protoporphyrin IX (**6**) and biliverdin (**8**) were identified from these fossils using HPLC-ESI-MS and qTOF-MS, and confirmed by similar retention times and exact mass to those of standard samples, whereas these peaks were not found in samples from the surrounding sediment.[38] Photo by Tzu-Ruei Yang, National Museum of Natural Science, Taiwan.
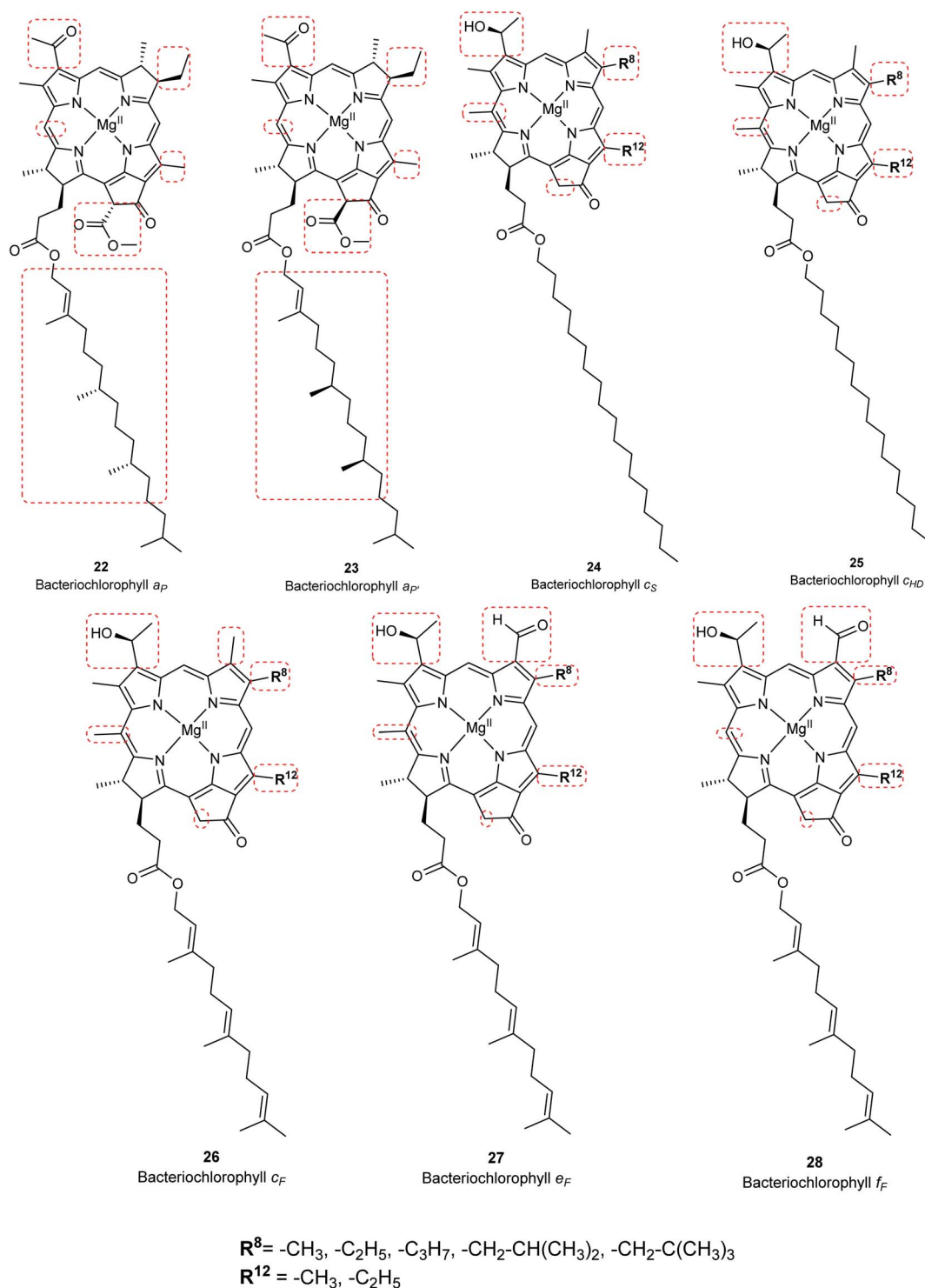
of the structures may occur, such as loss of functional groups (*e.g.*, hydrolysis of esters), reduction, isomerization, aromatization, or condensation. Moreover, on the macromolecular level, several mechanisms also play a role in preservation. For instance, the compact tertiary structures of myoglobin and hemoglobin are stabilized by hydrogen bonding and disulfide linkages, reducing exposure to water and degradative enzymes. In other cases, minerals can be deposited around proteins such as collagen, thereby blocking interstitial spaces and hindering the movement of water and microorganisms.[23,24]

Regardless of the mechanism, initial preservation must occur before complete decay, which may range from hours to days depending on the tissue type. Afterwards, other factors come into play to maintain the integrity of the fossil. For example, compression of the fossil by the sediment preserves integrity and, on the chemical level, promotes cross-linking with macromolecules because the molecules are brought closer to one another.[23]

Heme

The most common biologically relevant metalloporphyrin is heme (**10**, Fig. 2), the ferrous [Fe(II)] complex of protoporphyrin IX (**6**, Fig. 3).[4] Fe(II) has a coordination number of 6 in most of its complexes. In free heme, only four complex bonds are formed with the four pyrrole nitrogen atoms of the porphyrin macrocycle, resulting in a planar complex. In hemoglobin, the iron(II) center of heme is additionally bound to a histidine residue of the protein

globin and to oxygen (O$_2$), resulting in an octahedral complex. Hemoglobin and the related myoglobin are the main proteins responsible for oxygen transport in blood and storage in muscle, respectively. Other hemoproteins include cytochromes (*e.g.*, the cytochrome P450 enzymes and the respiratory cytochromes), and the enzymes catalase, peroxidase, tryptophan pyrrolase, and NO synthase. Free heme is kept at very low concentrations because it is involved in free-radical formation and can oxidize biomolecules. In addition, it may accumulate in cellular membranes due to its high hydrophobicity by which it could damage the phospholipid bilayer. Heme is responsible for the red color of blood.[12,16]

Hemin and hematin. The corresponding ferric [Fe(III)] complexes with **6**, hemin **7** and hematin (**11**, Fig. 2), have an overall positive charge and thus associate with chloride and hydroxide ions, respectively. They are commercially available as stable precursors of heme used as analytical standards.[12,16] Hematin (**11**) is formed from **7** in aqueous alkaline solutions and is a cofactor of peroxidases and cytochromes. Hemin (**7**) acts as an allosteric regulator of heme biosynthesis by inhibiting the enzyme δ-aminolevulinic acid (ALA) synthase.[25] It is also used for the treatment of acute porphyrias in individuals with defective heme biosynthesis.[26]

Heme in the fossil record. Heme (**10**) was previously characterized from the *ca.* 66 million year-old bones of *Tyrannosaurus rex* from the Upper Cretaceous Hell Creek Formation of eastern Montana, USA, by several analytical methods. Bone extracts analyzed

Fig. 6 Structures of the known chlorophylls.

RSC Advances

Fig. 7 Structures of bacteriochlorophylls and *Chlorobium* chlorophylls.

using UV-vis spectroscopy showed a Soret absorption peak at 410 nm, which was absent in control and sediment samples. ^{1}H-NMR analyses showed that the iron atom was in the ferric [Fe(III)] state, indicating oxidation might have occurred during diagenesis. Resonance Raman analyses displayed four of the six characteristic bands for **10** confirming its presence.[27]

Compound **10** was indirectly detected in the abdomen of 46-million-year-old female mosquitoes (*Culiseta* spp., Fig. 4) from the middle Eocene Kishenehn Formation in northwest Montana. These were the first fossils of its kind to be identified. Elemental analysis using energy-dispersive X-ray spectroscopy showed an eightfold elevation in iron levels in the abdomen compared to the thorax. Since only female mosquitoes ingest blood,

129

Review

this iron was thought to originate from the degradation of hemoglobin in their abdomen. In comparison, the iron levels in the abdomen of fossil male mosquitoes were found to be as low as those in the female mosquitos' thorax. Using time-of-flight secondary ion mass spectrometry (ToF-SIMS), other forms of iron such as pyrite (FeS_2) or siderite ($FeCO_3$), normally present in surrounding sediments, were not detected in the fossil confirming, that the source of iron was endogenous. Intact **10** in the fossil was not detected by ToF-SIMS compared to controls of purified hemoglobin, but the fragmentation patterns were very similar. Given the high iron levels, this was expected. Analyses of surrounding sediment and the abdomen of male fossil mosquitoes showed different fragmentation patterns.[28]

Fragments of **10** were detected in fossil sea turtles (*Tasbacka danica*, at least 54 million years old) with soft-tissue preservation from the marine sediments of the early Eocene Fur Formation in Jütland, Denmark. ToF-SIMS analysis showed similar fragmentation patterns when compared with standard samples of hemin and related porphyrins such as **6** and **15**. These molecular analyses were complementary to immunological techniques carried out, which showed a positive reaction after the addition of antibodies against alligator and ostrich hemoglobin.[29]

Degradation products of heme: biliverdin and bilirubin

As the life span of red blood cells nears their end, **10** is degraded by heme oxygenase, which oxidizes and subsequently cleaves **10** at an interpyrrolic position, preferably at the α-position,[30] to form biliverdin IX-α **8** (Fig. 2), a hydrophilic, blue-green bilatriene pigment. Carbon monoxide and Fe(ɪɪ) are released as side products, and the iron is recycled for heme production. Compound **8** is responsible for the blue-green coloration in the eggshells of many birds.[30,31] As ring opening can occur at any of the interpyrrolic positions in heme, four biliverdin isomers can be formed: biliverdin-IX α, β, δ, and γ (Fig. 2 (**8**) and 3 (**12–14**)). Biliverdin is immediately reduced at another interpyrrolic position to the hydrophobic yellow pigment, bilirubin IX-α (**9**, Fig. 2), a biladiene, by the enzyme biliverdin reductase, which is present in all tissues but most active in the liver and spleen.[32] Bilirubin is later conjugated with glucuronic acid and excreted in bile.[16,33,34]

Protoporphyrin IX

Protoporphyrin IX (**6**, Fig. 2) is a major precursor of chlorophyll and the immediate precursor of heme biosynthesis. The compound bears two carboxylic acid groups and is liable to oxidation.[4,17]

Protoporphyrin IX and biliverdin in the fossil record. As the major pigments responsible for eggshell color,[31,35] protoporphyrin IX (**6**) and biliverdin (**8**) were detected in several extinct avian species using both destructive and nondestructive techniques. Samples were analyzed after extraction from subfossil upland moa eggshell fragments from New Zealand using HPLC-ESI ion trap mass spectrometry,[36] and nondestructively using Raman spectroscopy confirmed by micro-time-of-flight-ESI-MS (micro-TOF-ESI-MS).[37]
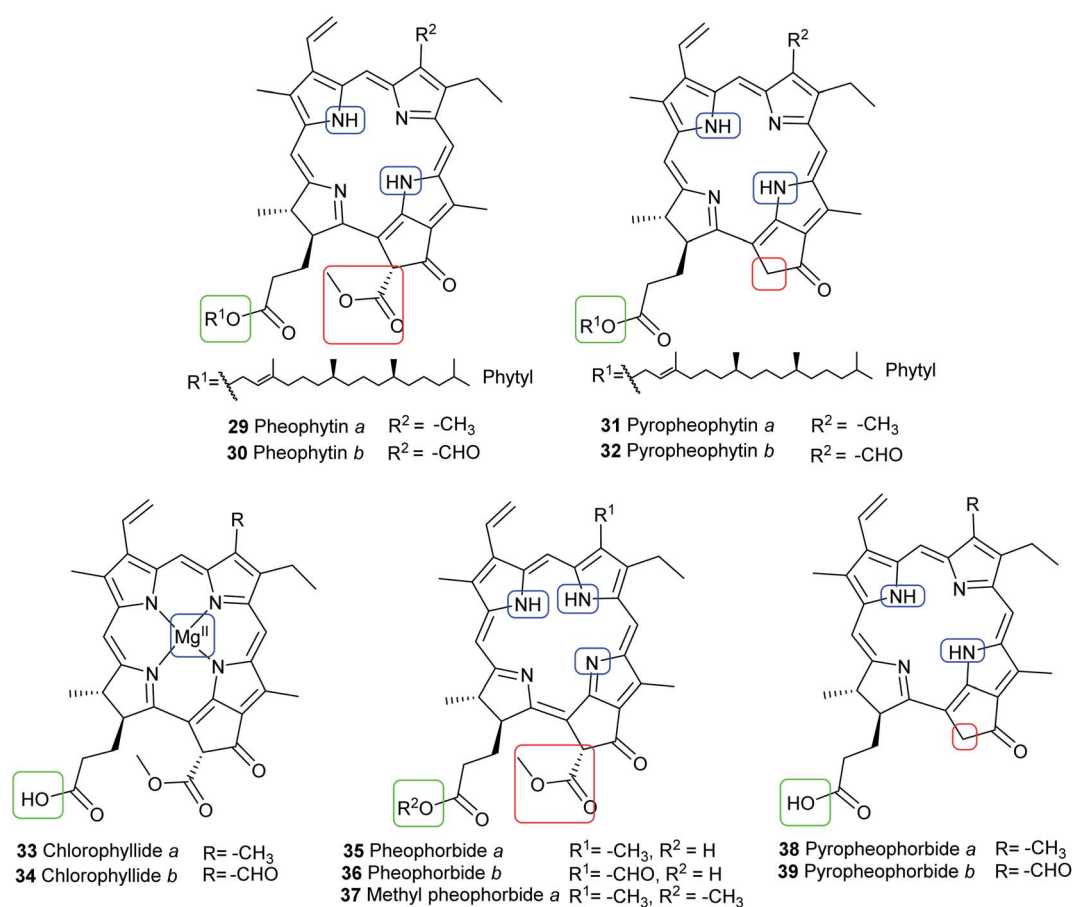
Fig. 8 Structures of chlorophyll metabolites with intact macrocycles.
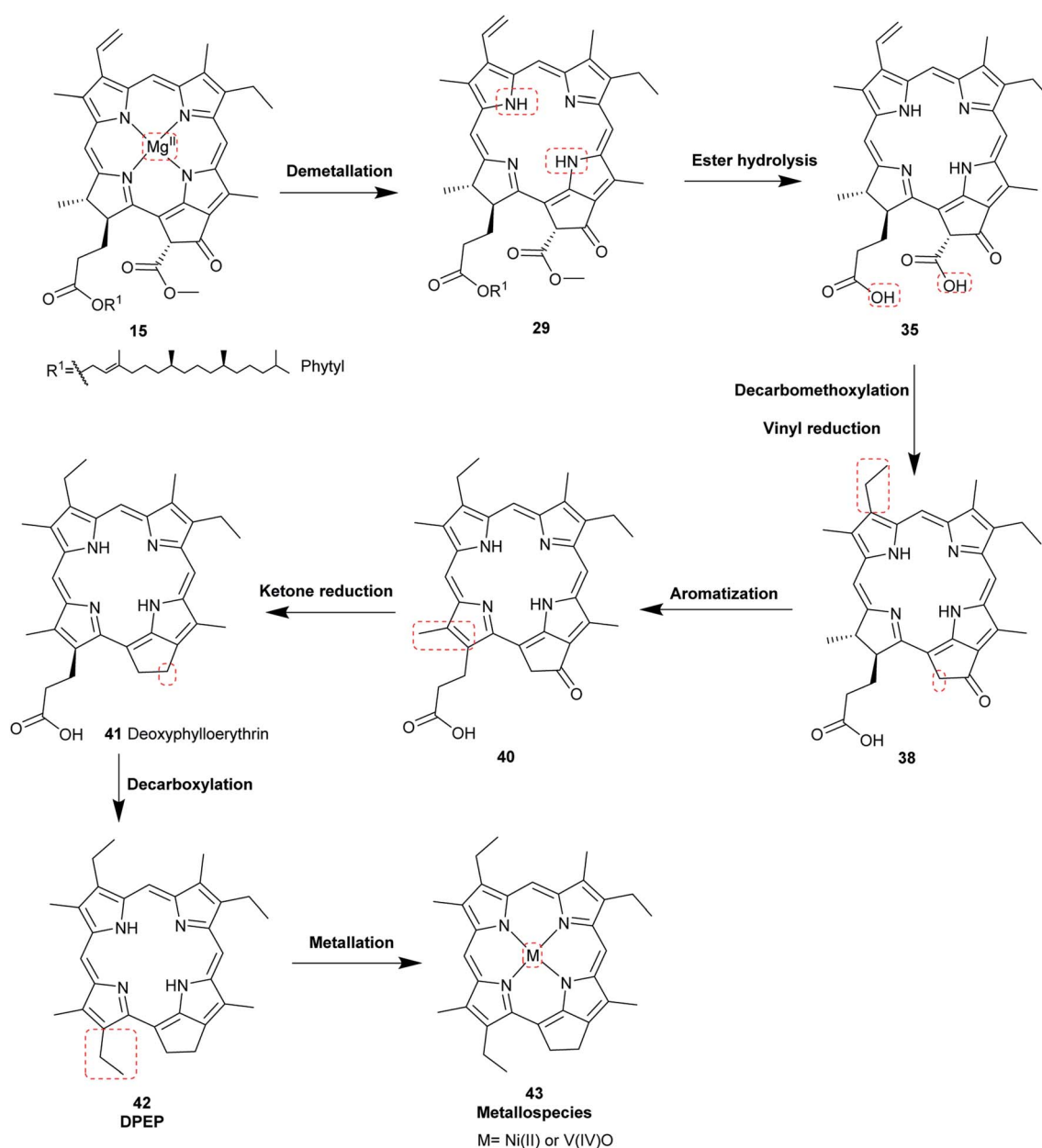
Fig. 9 Diagenetic changes of chlorophyll *a* (**15**) as proposed by A. E. Treibs.[49]

Furthermore, the protoporphyrin IX (**6**) and biliverdin (**8**) were identified from dark gray to slightly greenish colored fossil eggshells of the oviraptorid dinosaur *Heyuannia huangi* (Fig. 5) from the Upper Cretaceous deposits (66 million years old) in eastern and southern China using HPLC-ESI-MS and qTOF-MS, confirmed by similar retention times and exact mass to those of standard samples, whereas the peaks were not found in samples from the surrounding sediment.[38]

Chlorophylls

Chlorophylls are natural pigments found in higher plants, photosynthetic algae, and cyanobacteria. They are classified as chlorophylls (Fig. 6), bacteriochlorophylls, and *Chlorobium* chlorophylls (Fig. 7). The magnesium(II) complexes derived from phorbin include chlorophyll *a* (**15**), chlorophyll *b* (**16**), chlorophyll c_1 (**19**),

chlorophyll c_2 (**20**), chlorophyll c_3 (**21**), chlorophyll *d* (**17**), chlorophyll *f* (**18**),[14,39] and the bacteriochlorophylls **22–28**, all of which feature a 5-membered carbocyclic ring fused to ring C of the porphyrin core structure (Fig. 6 and 7).

Chlorophyll *a* (**15**) is the major pigment involved in the photosynthesis in higher plants, algae, and cyanobacteria. Chlorophyll *b* (**16**) is typically present together with **15** at a ratio of 1 : 3.[4] The prominent chlorophylls in photosynthetic bacteria and algae are **19–21**, whereby the red-shifted chlorophylls *d* (**17**) and *f* (**18**) are only present in some cyanobacteria.[40–43] Bacteriochlorophylls are found in anaerobic bacteria,[43,44] most of which are depicted in Fig. 7. They differ in the parent structure from which they are derived. Compound **22** is the most abundant, while **24–28** are only found naturally in green bacteria

131
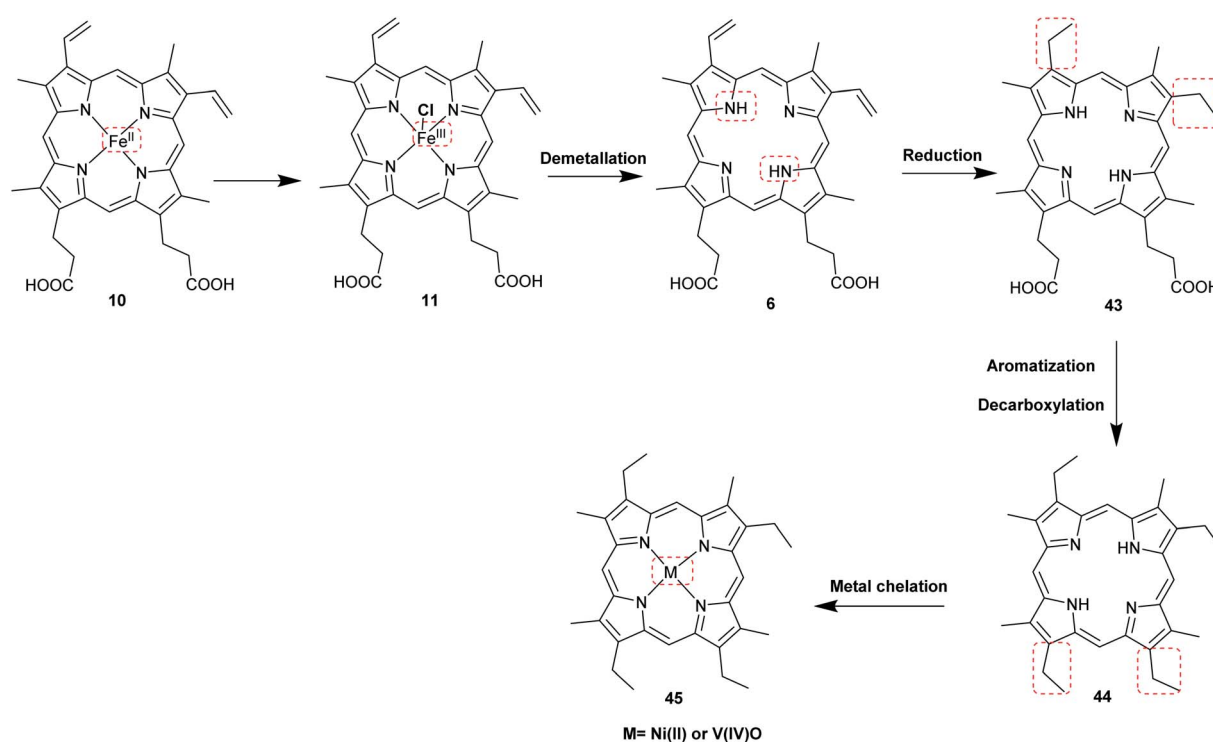
Fig. 10   Diagenetic changes of heme (10) as proposed by A. E. Treibs.[9,11,49]

such as *Chlorobium* and *Chloropseudomonas* and are sometimes separately classified as *Chlorobium* chlorophylls.[45]

Degradation products of chlorophylls

Chlorophyll metabolites with intact macrocycle. *In vivo*, chlorophylls are enzymatically degraded by chlorophyllase which is present in all photosynthetic tissues. Ester hydrolysis occurs, forming chlorophyllide *a* (33) and chlorophyllide *b* (34) from chlorophyll *a* (15) and chlorophyll *b* (16), respectively. Chlorophyllides are green in color and are more hydrophilic than their parent chlorophylls because the hydrophobic long-chain phytol is removed. A magnesium-dechelating enzyme (Mg dechelatase) leads to demetallation, forming pheophorbide *a* (35) and pheophorbide *b* (36), which are blue or dark brown to black in color. Additionally, the brown-colored pheophytin *a* (29) and pheophytin *b* (30) can be formed if magnesium dechelatase acts directly on 15 or 16. These metabolites are commonly formed during senescence of leaves in the autumn and winter months or as by-products during the extraction process.[46–48] Heat results in formation of pyropheophorbide *a* (38) and pyropheophorbide *b* (39), pyropheophytin *a* (31), and pyropheophytin *b* (32).[43] The structures of chlorophyll metabolites bearing an intact phorbin ring are shown in Fig. 8.

Proposed diagenesis of heme and chlorophyll *a* with evidence from sedimentary porphyrins

The most common porphyrin found in sediments is deoxy-phylloerythroetioporphyrin (42, DPEP, Fig. 9), a cyclic alkyl-porphyrin. In the 1930s, the late organic geochemist Alfred E.

Treibs extensively studied 42 and proposed that it originated from chlorophyll *a* (15) *via* diagenesis after decay of its biological origin.[9,49,50] He suggested a set of reactions that must have happened to convert 15 into 42, as shown in Fig. 9. Treibs subdivided them into reactions that readily occur and those that require harsher conditions, such as heat. Demetallation, ester hydrolysis, decarboxylation at the isocyclic ring, reduction of the vinyl group, and aromatization were considered to occur spontaneously, whereas ketone reduction and metal chelation would require harder conditions. Sedimentary porphyrins are almost always found as complexes with nickel(ɪɪ) or oxovanadium(ɪv). Treibs also suggested a similar set of reactions for the diagenesis of heme (10) to produce nickel(ɪɪ) and oxovanadium(ɪv) complexes of etio-type porphyrins, as shown in Fig. 10.[5,6,11,49,50]

Advancements over the years in the power and sensitivity of analytical techniques have enabled scientists to extract, purify, and elucidate the structures of porphyrins found in sediments, oil shales, and petroleum. Furthermore, many of the intermediates and their derivatives proposed by Treibs could be described and correlated to chlorophylls, bacteriochlorophylls, and heme. Other diagenetic pathways were suggested, including condensation or rearrangements to form five- or seven-membered isocycles,[6] and fusion with one or more benzene rings and/or aromatic heterocycles (*e.g.* thiophene).[9,51] These are collectively known as geoporphyrins or petroporphyrins and have been extensively reviewed.[5–9,11] Selected structures are shown in Fig. 11 along with their supposed biological origins.

The oldest record of fossil porphyrins (1.1 billion years old) was reported from extracts of marine sediments in Mauritania, West Africa. A mixture of nickel(ɪɪ)- and oxovanadium(ɪv)-coordinated porphyrins were separated by reversed-phase HPLC-UV-
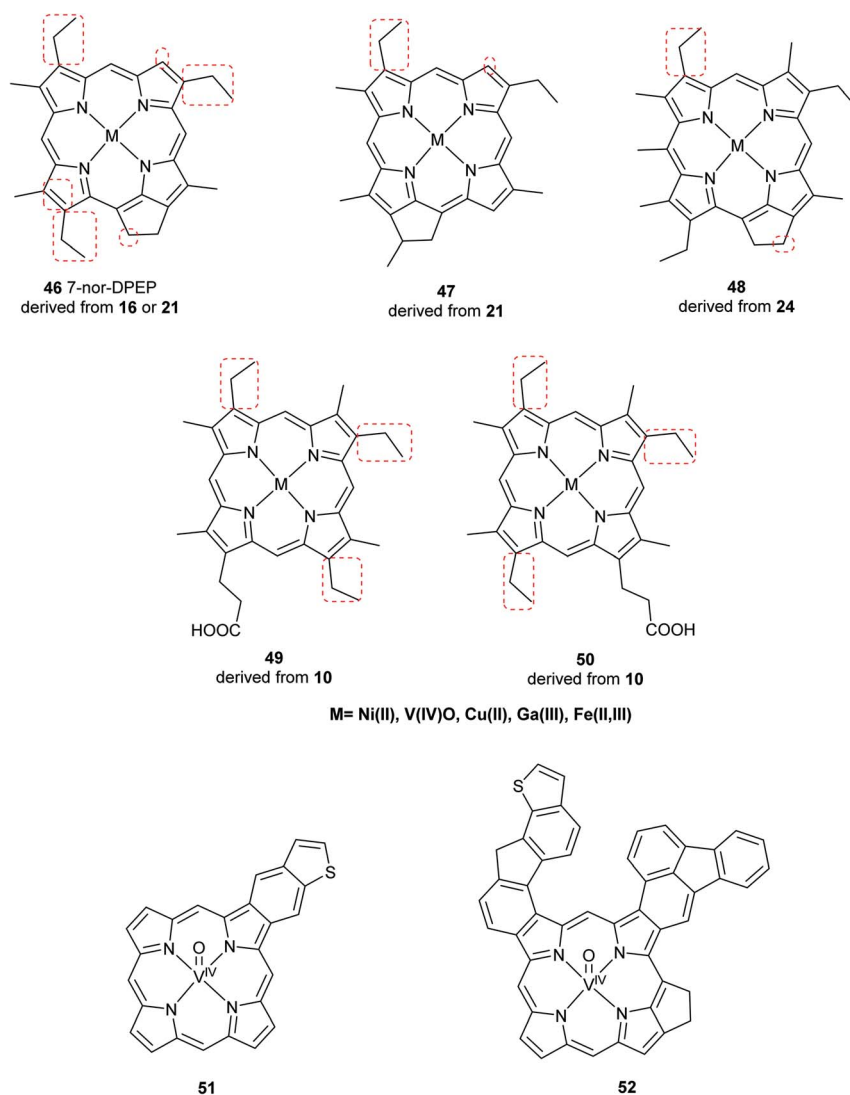
Fig. 11 Structures of selected sedimentary porphyrins, highlighting their differences to the natural porphyrins from which they are supposedly derived.

vis and identified by diode array detector and Fourier-transform cyclotron resonance mass spectrometry (Fig. 12). Nickel(II) porphyrins showed absorbance maxima at 400 and 550 nm, and the oxovanadium(IV) porphyrins showed peak maxima at 415 and 570 nm. They were later purified and their spectra compared to those of standard compounds. Their biological origin could not be correlated to a specific chlorophyll structure, although their origin was shown to be cyanobacterial.[1] Isotopic analysis of the sediment showed a composition of nitrogen-15 isotopes specific for cyanobacteria and different from those of algal and plant origins.[52,53] These findings support the predominance of cyanobacteria rather than algae in the Precambrian ocean.[1]

Chlorophylls in the fossil record

Chlorophylls, bacteriochlorophylls, and their degradation products found in terrestrial (*e.g.*, petroleum) or marine sediments (*e.g.*, mud from the ocean bottom) have been more

commonly described than heme-derived sedimentary porphyrins. The main pigments detected in such sediments include the chlorophyll derivatives **29–39**.[54]

The oldest record of fossil phorbin derivatives is the green pigment **37**, the methyl ester of **35** (see Fig. 8). It was identified in chloroform extracts of green-colored fossil leaves from the middle Eocene brown coals in Geiseltal near Halle, eastern Germany. Several techniques including UV-vis spectroscopy, infrared spectroscopy, paper chromatography, and mass spectrometry indicated the intact isocyclic ring of phorbin and confirmed the pigment's identity when compared to the spectra of standard compound **37**.[55] Fig. 13 shows a distinctly green-colored fossil leaf from the Geiseltal.[56] Seven years later, **37** was identified in the Oligocene to Miocene Succor Creek Flora (25–36 million years old) in Oregon, USA, from green-colored fossil *Zelkova*,[57] *Celtis*, and *Ulmus* leaves.[58] Interestingly, these findings indicated that the diagenesis of these chlorophyll derivatives, specifically in these two regions, was halted after demetallation (Fig. 9)[55,57] owing to anaerobic conditions,[55] the

133

16. Appendix
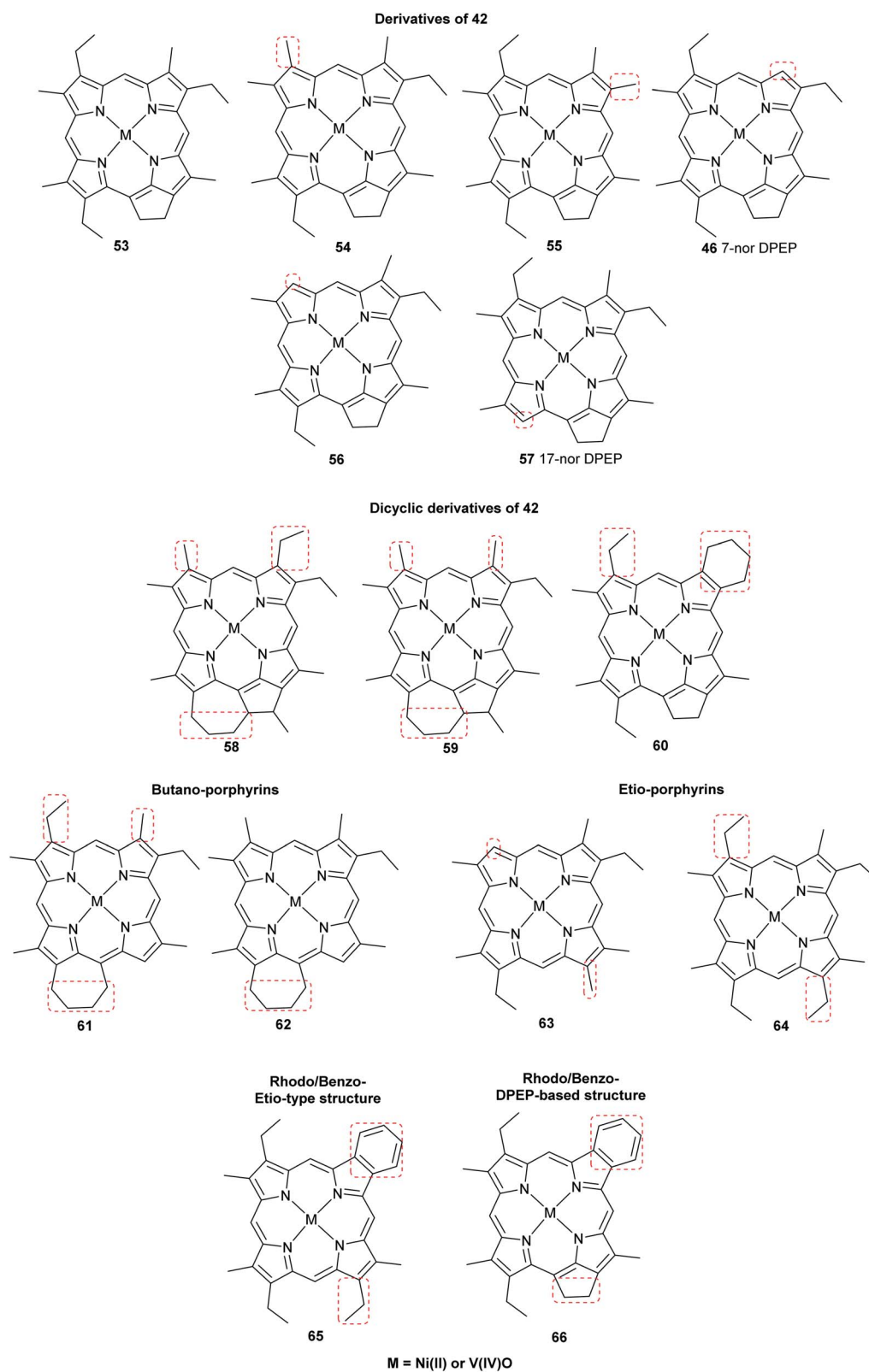
Fig. 12 Structures of the oldest reported porphyrins found as complexes with either nickel(II) or oxovanadium(IV). They are generally derived from chlorophylls.

RSC Advances

Review

Fig. 13 Green fossil leaf from the Eocene lignites in Geiseltal near Halle, eastern Germany, estimated to be around 46 million years old. It is deposited in the collections of the Naturkundemuseum Berlin, Germany. Based on its coloration, it is thought that chlorophyll or its diagenetic products would be present if extracted. Image taken by V. E. McCoy.

cold temperatures of coaly sediments,[55,58] and the absence of significant fluctuations in pH,[58] all of which promoted the preservation of chlorophylls and, accordingly, the green color of the leaves.

The chlorophyll metabolites **29** and **35** (Fig. 8) have been extracted and identified from well-preserved fossil leaves of *Platanus* spp., *Quercus* spp. and *Betula* spp. from the Miocene (15–22 million years old) deposits of the Clarkia Flora in North Idaho, USA. The fossils were shown to have intact chloroplasts among other ultrastructural organelles. These findings showed that, once again, chlorophyll diagenesis did not proceed to form alkylporphyrins. In contrast, the degraded chlorophyll derivative DPEP (**42**) and similar etioporphyrins were detected in fossil leaves of *Castanea* spp. and *Persea* spp. from the same deposits, in which no distinct organelles were preserved. These leaves may have been exposed to high temperatures or to oxidative conditions. No metal complexes were detected in any of the leaves.[59]

Conclusions & perspectives

Porphyrins comprise a large, diverse class of pigments that are present in a variety of plants and animals and play essential roles in the biochemistry of life. The major, biologically relevant (metallo)porphyrins include heme, protoporphyrin IX, chlorophylls, and bacteriochlorophylls. Porphyrins are able to resist decay, and their tetrapyrrole core structure often remains intact

despite structural modifications upon fossilization. Knowledge of the chemical diagenetic pathways in combination with aspects related to the depositional environment of the fossil will facilitate future discoveries of porphyrins in fossils. Moreover, taphonomy studies would contribute to elucidating the degradation processes of these molecules under controlled conditions. The recent advancement of analytical techniques and the development of highly sensitive analytical instruments and methods will certainly promote future research and discoveries in this field. Molecular paleontology is a blossoming area which bears great promises to advance fossilization research.

Conflicts of interest

There are no conflicts to declare.

Acknowledgements

References

1 N. Gueneli, A. M. McKenna, N. Ohkouchi, C. J. Boreham, J. Beghin, E. J. Javaux and J. J. Brocks, *Proc. Natl. Acad. Sci. U. S. A.*, 2018, **115**, E6978–E6986.

2 Z. Suo, R. Avci, M. H. Schweitzer and M. Deliorman, *Astrobiology*, 2007, **7**, 605–615.

3 L. R. Milgrom, *The Colours of Life: An Introduction to the Chemistry of Porphyrins and Related Compounds*, Oxford University Press, 1997.

4 K. M. Smith, in *Porphyrins and Metalloporphyrins: A New Edition Based on the Original Volume by J. E. Falk*, ed. K. M. Smith, Elsevier Scientific Publishing Company, Amsterdam, 1975, pp. 3–28.

5 B. J. Keely, W. G. Prowse and J. R. Maxwell, *Energy Fuels*, 1990, **4**, 628–634.

6 H. J. Callot, R. Ocampo and P. Albrecht, *Energy Fuels*, 1990, **4**, 635–639.

7 N. A. Mironov, D. V. Milordov, G. R. Abilova, S. G. Yakubova and M. R. Yakubov, *Pet. Chem.*, 2019, **59**, 1077–1091.

8 C. C. Naylor and B. J. Keely, *Org. Geochem.*, 1998, **28**, 417–422.

9 X. Zhao, C. Xu and Q. Shi, in *Structure and Modeling of Complex Petroleum Mixtures*, Springer, 2015, pp. 39–70.

10 E. Cappellini, A. Prohaska, F. Racimo, F. Welker, M. W. Pedersen, M. E. Allentoft, P. de Barros Damgaard, P. Gutenbrunner, J. Dunne, S. Hammann, M. Roffet-Salque, M. Ilardo, J. V. Moreno-Mayar, Y. Wang, M. Sikora, L. Vinner, J. Cox, R. P. Evershed and E. Willerslev, *Annu. Rev. Biochem.*, 2018, **87**, 1029–1060.

135

11 H. Falk and K. Wolkenstein, *Prog. Chem. Org. Nat. Prod.*, 2017, 52–59.

12 H. J. Kim, in *eLS*, John Wiley & Sons, Ltd, Chichester, UK, 2018, pp. 1–9.

13 J. W. Buchler, in *Porphyrins and Metalloporphyrins: A New Edition Based on the Original Volume by J. E. Falk*, ed. K. M. Smith, Elsevier Scientific Publishing Company, Amsterdam, 1975, pp. 157–231.

14 G. R. Seely, in *The Chlorophylls*, Elsevier, 1966, pp. 67–109.

15 R. Huszánk and O. Horváth, *Chem. Commun.*, 2005, 224–226.

16 U. Neugebauer, A. März, T. Henkel, M. Schmitt and J. Popp, *Anal. Bioanal. Chem.*, 2012, **404**, 2819–2829.

17 C. K. Lim, M. A. Razzaque, J. Luo and P. B. Farmer, *Biochem. J.*, 2000, **347**, 757–761.

18 M. Senge, A. Ryan, K. Letchford, S. MacGowan and T. Mielke, *Symmetry*, 2014, **6**, 781–843.

19 H. K. Lichtenthaler and C. Buschmann, *Curr. Protoc. Food Anal. Chem.*, 2001, **1**, F4.3.1–F.4.3.8.

20 L. Pilon and H. Berberoğlu, in *Handbook of Hydrogen Energy*, CRC Press, Boca Raton, 2014, pp. 369–418.

21 A. P. Razjivin, E. P. Lukashev, V. O. Kompanets, V. S. Kozlovsky, A. A. Ashikhmin, S. V. Chekalin, A. A. Moskalenko and V. Z. Paschenko, *Photosynth. Res.*, 2017, **33**, 289–295.

22 M. H. Schweitzer, *Annu. Rev. Earth Planet. Sci.*, 2011, **39**, 187–216.

23 G. Eglinton and G. A. Logan, *Philos. Trans. R. Soc., B*, 1991, **333**, 315–328.

24 N. L. Huq, S. M. Rambaud, L. C. Teh, A. D. Davies, B. McCulloch, M. M. Trotter and G. E. Chapman, *Biochem. Biophys. Res. Commun.*, 1985, **129**, 714–720.

25 N. V. Bhagavan and C.-E. Ha, in *Essentials of Medical Biochemistry*, Elsevier, 2015, pp. 511–529.

26 K. E. Anderson and S. Collins, *Am. J. Med.*, 2006, **119**, 801.e19, DOI: 10.1016/j.amjmed.2006.05.026.

27 M. H. Schweitzer, M. Marshall, K. Carron, D. S. Bohle, S. C. Busse, E. V. Arnold, D. Barnard, J. R. Horner and J. R. Starkey, *Proc. Natl. Acad. Sci. U. S. A.*, 1997, **94**, 6291–6296.

28 D. E. Greenwalt, Y. S. Goreva, S. M. Siljeström, T. Rose and R. E. Harbach, *Proc. Natl. Acad. Sci. U. S. A.*, 2013, **110**, 18496–18500.

29 J. Lindgren, T. Kuriyama, H. Madsen, P. Sjövall, W. Zheng, P. Uvdal, A. Engdahl, A. E. Moyer, J. A. Gren, N. Kamezaki, S. Ueno and M. H. Schweitzer, *Sci. Rep.*, 2017, **7**, 1–13.

30 P. O. Carra, in *Porphyrins and Metalloporphyrins: A New Edition Based on the Original Volume by J. E. Falk*, ed. K. M. Smith, Elsevier Scientific Publishing Company, Amsterdam, 1975, pp. 123–153.

31 G. Y. Kennedy and H. G. Vevers, *Comp. Biochem. Physiol., Part B: Biochem. Mol. Biol.*, 1976, **55**, 117–123.

32 M. Huang, H. Hu, L. Ma, Q. Zhou, L. Yu and S. Zeng, *Drug Metab. Rev.*, 2014, **46**, 362–378.

33 R. B. Frydman and B. Frydman, *Acc. Chem. Res.*, 1987, **20**, 250–256.

34 M. J. Terry, in *Heme, Chlorophyll, and Bilins*, ed. A. Smith and M. Witty, Humana Press, 2002, pp. 273–291.

35 A. Gorchein, C. K. Lim and P. Cassey, *Biomed. Chromatogr.*, 2009, **23**, 602–606.

36 B. Igic, D. R. Greenwood, D. J. Palmer, P. Cassey, B. J. Gill, T. Grim, P. L. R. Brennan, S. M. Bassett, P. F. Battley and M. E. Hauber, *Chemoecology*, 2010, **20**, 43–48.

37 D. B. Thomas, M. E. Hauber, D. Hanley, G. I. Waterhouse, S. Fraser and K. C. Gordon, *J. Exp. Biol.*, 2015, **218**, 2670–2674.

38 J. Wiemann, T. R. Yang, P. N. Sander, M. Schneider, M. Engeser, S. Kath-Schorr, C. E. Müller and P. M. Sander, *PeerJ*, 2017, **2017**, 1–20.

39 A. Gossauer and N. Engel, *J. Photochem. Photobiol., B*, 1996, **32**, 141–151.

40 A. Ben-Shem, F. Frolow and N. Nelson, *Nature*, 2003, **426**, 630–635.

41 H. Scheer, in *Chlorophylls and Bacteriochlorophylls*, Springer Netherlands, 2006, pp. 1–26.

42 A. N. Melkozernov and R. E. Blankenship, in *Chlorophylls and Bacteriochlorophylls*, Springer Netherlands, 2006, pp. 397–412.

43 M. Roca, K. Chen and A. Perez-Galvez, in *Handbook on Natural Pigments in Food and Beverages: Industrial Applications for Improving Food Color*, ed. R. Carle and R. Schweiggert, Woodhead Publishing, 2016, pp. 125–158.

44 J. L. Thweatt, D. P. Canniffe and D. A. Bryant, in *Advances in Botanical Research*, 2019, pp. 35–89.

45 K. G. Wallace, J. Rimmer, S. K. Manley, J. F. Unsworth, A. H. Jackson and N. Albert, *Philos. Trans. R. Soc., B*, 1976, **273**, 255–276.

46 S. Hörtensteiner, *Cell. Mol. Life Sci.*, 1999, **56**, 330–347.

47 S. Hörtensteiner, *Annu. Rev. Plant Biol.*, 2006, **57**, 55–77.

48 J. D. Barnes, L. Balaguer, E. Manrique, S. Elvira and A. W. Davison, *Environ. Exp. Bot.*, 1992, **32**, 85–100.

49 A. E. Treibs, *Angew. Chem.*, 1936, **49**, 682–686.

50 A. E. Treibs, *Justus Liebigs Ann. Chem.*, 1934, **510**, 42–62.

51 K. Qian, T. R. Fredriksen, A. S. Mennito, Y. Zhang, M. R. Harper, S. Merchant, J. D. Kushnerick, B. M. Rytting and P. K. Kilpatrick, *Fuel*, 2019, **239**, 1258–1264.

52 M. B. Higgins, F. Wolfe-Simon, R. S. Robinson, Y. Qin, M. A. Saito and A. Pearson, *Geochim. Cosmochim. Acta*, 2011, **75**, 7351–7363.

53 J. M. Fulton, M. A. Arthur and K. H. Freeman, *Global Biogeochem. Cycles*, 2012, **26**, 1–15.

54 T. S. Bianchi and E. A. Canuel, in *Chemical Biomarkers in Aquatic Ecosystems*, Princeton University Press, 2011.

55 D. L. Dilcher, R. J. Pavlick and J. Mitchell, *Science*, 1970, **168**, 1447–1449.

56 C. T. Gee and V. E. McCoy, in *Fossilization: Understanding the Material Nature of Ancient Plants and Animals*, ed. C. T. Gee, V. E. McCoy, and P. M. Sander, Johns Hopkins University Press, Baltimore, 2021.

57 K. J. Niklas and D. E. Giannasi, *Science*, 1977, **196**, 877–878.

58 D. E. Giannasi and K. J. Niklas, *Science*, 1977, **197**, 765–767.

59 K. J. Niklas and R. M. Brown, *Am. J. Bot.*, 1981, **68**, 332–341.

16.2. Appendix B – Chemistry and analysis of organic compounds in dinosaurs

This section contains the review article "Chemistry and analysis of organic compounds in dinosaurs" as it appears in the journal *Biology* by Multidisciplinary Digital Publishing Institute (MDPI). Reprinted from *Biology 2022, 11(5), 670*, Copyright (2022), with permission from MDPI. This work is licensed under the Creative Commons Attribution 4.0 International License. To view a copy of this license, visit http://creativecommons.org/licenses/by/4.0/. As guaranteed by the author rights policy of MDPI, copying and re-use of the article in any medium or format is allowed without permission or payment, as long as the original article is fully acknowledged.

Review

Chemistry and Analysis of Organic Compounds in Dinosaurs

Mariam Tahoun [1] [ID]**, Marianne Engeser** [2] [ID]**, Vigneshwaran Namasivayam** [1] [ID]**, Paul Martin Sander** [3]
and Christa E. Müller [1,*] [ID]

[1] PharmaCenter Bonn, Pharmaceutical Institute, Pharmaceutical & Medicinal Chemistry, University of Bonn, D-53121 Bonn, Germany; mtahoun@uni-bonn.de (M.T.); vnamasiv@uni-bonn.de (V.N.)
[2] Kekulé Institute for Organic Chemistry and Biochemistry, University of Bonn, D-53121 Bonn, Germany; marianne.engeser@uni-bonn.de
[3] Institute of Geosciences, Section Paleontology, University of Bonn, D-53113 Bonn, Germany; martin.sander@uni-bonn.de
* Correspondence: christa.mueller@uni-bonn.de

Simple Summary: Fossils of dinosaurs other than birds are at least 66 million years old. Nevertheless, many organic compounds have survived fossilization and can still be found in the fossils. This article describes the discovery of organic molecules in dinosaur fossils. It provides a review of the analytical methods used for their detection and characterization, and presents the wide range of chemical organic compounds, including small molecules and polymers, that have been found in dinosaurs to date. The difficulties in unambiguously confirming the presence of some of the organic molecules in these fossils are also discussed.

Abstract: This review provides an overview of organic compounds detected in non-avian dinosaur fossils to date. This was enabled by the development of sensitive analytical techniques. Non-destructive methods and procedures restricted to the sample surface, e.g., light and electron microscopy, infrared (IR) and Raman spectroscopy, as well as more invasive approaches including liquid chromatography coupled to tandem mass spectrometry (LC-MS/MS), time-of-flight secondary ion mass spectrometry, and immunological methods were employed. Organic compounds detected in samples of dinosaur fossils include pigments (heme, biliverdin, protoporphyrin IX, melanin), and proteins, such as collagens and keratins. The origin and nature of the observed protein signals is, however, in some cases, controversially discussed. Molecular taphonomy approaches can support the development of suitable analytical methods to confirm reported findings and to identify further organic compounds in dinosaur and other fossils in the future. The chemical properties of the various organic compounds detected in dinosaurs, and the techniques utilized for the identification and analysis of each of the compounds will be discussed.

Keywords: fossil; dinosaur; molecular paleontology; paleoproteomics; porphyrin; collagen; melanin; keratin

1. Introduction

After an organism's death, microbial decomposition of organic constituents occurs very fast, mostly leaving behind mineralized skeletal remains. If this degradation process is arrested early enough, due to factors related to the burial environment and dependent on the characteristics of the molecular or tissue components [1–3], preservation of "soft tissue" can occur. Such fossils are exceptional and very valuable because they may contain information related to evolution, biology, or the environment that can be revealed by analyzing their composition [2,3]. Preserved soft tissue has been reported from a variety of fossil fish, amphibians, reptiles, dinosaurs, and mammals. This includes cells, organelles, skin, scales, feathers, hair, colored structures, digestive organs, eggshells, and muscles [2]. This mode of preservation is unique because the original organic material is minimally

altered. Furthermore, this should be differentiated from fossilization involving alteration of original material, e.g., replacement of organic matter by minerals such as phosphates (phosphatization) or conversion to thin films of carbon (carbonization) [4,5].

Researchers try to understand the factors that hinder decay processes and contribute to the preservation of organic compounds present in soft tissues. These include (but are not limited to) intrinsic properties of the organic molecules, their environment (including metals such as Fe and Mn present) [6–8], and the type of preserved soft tissue. The presence of moisture, microorganisms or enzymes speeds up the decay process [1]. The most labile molecular bonds are first targeted during decomposition. For example, proteins and DNA are susceptible to degradation by hydrolysis of their peptide and phosphoric acid ester bonds, respectively. However, association of organic compounds with minerals (e.g., in bone or teeth) or with macromolecules may isolate and protect them from the external environment.

Oxidative conditions usually lead to faster decay than reductive conditions. Hydrophobic organic compounds are more likely to be preserved than hydrophilic compounds because of their limited water-solubility, which protects them from hydrolysis and other reactions. Polymeric structures may be preserved due to crosslinking and intramolecular interactions. Environmental factors greatly affect fossilization, e.g., by applying pressure on tissue, limiting the mobility of molecules and exposure to water, microbes, and enzymes. Moreover, extremes of temperature, pH, and salinity play a role in molecular preservation by inhibiting microbial activity and affecting the rate of the chemical decomposition process. Taphonomic studies at a molecular scale ("molecular taphonomy") can be used to establish analytical methods for understanding chemical processes that lead to the degradation of organic compounds upon fossilization ([1,2,9–15] and references therein).

Since the first discoveries of microstructures (collagen-like fibrils, vessels, and cells) in a 200-million-year-old dinosaur bone in 1966 [16] there has been an increased interest in studying the large number of available dinosaur fossils for signs of molecular preservation of organic compounds. Such finds provide information about the dinosaurs' biology, including their evolution, eating habits, and environment. Most reports on organic matter in fossilized dinosaurs have been focused on their bones. In recent years, studies on eggshells, cartilage, feathers, and integumentary structures have emerged, albeit mostly discussing in situ analyses, and relying on morphological and microscopic observations due the uniqueness of the studied fossils (reviewed in [2,10] and references therein).

To date, organic compounds have been recovered from a wide array of dinosaur taxa, including the early-branching coelurosaur *Sinosauropteryx* [17], the tyrannosaur *Tyrannosaurus rex* [18–20], the oviraptorosaurs *Heyuannia huangi* [21,22] and *Citipati osmolskae* [23], the alvarezsaurid *Shuvuuia deserti* [24], the dromaeosaur *Sinornithosaurus* [17], the early-branching avialan *Anchiornis huxleyi* [25], the early-branching sauropodomorph *Lufengosaurus sp.* [3], an unidentified titanosaurid dinosaur [26], the ankylosaur *Borealopelta markmitchelli* [27], the ceratopsian *Psittacosaurus* [28], the hadrosaur *Brachylophosaurus canadensis* [29,30], an indeterminate hadrosaur material [26], and *Hypacrosaurus stebingeri* [31]. Here, we review the chemistry of the organic molecules recovered to date from fossilized non-avian dinosaurs and discuss the analytical methods used for their detection.

2. Analytical Techniques to Investigate Preserved Organic Compounds

The principles of the analytical techniques used in paleontological research, along with their advantages and drawbacks, have recently been reviewed in detail [32,33]. The application of mass spectrometry in proteomic analysis of fossils was specifically discussed by Schweitzer et al. (2019) [34]. The following paragraphs present selected analytical techniques that have been utilized to detect organic compounds in fossilized dinosaurs.

2.1. Microscopy

Initial studies carried out on fossils in search of organic matter included a thorough screening of the fossils' surface or of petrographic thin sections to identify regions in which

16. Appendix

soft tissues and associated organic compounds could be preserved [35]. Imaging techniques such as optical microscopy (OM), scanning electron microscopy (SEM), and transmission electron microscopy (TEM) have been used for this purpose. Optical microscopy is useful for the visualization of petrographic thin sections to identify preserved cellular structures. Mineralization, diagenetic alteration, and/or microbial contamination of tissues can be detected by means of this technique [35].

Electron microscopy is more powerful due to its much higher resolution. It is therefore used to examine subcellular structures in greater detail. In SEM, electrons are directed onto the surface of the sample, generating and transmitting secondary electrons to a detector. Therefore, SEM is limited to studying the sample surfaces by generating a pseudo-3D gray-scale topographical image without collecting chemical signals [35,36]. However, a technique known as energy-dispersive X-ray spectrometry (EDS is often combined with SEM, which uses high energy X-rays characteristic for a specific element released alongside the secondary electrons [32,35,37]. Integration of the elemental information from EDS into the topographical map from SEM allows the localization of elements to be identified in the sample [35]. Other variations of SEM exist, such as field emission SEM (FESEM) [35] and variable pressure SEM (VPSEM) [38]. VPSEM allows for analysis of uncoated samples within a wider range of beam energies than traditional SEM [35]. VPSEM can also be used without prior sample preparation (e.g., dehydration or drying) in soft samples [39]. Thus, FESEM and VPSEM reduce the risk of sample contamination. Both techniques have been used for the study of soft tissues in dinosaur bones [35,38].

In transmission electron microscopy (TEM), electrons are directed to partially demineralized or very thin-cut sections of a sample in a way that only the electrons that cross through the sample are detected. This feature makes TEM a high-resolution technique that can be used for identifying subcellular structures such as organelles or characteristic structural patterns, e.g., the 67 nm bands of collagen fibers [35].

2.2. Spectroscopy and Spectrometry

2.2.1. UV/Vis Spectroscopy

Ultraviolet/visible light (UV/Vis) spectroscopy is an analytical technique to measure the absorption, transmittance, or reflectance of light by molecules upon irradiation with ultraviolet (190–380 nm) or visible (380–750 nm) light [40,41]. The functional group(s) of the molecule responsible for light absorption is known as the chromophore, e.g., due to conjugated C=C double bonds and/or aromatic rings. The chromophore contains valence electrons having low excitation energy, which become excited and transit to higher energy levels when the molecule is irradiated [41]. The wavelengths at which light is absorbed can be used to identify the structure of a compound. The amount of light absorbed is directly proportional to the concentration of the compound and thus allows for its quantification [42]. UV/Vis spectroscopy is frequently used in molecular paleontology, particularly when analyzing colored fossils, to detect characteristic absorption bands of pigments; it has, for example, been used for detecting heme [18].

2.2.2. Infrared and Raman Spectroscopy

Further studies on fossils use chemical imaging techniques such as Fourier transform infrared spectroscopy (FTIR) and Raman spectroscopy to search for chemical signals, e.g., of functional groups (e.g., amide or carbonyl group) in the samples [9,21,32]. FTIR excites the vibrations of chemical bonds using infrared irradiation. Each type of chemical bond will absorb infrared (IR) waves in a distinct wave number range in the near-IR ($12,500–4000$ cm^{-1}), mid-IR ($4000–400$ cm^{-1}), or far-IR ($400–10$ cm^{-1}) regions. Most of the important chemical signals that are indicative of functional groups will be present in the mid-IR range [43]. FTIR can be combined with light microscopy to identify the location of the detected functional groups in the sample. However, FTIR entails many disadvantages. The wave number ranges can overlap if the sample contains many organic signals leading to frequent misinterpretations of chemical signals, especially if diagenetic changes occurred

to the original structure. In addition, any contamination on the surface of the sample will be recorded in the spectra and may not be distinguishable from the sample signals. FTIR has been used to detect characteristic absorption bands of peptide bonds, amide I (C=O bond, ca. 1655 cm^{-1}) and amide II (N-H bond, ca. 1545 cm^{-1}), associated with collagen in cartilage, in addition to peptide bonds specific for melanin (1580 cm^{-1}) [32,34].

Other variants of IR spectroscopy have been used to study fossils. For example, synchrotron-radiation Fourier transformed infrared spectroscopy (SR-FTIR) uses a much brighter light source (synchrotron radiation) ranging from far-IR to near-IR [44] to produce chemical maps. SR-FTIR has a higher resolution and a better signal-to-noise ratio than classical FTIR [45]. In addition, attenuated-total reflection IR (ATR-IR) has been used for the analysis of liquid samples [46].

Raman spectroscopy applies monochromatic laser light (ultraviolet, infrared, or visible) to irradiate the layer directly below the surface of the sample. Some of the light is then scattered with a defined frequency generating a signal that can be detected and plotted as a graph of intensity versus wave number. The observed scattering depends on the type of functional group and its vibration [47]. It can be combined with other microscopic techniques such as confocal microscopy to form a chemical map of the functional groups present in the sample. Raman spectroscopy is currently one of the most preferred methods to search for preserved organic matter and other chemical constituents in fossils because it does not require exhaustive sample preparation. However, in contrast to FTIR, signals present on the outermost surface cannot be detected. The produced signals are weak, often requiring prolonged periods of intense irradiation [48], which can lead to a degradation of thermolabile compounds due to the heat produced by the laser [32,49]. Raman spectroscopy has been used for the detection of heme in dinosaur bones [18] and for the detection of the heme degradation product biliverdin and of its precursor protoporphyrin IX in dinosaur eggshells [21].

2.2.3. Mass Spectrometry

Mass spectrometric techniques are among the most sensitive, reliable methods to detect organic compounds. Soft ionization techniques allow measuring the mass-to-charge ratio of intact molecular ions. In addition, different chemical classes of compounds have characteristic fragmentation patterns observed in mass spectrometry [50]. However, detecting only fragments or only molecular ions is often not sufficient for identification of specific organic molecules [32,35], whereas a combination of both can be highly informative.

Chemical information, especially on molecular fragments, can be obtained by time-of-flight secondary ion mass spectrometry (TOF-SIMS) and pyrolysis coupled to gas chromatography-mass spectrometry (Py-GC-MS). Only fragments can be detected by the latter method because of the harsh ionization conditions used, often leading to a complete destruction of the sample.

TOF-SIMS is a surface imaging technique with ultra-high spatial resolution which directs high energy ionizing beams (e.g., gallium ions) over the sample surface. Molecules are released, ionized and often fragmented [51]. The ions are transmitted to the time-of-flight mass spectrometer and detected according to the time it takes for them to reach the detector. The heavier their masses are, the more time it will take. It can be used for analyzing fragile or small amounts of fossil samples because measurements take place at the surface without the need for extractions. Determination of the location of the signal in the sample is the main advantage of the method, and it is therefore useful for organic compound screening [52]. However, as TOF-SIMS only analyzes the surface, any changes on the surface or contamination will influence the results [32,35]. This method has been used to detect heme [53], melanin [54], protein fragments of β-keratin [24], and collagen [26] in fossils.

To overcome the extensive fragmentation, especially of higher molecular weight ions, a variant of TOF-SIMS known as cluster secondary ion mass spectrometry was developed. Its principle relies on bombardment of the sample using a polyatomic cluster of ions,

such as gold (Au$_3$) or a C$_{60}$-based ion cluster, buckminsterfullerene. This allows the detection of intact molecular ions in the range of 1000–3000 D, which was not possible with traditional TOF-SIMS [55]. In addition, spatial resolution beyond the micrometer range can be achieved [56].

Py-GC-MS is a technique that uses intense heat (ca. 400–600 °C) to fragment molecular bonds. The generated fragments are gaseous; they are separated by gas chromatography and detected by mass spectrometry. Unlike TOF-SIMS, the sample is destroyed, and the location of the chemical signal in the original sample cannot be determined. This method does not require sample preparation, and therefore, the risk of detecting artifacts is lowered [57]. It has been used to detect molecular fragments characteristic of proteins, lignin and chitin in fossils [58–60]. Due to the destruction of the sample, Py-GC-MS is not preferred if alternative approaches are possible; therefore, it is only used for analyses of insoluble fossil material which cannot be analyzed otherwise [35].

All of the aforementioned analytical techniques are often not suitable for unambiguously determining the identity of organic compounds. However, they can help narrowing down sample regions that contain organic compounds, which may then be subjected to more invasive mass spectrometry techniques.

On rare or unique fossils, only non-destructive or highly sensitive methods can be applied. Modern mass spectrometry techniques now provide options for analyzing such precious samples since they require only small quantities of material.

In order to identify intact organic compounds, mild ionization methods, such as electrospray ionization, need to be applied [61]. In most cases, samples are extracted, separated by reverse-phase liquid chromatography, which is coupled to tandem mass spectrometry (LC-MS/MS). The prerequisite for this type of analysis is a solution of the analytes; thus, compounds that are insoluble in the typically used solvents (methanol, acetonitrile, water, and their mixtures) cannot be analyzed [62].

The type of mass analyzer used is decisive for mass accuracy and sensitivity of mass spectrometric measurements. Quadrupole, time-of-flight, linear ion-trap, Fourier transform ion cyclotron resonance (FT-ICR) and Orbitrap analyzers are commonly used for organic compounds in fossils. Instruments with high mass accuracy are needed to determine elemental compositions of organic compounds. With ion trap instruments or when two types of mass analyzers are combined in series, more advanced mass spectrometric analyses are possible, known as tandem mass spectrometry. Typical combinations are quadrupole/quadrupole, quadrupole/time-of-flight (q/TOF), and quadrupole or linear ion-trap coupled to Orbitrap. Tandem mass spectrometers allow for a unique type of analysis known as collision-induced dissociation, in which intact ions of a defined mass-to-charge ratio are selected and then deliberately fragmented to analyze the fragments [62]. This method is used to achieve ultra-high sensitivity, and it provides structural information on the molecules of interest. It is the method of choice in proteomics to identify peptide sequences and to obtain information about diagenetic changes to the chemical structure, and to identify post-translational modifications [34,35]. For fossils, LC-MS/MS is one of the most selective, accurate and sensitive methods to identify organic compounds. However, this is often not applicable due to limited sample availability and/or difficulties in extracting the target compounds due to a lack of solubility [33,35].

2.3. Immunological Techniques

Immunological techniques are based on antigen–antibody reactions. Antibodies used in the process are specific to a certain epitope in the target tissue. These sensitive techniques are used to screen for the presence of macromolecules such as proteins or DNA. Using antibodies, sequence determination is not possible, but regions in the sample may be located, in which proteinaceous or genetic material has been preserved, and which can be selected subsequently for mass spectrometric analysis [34]. Immunological techniques include enzyme-linked immunosorbent assays (ELISAs), Western blotting (immunoblotting), and immunohistochemistry/immunostaining procedures.

A prerequisite for the detection of proteins by Western blot and ELISA is a liquid extract containing the protein of interest. ELISA is the more sensitive technique [63]. There are different forms of ELISA: direct ELISA, indirect ELISA, sandwich ELISA and competitive ELISA, which are typically performed in well plates. The first step is to immobilize the antigen of interest by direct adsorption to the surface or through binding to a capture antibody fixed to the plate. Direct and indirect ELISA are used for antigens immobilized directly to the well plate, whereas sandwich ELISA is used for antigens bound to a capture antibody [64]. Direct ELISA uses an enzyme-linked antibody that binds directly to the antigen of interest. Upon washing to remove unbound antibodies, and subsequent addition of the suitable substrate, a color change will occur only in the wells that contain the antigen–antibody complex [65]. Indirect ELISA is used to detect the presence of antibodies rather than antigens. Addition of a sample expected to contain a primary antibody specific to the antigen of interest results in the formation of a complex with the immobilized antigen. A secondary antibody linked to an enzyme and specific to the primary antibody is added. After washing, any unbound antibodies are removed. The substrate is added and the enzymatic reaction occurs to produce a colored product that confirms the presence of the antibody [64,65].

Sandwich ELISA is used to detect the presence of antigens and is the most commonly used form of ELISA. The well surface is first coated with a capture antibody specific to the antigen of interest, onto which the antigen from a sample will be immobilized. A primary antibody specific to the antigen will then be added. If the antigen is present, the primary antibody will bind to it. The next steps are the same as those for indirect ELISA, by which the color change will confirm the presence of the antigen [64,65]. It is worth noting that sandwich ELISA will only be possible for antigens which have two separate epitopes for binding a capture antibody and a primary antibody. Using two antibodies for detection of the same antigen makes sandwich ELISA highly specific [66]. In ELISA, proteins are detected in their natural conformation.

In competitive ELISA, antigens in a sample compete with a reference antigen coated on the surface of a well in binding to a labeled primary antibody of known concentration. The sample is incubated first with the primary antibody. Then this solution is added to the wells. The more antigens are present in the sample, the more primary antibodies will bind to them [67]. Any unbound antibody will then bind to the reference antigen. Following a washing step, an enzyme-linked secondary antibody is added. The substrate for the enzyme is then added, and the intensity of the resulting color is inversely related to the concentration of the antigens present in the sample. If few primary antibodies are bound to the reference antigen, a faint color will be observed, and this indicates a high concentration of antigens in the sample [68].

Western blot is used to identify a protein from a complex mixture [64]. Before performing a Western blot experiment, the mixture of proteins in a sample are separated by polyacrylamide gel electrophoresis according to size [69,70]. There are two main types of gel electrophoresis, depending on the type of additives used: sodium dodecyl sulfate-polyacrylamide gel electrophoresis (SDS-PAGE) and blue native-polyacrylamide gel electrophoresis (BN-PAGE). SDS-PAGE uses the detergent sodium dodecyl sulfate which denatures the proteins, whereas BN-PAGE uses the mild Coomassie blue dye and does not denature the protein of interest [69,71,72]. The bands containing the separated proteins are transferred to an immobilizing nitrocellulose or polyvinylidene difluoride membrane. This is followed by adding a blocking buffer containing non-fat dried milk or 5% bovine serum albumin, in order to prevent binding of antibodies to the membrane [70]. A primary antibody specific to the protein of interest is incubated with the membrane, followed by washing to remove unbound antibodies. Then, a secondary antibody is added that binds specifically to the primary antibody, and which is radiolabeled or linked to an enzyme. Afterwards, either a substrate is added to initiate the enzymatic reaction, or a photographic film for a radio-labeled substrate is used for detection of the target antigen–antibody complex and to locate the protein [64].

To account for diagenetic changes to the original structure, polyclonal antibodies are often used during analysis of fossil extracts; however, problems with poor specificity of antibodies may arise. Both Western blot and ELISA are prone to contamination and/or interference from extraction buffer components [34].

Immunohistochemistry is based on the same principles as ELISA and Western blot, the only difference is that the antibodies are applied in situ on intact tissue instead of utilizing extracts [73]. In situ analyses are preferred to destructive techniques because they minimize the loss of precious sample material and/or degradation of organic material during preparation (e.g., after exposure to chemicals or air) [34]. Suitable microscopic tissue slides containing the epitopes of interest are fixed, usually by formalin, into a polymer or paraffin wax [74]. If the fixation process is known to mask the antigens of interest, an extra step is usually performed by physical (e.g., heat or ultrasound) or chemical (e.g., enzymatic digestion) methods to break any cross-links formed, making the antigens re-accessible to antibodies [75]. The next step is incubation with a blocking buffer such as bovine serum albumin to prevent non-specific binding. This is followed by adding primary antibodies specific to the antigen of interest, then washing to remove unbound antibodies. Fluorescence-labeled or enzyme-linked (e.g., peroxidase or alkaline phosphatase) secondary antibodies are then added [73]. Visualization of positive reactivity takes place by light or fluorescence microscopy, or after addition of substrate and monitoring of the color change due to the enzymatic reaction. This immunological assay allows for the localization of target antigens in tissues, which is not possible with ELISA and Western blot techniques [74].

3. Organic Compounds Found in Dinosaurs

The following sections will describe the evidence and chemistry of organic compounds found to date in non-avian dinosaurs. An overview of the localities and age of the dinosaurs is depicted in Figure 1.
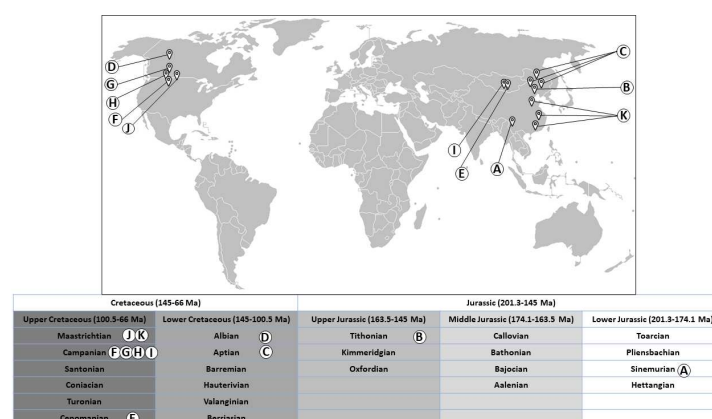
Figure 1. World map showing localities and age of dinosaurs in which organic compounds have been detected to date: (**A**) Dawa, Lufeng County, Yunnan Province, China [3]. (**B**) Yaolugao locality in Jianching County, western Liaoning Province, China [25]. (**C**) Dawangzhangzhi, Lingyuan City, Liaoning Province, China) and Sihetun, Beipiao City, Liaoning Province, China), and Yixian Formation, China [17,28]. (**D**) Suncor Millenium Mine, Fort McMurray, Alberta, Canada [27]. (**E**) Ukhaa Tolgod in southwestern Mongolia [24]. (**F**) Judith River Formation, eastern Montana, USA [29,30]. (**G**) Dinosaur Park Formation, Alberta, Canada [26]. (**H**) Two Medicine Formation, northern Montana, USA [31]. (**I**) Djadokhta Formation, Mongolia [23]. (**J**) Hell Creek Formation, eastern Montana, USA [18–20] (**K**) Chinese provinces (Henan, Jiangxi, and Guangdong) [21,22]. Concept adapted from reference [76]. The world map "BlankMap-World-IOC" by Chanheigeorge (https://commons.wikimedia.org/wiki/File:BlankMap-World-IOC.PNG, accessed on 19 March 2022) from 2008 has been used as a template onto which location markers, lines and letters were added. It is licensed under CC-BY-SA 3.0 (https://creativecommons.org/licenses/by-sa/3.0/legalcode, accessed on 19 March 2022) via Wikimedia Commons.
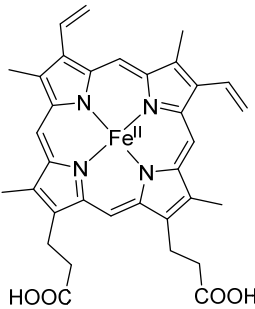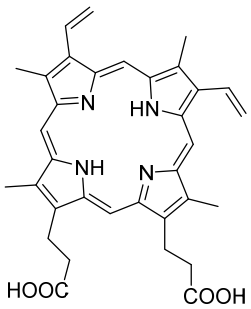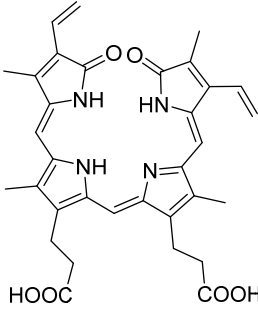
3.1. Pigments

Pigments are molecules that absorb light of wavelengths in the visible range (ca. 380–750 nm) and, accordingly, are responsible for the colors seen in many organisms and some minerals. Examples of naturally occurring pigments or biochromes are porphyrins, melanins and carotenoids [77]. Recent research has focused on investigating the preservation of pigments that are responsible for colors seen in fossils. Based on molecular analyses, scientists have been able to reconstruct the original color of some dinosaurs, also referred to as paleocolor reconstructions [78,79]. The pigments believed to have been preserved in dinosaur fossils include porphyrins (heme and protoporphyrin IX), their open-chain tetrapyrrole derivatives (biliverdin) and the biopolymer melanin (eumelanin and pheomelanin).

3.1.1. Porphyrins

Porphyrins are a family of organic compounds containing four pyrrole rings connected by methine bridges. Examples are heme (**1**), the iron-complexing main prosthetic group of hemoglobin, and protoporphyrin IX (**2**), the metal-free precursor of heme (see Table 1 for structures). Metabolic degradation products include linear tetrapyrrole derivatives, e.g., biliverdin (**3**) (see Table 1). Porphyrins and their derivatives are relatively stable, even for hundreds of millions of years; they have been recovered from sediments and crude oil extracts, the oldest record being from 1.1-billion-year-old sediments [80]. Porphyrins have also been detected in fossil tissues from dinosaurs [eggshells [22] and trabecular bone [18]] and the abdomen of a female mosquito [53]. The chemistry of porphyrins in fossils has been recently reviewed [81]; the porphyrins detected in fossils derived from dinosaurs are compiled in Table 1.

Table 1. Porphyrins detected in dinosaurs.

Organic Compound	Heme	Protoporphyrin IX	Biliverdin
Structure and exact mass	 **Heme** **(1)** Exact Mass: 616.18	 **Protoporphyrin IX** **(2)** Exact Mass: 562.26	 **Biliverdin** **(3)** Exact Mass: 582.25
Analytical technique	HPLC-UV UV/Vis spectroscopy Raman spectroscopy	LC-ESI-q/TOF-MS Raman spectroscopy	LC-ESI-q/TOF-MS Raman spectroscopy
Dinosaur species and age	*Tyrannosaurus rex* (67 Ma)	*Heyuannia huangi* (66 Ma)	*Heyuannia huangi* (66 Ma)
Location of fossil	Hell Creek formation, eastern Montana, USA	Chinese provinces (Henan, Jiangxi, and Guangdong)	Chinese provinces (Henan, Jiangxi, and Guangdong)
Type of tissue	Extracts of trabecular bone tissues	Extract of eggshells	Extract of eggshells
Reference	[18]	[21,22]	[21,22]

Heme was identified in trabecular bone extracts of *Tyrannosaurus rex* in 1997 [18]. The distinct chemical feature which made it possible to confirm the identity of heme was its

145

chromophore in the ultraviolet/visible light range [18]. The porphyrin ring has a very characteristic band in the ultraviolet range of around 410 nm, known as the *Soret* band, which could be detected using ultraviolet/visible light (UV/Vis) spectroscopy. This band was observed in bone extracts but not in controls, indicating that the signals were derived solely from the bone and not from contaminating factors in the surrounding sandstone sediment or extraction buffers. In addition, four of the six characteristic Raman peaks for hemoglobin (marker bands I, II, IV, and V) were detected with high intensity in the extracts. The six marker bands are found in the following spectral regions: band I (1340–1390 cm^{-1}), band II (1470–1505 cm^{-1}), band III (1535–1575 cm^{-1}), band IV (1550–1590 cm^{-1}), band V (1605–1645 cm^{-1}), and band VI (1560–1600 cm^{-1}) [82]. Resonance Raman spectroscopy analyses on extracts also showed that iron was present in the oxidized ferric state, which indicates a diagenetic alteration of heme (Fe^{2+} complex) to the oxidized hemin form. In addition, proton NMR spectra on the fossil extract were similar to those from degraded hemoproteins containing ferric iron [18].

A further case of heme in the fossil record, although not in dinosaurs, was reported 16 years later, when traces of heme were found in the abdomen of a female fossil mosquito (46 Ma), analyzed in situ by TOF-SIMS [53].

Only recently, the metal-free porphyrin, protoporphyrin IX (**2**), and the linear tetrapyrrole derivative biliverdin (**3**) were detected in extracts of eggshells from the oviraptorid dinosaur *Heyuannia huangi* by liquid-chromatography electrospray ionization-quadrupole-time-of-flight mass spectrometry (LC-q/TOF-MS) [22]. The exact masses were detected with high resolution in the mass spectra as protonated molecular ions, [M + H]$^+$, from three fossil eggshell samples. For confirmation, extant emu eggshell extracts and commercial standards of the two compounds were also analyzed. These peaks were not detected either in the sediment samples or in control samples, indicating that the peaks truly belonged to the analyzed fossil. Protoporphyrin IX (**2**) is more hydrophobic than biliverdin (**3**) and therefore more likely to be preserved due to its resistance to hydrolytic attack. In addition, the ring system of protoporphyrin is more stable than the open chain structure of biliverdin. Based on these results, a reconstruction of eggshell color as blue-green was performed [22]. A year later, protoporphyrin IX and biliverdin were reported using Raman spectroscopy in various fossilized eggshells, including *Heyuannia huangi* [21]. This study has been criticized by experts in Raman spectroscopy because the authors had based their observations only on a single analytical technique; Alleon et al. even argued that the observed signals were due to instrumental artefacts caused by background luminescence, and not due to Raman scattering [83,84].

There appears to be still much potential for future discoveries of porphyrins and their metabolites and degradation products in dinosaurs and other fossils.

3.1.2. Melanins

Melanins are a group of dark-colored biopolymeric structures. Different types of melanin are known: eumelanin (**4**), pheomelanin (**5**), allomelanin, pyomelanin and neuromelanin (see Figure 2). Eumelanin, pheomelanin, and allomelanin are most relevant when studying fossils. Eumelanin (**4**) and pheomelanin (**5**) are nitrogen-containing melanins found in animals. Allomelanin is a nitrogen-free melanin (see Figure 3) which is found in plants, fungi and bacteria; it is relevant when studying fossils because detection of its chemical signals can imply external microbial contamination [25].
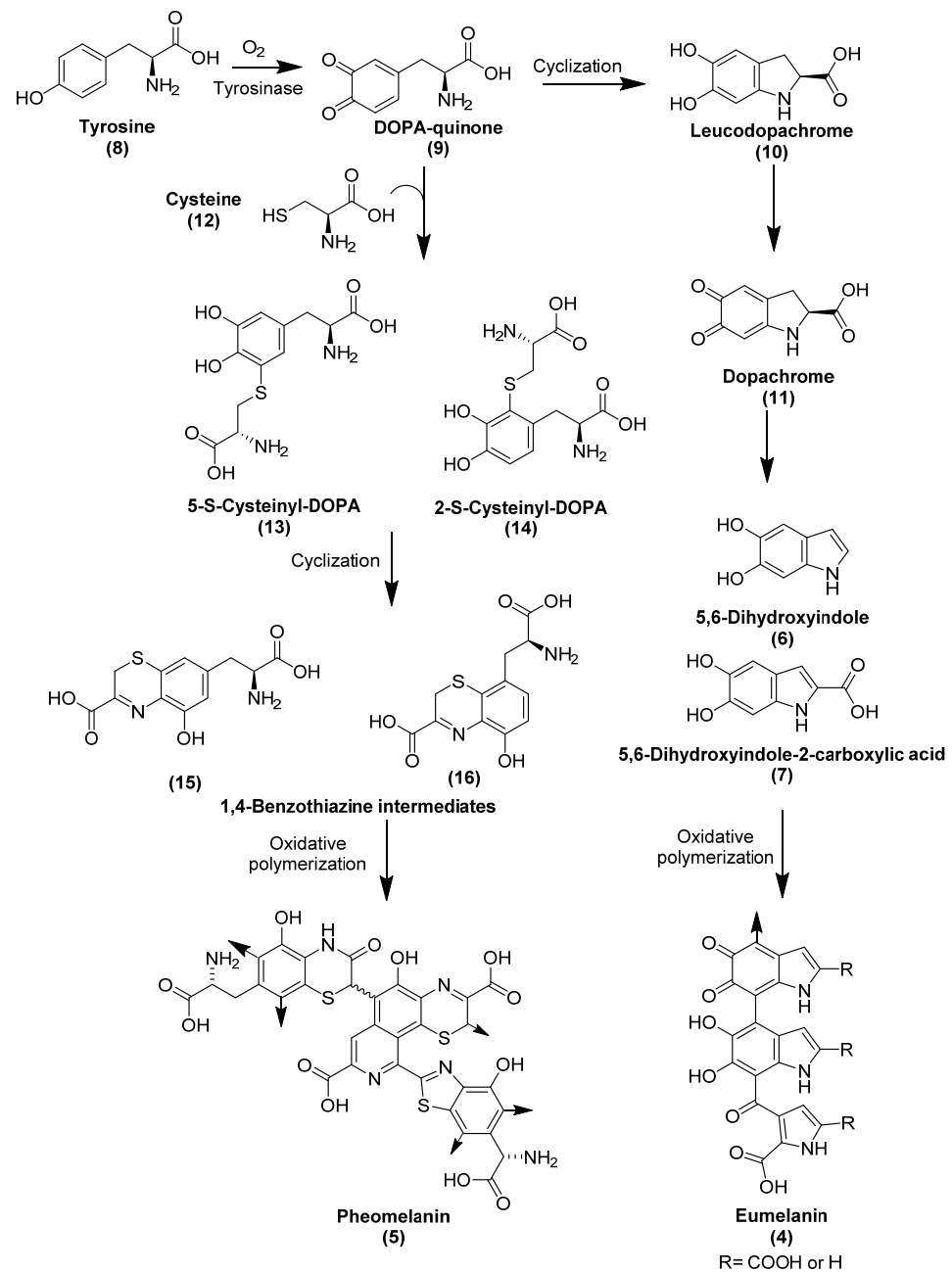
Figure 2. Structures and biosynthesis of eumelanin and pheomelanin. Arrows on structures (**4**) and (**5**) show points of polymer expansion [85,86].

1,8-Dihydroxy-naphthalene (17)

1,4,6,7,9,12-Hexahydroxyperylene-3,10-quinone (18)
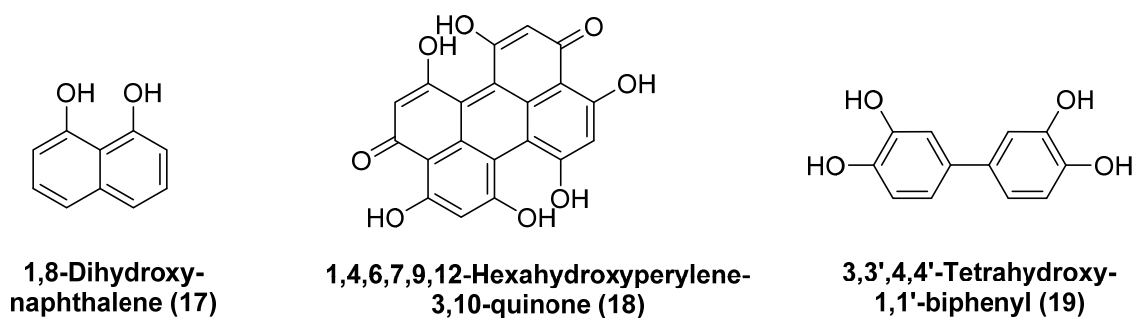
3,3',4,4'-Tetrahydroxy-1,1'-biphenyl (19)

Figure 3. Structures of precursors involved in different types of allomelanin.

The biosynthesis of eumelanin and pheomelanin takes place in melanocytes in the dermis. Figure 2 shows the biosynthesis of eumelanin and pheomelanin, including their intermediates. The synthesized melanins are transported into the keratinocytes, found in the epidermis, in special lysosome-like vesicles known as eumelanosomes and pheomelanosomes [85,87]. Both types of melanosomes are then incorporated into the outer layer of the skin, determining the color of skin, hair, and eyes. Melanins are responsible for absorbing UV light and for scavenging free radicals that can be formed upon exposure to UV light, in order to protect the inner layers of the skin from harmful radiation and radical reactions [86,88].

Eumelanin is brown to black in color and contains repeating units of 5,6-dihydroxyindole (**6**) and 5,6-dihydroxyindole-2-carboxylic acid (**7**). In its biosynthesis, it is derived from the amino acid tyrosine (**8**), which, upon action of tyrosinase, or by oxidation, is converted to DOPA-quinone (**9**), which is then cyclized and decarboxylated to form 5,6-dihydroxyindole (**6**) through the intermediate compounds leucodopachrome (**10**) and dopachrome (**11**) [25,85,86] (for structures see Figure 2). Some indole units may randomly undergo partial oxidative cleavage via formation of an ortho-benzoquinone leading to pyrrole-di-carboxylic acid derivatives, which are incorporated into the polymeric structure of eumelanin [89,90]. Pheomelanin is a reddish-yellow sulfur-containing melanin which contains units of 1,4-benzothiazine and 1,3-benzothiazole [91]. Similar to eumelanin, pheomelanin is derived from tyrosine (**8**), and additionally from cysteine (**12**), that is fused with DOPA-quinone (**9**) to form cysteinyl-DOPA derivatives **13** and **14**, which undergo several oxidation steps to form 1,4-benzothiazine intermediates **15** and **16** [85] (see Figure 2).

Allomelanin has not been studied as much as eumelanin and pheomelanin. However, it is established that several subtypes of allomelanin can be distinguished according to the precursors from which they are derived. The precursors comprise 1,8-dihydroxynapthalene (**17**), 1,4,6,7,9,12-hexahydroxyperylene-3,10-quinone (**18**) and biphenolic dimers such as 3,3′,4,4′-tetrahydroxy-1,1′-biphenyl (**19**), biosynthesized from acetyl-CoA, malonyl-CoA, and catechol, respectively (see Figure 3). Accordingly, three types of allomelanin are distinguished:1,8-dihydroxynapthalene melanin, 1,4,6,7,9,12-hexahydroxyperylene-3,10-quinonemelanin, and catechol-melanin [92].

There is emerging morphological and chemical evidence for eumelanin and pheomelanin detected in a variety of fossils with or without association with melanosomes. Examples are fossilized marine reptiles such as a Paleogene turtle (55 Ma), Cretaceous mosasaur (86 Ma), and Jurassic ichthyosaur (ca. 196–190 Ma) [93]. The compounds were also found in several species of fish (359–366 Ma), amphibians (Ypresian/Lutetian, Eocene, Aquitanian, Miocene, Chattian, Oligocene), birds (56–34 Ma), and mammals (56-34 Ma) [94]. Furthermore, they were detected in dinosaurs (150–112 Ma) [25,27]. A summary of findings on melanins and/or melanosomes in the dinosaur fossil record is compiled in Table 2, along with the analytical methods used.

Imaging studies using SEM in combination with EDS have been used to detect melanin based on the presence and shape of melanosomes in preserved integumentary structures of the theropods *Sinosauropteryx* and *Sinornithosaurus* [17], as well as *Psittacosaurus* [28]. More recently, analytical techniques such as TOF-SIMS and Py-GC-MS have been utilized to confirm the chemical fingerprint of melanin in the early avialan *Anchiornis huxleyi* [25] and the ankylosaur *Borealopelta markmitchelli* [27]. Due to the resemblance between melanosomes of dinosaurs and keratinophilic bacteria on the microscopic level [17,95], a chemical analysis is necessary in order to confirm the presence of melanin [25].

TOF-SIMS analyses of a feather fossil derived from *Anchiornis huxleyi* (150 Ma) showed negative ion spectra characteristic for melanins in the areas where microscopic melanosome-like structures were observed [25]. Compared to spectra of synthetic and natural variants of eumelanin and pheomelanin, many high-intensity mass signals were in common, indicating the presence of eumelanin of animal origin. Absorption bands suggesting the presence of eumelanin as well were detected using infrared spectroscopy. Bacterial contamination was excluded in the examined areas due to the absence of peaks corresponding to

peptidoglycans and hopanoids [25]. Peptidoglycans, polymers consisting of sugars and peptides, are cell wall components of Gram-positive and Gram-negative bacteria [96], while hopanoids are cyclic lipophilic triterpenoids that are located in the bacterial cell membrane and have been detected in the fossil record of bacteria [97,98]. The TOF-SIMS spectra of bacteria-derived melanin, namely allomelanin, which does not contain nitrogen (see Figure 3), does not show any of the nitrogen-derived peaks that were found in the fossil (mass-to-charge ratios of 50, 66, 74, 98, 122, and 146). Analysis of the surrounding sediment using the same method showed negative ion spectra corresponding to silicate-rich minerals, but no nitrogen-containing peaks were observed. Signals for sulfur-containing compounds that could originate from pheomelanin were not intense enough to confirm its presence in the fossil [25].

Table 2. Melanin detected in dinosaurs.

	Eumelanosomes and Pheomelanosomes	Eumelanin-like Pigmentation (Black and Yellow)	Eumelanin	Mixture of Pheomelanin and Eumelanin
Analytical technique	SEM imaging combined with EDS	Imaging with digital camera	TOF-SIMS EDS IR micro-spectroscopy	TOF-SIMS Py-GC-MS EDS
Dinosaur, location and age of fossil	*Sinosauropteryx* (125 Ma, Dawangzhangzhi, Lingyuan City, Liaoning Province, China) *Sinornithosaurus* (125 Ma, Sihetun, Beipiao City, Liaoning Province, China)	*Psittacosaurus* (125 Ma) Yixian formation in China	*Anchiornis huxleyi* (150 Ma) Yaolugao locality in Jianching County, western Liaoning, China	*Borealopelta markmitchelli* (112 Ma) Suncor Millenium Mine, Fort McMurray, Alberta, Canada
Type of tissue	Integumentary filaments from the tail	Preserved epidermal scales scattered from head to tail	Filamentous epidermal appendages ("feathers")	Integumentary structures (epidermis and keratinized scales)
Reference	[17]	[28]	[25]	[27]

The preserved integumentary structures of the ankylosaur *Borealopelta markmitchelli* (112 Ma) were analyzed by TOF-SIMS and pyrolysis-GC-MS to investigate the presence of melanin [27]. TOF-SIMS analysis showed negative ions similar to those of melanin in previously reported fossils [93], resembling natural and synthetic melanin. In addition, ions containing sulfur (1,3-benzothiazole) indicative of pheomelanin [93] were detected, suggesting that a mixture of eumelanin and pheomelanin was present [27]. Pyrolysis-GC-MS analysis showed signals corresponding to eumelanin (N- and O-heterocyclic and aromatic compounds), as reported previously in fossils [99,100]. Signals derived from pheomelanin (1,3-benzothiazole) were also present, which were not detected in the surrounding sediment [27].

3.2. Proteins

Although met with controversy, especially when considering chemical instability, there are more and more reports on proteins and their fragments detected in fossils. In the early years, this was backed mainly by morphological examination and the application of vibrational spectroscopy and immunological techniques. In recent years, the field of paleoproteomics has flourished, applying high-resolution mass spectrometry to determine peptide sequences and to map them on the extant versions of the proteins of interest [33,34,101]. Further paleoproteomic research, especially sequencing of proteins by mass spectrometry, would be required to confirm the endogeneity of the detected protein fragments [34]. It has to be kept in mind that cross-contamination remains an important issue when analyzing peptide sequences [102]. Not only can cross-contamination arise from laboratory reagents and controls, it can also occur due to previously analyzed samples. Thus, it is necessary to rule out cross-contamination by suitable measures, such as careful and self-critical approaches, and appropriate controls [102].

Vibrational methods such as infrared spectroscopy have been used to detect proteins, showing characteristic absorption bands of the amide bonds; however, these signals are non-specific and it is not possible to identify the type of protein or its sequence [34]. Early trials to detect proteins utilized amino acid analysis after degradation of the proteins. This method is also insufficient for determining the original peptide sequence [33]. TOF-SIMS employs a harsh ionization method which causes extensive fragmentation of proteins. Therefore, while it cannot be used for sequencing, it is useful for obtaining a chemical map, revealing the regions where amino acid fragments are found in a fossil, which may then be further analyzed [32,34,76].

Immunological techniques including immunohistochemistry, Western blotting, and ELISA rely on positive antigen–antibody reactions, detecting specific epitopes of a protein or nucleic acid. Specificity depends on the employed antibodies, but protein or nucleic acid sequences cannot be determined. These methods can be useful to locate the regions that may contain preserved proteins (or nucleic acids) suitable for subsequent mass spectrometric analysis. In addition, liquid chromatography coupled to electrospray ionization high-resolution mass spectrometry is used for the identification of proteins. The techniques used in paleoproteomics and their limitations were recently reviewed [33,34]. Most of the proteins detected in dinosaur fossils belonged to the most abundant ones including collagen type I (found in bones), collagen type II (found in cartilage), and beta-keratin (found in scales, turtle shell, claws of reptiles, and in avian feathers) [103]. The following section will discuss the evidence for proteins detected to date in dinosaurs and their chemistry.

3.2.1. Collagens

Collagens constitute a family of glycoproteins that are the main components of the extracellular matrix of different tissues. In animals, 29 different types of collagen have been found, but only 3 types (collagen I, II and III) constitute around 80–90% of the total collagen. Collagens are structural proteins in the extracellular matrix which confer mechanical strength especially to connective tissues. They directly interact with other components of the extracellular matrix, such as proteoglycans, fibronectin and laminin. Proteoglycans are glycoproteins that form a gel-like network in the extracellular matrix. Collagens and other fibrous proteins (fibronectin and laminin) are located within this network. Fibronectin and laminin are non-collagenous glycoproteins that form fibrous networks and affect the shape of the extracellular matrix. They possess binding sites important for cell adhesion [104]. In addition, collagens interact with secreted soluble factors such as the von Willebrand factor and interleukin-2, and with cell surface receptors such as integrins [105]. These interactions aim to regulate tissue development and mechanical responses to cell signaling such as cell adhesion, migration and chemotaxis [106,107]. The primary polypeptide structure of collagen is known as the α-chain. All types of collagens share the repeating amino acid sequence [Gly-X-Y], where X and Y are usually proline and hydroxyproline, respectively (see Figure 4). In 12% of collagen sequences, both proline and hydroxyproline are present in their respective positions, while in 44% of the sequences, only one of them is present [108]. The secondary structure of collagen is formed from three α-chains arranged in parallel. They are twisted together to form the tertiary structure, a rope-like triple helix with a molecular weight of ca. 300 kDa, a length of 280 nm and a diameter of 1.4 nm. The abundance of the cyclic amino acids, proline and hydroxyproline, sterically hinders rotation around the peptide bonds in the α-chains which contributes to the stability and rigidity of the triple helix. In addition, two types of hydrogen bonds stabilize the triple helix. The first type of intermolecular hydrogen bonds are formed between the NH of glycine and the carbonyl group of proline residues in neighboring α-chains. The second type are intramolecular hydrogen bonds, formed between the carbonyl or hydroxyl groups of hydroxyproline and the carbonyl group of glycine or hydroxyproline residues in the same α-chain, mediated by a water molecule [108]. Moreover, the X and Y positions in further collagen sequences are occupied by other amino acids, but never contain tryptophan, tyrosine, or cysteine, as these would destabilize the triple helix [109]. Post-translational

modifications such as hydroxylation of proline and lysine residues or glycosylation (with galactose or a disaccharide of glucose and galactose) also contribute to stability and are typical of collagen. The more hydroxyproline residues there are, the more thermally stable the triple helix is. Post-translational hydroxylation of proline residues is often used in identification of collagen from fossils, especially since this cannot be performed by bacteria [108]. Hydroxylysine is the point of attachment of the sugars via an O-glycosidic linkage, and this stabilizes the collagen fibrils mechanically by formation of covalent crosslinks [108].

Figure 4. (**A**) The most common repeating sequence present in collagen types I and II. Positions X and Y can be occupied by any amino acid except tryptophan, tyrosine or cysteine. The most common amino acids in positions X and Y are proline and hydroxyproline, respectively. (**B**) Schematic representation of the triple helical structure of collagens type I and II. In collagen type I, there are two α1 chains and one α2 chain, whereas in collagen type II, there are three α1 chains. (**C**) Diagram of a collagen molecule showing the post-translational modifications that occur, which are hydroxylation of lysine residues and glycosylation of hydroxylysine by galactose and glucose. (**D**) The stacked arrangement of collagen fibers, visible under a transmission electron microscope, shows a characteristic staggered pattern known as the D-band or D-period of approximately 67 nm in periodicity. This banding is a unique feature used for identification of collagen fibers under the microscope. Adapted from [110,111].

Collagen Type I

Collagen type I is the major component of bone organic phase, but is also present in skin, tendons, ligaments, lung, blood vessels, cornea, brain and spinal cord [108,112] (see Figure 4 for structures). Collagen I is composed of two α1(I) chains and one α2(I) chain and assembles into elongated fibrils of 500 µm in length and 500 nm in diameter. The fibrils have a characteristic tight arrangement. Every 64–67 nm, there also is a pattern repeating itself, known as *D*-banding. This pattern is visible in the electron microscope and can be utilized for identification of collagen type I [108,113–116]. Studies reporting evidence for collagen type I found in the dinosaur fossil record are compiled in Table 3.

Table 3. Collagen type I and II in the dinosaur fossil record.

Study	Collagen Type I	Analytical Technique(s)	Dinosaur Name, Location and Age	Type of Tissue	Reference
1	Amino acid fragments and peptide sequences (5 from α1 chain, 1 from α2 chain)	Immuno-histochemistry, ELISA, TOF-SIMS and LC-MS/MS	*Tyrannosaurus rex* (68 Ma) Hell Creek Formation, eastern Montana, USA	Trabecular bone	[19,20]
2	Infrared absorption bands	SR-FTIR and confocal Raman microscopy	*Lufengosaurus* (ca. 195 Ma) Dawa, Lufeng County, Yunnan Province, China	Rib bone (thin sections)	[3]
3	Amino acid fragments (alanine, arginine, glycine, and proline)	TOF-SIMS	Various Dinosauria (75 Ma) Dinosaur Park Formation, Alberta, Canada	Claw, ungual phalanx, astragalus, tibia, rib	[26]
4	Peptide sequences (6 for α1 chain, 2 for α2 chain)	Immuno-histochemistry, Western blot, ATR-IR, TOF-SIMS, and LC-MS/MS	*Brachylophosaurus canadensis* (80 Ma) Judith River Formation, eastern Montana, USA	Femur from hind limb (4 different samples)	[29]
5	Peptide sequences (6 for α1 chain, 2 for α2 chain)	Nano-LC-MS/MS and FT-ICR-MS	*Brachylophosaurus canadensis* (80 Ma) Judith River Formation, eastern Montana, USA	Femur from hind limb (4 different samples)	[30]
6	Collagen type II	Immunohisto-chemistry	*Hypacrosaurus stebingeri* (75 Ma) Two Medicine Formation, northern Montana, USA.	Calcified cartilage from supraoccipital	[31]

Attempts to detect collagen type I in dinosaurs were performed on samples of *Tyrannosaurus rex* [19] (see Table 3). Trabecular bone extracts showed positive reactivity in an ELISA employing avian collagen I antibodies. The signal was weaker in the dinosaur as compared to extant emu cortical and trabecular bone, but the signal detected in the fossil was larger than those in buffer controls and in the sediment. The same pattern was observed by in situ immunohistochemistry studies. Antibody binding decreased significantly when the fossil tissue was digested with collagenase I before exposure to the antibodies. TOF-SIMS analysis revealed amino acid residues in the fossil including glycine (highest relative signal intensity), alanine, proline, lysine, leucine and isoleucine [19]. A subsequent study [20] applied a softer mass spectrometric technique to avoid undesired fragmentation, liquid chromatography tandem mass spectrometry (LC-MS/MS). In this study, the dinosaur fossil was compared to similarly treated ostrich and mastodon samples. The mass spectra obtained from *T. rex* bone extracts detected seven collagen peptide sequences, five from the α1(I) chain, one from the α2(I) chain, and one belonging to the α1(II) chain of type II collagen, that were aligned with database sequences from extant vertebrates. Post-translational modifications, especially hydroxylation of proline, lysine

and glycine, were detected in the dinosaur fossil as well as in the mastodon and ostrich samples, while no collagen sequences were detected in control samples of the surrounding sediment and the extraction buffers. The sediment contained peptides of bacterial origin, but no collagen [20].

In another study, investigation of the hadrosaurid dinosaur *Brachylophosaurus canadensis* provided evidence for collagen type I [29]. This was confirmed by studies in different laboratories and at different times using different methodology including sample preparation technique, mass spectrometry instrument, and data analysis software [29,30]. Microscopic observation (by field-emission SEM) of fibrous structures in demineralized femur bones was followed up by immunoblot assays. A positive reactivity to antibodies raised against avian collagen type I was observed in whole fossil bone extracts and in intact demineralized fossil bones [29]. In situ immunohistochemistry studies performed on demineralized fossil bones confirmed the results. The extraction buffers and the surrounding sediments showed no reactivity. Antibody binding decreased significantly when the samples were digested with collagenase before exposure to the antibodies, or when exposed to antibodies that had been pre-incubated with excess collagen. Gel electrophoresis studies on samples of the surrounding sediment did not show any visible protein bands. Infrared spectroscopy showed absorption bands of amide bonds (Amide I and Amide II). Analysis using TOF-SIMS indicated fragments of lysine, proline, alanine, glycine, and leucine residues in intact blood vessels and in matrix of demineralized bone. Further experiments using reversed-phase microcapillary liquid chromatography tandem mass spectrometry (linear ion-trap alone or hybridized with Orbitrap mass spectrometry) recovered eight collagen type I sequences, containing a total of 149 amino acids. Six of these sequences were attributed to the α1 chain and two to the α2 chain [29].

High-resolution measurements performed eight years later by LC-tandem mass spectrometry coupled to Fourier-transform ion cyclotron resonance mass spectrometry (FT-ICR-MS) again showed eight collagen type I sequences in the range of 250 kDa, two of which had previously been detected for the α1 chain, in addition to three new α1 chain sequences, and three new sequences for the α2 chain [30]. In both studies, no collagen sequences could be detected in spectra of extraction buffer or samples of the surrounding sediment. In addition, post-translational modification of hydroxylated proline was observed, which is important for the triple helix structure of collagen I and cannot be produced by microbes [29,30].

Amino acid fragments in association with direct observations of fibrous structures showing the 67 nm banding of typical collagen were detected using TOF-SIMS by Bertazzo et al. (2015) in a variety of dinosaur bone samples from the Late Cretaceous Dinosaur Park Formation of Alberta, Canada [26]. The banding indicated that the quaternary structure of collagen may have been preserved. In addition, TOF-SIMS analyses were performed to search for amino acids using thick sections of the fossil bone sample, as well as modern rabbit bone, non-calcified fossil samples, surrounding sediment, and the sample holder made of copper as controls. The fossil dinosaur bone samples and the rabbit bone contained similar amino acid peaks which were neither present in the non-calcified fossil samples nor in the surrounding sediment or in the sample holder. Fragments belonging to glycine, arginine, alanine, and proline were detected only in the permineralized fossil samples [26].

Synchrotron-radiation Fourier transformed infrared spectroscopy (SR-FTIR) and confocal Raman spectroscopy were used to identify characteristic vibrations of chemical bonds at specific absorption bands for each functional group, producing high resolution images and spectra [34]. Infrared absorption bands characteristic for collagen type I were detected in thin sections of the rib bone of a 195-million-year-old *Lufengosaurus*, and early-branching sauropodomorph, and the geologically oldest dinosaur sample analyzed to date. The detection was especially in the regions where vascular canals could microscopically be observed. The infrared absorption bands of the fossil samples were very similar to the reference samples of extant collagen I extracted from calf skin [3].

The published evidence for collagen type I and other proteins and their sequences in dinosaurs should still be treated with caution. For example, TOF-SIMS is not suitable for

sequencing but can only help to locate samples for subsequent tandem-mass spectrometry experiments. A combination of different analytical techniques is usually needed, combined with the proper controls. Tandem mass spectrometry is the main technique to prove the presence of peptides and to sequence polypeptides/proteins.

Collagen Type II

Collagen type II is a structural protein mostly present in cartilage, tendons, and in the intervertebral disc [108]. In contrast to collagen type I, it is a homotrimer, composed of 3 α1(II) chains [113]. Similar to collagen type I, it also forms a triple helix of around 1000 amino acids in length and has the repeating amino acid pattern of Gly-X-Y [117], forming an aggregated fibrous structure.

The first report on collagen II associated with preserved calcified cartilage in dinosaurs [31] was from *Hypacrosaurus stebingeri*, a 75-million-year-old hadrosaur nestling discovered in the Two Medicine Formation of northern Montana, USA. Techniques used to chemically characterize the observed chondrocyte-like microstructures were histochemical and immunological techniques, as shown in Table 3. Thin sections of demineralized fossil cartilage exposed to antibodies raised against avian collagen type II showed positive reactivity after visualization by green fluorescence. The observed pattern was interrupted and less intense compared to the homogenous distribution of the binding pattern in extant cartilage from emu (*Dromaius novaehollandiae*), suggesting that either the epitopes are few or that the epitopes recognized by avian collagen I antibodies are not similar to those present in the dinosaur. Collagen II is not produced by bacteria; thus, contamination is less likely to have occurred [31].

Specificity of the antibodies was checked by prior digestion of the thin sections by collagenase II and exposure to the antibodies, after which the binding decreased significantly in both fossil and recent material under the same conditions. This supports the interpretation that collagen II is likely present in the fossil. Antibodies against avian collagen I did not show any binding in both fossil and recent cartilage, which is not expected to be found there [31].

3.2.2. Keratins

Keratins are structural proteins which are the major constituents of hair, nails, feathers, horns, and hooves [118]. They are characterized by a high cysteine content (7–13%). Keratins have several biological functions, including (i) mechanical effects and (ii) altering cellular metabolism. By disassembly and reassembly, keratins provide flexibility to the cytoskeletal structure, making cells and tissues withstand mechanical stress and maintain their shape. Keratins affect the response to cellular signaling by binding to various signaling proteins such as protein kinases and phosphatases. Thus, keratins are involved in the regulation of cell growth, cell differentiation, mitosis, and protein synthesis, which may lead to a change in cellular metabolism [119–121].

Keratins have a molecular weight of 40–70 kDa [119,122]. The amino acids in the primary sequence of keratins are often cysteine, glycine, proline, and serine, and to a lesser extent lysine, histidine, and methionine. Tryptophan is rarely present [118,123]. The secondary structure of keratins is either an α-helix or a β-sheet, depending on the type of amino acids present. Accordingly, two types of keratins can be distinguished: α-keratin and β-keratin [119] (see Figure 5).

Isoleucine   Glycine   Glutamic acid   Histidine

Cysteine   Phenylalanine   Methionine

α-keratin   α-helix

β-keratin   β-sheet

Dimer   ~2 nm   ~2 nm

Intermediate filament   ~7 nm   ~3 – 4 nm
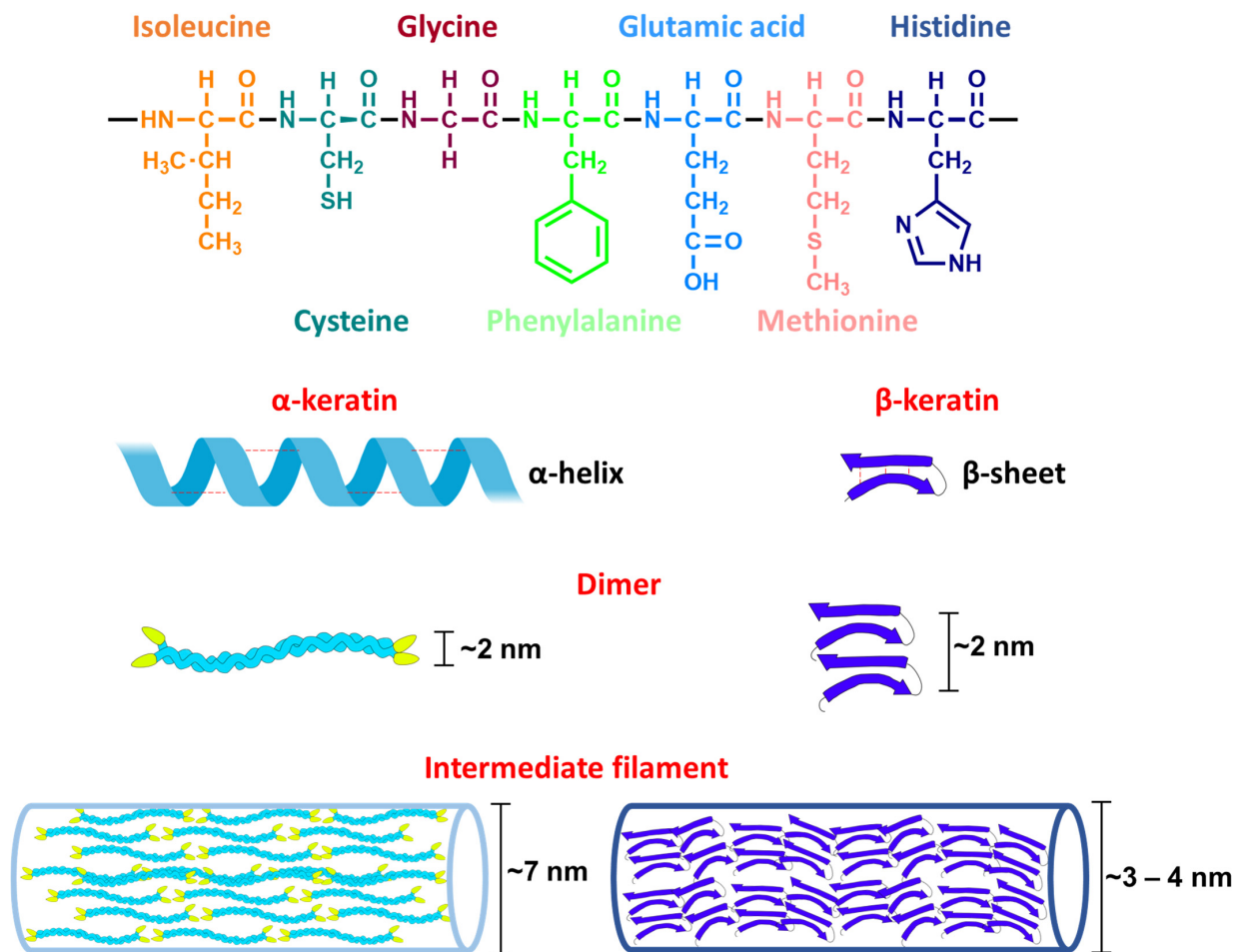
Figure 5. Diagram of the four different levels of keratin structure. The primary sequence of keratin is shown, including the most common amino acids present (the amino acids are L-configurated, but the stereochemistry is not shown). The secondary structure of keratins can be either an α-helix or a β-sheet, classifying them into α-keratins and β-keratins, respectively. The tertiary structures of both keratin types are heterodimers. The quaternary structure is composed of intermediate filaments, that are 7 nm in diameter for α-keratin and 3–4 nm in diameter in β-keratin. Adapted from [124].

The tertiary structure of keratins is composed of a dimer that forms the building block of keratin filaments. It is stabilized by inter- and intra-molecular interactions such as disulfide bridges, hydrogen bonds, hydrophobic interactions, and ionic bonds [118]. Their quaternary structure consists of self-assembling intermediate filaments having a characteristic electron-lucent region of 7–8 nm in diameter observed under the electron microscope. The formation of keratin filaments is affected by pH and osmolarity [119].

Post-translational modifications occur to the secondary structure of keratins, which in turn affect their overall structure, physicochemical properties and functions. Phosphorylation or formation of intra- and interchain covalent bonds (e.g., disulfide bonds) can directly modify the structure. Changes in pH, the types of ions present, and osmolarity can alter the physicochemical properties indirectly, for example, by changing the isoelectric point. Keratins can modify their filaments due to mechanical stress such as tension, compression, and shearing [119].

Keratins are insoluble in water, alkali, weak acids, and organic solvents. They are stable in the presence of proteases such as pepsin and trypsin. The crosslinking via disulfide bonds stabilizes the overall tertiary structure and lowers the water solubility [118,123].

α-Keratin is expressed in all vertebrates [23]. Its structure is better described than that of β-keratin [119]. α-Keratins are classified into two types according to their isoelectric

point (pI) range: type I (pI = 4.9–5.4) and type II (pI = 6.5–8.5). α-Keratins with more acidic amino acids are of type I, while those containing more basic amino acids belong to type II [119] (see Figure 5).

β-Keratins are exclusively expressed in reptiles and birds (e.g., claw sheaths and feathers), and differ from the α-keratins in their lower solubility and the high rigidity of their microfibril filaments [24]. β-keratin has a core of 30 amino acids and forms antiparallel β-sheets, joined by regions of β-turns and stabilized by hydrogen bonds. The quaternary structure of β-keratin is characterized by microfibril filaments of 3 nm in diameter [125]. The presence of hydrophobic amino acids in the core, such as valine and proline [125], increases their preservation potential because they will not be readily hydrolyzed [23]. β-Keratins are not expressed in humans or microorganisms; thus, if β-keratins are detected in fossils, exogenous contamination can likely be ruled out [23]. β-Keratin has been detected in fossil dinosaurs mainly by immunohistochemistry techniques as shown in Table 4.

Table 4. Evidence of beta-keratin in the dinosaur fossil record.

	β-Keratin and Its Amino Acid Fragments	β-Keratin Epitopes
Analytical technique(s)	TOF-SIMS Immunohistochemistry	Immunohistochemistry
Dinosaur species Location and age of fossil	*Shuvuuia deserti* (100 Ma) Ukhaa Tolgod in southwestern Mongolia	*Citipati osmolskae* (75 Ma) Djadokhta Formation of Mongolia
Type of tissue	Feather-like epidermal appendages	Original keratinous-like claw sheath
Reference	[24]	[23]

There are some amino acids which are common in the sequence of both types of keratins, such as glycine, serine, valine, leucine, glutamate, cysteine, and alanine [119,126]. Amino acids which are more abundant in α-keratin are methionine, histidine, phenylalanine, and isoleucine [127]. Amino acids that are more abundant in α-keratin are proline and aspartate [119], whereas histidine, methionine, tryptophan, and tyrosine are rarely present [126].

The first characterization of β-keratin in fossil dinosaurs was from feather-like structures of the 100-million-year-old *Shuvuuia deserti* collected at Ukhaa Tolgod in southwestern Mongolia (see Table 4) [24]. Immunohistochemical studies using antibodies raised against avian α- and β-keratins showed a strong reactivity in both fossil and extant (duck feather) tissue samples for β-keratin, and less reactivity for α-keratin. No reactivity was seen in control samples, including incubation with antibodies not specific to β-keratin. Reduced binding was observed when the antibodies against β-keratin were incubated with excess β-keratin before exposure to the tissues, thus confirming the specificity of this approach. Furthermore, TOF-SIMS analysis was performed on isolated fiber structures to search for amino acids to support the immunological findings. Several amino acid fragments, containing glycine, serine, leucine, cysteine, proline, valine and alanine, were detected in the mass spectra. The targeted sampling location supports that these amino acids could belong to the fossil, but sequencing by higher resolution methods would be needed for confirmation [24].

Antibodies raised against β-keratin have shown positive binding to demineralized thin sections of claw sheaths from the 75-million-year-old oviraptorid dinosaur, *Citipati osmolskae*, from the Djadokhta Formation of Mongolia, which showed keratinous-like microstructures [23]. Reference samples of extant emu and ostrich claw sheath were additionally studied. An in situ immunohistochemical approach combined with immunofluorescence and electron microscopy was employed that reaffirmed the previous claims that β-keratin can be preserved over millions of years. However, the available sample material from dinosaur fossils limits sequencing approaches. Yet, a targeted high-resolution mass spec-

trometric approach has been suggested for further studies based on sampling the regions which exhibited positive reactivity to β-keratin antibodies [23].

4. Conclusions

This review provides a collection of organic compounds identified in dinosaur bone and soft tissues to date, giving insights into their chemistry and the analytical techniques used for their identification. Reports on organic compounds are increasing as more targeted sensitive analytical approaches that use less and less sample material are being developed. Organic compounds detected from dinosaurs so far comprise pigments, such as porphyrins and melanins, and proteins, including collagen type I, collagen type II and β-keratin. The analytical techniques used have been a combination of imaging using microscopy, absorption, reflectance and vibrational spectroscopy. Chemical imaging on the sample surface using time-of-flight secondary ion mass spectrometry, and more invasive techniques, namely liquid chromatography coupled with tandem mass spectrometry were also employed. Yet, even as analytical techniques become more advanced and highly sensitive, it still remains challenging to prove the endogeneity of the detected structures, especially when searching for proteins or DNA. Further development of sample preparation techniques that minimizes contamination is required.

Abbreviations

ATR-IR	Attenuated-total reflection infrared spectroscopy
BN-PAGE	Blue native-polyacrylamide gel electrophoresis
EDS	Energy-dispersive X-ray spectrometry
ELISA	Enzyme linked immunosorbent assay
ESI-MS	Electrospray ionization mass spectrometry
FESEM	Field emission scanning electron microscopy
FT-ICR-MS	Fourier transform ion cyclotron resonance mass spectrometry
FTIR	Fourier transform infrared spectroscopy
IR	Infrared spectroscopy
LC-MS/MS	Liquid chromatography tandem mass spectrometry
NMR	Nuclear magnetic resonance
OM	Optical microscopy
Py-GC-MS	Pyrolysis gas-chromatography mass spectrometry
q/TOF-MS	Quadrupole time-of-flight mass spectrometry
SDS-PAGE	Sodium dodecyl sulfate-polyacrylamide gel electrophoresis
SEM	Scanning electron microscopy
SR-FTIR	Synchrotron-radiation Fourier transform infrared spectroscopy
TEM	Transmission electron microscopy
TOF-SIMS	Time-of-flight secondary-ion mass spectrometry
UV/VIS	Ultraviolet-visible light
VPSEM	Variable-pressure scanning electron microscopy

16. Appendix

References

1. Eglinton, G.; Logan, G.A. Molecular preservation. *Philos. Trans. R. Soc.* **1991**, *333*, 315–328. [CrossRef]
2. Schweitzer, M.H. Soft tissue preservation in terrestrial Mesozoic vertebrates. *Annu. Rev. Earth Planet. Sci.* **2011**, *39*, 187–216. [CrossRef]
3. Lee, Y.C.; Chiang, C.C.; Huang, P.Y.; Chung, C.Y.; Huang, T.D.; Wang, C.C.; Chen, C.I.; Chang, R.S.; Liao, C.H.; Reisz, R.R. Evidence of preserved collagen in an Early Jurassic sauropodomorph dinosaur revealed by synchrotron FTIR microspectroscopy. *Nat. Commun.* **2017**, *8*, 2–9. [CrossRef]
4. Ji, Q.; Luo, Z.-X.; Yuan, C.-X.; Wible, J.R.; Zhang, J.-P.; Georgi, J.A. The earliest known eutherian mammal. *Nature* **2002**, *416*, 816–822. [CrossRef]
5. Gioncada, A.; Collareta, A.; Gariboldi, K.; Lambert, O.; Di Celma, C.; Bonaccorsi, E.; Urbina, M.; Bianucci, G. Inside baleen: Exceptional microstructure preservation in a late Miocene whale skeleton from Peru. *Geology* **2016**, *44*, 839–842. [CrossRef]
6. Cadena, E.-A. In situ SEM/EDS compositional characterization of osteocytes and blood vessels in fossil and extant turtles on untreated bone surfaces: Different preservational pathways microns away. *PeerJ* **2020**, *8*, e9833. [CrossRef]
7. Surmik, D.; Dulski, M.; Kremer, B.; Szade, J.; Pawlicki, R. Iron-mediated deep-time preservation of osteocytes in a Middle Triassic reptile bone. *Hist. Biol.* **2019**, *33*, 186–193. [CrossRef]
8. Schweitzer, M.H.; Zheng, W.; Cleland, T.P.; Goodwin, M.B.; Boatman, E.; Theil, E.; Marcus, M.A.; Fakra, S.C. A role for iron and oxygen chemistry in preserving soft tissues, cells and molecules from deep time. *Proc. R. Soc. B Biol. Sci.* **2014**, *281*, 20132741. [CrossRef]
9. Wiemann, J.; Fabbri, M.; Yang, T.R.; Stein, K.; Sander, P.M.; Norell, M.A.; Briggs, D.E.G. Fossilization transforms vertebrate hard tissue proteins into N-heterocyclic polymers. *Nat. Commun.* **2018**, *9*, 4741. [CrossRef]
10. Schweitzer, M.H.; Wittmeyer, J.L.; Horner, J.R. Soft tissue and cellular preservation in vertebrate skeletal elements from the Cretaceous to the present. *Proc. R. Soc. B Biol. Sci.* **2007**, *274*, 183–197. [CrossRef]
11. Briggs, D.E.G. Molecular taphonomy of animal and plant cuticles: Selective preservation and diagenesis. *Philos. Trans. R. Soc. Lond. Ser. B Biol. Sci.* **1999**, *354*, 7–17. [CrossRef]
12. Collins, M.J.; Nielsen-Marsh, C.M.; Hiller, J.; Smith, C.I.; Roberts, J.P.; Prigodich, R.V.; Wess, T.J.; Csapò, J.; Millard, A.R.; Turner-Walker, G. The survival of organic matter in bone: A review. *Archaeometry* **2002**, *44*, 383–394. [CrossRef]
13. Briggs, D.E.G.; Mcmahon, S. The role of experiments in investigating the taphonomy of exceptional preservation. *Palaeontology* **2016**, *59*, 1–11. [CrossRef]
14. Keenan, S.W. From bone to fossil: A review of the diagenesis of bioapatite. *Am. Mineral.* **2016**, *101*, 1943–1951. [CrossRef]
15. Butterfield, N.J. Exceptional fossil preservation and the Cambrian Explosion. *Integr. Comp. Biol.* **2003**, *43*, 166–177. [CrossRef]
16. Pawlicki, R.; Korbel, A.; Kubiak, H. Cells, collagen fibrils and vessels in dinosaur bone. *Nature* **1966**, *211*, 655–657. [CrossRef]
17. Zhang, F.; Kearns, S.L.; Orr, P.J.; Benton, M.J.; Zhou, Z.; Johnson, D.; Xu, X.; Wang, X. Fossilized melanosomes and the colour of Cretaceous dinosaurs and birds. *Nature* **2010**, *463*, 1075–1078. [CrossRef]
18. Schweitzer, M.H.; Marshall, M.; Carron, K.; Bohle, D.S.; Busse, S.C.; Arnold, E.V.; Barnard, D.; Horner, J.R.; Starkey, J.R. Heme compounds in dinosaur trabecular bone. *Proc. Natl. Acad. Sci. USA* **1997**, *94*, 6291–6296. [CrossRef]
19. Schweitzer, M.H.; Suo, Z.; Avci, R.; Asara, J.M.; Allen, M.A.; Arce, F.T.; Horner, J.R. Analyses of soft tissue from *Tyrannosaurus rex* suggest the presence of protein. *Science* **2007**, *316*, 277–280. [CrossRef]
20. Asara, J.M.; Schweitzer, M.H.; Freimark, L.M.; Phillips, M.; Cantley, L.C. Protein sequences from mastodon and *Tyrannosaurus rex* revealed by mass spectrometry. *Science* **2007**, *316*, 280–285. [CrossRef]
21. Wiemann, J.; Yang, T.R.; Norell, M.A. Dinosaur egg colour had a single evolutionary origin. *Nature* **2018**, *563*, 555–558. [CrossRef]
22. Wiemann, J.; Yang, T.R.; Sander, P.N.; Schneider, M.; Engeser, M.; Kath-Schorr, S.; Müller, C.E.; Sander, P.M. Dinosaur origin of egg color: Oviraptors laid blue-green eggs. *PeerJ* **2017**, *5*, e3706. [CrossRef]
23. Moyer, A.E.; Zheng, W.; Schweitzer, M.H. Microscopic and immunohistochemical analyses of the claw of the nesting dinosaur, *Citipati osmolskae*. *Proc. R. Soc. B Biol. Sci.* **2016**, *283*, 20161997. [CrossRef]
24. Schweitzer, M.H.; Watt, J.A.; Avci, R.; Knapp, L.; Chiappe, L.; Norell, M.; Marshall, M. Beta-keratin specific immunological reactivity in feather-like structures of the cretaceous alvarezsaurid, *Shuvuuia deserti*. *J. Exp. Zool.* **1999**, *285*, 146–157. [CrossRef]
25. Lindgren, J.; Sjövall, P.; Carney, R.M.; Cincotta, A.; Uvdal, P.; Hutcheson, S.W.; Gustafsson, O.; Lefèvre, U.; Escuillié, F.; Heimdal, J.; et al. Molecular composition and ultrastructure of Jurassic paravian feathers. *Sci. Rep.* **2015**, *5*, 13520. [CrossRef]
26. Bertazzo, S.; Maidment, S.C.R.; Kallepitis, C.; Fearn, S.; Stevens, M.M.; Xie, H.N. Fibres and cellular structures preserved in 75-million-year-old dinosaur specimens. *Nat. Commun.* **2015**, *6*, 7352. [CrossRef]
27. Brown, C.M.; Henderson, D.M.; Vinther, J.; Fletcher, I.; Sistiaga, A.; Herrera, J.; Summons, R.E. An exceptionally preserved three-dimensional armored dinosaur reveals insights into coloration and Cretaceous predator-prey dynamics. *Curr. Biol.* **2017**, *27*, 2514–2521.e3. [CrossRef]
28. Lingham-Soliar, T.; Plodowski, G. The integument of *Psittacosaurus* from Liaoning Province, China: Taphonomy, epidermal patterns and color of a ceratopsian dinosaur. *Naturwissenschaften* **2010**, *97*, 479–486. [CrossRef]
29. Schweitzer, M.H.; Zheng, W.; Organ, C.L.; Avci, R.; Suo, Z.; Freimark, L.M.; Lebleu, V.S.; Duncan, M.B.; Heiden, M.G.V.; Neveu, J.M.; et al. Biomolecular characterization and protein sequences of the Campanian hadrosaur *B. canadensis*. *Science* **2009**, *324*, 626–631. [CrossRef]

30. Schroeter, E.R.; Dehart, C.J.; Cleland, T.P.; Zheng, W.; Thomas, P.M.; Kelleher, N.L.; Bern, M.; Schweitzer, M.H. Expansion for the *Brachylophosaurus canadensis* collagen I sequence and additional evidence of the preservation of Cretaceous protein. *J. Proteome Res.* **2017**, *16*, 920–932. [CrossRef]

31. Bailleul, A.M.; Zheng, W.; Horner, J.R.; Hall, B.K.; Holliday, C.M.; Schweitzer, M.H. Evidence of proteins, chromosomes and chemical markers of DNA in exceptionally preserved dinosaur cartilage. *Natl. Sci. Rev.* **2020**, *7*, 815–822. [CrossRef]

32. Pan, Y.; Hu, L.; Zhao, T. Applications of chemical imaging techniques in paleontology. *Natl. Sci. Rev.* **2019**, *6*, 1040–1053. [CrossRef]

33. Cleland, T.P.; Schroeter, E.R. A comparison of common mass spectrometry approaches for paleoproteomics. *J. Proteome Res.* **2018**, *17*, 936–945. [CrossRef]

34. Schweitzer, M.H.; Schroeter, E.R.; Cleland, T.P.; Zheng, W. Paleoproteomics of Mesozoic dinosaurs and other Mesozoic fossils. *Proteomics* **2019**, *19*, 1800251. [CrossRef]

35. Schweitzer, M.H.; Avci, R.; Collier, T.; Goodwin, M.B. Microscopic, chemical and molecular methods for examining fossil preservation. *Comptes Rendus Palevol* **2008**, *7*, 159–184. [CrossRef]

36. Zhou, W.; Apkarian, R.; Wang, Z.L.; Joy, D. Fundamentals of scanning electron microscopy (SEM). In *Scanning Microscopy for Nanotechnology*; Springer: New York, NY, USA, 2006; pp. 1–40.

37. Adams, F.; Barbante, C. Electron-based imaging techniques. In *Comprehensive Analytical Chemistry*; Elsevier: Amsterdam, The Netherlands, 2015; Volume 69, pp. 269–313.

38. Saitta, E.T.; Liang, R.; Lau, M.C.; Brown, C.M.; Longrich, N.R.; Kaye, T.G.; Novak, B.J.; Salzberg, S.L.; Norell, M.A.; Abbott, G.D.; et al. Cretaceous dinosaur bone contains recent organic material and provides an environment conducive to microbial communities. *Elife* **2019**, *8*, e46205. [CrossRef]

39. Relucenti, M.; Familiari, G.; Donfrancesco, O.; Taurino, M.; Li, X.; Chen, R.; Artini, M.; Papa, R.; Selan, L. Microscopy methods for biofilm imaging: Focus on SEM and VP-SEM pros and cons. *Biology* **2021**, *10*, 51. [CrossRef]

40. Klijn, M.E.; Hubbuch, J. Application of ultraviolet, visible, and infrared light imaging in protein-based biopharmaceutical formulation characterization and development studies. *Eur. J. Pharm. Biopharm.* **2021**, *165*, 319–336. [CrossRef]

41. Picollo, M.; Aceto, M.; Vitorino, T. UV-Vis spectroscopy. *Phys. Sci. Rev.* **2019**, *4*, 20180008. [CrossRef]

42. Akash, M.S.H.; Rehman, K. Ultraviolet-visible (UV-VIS) spectroscopy. In *Essentials of Pharmaceutical Analysis*; Springer: Singapore, 2020; pp. 29–56, ISBN 978-981-15-1547-7.

43. Olcott Marshall, A.; Marshall, C.P. Vibrational spectroscopy of fossils. *Palaeontology* **2015**, *58*, 201–211. [CrossRef]

44. Loutherback, K.; Birarda, G.; Chen, L.; N Holman, H.-Y. Microfluidic approaches to synchrotron radiation-based Fourier transform infrared (SR-FTIR) spectral microscopy of living biosystems. *Protein Pept. Lett.* **2016**, *23*, 273–282. [CrossRef] [PubMed]

45. Wang, M.; Lu, X.; Yin, X.; Tong, Y.; Peng, W.; Wu, L.; Li, H.; Yang, Y.; Gu, J.; Xiao, T.; et al. Synchrotron radiation-based Fourier-transform infrared spectromicroscopy for characterization of the protein/peptide distribution in single microspheres. *Acta Pharm. Sin. B* **2015**, *5*, 270–276. [CrossRef] [PubMed]

46. Baeten, V.; Dardenne, P. Spectroscopy: Developments in instrumentation and analysis. *Grasas Aceites* **2002**, *53*, 45–63. [CrossRef]

47. Lohumi, S.; Kim, M.S.; Qin, J.; Cho, B.-K. Raman imaging from microscopy to macroscopy: Quality and safety control of biological materials. *TrAC Trends Anal. Chem.* **2017**, *93*, 183–198. [CrossRef]

48. Raman, C.V.; Krishnan, K.S. A new type of secondary radiation. *Nature* **1928**, *121*, 501–502. [CrossRef]

49. Marigheto, N.A.; Kemsley, E.K.; Potter, J.; Belton, P.S.; Wilson, R.H. Effects of sample heating in FT-Raman spectra of biological materials. *Spectrochim. Acta Part A Mol. Biomol. Spectrosc.* **1996**, *52*, 1571–1579. [CrossRef]

50. Milman, B.L. General principles of identification by mass spectrometry. *TrAC Trends Anal. Chem.* **2015**, *69*, 24–33. [CrossRef]

51. Altelaar, A.F.M.; Luxembourg, S.L.; McDonnell, L.A.; Piersma, S.R.; Heeren, R.M.A. Imaging mass spectrometry at cellular length scales. *Nat. Protoc.* **2007**, *2*, 1185–1196. [CrossRef]

52. Thiel, V.; Sjövall, P. Using time-of-flight secondary ion mass spectrometry to study Biomarkers. *Annu. Rev. Earth Planet. Sci.* **2011**, *39*, 125–156. [CrossRef]

53. Greenwalt, D.E.; Goreva, Y.S.; Siljeström, S.M.; Rose, T.; Harbach, R.E. Hemoglobin-derived porphyrins preserved in a Middle Eocene blood-engorged mosquito. *Proc. Natl. Acad. Sci. USA* **2013**, *110*, 18496–18500. [CrossRef]

54. Lindgren, J.; Uvdal, P.; Sjövall, P.; Nilsson, D.E.; Engdahl, A.; Schultz, B.P.; Thiel, V. Molecular preservation of the pigment melanin in fossil melanosomes. *Nat. Commun.* **2012**, *3*, 824. [CrossRef] [PubMed]

55. Winograd, N. The Magic of Cluster SIMS. *Anal. Chem.* **2005**, *77*, 142 A–149 A. [CrossRef]

56. Kozole, J.; Winograd, N. Cluster secondary ion mass spectrometry. In *Surface Analysis and Techniques in Biology*; Smentkowski, V.S., Ed.; Springer: Cham, Switzerland, 2014; pp. 71–98.

57. Meier, D.; Faix, O. Pyrolysis-gas chromatography-mass spectrometry. In *Methods in Lignin Chemistry*; Lin, S.Y., Dence, C.W., Eds.; Springer: Berlin/Heidelberg, Germany, 1992; pp. 177–199, ISBN 13:978-3-642-74065-7.

58. Stankiewicz, B.A.; Briggs, D.E.G.; Evershed, R.P.; Flannery, M.B.; Wuttke, M. Preservation of chitin in 25-million-year-old fossils. *Science* **1997**, *276*, 1541–1543. [CrossRef]

59. Stankiewicz, B.A.; Poinar, H.N.; Briggs, D.E.G.; Evershed, R.P.; Poinar, J. Chemical preservation of plants and insects in natural resins. *Proc. R. Soc. B Biol. Sci.* **1998**, *265*, 641–647. [CrossRef]

60. Stankiewicz, B.A.; Mastalerz, M.; Kruge, M.A.; Van Bergen, P.F.; Sadowska, A. A comparative study of modern and fossil cone scales and seeds of conifers: A geochemical approach. *New Phytol.* **1997**, *135*, 375–393. [CrossRef]

61. Fenn, J.B.; Mann, M.; Meng, C.K.; Wong, S.F.; Whitehouse, C.M. Electrospray ionization for mass spectrometry of large biomolecules. *Science* **1989**, *246*, 64–71. [CrossRef]

62. El-Aneed, A.; Cohen, A.; Banoub, J. Mass spectrometry, review of the basics: Electrospray, MALDI, and commonly used mass analyzers. *Appl. Spectrosc. Rev.* **2009**, *44*, 210–230. [CrossRef]

63. Crowther, J.R. Overview of ELISA in relation to other disciplines. In *The ELISA Guidebook. Methods in Molecular Biology*; Walker, J.M., Ed.; Humana Press: New York, NY, USA, 2009; pp. 1–8, ISBN 978-1-60327-254-4.

64. Yu, H.-W.; Halonen, M.J.; Pepper, I.L. Immunological methods. In *Environmental Microbiology*; Pepper, I.L., Gerba, C.P., Gentry, T.J., Eds.; Elsevier: Amsterdam, The Netherlands, 2015; pp. 245–269, ISBN 978-0-12-394626-3.

65. Aydin, S. A short history, principles, and types of ELISA, and our laboratory experience with peptide/protein analyses using ELISA. *Peptides* **2015**, *72*, 4–15. [CrossRef]

66. Stanker, L.H.; Hnasko, R.M. A double-sandwich ELISA for identification of monoclonal antibodies suitable for sandwich immunoassays. In *Methods in Molecular Biology*; Hnasko, R., Ed.; Humana Press: New York, NY, USA, 2015; pp. 69–78, ISBN 978-1-4939-2741-8.

67. Gan, S.D.; Patel, K.R. Enzyme immunoassay and enzyme-linked immunosorbent assay. *J. Investig. Dermatol.* **2013**, *133*, e12. [CrossRef]

68. Makarananda, K.; Weir, L.R.; Neal, G.E. Competitive ELISA. In *Immunochemical Protocols*; Pound, J.D., Ed.; Humana Press: Totowa, NJ, USA, 1998; pp. 155–160, ISBN 978-1-59259-257-9.

69. Gallagher, S.R. SDS-polyacrylamide gel electrophoresis (SDS-PAGE). *Curr. Protoc. Essent. Lab. Tech.* **2008**, *6*, 7-3. [CrossRef]

70. Yang, P.-C.; Mahmood, T. Western blot: Technique, theory, and trouble shooting. *N. Am. J. Med. Sci.* **2012**, *4*, 429. [CrossRef]

71. Crichton, P.G.; Harding, M.; Ruprecht, J.J.; Lee, Y.; Kunji, E.R.S. Lipid, detergent, and Coomassie Blue G-250 affect the migration of small membrane proteins in Blue Native gels. *J. Biol. Chem.* **2013**, *288*, 22163–22173. [CrossRef]

72. Na Ayutthaya, P.P.; Lundberg, D.; Weigel, D.; Li, L. Blue native polyacrylamide gel electrophoresis (BN-PAGE) for the analysis of protein oligomers in plants. *Curr. Protoc. Plant Biol.* **2020**, *5*, e20107. [CrossRef]

73. Gillett, C.E. Immunohistochemistry. In *Breast Cancer Research Protocols*; Brooks, S.A., Harris, A.L., Eds.; Humana Press: Totowa, NJ, USA, 2006; pp. 191–200.

74. Magaki, S.; Hojat, S.A.; Wei, B.; So, A.; Yong, W.H. An introduction to the performance of immunohistochemistry. In *Biobanking: Methods and Protocols*; Yong, W.H., Ed.; Springer: New York, NY, USA, 2019; pp. 289–298, ISBN 978-1-4939-8935-5.

75. D'Amico, F.; Skarmoutsou, E.; Stivala, F. State of the art in antigen retrieval for immunohistochemistry. *J. Immunol. Methods* **2009**, *341*, 1–18. [CrossRef]

76. Alfonso-Rojas, A.; Cadena, E.-A. Exceptionally preserved 'skin' in an Early Cretaceous fish from Colombia. *PeerJ* **2020**, *8*, e9479. [CrossRef]

77. Roy, A.; Pittman, M.; Saitta, E.T.; Kaye, T.G.; Xu, X. Recent advances in amniote palaeocolour reconstruction and a framework for future research. *Biol. Rev.* **2020**, *95*, 22–50. [CrossRef]

78. Vinther, J. A guide to the field of palaeo colour. *BioEssays* **2015**, *37*, 643–656. [CrossRef]

79. Vinther, J. Reconstructing vertebrate paleocolor. *Annu. Rev. Earth Planet. Sci.* **2020**, *48*, 345–375. [CrossRef]

80. Gueneli, N.; Mckenna, A.M.; Ohkouchi, N.; Boreham, C.J.; Beghin, J.; Javaux, E.J.; Brocks, J.J. 1.1-billion-year-old porphyrins establish a marine ecosystem dominated by bacterial primary producers. *Proc. Natl. Acad. Sci. USA* **2018**, *115*, E6978–E6986. [CrossRef]

81. Tahoun, M.; Gee, C.T.; McCoy, V.E.; Sander, P.M.; Müller, C.E. Chemistry of porphyrins in fossil plants and animals. *RSC Adv.* **2021**, *11*, 7552–7563. [CrossRef]

82. Asher, S.A. Resonance Raman spectroscopy of hemoglobin. In *Methods in Enzymology*; Antonini, E., Chiancone, E., Rossi-Bernardi, L., Eds.; Academic Press: New York, NY, USA, 1981; pp. 371–413.

83. Alleon, J.; Montagnac, G.; Reynard, B.; Brulé, T.; Thoury, M.; Gueriau, P. Pushing Raman spectroscopy over the edge: Purported signatures of organic molecules in fossil animals are instrumental artefacts. *BioEssays* **2021**, *43*, 2000295. [CrossRef]

84. Wiemann, J.; Briggs, D.E.G. Raman spectroscopy is a powerful tool in molecular paleobiology: An analytical response to Alleon et al. (https://doi.org/10.1002/bies.202000295). *BioEssays* **2022**, *44*, 2100070. [CrossRef]

85. Nasti, T.H.; Timares, L. MC1R, Eumelanin and Pheomelanin: Their role in determining the susceptibility to skin cancer. *Photochem. Photobiol.* **2015**, *91*, 188–200. [CrossRef]

86. Suzukawa, A.A.; Vieira, A.; Winnischofer, S.M.B.; Scalfo, A.C.; Di Mascio, P.; Ferreira, A.M.D.C.; Ravanat, J.-L.; Martins, D.D.L.; Rocha, M.E.M.; Martinez, G.R. Novel properties of melanins include promotion of DNA strand breaks, impairment of repair, and reduced ability to damage DNA after quenching of singlet oxygen. *Free Radic. Biol. Med.* **2012**, *52*, 1945–1953. [CrossRef]

87. Lindgren, J.; Moyer, A.; Schweitzer, M.H.; Sjövall, P.; Uvdal, P.; Nilsson, D.E.; Heimdal, J.; Engdahl, A.; Gren, J.A.; Schultz, B.P.; et al. Interpreting melanin-based coloration through deep time: A critical review. *Proc. R. Soc. B Biol. Sci.* **2015**, *282*, 20150614. [CrossRef]

88. Ortonne, J.-P. Photoprotective properties of skin melanin. *Br. J. Dermatol.* **2002**, *146*, 7–10. [CrossRef]

89. D'Ischia, M.; Napolitano, A.; Ball, V.; Chen, C.-T.; Buehler, M.J. Polydopamine and Eumelanin: From structure–property relationships to a unified tailoring strategy. *Acc. Chem. Res.* **2014**, *47*, 3541–3550. [CrossRef]

90. Pezzella, A.; Napolitano, A.; D'Ischia, M.; Prota, G.; Seraglia, R.; Traldi, P. Identification of partially degraded oligomers of 5,6-dihydroxyindole-2-carboxylic acid in sepia melanin by matrix-assisted laser desorption/ionization mass spectrometry. *Rapid Commun. Mass Spectrom.* **1997**, *11*, 368–372. [CrossRef]

91. Falk, H.; Wolkenstein, K. Natural product molecular fossils. In *Progress in the Chemistry of Organic Natural Products*; Kinghorn, A.D., Falk, H., Gibbons, S., Kobayashi, J., Eds.; Springer: Cham, Switzerland, 2017; pp. 1–126, ISBN 978-3-319-45618-8.

92. Cao, W.; Zhou, X.; McCallum, N.C.; Hu, Z.; Ni, Q.Z.; Kapoor, U.; Heil, C.M.; Cay, K.S.; Zand, T.; Mantanona, A.J.; et al. Unraveling the structure and function of melanin through synthesis. *J. Am. Chem. Soc.* **2021**, *143*, 2622–2637. [CrossRef]

93. Lindgren, J.; Sjövall, P.; Carney, R.M.; Uvdal, P.; Gren, J.A.; Dyke, G.; Schultz, B.P.; Shawkey, M.D.; Barnes, K.R.; Polcyn, M.J. Skin pigmentation provides evidence of convergent melanism in extinct marine reptiles. *Nature* **2014**, *506*, 484–488. [CrossRef]

94. Colleary, C.; Dolocan, A.; Gardner, J.; Singh, S.; Wuttke, M.; Rabenstein, R.; Habersetzer, J.; Schaal, S.; Feseha, M.; Clemens, M.; et al. Chemical, experimental, and morphological evidence for diagenetically altered melanin in exceptionally preserved fossils. *Proc. Natl. Acad. Sci. USA* **2015**, *112*, 12592–12597. [CrossRef]

95. Moyer, A.E.; Zheng, W.; Johnson, E.A.; Lamanna, M.C.; Li, D.; Lacovara, K.J.; Schweitzer, M.H. Melanosomes or microbes: Testing an alternative hypothesis for the origin of microbodies in fossil feathers. *Sci. Rep.* **2015**, *4*, 4233. [CrossRef]

96. Schleifer, K.H.; Kandler, O. Peptidoglycan types of bacterial cell walls and their taxonomic implications. *Bacteriol. Rev.* **1972**, *36*, 407–477. [CrossRef] [PubMed]

97. Härtner, T.; Straub, K.L.; Kannenberg, E. Occurrence of hopanoid lipids in anaerobic *Geobacter* species. *FEMS Microbiol. Lett.* **2005**, *243*, 59–64. [CrossRef]

98. Belin, B.J.; Busset, N.; Giraud, E.; Molinaro, A.; Silipo, A.; Newman, D.K. Hopanoid lipids: From membranes to plant–bacteria interactions. *Nat. Rev. Microbiol.* **2018**, *16*, 304–315. [CrossRef] [PubMed]

99. Glass, K.; Ito, S.; Wilby, P.R.; Sota, T.; Nakamura, A.; Bowers, C.R.; Vinther, J.; Dutta, S.; Summons, R.; Briggs, D.E.G.; et al. Direct chemical evidence for eumelanin pigment from the Jurassic period. *Proc. Natl. Acad. Sci. USA* **2012**, *109*, 10218–10223. [CrossRef] [PubMed]

100. Glass, K.; Ito, S.; Wilby, P.R.; Sota, T.; Nakamura, A.; Russell Bowers, C.; Miller, K.E.; Dutta, S.; Summons, R.E.; Briggs, D.E.G.; et al. Impact of diagenesis and maturation on the survival of eumelanin in the fossil record. *Org. Geochem.* **2013**, *64*, 29–37. [CrossRef]

101. Smejkal, G.B.; Schweitzer, M.H. Will current technologies enable dinosaur proteomics? *Expert Rev. Proteom.* **2007**, *4*, 695–699. [CrossRef]

102. Buckley, M.; Warwood, S.; van Dongen, B.; Kitchener, A.C.; Manning, P.L. A fossil protein chimera; difficulties in discriminating dinosaur peptide sequences from modern cross-contamination. *Proc. R. Soc. B Biol. Sci.* **2017**, *284*, 20170544. [CrossRef]

103. Sawyer, R.H.; Glenn, T.; French, J.O.; Mays, B.; Shames, R.B.; Barnes, G.L.; Rhodes, W.; Ishikawa, Y. The expression of beta (β) keratins in the epidermal appendages of reptiles and birds. *Am. Zool.* **2000**, *40*, 530–539. [CrossRef]

104. Alberts, B.; Johnson, A.; Lewis, J.; Raff, M.; Roberts, K.; Walter, P. Cell junctions, cell adhesion, and the extracellular matrix. In *Molecular Biology of the Cell*, 4th ed.; Garland Science: New York, NY, USA, 2002; pp. 1065–1126.

105. Koide, T. Triple helical collagen-like peptides: Engineering and applications in matrix biology. *Connect. Tissue Res.* **2005**, *46*, 131–141. [CrossRef] [PubMed]

106. Frantz, C.; Stewart, K.M.; Weaver, V.M. The extracellular matrix at a glance. *J. Cell Sci.* **2010**, *123*, 4195–4200. [CrossRef] [PubMed]

107. Rozario, T.; DeSimone, D.W. The extracellular matrix in development and morphogenesis: A dynamic view. *Dev. Biol.* **2010**, *341*, 126–140. [CrossRef] [PubMed]

108. Sorushanova, A.; Delgado, L.M.; Wu, Z.; Shologu, N.; Kshirsagar, A.; Raghunath, R.; Mullen, A.M.; Bayon, Y.; Pandit, A.; Raghunath, M.; et al. The collagen suprafamily: From biosynthesis to advanced biomaterial development. *Adv. Mater.* **2019**, *31*, 1801651. [CrossRef]

109. Shoulders, M.D.; Raines, R.T. Collagen structure and stability. *Annu. Rev. Biochem.* **2009**, *78*, 929–958. [CrossRef]

110. Curtis, R.W.; Chmielewski, J. A comparison of the collagen triple helix and coiled-coil peptide building blocks on metal ion-mediated supramolecular assembly. *Pept. Sci.* **2021**, *113*, e24190. [CrossRef]

111. Yamauchi, M.; Sricholpech, M. Lysine post-translational modifications of collagen. *Essays Biochem.* **2012**, *52*, 113–133. [CrossRef]

112. Hulmes, D.J.S. Collagen diversity, synthesis and assembly. In *Collagen*; Fratzl, P., Ed.; Springer: Boston, MA, USA, 2008; pp. 15–47.

113. Line, S.; Rhodes, C.; Yamada, Y. Molecular Biology of Cartilage Matrix. In *Cellular and Molecular Biology of Bone*; Noda, M., Ed.; Academic Press: San Diego, CA, USA, 1993; pp. 539–555.

114. Fedarko, N.S. Osteoblast/osteoclast development and function in osteogenesis imperfecta. In *Osteogenesis Imperfecta*; Shapiro, J.R., Ed.; Academic Press: San Diego, CA, USA, 2014; pp. 45–56, ISBN 9780123971654.

115. Henriksen, K.; Karsdal, M.A. Type I collagen. In *Biochemistry of Collagens, Laminins and Elastin*; Karsdal, M.A., Ed.; Elsevier: Amsterdam, The Netherlands, 2019; pp. 1–12, ISBN 9780128170687.

116. Byers, P.H.; Bonadio, J.F. The molecular basis of clinical heterogeneity in osteogenesis imperfecta: Mutations in type I collagen genes have different effects on collagen processing. In *Genetic and Metabolic Disease in Pediatrics*; Lloyd, J.K., Scriver, C.R., Eds.; Butterworth & Co. (Publishers) Ltd.: Bodmin, UK, 1985; pp. 56–90.

117. Bächinger, H.P.; Mizuno, K.; Vranka, J.A.; Boudko, S.P. Collagen formation and structure. In *Comprehensive Natural Products II: Chemistry and Biology*; Liu, H.-W., Mander, L., Eds.; Elsevier: Amsterdam, The Netherlands, 2010; Volume 5, pp. 469–530, ISBN 9780080453828.

118. Shavandi, A.; Silva, T.H.; Bekhit, A.A.; Bekhit, A.E.-D.A. Keratin: Dissolution, extraction and biomedical application. *Biomater. Sci.* **2017**, *5*, 1699–1735. [CrossRef]

16. Appendix

119. Bragulla, H.H.; Homberger, D.G. Structure and functions of keratin proteins in simple, stratified, keratinized and cornified epithelia. *J. Anat.* **2009**, *214*, 516–559. [CrossRef]

120. Coulombe, P.A.; Omary, M.B. 'Hard' and 'soft' principles defining the structure, function and regulation of keratin intermediate filaments. *Curr. Opin. Cell Biol.* **2002**, *14*, 110–122. [CrossRef]

121. Gu, L.-H.; Coulombe, P.A. Keratin function in skin epithelia: A broadening palette with surprising shades. *Curr. Opin. Cell Biol.* **2007**, *19*, 13–23. [CrossRef]

122. Sun, T.-T.; Eichner, R.; Nelson, W.G.; Scheffer Tseng, C.G.; Weiss, R.A.; Jarvinen, M.; Woodcock-Mitchell, J. Keratin classes: Molecular markers for different types of epithelial differentiation. *J. Investig. Dermatol.* **1983**, *81*, S109–S115. [CrossRef] [PubMed]

123. Korniłłowicz-Kowalska, T.; Bohacz, J. Biodegradation of keratin waste: Theory and practical aspects. *Waste Manag.* **2011**, *31*, 1689–1701. [CrossRef] [PubMed]

124. Wang, B.; Yang, W.; McKittrick, J.; Meyers, M.A. Keratin: Structure, mechanical properties, occurrence in biological organisms, and efforts at bioinspiration. *Prog. Mater. Sci.* **2016**, *76*, 229–318. [CrossRef]

125. Fraser, R.D.B.; Parry, D.A.D. Molecular packing in the feather keratin filament. *J. Struct. Biol.* **2008**, *162*, 1–13. [CrossRef]

126. Toni, M.; Dalla Valle, L.; Alibardi, L. Hard (beta-)keratins in the epidermis of reptiles: Composition, sequence, and molecular organization. *J. Proteome Res.* **2007**, *6*, 3377–3392. [CrossRef]

127. Perța-Crișan, S.; Ursachi, C.Ș.; Gavrilaș, S.; Oancea, F.; Munteanu, F.-D. Closing the loop with keratin-rich fibrous materials. *Polymers* **2021**, *13*, 1896. [CrossRef]

16.3. Appendix C – Molecular taphonomy of heme: Chemical degradation of hemin under presumed fossilization conditions

This section contains the article and supporting information of "Molecular taphonomy of heme: Chemical degradation of hemin under presumed fossilization conditions" as it appears in the journal *Molecules* by MDPI. Reprinted from *Molecules* **2023***, 28(13), 4887, copyright (2023), with permission from MDPI. This work is licensed under the Creative Commons Attribution 4.0 International License (CC-BY). To view a copy of this license, visit http://creativecommons.org/licenses/by/4.0/. As guaranteed by the author rights policy of MDPI, copying and re-use of the article in any medium or format is allowed without permission or payment, as long as the original article is fully acknowledged.

molecules

Article

Molecular Taphonomy of Heme: Chemical Degradation of Hemin under Presumed Fossilization Conditions

Mariam Tahoun [1], Marianne Engeser [2,*], Luca Svolacchia [1], Paul Martin Sander [3] and Christa E. Müller [1,*]

[1] PharmaCenter Bonn & Pharmaceutical Institute, Department of Pharmaceutical & Medicinal Chemistry, University of Bonn, An der Immenburg 4, 53121 Bonn, Germany; mtahoun@uni-bonn.de (M.T.); s6lusvol@uni-bonn.de (L.S.)
[2] Kekulé Institute for Organic Chemistry and Biochemistry, University of Bonn, 53121 Bonn, Germany
[3] Section Paleontology, Institute of Geosciences, University of Bonn, 53115 Bonn, Germany; paulmartinsander@gmail.com
* Correspondence: marianne.engeser@uni-bonn.de (M.E.); christa.mueller@uni-bonn.de (C.E.M.)

Abstract: The metalloporphyrin heme acts as the oxygen-complexing prosthetic group of hemoglobin in blood. Heme has been noted to survive for many millions of years in fossils. Here, we investigate its stability and degradation under various conditions expected to occur during fossilization. Oxidative, reductive, aerobic, and anaerobic conditions were studied at neutral and alkaline pH values. Elevated temperatures were applied to accelerate degradation. High-performance liquid chromatography coupled to tandem mass spectrometry (HPLC-MS/MS) identified four main degradation products. The vinyl residues are oxidized to formyl and further to carboxylate groups. In the presence of air or H_2O_2, cleavage of the tetrapyrrole ring occurs, and hematinic acid is formed. The highest stability of heme was observed under anaerobic reductive conditions (half-life 9.5 days), while the lowest stability was found in the presence of H_2O_2 (half-life 1 min). We confirmed that the iron cation plays a crucial role in degradation, since protoporphyrin IX, lacking iron, remained significantly more stable. Under anaerobic, reductive conditions, the above-mentioned degradation products were not observed, suggesting a different degradation pathway. To our knowledge, this is the first molecular taphonomy study on heme, which will be useful for understanding its fate during fossilization.

Keywords: heme; porphyrin; paleontology; fossilization; molecular taphonomy; preservation; mass spectrometry; dinosaurs; oxidation; hematinic acid

1. Introduction

Heme (**1**, Figure 1) is the prosthetic group of hemoglobin, the oxygen-binding component of red blood cells in humans and all other vertebrates [1]. Heme belongs to the chemical class of metalloporphyrins, which are tetrapyrroles linked via methine bridges that coordinate a metal ion in the center of the polycyclic ring [2]. Fe^{2+} forms bonds with each of the four pyrrolic nitrogen atoms and an additional bond to the nitrogen atom of a histidine present in globin. This complex is known as deoxyhemoglobin. The Fe^{2+} can coordinate with an additional ligand, e.g., oxygen (forming oxyhemoglobin; see Figure 1), or with water or carbon monoxide [3].

A previously studied pathway of heme degradation is the enzymatic degradation by heme oxygenase that occurs in vivo [4]. Heme undergoes a stepwise regiospecific oxidation of an α-methine bridge leading to ring cleavage forming α-hydroxyhemin (**2**), verdoheme (**3**), and iron(III) biliverdin (**4**) as intermediates (see Figure 2). During this reaction sequence, carbon monoxide and then iron are released subsequently, and the linear tetrapyrrole derivative biliverdin (**5**) is formed. Biliverdin reductase converts **5** to bilirubin (**6**, Figure 2), which can be conjugated with glucuronic acid to facilitate excretion. Heme oxygenase is expressed in vertebrates [5], insects, plants [6], cyanobacteria [7], algae [8], fungi [9], and bacteria [10–14]. This process also occurs in vitro upon the incubation of

164

hemin, the iron(III) derivative of heme, with liver, kidney, or spleen microsomes in the presence of nicotinamide adenine dinucleotide phosphate (NADPH) [15]. This reaction is employed in coupled oxidation assays, leading to the cleavage of any of the four methine bridges and forming a mixture of four biliverdin isomers [16]. These assays serve to investigate to what extent heme is protected from free radical species in the presence of certain amounts of antioxidants, e.g., ascorbic acid [17].
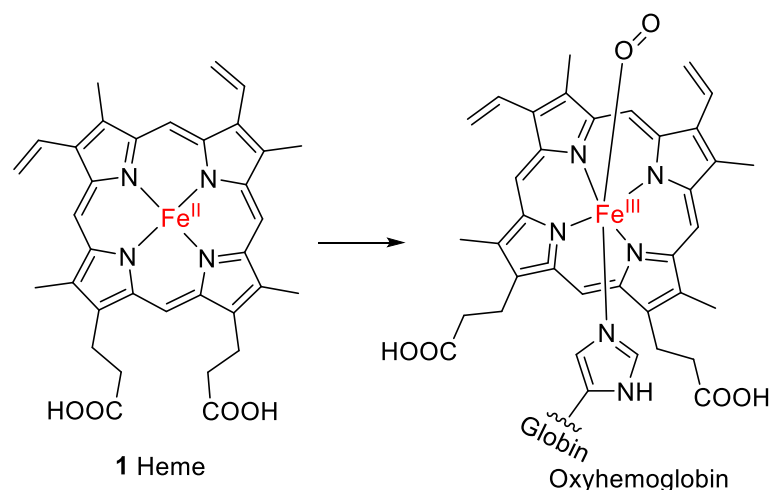
Figure 1. Structure of heme (**1**), the prosthetic group of oxyhemoglobin.
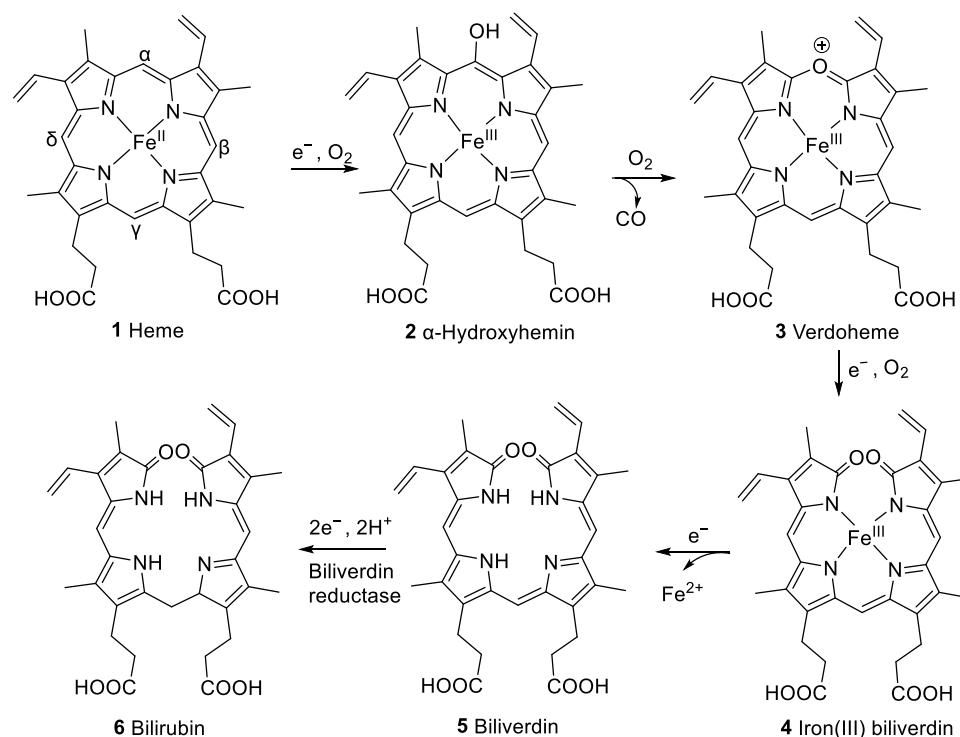
Figure 2. Pathway of heme (**1**) degradation by heme oxygenase to form biliverdin (**5**), including intermediate compounds **2**–**4**, and subsequent formation of bilirubin (**6**) by biliverdin reductase [4].

However, not all heme degradation pathways lead to biliverdin. NADPH-cytochrome P450 reductase degrades heme to the mono- and di-pyrrolic structures **11**–**16** via the intermediate oxidation products **7**–**10** (see Figure 3) and **4** [18–20]. The detailed mechanism of heme degradation by NADPH-cytochrome P450 reductase, and especially the non-enzymatic degradation of heme, e.g., under oxidative conditions, which does not lead to biliverdin, is not yet fully understood. It has been proposed that iron plays a role in the

degradation by forming perferryl [iron(V)] oxygen- or oxo-iron(IV)-porphyrin π-cation radical intermediates (e.g., **7**, Figure 3) in the presence of hydrogen peroxide [18,21]. The intermediate high-valent iron complex was proposed to react with one of the methine carbon bridges forming a glycol (**8**, Figure 3). In this process, an electron is transferred, and the high-valent iron is reduced to iron(III) [22]. Another H_2O_2 molecule can react with the iron(III)-complex (**9**, Figure 3) leading to further cleavage of the glycol forming a compound with a *2H*-pyrrol-2-one and an α-formyl pyrrole ring (**10**, Figure 3). The α-formyl group can be hydrated and subsequently converted to an α-ketone (**4**, iron(III) biliverdin, Figure 3) after an attack by a high-valent iron oxide complex. This process takes place at each of the carbon bridges. Intermediate products are the propentdyopents, represented by a group of selected structures **11**–**14**, and the final products are the maleimides hematinic acid (**15**) and methylvinylmaleimide (**16**) and formic acid as a side product [18].
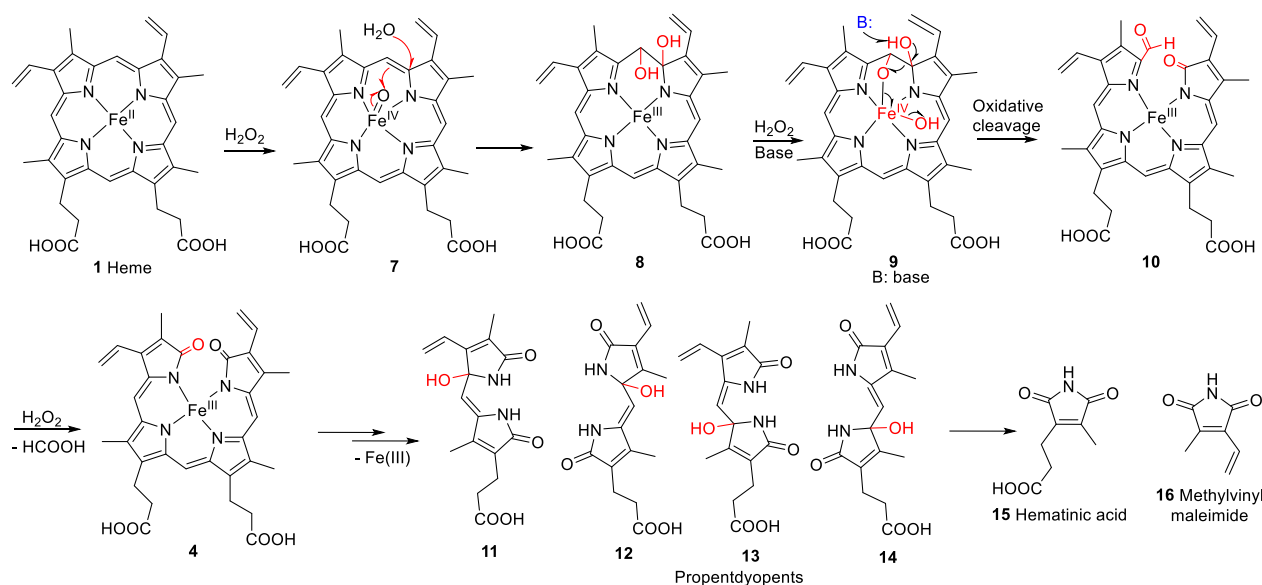
Figure 3. Proposed mechanism for non-enzymatic oxidative cleavage of heme (**1**) to generate monopyrrolic hematinic acid (**15**) and methylvinylmaleimide (**16**), through intermediate tetrapyrrolic (**4**, **7**–**10**) and dipyrrolic degradation products, namely the propentdyopents **11**–**14** [18,23]. The red arrows in compound **7** illustrate the rearrangement of bonds. "B" represents any base, and the black arrow illustrates the site of attack.

Hematinic acid has been described before as a degradation product of bilirubin (**6**) after photo-oxidation [24] and was found in the urine of newborns undergoing jaundice phototherapy [25]. It was also formed after the oxidation of Fe(III) hemin in the presence of 5% H_2O_2 [18] and by the oxidation of bilirubin (**6**) [26], mesoporphyrin IX [27], and chlorophyll *a* [23] with chromic acid. Hematinic acid was also described as a degradation product of hemoglobin after hemolysis with phenylhydrazine [28] and of chlorophyll *a* in senescent barley leaves [29]. Furthermore, it was detected as a bacterial degradation product of heme in *E. coli*, produced by the *E. coli* heme-utilization protein S (ChuS) [20].

Porphyrin derivatives such as heme (**1**), its iron-free derivative protoporphyrin IX (**17**, Figure 4), and biliverdin (**5**, Figure 2) have been reported to be preserved in fossils (reviewed in [2]). Preliminary evidence for the presence of heme was found in the trabecular bone of a 66-million-year-old dinosaur, *Tyrannosaurus rex* [30], by high-performance liquid chromatography (HPLC) coupled to UV/Vis detection. Heme has also been detected in 46-million-year-old mosquitoes (*Culiseta* sp.) using time-of-flight secondary-ion mass spectrometry (ToF-SIMS) [31]. A sea turtle with heme preservation in its soft tissue was preserved under similar conditions, in anaerobic fine mud at the bottom of the ancestral North Sea [32]. Protoporphyrin IX and biliverdin have been detected in 66-million-year-old

fossil eggshell extracts of the oviraptorid dinosaur *Heyuannia huangi* by HPLC coupled to electrospray ionization quadrupole time-of-flight mass spectrometry [33].
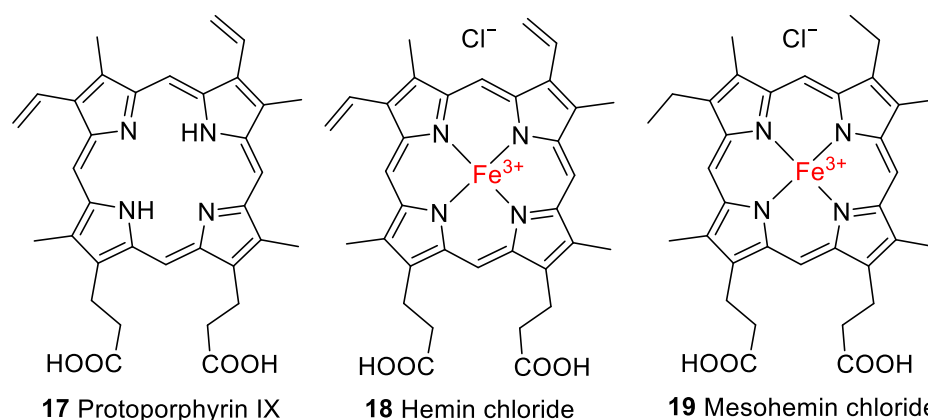
Figure 4. Structures of protoporphyrin IX (**17**), hemin chloride (**18**), and mesohemin chloride (**19**) employed in this study.

Preserved organic compounds and tissue structures, e.g., blood vessels and osteocytes in dinosaurs, have become an emerging subject of interest in paleontology [34–36]. Organic compounds in fossils have been studied using a number of analytical methods and techniques (reviewed in [37]). To better understand the process of fossilization, experimental taphonomic studies may be performed, in which different conditions expected to have occurred during fossilization are applied to fresh material derived from living organisms [38–41]. Taphonomic studies can not only be perf–ormed on plants and animals but also on molecules. The latter approach, designated molecular taphonomy [42,43], helps to understand the possible degradation profiles of specific molecules upon fossilization.

In the present study, we performed molecular taphonomy experiments on heme under conditions that are typical for fossilization with the aim to support future analytical studies, e.g., on dinosaur bone. The employed conditions included heating, the absence or presence of air, reductive or oxidative conditions, and different pH values. Of special interest were combinations of low-oxygen or reductive conditions with mildly alkaline pH values ranging from 8 to 10, which appear to be particularly relevant for the early-stage fossilization of bone. These conditions were based on models proposed by Retallack (2001) [44] and Pfretzschner (2004) [45], who studied the relationship between pH values and oxidation/reduction potential and how this affects the preservation of fossil bones buried in soil and deposited under water, respectively. Low-oxygen conditions were likely present upon the burial of bone and inside decaying bone, even if the surroundings are oxygenated. A mildly alkaline pH value may be observed upon the dissolution of bone hydroxyapatite [45]. We are aware that the temperatures of 70 °C, 75 °C, and 95 °C used in some of our experiments are beyond what occurs during fossilization (apart from exceptional circumstances). However, heating can be expected to speed up the rate of reactions and shorten the duration of the experiment to a few days [46]. Nevertheless, the interpretation of taphonomic studies performed at high temperatures, which is a widespread approach [47], should be conducted with great care [42]. Increased temperatures may induce reactions that do not occur at lower temperatures; results might therefore not in all cases reflect the processes that happen during fossilization [42]. Another factor to consider in the interpretation of taphonomy studies is that the controlled laboratory environment is not fully realistic because the diversity of conditions that occur during fossilization may lead to incorrect interpretations of the experiments [47].

For the experiments, the iron(III) derivative of heme, known as hemin (**18**, Figure 4), with a chloride counterion was employed, which is formed by the oxidation of the iron center to the ferric form upon exposure to air. As controls, some experiments were performed with protoporphyrin IX (**17**), which lacks the iron center, or with a closely related synthetic

16. Appendix

derivative of **1**, mesohemin (iron(III) mesoporphyrin IX chloride, **19**, Figure 4), in which the vinyl residues of **1** are replaced by ethyl groups.

To monitor hemin degradation under a variety of conditions and to separate, identify, and characterize its degradation products, we used HPLC coupled to mass spectrometry and a diode array UV/Vis detector (DAD-UV/Vis), in addition to high-resolution tandem mass spectrometry (HRMS/MS). The results will be useful for understanding the degradation pathway of hemin under various conditions of fossilization.

2. Results and Discussion

Hemin chloride (**18**) was exposed to various conditions for different periods of time, followed by lyophilization or evaporation to dryness, dissolution in methanol or a mixture of methanol and water, and HPLC-(DAD-UV/Vis)-MS analysis. An overview of the different experimental conditions is presented in Table 1.

Table 1. Experimental conditions employed for studying the degradation of hemin (**18**) and its observed half-life.

Condition	Medium	Concentration [a]	Temperature	Observed Half-Life of Hemin	Identified Degradation Product(s)
		Oxidation under alkaline conditions			
A	1% NH_3 in methanol + aq. H_2O_2 (final conc. 5%)	5 mg/mL hemin	Room temperature	$\leq$1 min	Hematinic acid (**15**)
B	1% NH_3 in water (pH 10.5) + aq. H_2O_2 (final conc. 5%)	5.5 mg/mL hemin	60 °C for the initial 30 min, then room temperature	$\leq$1 min	Hematinic acid (**15**)
		Oxidation at physiological pH value			
C	Phosphate-buffered saline (PBS pH 7.4) + aq. H_2O_2 (final conc. 3%)	1.3 mg/mL hemin	Room temperature	$\leq$1 min	Hematinic acid (**15**)
		Heating at physiological pH value			
D	PBS (pH 7.4) in the presence of air	1.3 mg/mL hemin	75 °C	2.6 days	Hematinic acid (**15**) DP-1 (**20**)
E	PBS (pH 7.4) in the presence of air	1.3 mg/mL hemin	95 °C	0.73 days	Hematinic acid (**15**) DP-1 (**20**)
F	PBS (pH 7.4) under an argon atmosphere	1.3 mg/mL hemin	75 °C	n.d. [b]	Hematinic acid (**15**) DP-1 (**20**)
		Heating under alkaline conditions			
G	0.1N aq. NaOH (pH 8) under an argon atmosphere (control experiments using compounds 18 and 20)	12 mg/mL hemin, 1.8 mg/mL ferric mesoporphyrin IX (19), or 12 mg/mL protoporphyrin IX (17)	70 °C	5.5 days (17: minor degradation; 19: no degradation)	DP-1 (**20**) DP-2 (**21**) DP-3
H	0.1 N aq. NaOH (pH 8) + 0.9% $Na_2S_2O_4$ under an argon atmosphere	12 mg/mL hemin		9.5 days	Unknown degradation product (mass of 650 Da)

[a] The highest concentration possible was used to identify as many degradation products as possible. Half-lives were determined for each condition from the curve showing exponential degradation. [b] The half-life could not be predicted since the experiment was stopped after 2 days before 50% of hemin degradation had occurred. Note that the conditions **A**–**H** are given in bold in order to facilitate identifying them.

2.1. Oxidative Conditions Lead to Hematinic Acid

The oxidative degradation of hemin chloride (**18**) in the presence of 5% H_2O_2 at alkaline or neutral pH values (see conditions **A**–**C** in Table 1) was rapid. Within minutes, **18** was completely degraded, and one major degradation product was detected (Figure 5a), which was found to be hematinic acid (**15**). Its structure was elucidated after isolation from the crude reaction mixture by preparative HPLC and subsequent analysis by nuclear magnetic resonance spectroscopy (NMR; see Supplementary Figures S1 and S2 for ^{1}H-

and ^{13}C-APT-NMR spectra). Additionally, the exact mass and fragmentation pattern were confirmed by high-resolution tandem mass spectrometry: 184.06042 measured, 184.06043 calculated for [M + H]$^+$; 206.04239 measured and 206.04238 calculated for [M + Na]$^+$ (see Supplementary Figures S3 and S4 for mass spectra). NMR signals matched the chemical shifts reported in the literature for hematinic acid, and mass spectral data confirmed its structure [18,24,48]. Performing the experiment in methanol (in the presence of 1% NH$_3$, 5% H$_2$O$_2$, at room temperature (RT), condition **A**, Table 1) or in water, at an alkaline pH value (1% NH$_3$, pH 10.5, 5% H$_2$O$_2$, 60 °C for 0.5 h followed by RT, condition **B**, Table 1), or at a physiological pH value of 7.4 (phosphate-buffered saline, pH 7.4, 5% H$_2$O$_2$, RT, condition **C**, Table 1), had no major effect on the degradation profile.
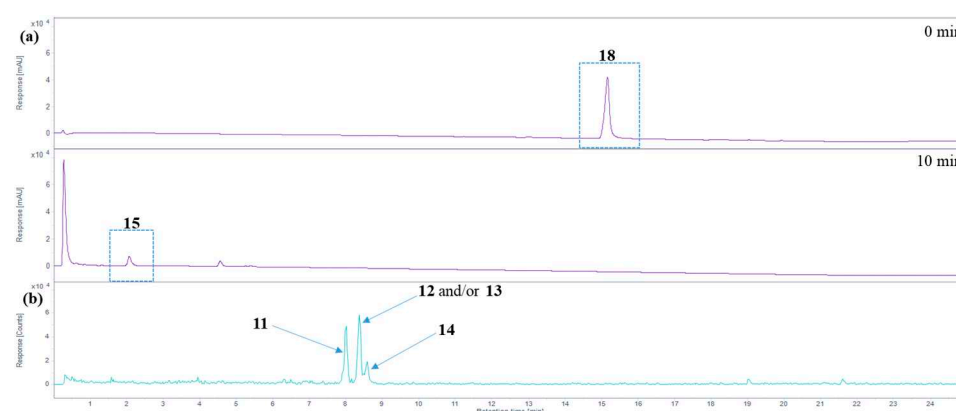
Figure 5. Analysis of hemin degradation. (**a**) HPLC-DAD total wavelength chromatogram before and 10 min after applying oxidizing conditions to hemin (phosphate-buffered saline, pH 7.4, 3% H$_2$O$_2$, RT, condition **C**, see Table 1) using HPLC-(DAD/UV)-ESI-MS. Hemin (**18**) forms hematinic acid (**15**) as the major degradation product. (**b**) Extracted ion chromatogram of m/z 319.1 ± 0.7 Da (positive ion mode), tentatively assigned to propentdyopents **11**–**14**.

In addition to hematinic acid (**15**), minor degradation products appeared under condition **A** (performed in methanol), the most prominent ones all showing a signal at m/z 319.1 in the positive ion mode and at m/z 317.1 in the negative mode. These mass spectra indicate the presence of molecules with a monoisotopic mass of 318.1 Da (ESI(+): [M + H]$^+$ at m/z 319.1; ESI(−): [M − H]$^-$ at m/z 317.1; see Figure 5b). These may be the propentdyopents **11**–**14** (reviewed in [49]), displaying a dipyrrin-1,9-dione structure (see Figure 3). As their yield was very low, no attempts were made to further characterize them beyond their mass spectra. There were three peaks for molecules with a mass of 318.1 Da, which may indicate positional isomers, of which compound **11** is possibly the first one to elute, followed by **12** and/or **13**, and finally **14**, based on previous studies on propentdyopents [23].

2.2. Thermal Degradation and Structural Elucidation of Intermediate Degradation Products

Heating at 95 °C (see condition **E**, Table 1) at a physiological pH value of 7.4 in phosphate-buffered saline in the presence of air for several days led to a complete degradation of hemin (see Figure 6a). Hemin degradation was slower at 75 °C (see condition **D**, Table 1) as expected. The new chromatographic peaks that appeared (representing degradation products of hemin) were the same under both conditions. Hemin showed a half-life of 2.6 days at 75 °C and 0.73 days at 95 °C (Figure 6a). When the reaction was performed under argon at 75 °C (condition **F**, Table 1), hemin was found to be more stable, and 70% of the original amount remained after 2 days when the experiment was stopped. Figure 6a illustrates the degradation of hemin under conditions **D**–**F** (see Table 1 for details).

Hematinic acid (**15**, Figure 3) was the most common degradation product of hemin chloride (**18**) formed after oxidation (conditions **A**–**C**) and after heating in the presence of air (conditions **D** and **E**). A plot of the time-dependent formation of **15** under condition **D** (phosphate-buffered saline, pH 7.4, 75 °C, air) and **E** (phosphate-buffered saline, pH 7.4, 95

°C, air) is shown in Figure 6b. At 75 °C, the formation of hematinic acid (**15**) reached its maximum after 4 days. At 95 °C, the formation of **15** started earlier, but it was also further degraded, and the observed amount was lower, decreasing on the third day. The other monopyrrolic degradation product, methylvinylmaleimide (**16**), which theoretically may have been formed by heme degradation along a pathway similar to the one depicted in Figure 3, was not detected in our experiments. Hematinic acid (**15**) was not detected upon heating in the absence of oxygen under condition **F** (phosphate-buffered saline, pH 7.4, 75 °C under argon) and **G** (0.1 N NaOH, pH 8, 70 °C under argon).
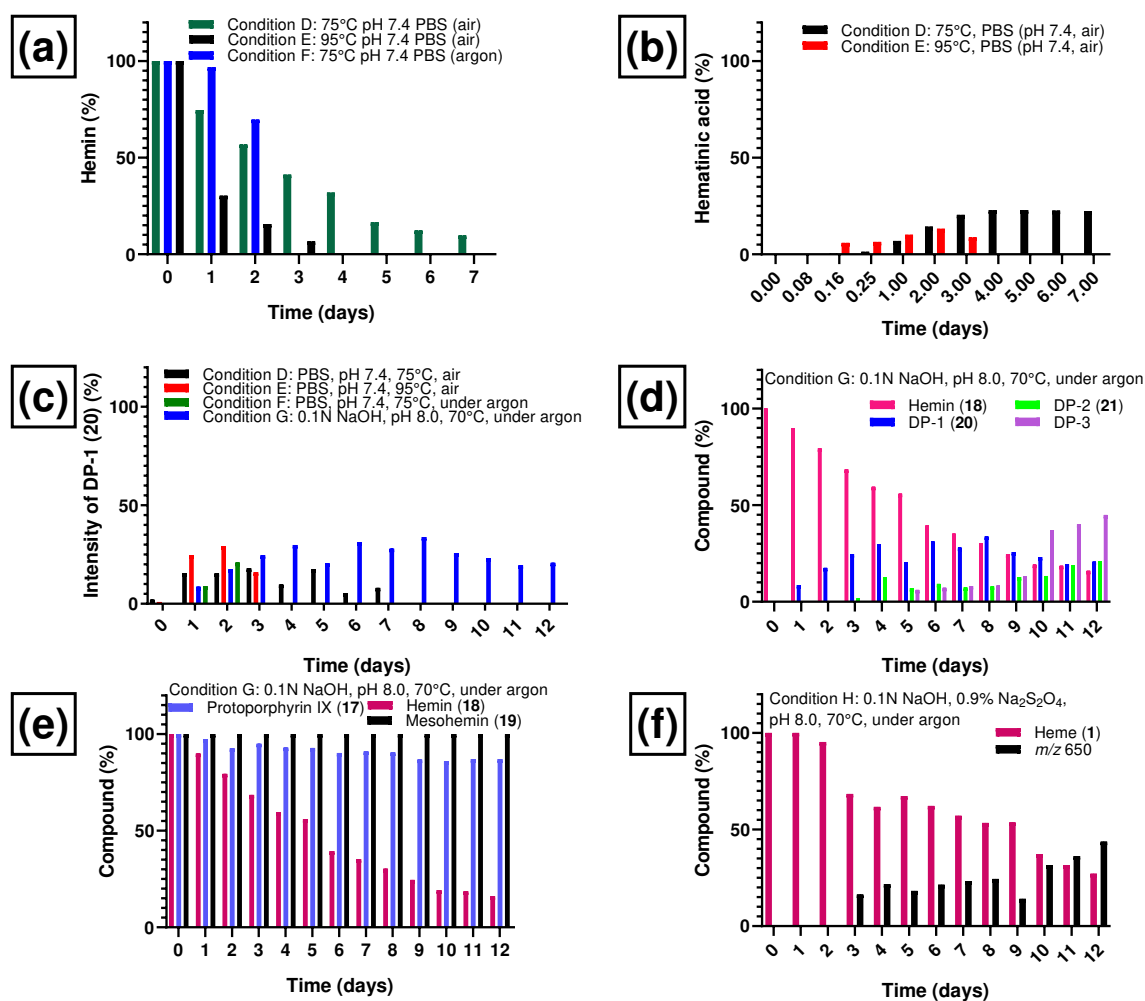
Figure 6. Degradation of hemin chloride (**18**) and formation of degradation products under various conditions. (**a**) Degradation of hemin chloride at pH 7.4 at elevated temperatures, in the presence or absence of air oxygen. (**b**) Formation of hematinic acid (**15**) from hemin chloride under condition **D** (phosphate-buffered saline, pH 7.4, 75 °C, air) and condition **E** (phosphate-buffered saline, pH 7.4, 95 °C, air). (**c**) Formation of degradation product DP-1 (**20**) from hemin chloride (**18**) at elevated temperatures (pH 7.4 and pH 8), in the presence or absence of air oxygen. (**d**) Degradation of hemin chloride and appearance of degradation products DP-1 (**20**), DP-2 (**21**), and DP-3 during 12 days of heating under condition **G** (in 0.1 N NaOH, pH 8, 70 °C, under argon). (**e**) Degradation profiles of protoporphyrin IX (**17**), hemin chloride (**18**), and mesohemin chloride (**19**) during 12 days of heating at 70 °C under an argon atmosphere (pH 8, condition **G**). (**f**) Degradation of heme (**1**) under condition **H** (0.1 N aq. NaOH, 0.9% sodium dithionite, pH 8, 70 °C, under argon) and formation of a major degradation product detected with mass-to-charge ratio of 650. The percentage of degradation product formation was calculated based on the ratio of its peak area to the total peak area (100%). The percentage of remaining hemin was estimated by relating its peak area to the peak area on day 0 (considered as 100% hemin).

Under thermal degradation conditions, we detected three other common degradation products, DP-1, DP-2, and DP-3 of initially unknown structure. DP-1, detected with a mass-to-charge ratio of 618.2, was formed in thermal degradation experiments in the presence of air (conditions **D** and **E** in Table 1) and under argon (conditions **F** and **G** in Table 1). The time-dependent formation of DP-1 under those conditions is shown in Figure 6c. In the presence of air, DP-1 reached its maximum around day 3 (18%, Figure 6c) when heated under condition **D** (phosphate-buffered saline, pH 7.4, air, 75 °C) and on day 2 (29%, Figure 6c) at 95 °C in the same medium (condition **E**). Even when heated under condition **F** (phosphate-buffered saline, pH 7.4, under argon, 75 °C), significant amounts of DP-1 were formed (Figure 6c). Thus, oxygen did not appear to be required in large amounts for its formation. The highest percentage of DP-1 was formed under weakly basic conditions (condition **G**, 0.1 N NaOH, pH 8, under argon, 70 °C), most likely due to a combination of changing the pH value, using a lower temperature, and avoiding an excess of oxygen. All of these factors may reduce the probability of further degradation of DP-1. DP-1 could not be detected after applying strongly oxidizing conditions (see conditions **A**–**C**, Table 1) due to the rapid degradation of hemin under these conditions.

The heating of hemin under condition **G** (0.1 N NaOH, pH 8, 70 °C for 12 days under argon, Figure 6d) resulted in a slightly longer half-life (5.5 days), and more degradation products were detectable under condition **G** compared to heating condition **F**. In addition to DP-1 and many minor degradation intermediates and products, at least two other major degradation products were formed, denominated DP-2 and DP-3 according to their order of appearance (see Figures 6d and 7a). Figure 6d depicts the time-dependent formation of degradation products DP-1, DP-2, and DP-3 and the parallel degradation of hemin under condition **G**. DP-1 appeared already after 1 day of heating the hemin solution at 70 °C and pH 8 under argon and reached a plateau between day 4 and day 9 (33%), followed by a steady decrease until the experiment was stopped on day 12 (21%). DP-2 was detected after 3 days and increased on day 4, when DP-1 began to reach a plateau, indicating that DP-2 could be formed from DP-1. DP-3 appeared on day 5 (Figure 6d) and steadily increased until the experiment was stopped at day 12. The minimum amount of DP-1 (21%) and the maximum amounts of DP-2 (21%) and DP-3 (45%) were thus reached on the last day of the experiment (day 12). The whole kinetic profile is in accordance with a subsequent reaction scheme in which DP-1 is formed first, followed by DP-2. DP-3 might be a subsequent reaction product of DP-1 and/or DP-2.

Accurate mass determination of the signal for DP-1 at m/z 618.1576 by high-resolution mass spectrometry (Table 2) revealed an elemental composition of $C_{33}H_{30}N_4O_5Fe^+$, i.e., an oxygen atom was incorporated into the structure of hemin, and a methylene moiety was eliminated. The isotope pattern as well as the fragmentation behavior (Figure 7b) of the mass-selected ion confirmed that the iron remained complexed and the propionyl groups of hemin were still present. There was no indication that the porphyrin ring of DP-1 had not remained intact. Thus, structure **20** is proposed for the formed compound DP-1 (Figure 8), in which one of the two original vinyl groups is oxidatively degraded to an aldehyde. Note that two isomers are possible because the two vinyl groups in heme are not equivalent but probably oxidized during the degradation experiments with equal probability.

DP-2 was detected with a mass-to-charge ratio of 620.1332 in accordance with an elemental composition of $C_{32}H_{28}N_4O_6Fe^+$. This result revealed that two oxygen atoms had been incorporated into the structure of hemin, and two CH_2 moieties were eliminated (Table 2 and Figure 8). The CID gas-phase fragmentation is consistent with the presence of aldehyde groups, in addition to the two unaltered carboxyethyl side chains (Figure 7b). Thus, this corroborates the assignment of DP-2 to structure **21**. From a chemical point of view, it is plausible that both vinyl groups in heme (**1**) were successively oxidized to aldehydes yielding first DP-1 (**20**) and then DP-2 (**21**). Our determination of the structure of DP-1 and DP-2 is consistent with previous studies in which the stability of hemin used for medical purposes, e.g., to treat various porphyrias [51], was tested in solutions containing 0.1 N aq. NaOH and while studying its degradation during γ-radiotherapy [52].

However, the degradation products have only been predicted based on monitoring UV-Vis spectra [52] so far. We have now for the first time elucidated the structures of these hemin degradation products by HPLC-coupled high-resolution tandem mass spectrometry.
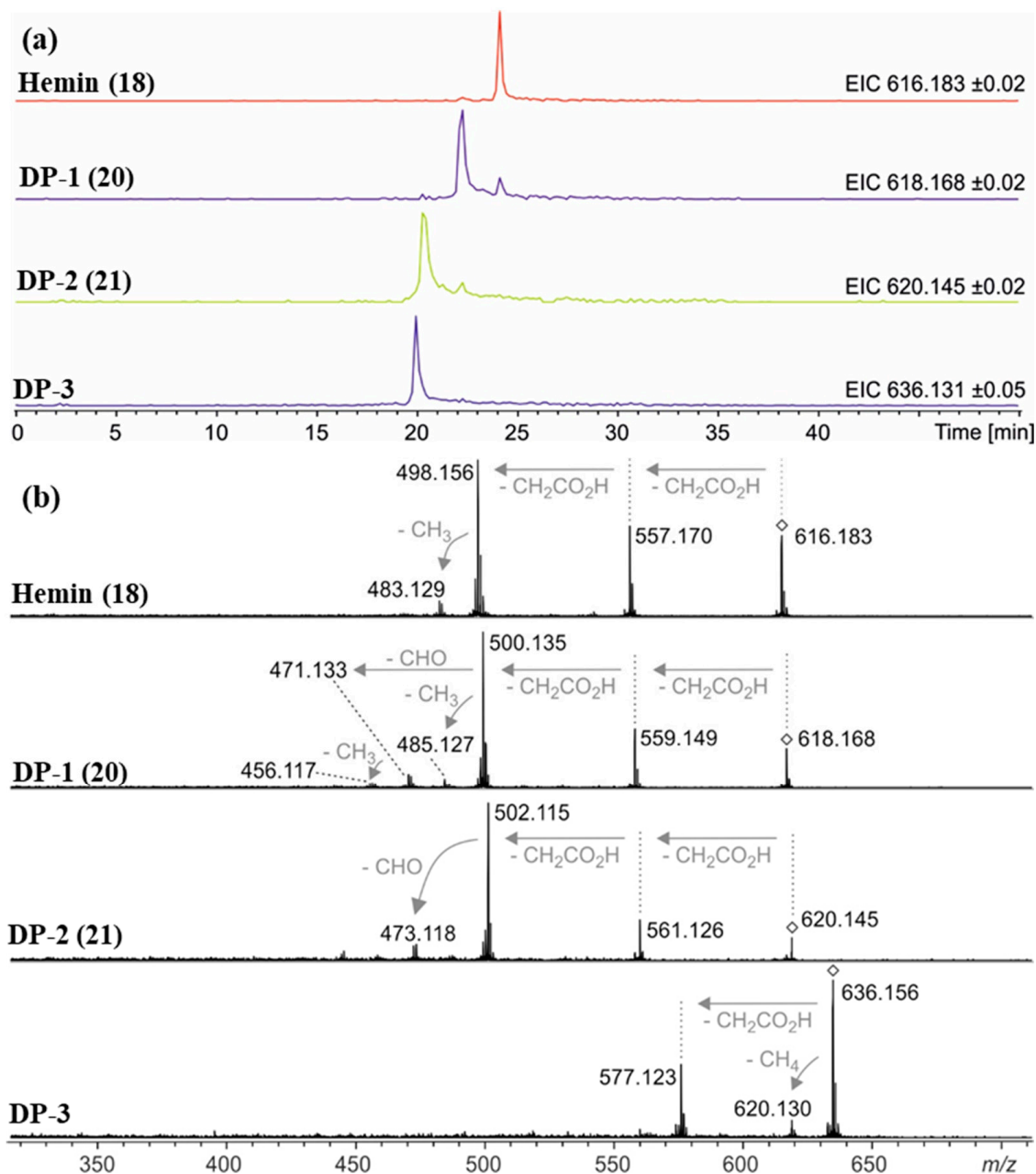
Figure 7. (**a**) Extracted ion chromatograms of hemin (**18**, m/z 616.2 ± 0.1 Da), degradation product 1 (DP-1, **20**, m/z 618.2 ± 0.1 Da), degradation product 2 (DP-2, **21**, m/z 620.2 ± 0.1 Da), and degradation product 3 (DP-3, m/z 636.2 ± 0.1 Da) detected via HPLC-ESI mass spectrometry after 12 days under condition G (0.1 N NaOH, pH 8, 70 °C under argon). The smaller signals approx. 2 min after the main peak for DP-1 and DP-2 are due to the isotope patterns of hemin and DP-1, respectively, as their masses fall into the mass ranges of the extracted ion chromatograms. (**b**) Collision-induced dissociation (CID) mass spectra showing the fragmentation behavior of mass-selected signals (◊) for hemin (**18**), DP-1 (**20**), DP-2 (**21**), and DP-3. In accordance with reference [50], gas-phase fragmentation of hemin proceeds via two consecutive losses of carboxymethyl radicals (Δm = 59.01 Da) followed by loss of methyl (Δm = 15.02 Da). DP-1 fragmentation starts similarly, but the third step is different: loss of CHO (Δm = 29.00 Da) is another indication of the formation of an aldehyde. Mass-selected ions around m/z 636.2 (DP-3) do not show loss of a CHO radical but loss of CH_4 instead (Δm = 16.03 Da).

Table 2. Mass-spectrometric data of hemin and its degradation products determined by high-resolution mass spectrometry (HRMS).

Compound [a]	Molecular Ion (Calculated Mass)	Molecular Formula	Accurate Mass Determination (HRMS)
Hemin (**18**)	616.1768	$C_{34}H_{32}N_4O_4Fe$	616.1785
DP-1 (**20**)	618.1561	$C_{33}H_{30}N_4O_5Fe$	618.1576
DP-2 (**21**)	620.1353	$C_{32}H_{28}N_4O_6Fe$	620.1332
DP-3	636.1302 636.1666	$C_{32}H_{28}N_4O_7Fe$ or $C_{33}H_{32}N_4O_6Fe$	636.137–636.159

[a] DP, degradation product.
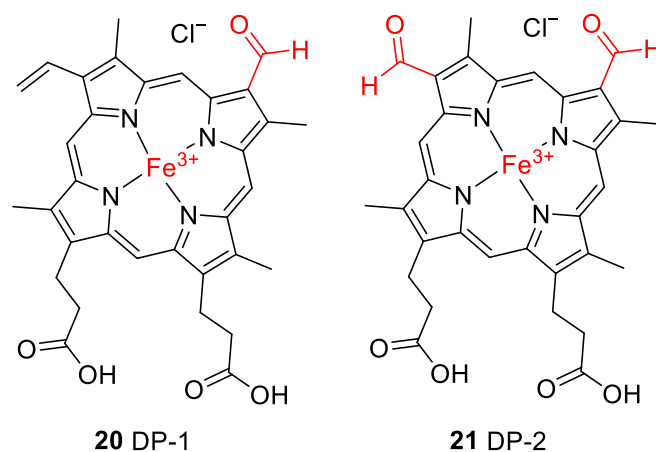
Figure 8. Proposed structures for hemin degradation products **20** and **21**. Note that two isomers are possible for **20** because the two inequivalent vinyl groups are oxidized with similar probability.

The recorded mass spectra for DP-3 (*m/z* 636.2) are not as clear as the previously discussed cases. A broadened signal is observed with an averaged mass shifting from *m/z* 636.159 down to 636.137 in the course of the chromatographic peak (Table 2). These findings are in accordance with a superposition of two compounds with overlapping retention times and similar masses around *m/z* 636.15 that are present in varying relative abundances and that unfortunately could not be separated by the limited resolving power of our Q/TOF mass spectrometer. Two matching elemental compositions are $C_{33}H_{32}N_4O_6Fe^+$ (calculated *m/z* 636.1666) in accordance with a formal addition of H_2O to DP-1, and $C_{32}H_{28}N_4O_7Fe^+$ (calculated *m/z* 636.1302) indicating that three oxygen atoms were incorporated into the structure of hemin while two methylene moieties had been eliminated (Table 2). A chemically plausible putative structure for the latter ion is a structure in which one of the two aldehyde groups of **21** was oxidized to a carboxyl group. In addition to the discussed degradation products DP-1–DP-3, a series of several other minor degradation products were formed under condition **G** (in 0.1 N NaOH, pH 8, 70 °C under argon), with more than three oxygen atoms incorporated into the structure according to the detected accurate masses. This suggests that further oxidation took place, but yields were too low for structural elucidation.

2.3. Control Experiments Reveal Site of Degradation and Role of Iron

To further verify the involvement of the vinyl groups in hemin degradation, a control experiment under condition **G** (0.1 N NaOH, pH 8, 70 °C, under argon) was performed with mesohemin chloride, a synthetic analog of hemin chloride, in which the vinyl groups are replaced by ethyl residues (compound **19**, Figure 4). Compound **19** remained completely stable over the entire experimental period of 12 days (Figure 6e). Thus, degradation products DP-1 and DP-2 are clearly formed by the reaction of the vinyl double bond(s) in hemin

by oxidative transformation to formyl groups. In accordance with the mass-spectrometric results described above, DP-1 can be assigned to **20**, ferric 2-formyl-8-vinyldeuteroporphyrin IX, and ferric 8-formyl-2-vinyldeuteroporphyrin IX, also known as *Spirographis* hemin or chlorocruorohemin (Figure 8) [53,54]. Compound **20** is found naturally as a prosthetic group of the oxygen-carrying pigment of certain species of worms from four families of marine polychaete annelids (chlorocruorin) but has not been detected in vertebrates. It was previously synthesized by the oxidation of 2-hydroxyethyl-8-vinylporphyrin [55] and protoporphyrin IX dimethyl ester [56] but has not yet been described as a degradation product of heme. Although two isomers of **20** are feasible, depending on which vinyl group was transformed into the formyl group, we only detected a single peak in the chromatogram (Figure 7) that probably represents the unresolved mixture of both isomers.

The kinetic profile of the formation of DP-2, as well as its mass-spectrometric characterization, shows that it is likely a degradation product derived from DP-1 with structure **20**. It can be concluded that DP-2 has structure **21** with two formyl groups in positions 2 and 8 of the porphyrin ring. Ferric 2,8-diformylporphyrin IX (**21**, Figure 8) has been previously synthesized [57,58]. In addition, the iron-free derivatives of **20** [59] and **21** [60] were described as photooxidation products of protoporphyrin IX (**17**). Since compounds similar to **20** and **21** could not be observed when mesohemin was studied in which reactive terminal double bonds were absent, the instability of hemin is clearly due to the presence of the vinyl groups, which is in agreement with our results as well as previous findings [61–63].

Among other degradation routes, one of the formyl groups in **21** may be further oxidized to a carboxylic acid yielding ferric 2-formylporphyrin IX-8-carboxylic acid as well as its positional isomer. The mass-spectrometric data give some indications for its presence in the reaction mixture of the degradation experiments. The corresponding dicarboxylic acid derivative has previously been synthesized from hemin [64].

An additional control experiment was carried out again under condition **G** (0.1 N NaOH, pH 8, 70 °C under argon) using protoporphyrin IX (**17**), the iron-free derivative of heme (Figure 4). Our aim was to investigate whether iron is involved in the oxidation reaction. Protoporphyrin IX was much more stable than hemin, with around 85% of the starting compound remaining intact after 12 days (Figure 6e). Very minor new peaks were detected in the chromatograms (amounting to less than 5% of the total peak area) at m/z 579 and 581 probably according to an incorporation of an oxygen atom and a formal addition of water, respectively. These results confirm that the iron center plays a major role in the degradation of hemin and the oxidation of its vinyl groups (see Figure 6). A putative degradation mechanism involves the addition of O_2 to the vinyl group(s), leading to the formation of a 1,2-dioxetane, which is subsequently cleaved, generating the formyl group (Figure 9) [65]. Iron species likely catalyze this oxidative reaction [66].
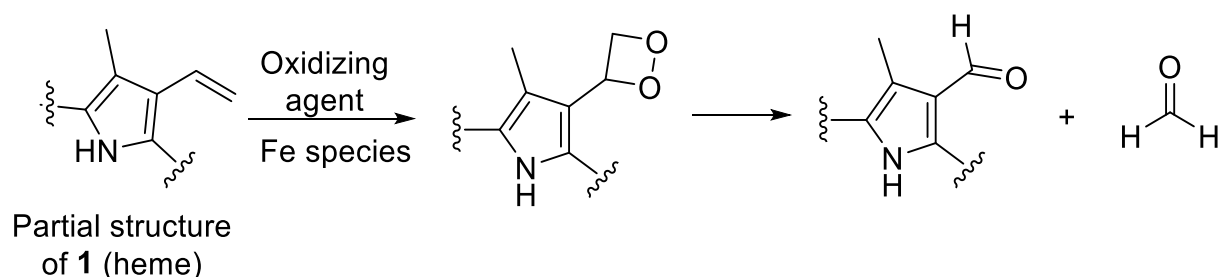
Figure 9. Putative mechanism for the oxidation of a vinyl group of heme to a formyl group, which is accelerated in the presence of iron [65,66].

2.4. Reductive Conditions

Finally, hemin degradation was studied under reductive conditions in the presence of sodium dithionite (condition **H**, 0.1 N NaOH and 0.9% sodium dithionite, pH 8, 70 °C, under argon). Here, iron is in the ferrous (Fe^{2+}) state, and the predominant species present in solution is heme (**1**), although it is detected at m/z 616 in the electrospray mass spectra

due to oxidation in the course of the ionization process. Under condition **H**, this compound was completely stable until day 2 (Figure 6f). On day 3, heme started to degrade with a half-life of about 9.5 days and was still detectable on day 12, the last day of the experiment (Figure 6f). The major degradation product was a compound with a mass-to-charge ratio of *m/z* 650 detected in positive mode, which appeared on day 3, increasing steadily, reaching 43% of the total peak area on day 12 (Figure 6f). We could not identify this ion so far. The elucidation of the identity of this ion is the subject of future work. Additional minor compounds were detected with mass-to-charge ratios of *m/z* 618 and 634, which may imply that DP-1 (**20**) was formed in small amounts followed by oxidation to the carboxylic acid derivative. DP-2 (**21**) and DP-3 were not detected under these reductive conditions. Sodium dithionite may induce a combination of oxidations and reductions, involving reactive sulfur and oxygen species. In the presence of sodium dithionite, hemin (Fe^{3+}) is reduced to heme (Fe^{2+}). Fe(II) is a powerful reducing agent [67,68]. Our results show that hemin is more stable under reductive conditions (half-life 9.5 days) than in the absence of reducing agents (condition **G**, 0.1 N NaOH, pH 8, 70 °C under argon, half-life 5.5 days). Reductive conditions may play a role in the early stages of fossilization and could contribute to the preservation of heme in fossils. This is consistent with the reports of heme preservation in the fossil record. The mosquitoes discussed above were embedded in an anaerobic mud at the bottom of a lake [31]. A sea turtle with heme preservation in its soft tissue was preserved under similar conditions, in anaerobic fine mud at the bottom of the ancestral North Sea [32]. In addition, the single report so far of heme in fossil bone is also plausible because of the anaerobic and alkaline microenvironment that developed quickly during decay experiments on bone [45]. We observed that in the absence of air, under slightly basic conditions of pH 8, stability was higher, while it decreased at pH 7.4. This again is consistent with decay studies on fresh bone where a pH value of 8.0–8.5 was measured [45].

3. Materials and Methods

The conditions used for the degradation studies on hemin are summarized in Table 1 and described in detail below.

3.1. Materials

Hemin chloride (product number 51280), protoporphyrin IX disodium salt (product number 258385**)**, and sodium dithionite (product number 71699) were purchased from Sigma Aldrich (Darmstadt, Germany). Ferric mesoporphyrin IX chloride (mesohemin chloride, product number sc-396889) was purchased from Santa Cruz Biotechnology Inc. (Heidelberg, Germany). Millipore water was used for LC-MS analysis (from an in-house Millipore water purification system, Darmstadt, Germany). LC-MS-grade methanol (product number 34966) was purchased from Honeywell (Offenbach/Main, Germany). Formic acid (LC-MS grade, product number 84865.180) and hydrochloric acid (37%, product number 20252.290) were purchased from VWR Chemicals (Darmstadt, Germany). Analytical-grade sodium hydroxide (product number 1375.1000) and ammonia solution (25% in water, product number 2672.1011) were purchased from Chemsolute (Renningen, Germany). Hydrogen peroxide (30% in water, product number AB129030) was purchased from abcr (Karlsruhe, Germany). Ammonium acetate (LC-MS grade, product number 73594) was purchased from Merck (Darmstadt, Germany).

3.2. Oxidative Degradation (Conditions *A–C*, Table 1)

Oxidative degradation was carried out using hydrogen peroxide in methanol containing 1% ammonia at room temperature for 10 min or in phosphate-buffered saline (pH 7.4) at room temperature for 7 h, or in water containing 1% ammonia (pH 10) at 60 °C for the initial 30 min, then continued at room temperature for up to 7 h.

3.2.1. Oxidation under Alkaline Methanolic Conditions (Condition **A**, Table 1)

Hemin chloride (300 mg) was dissolved in 60 mL of methanol containing 1% ammonia, and 5 drops (0.25 mL) of aq. H_2O_2 were added to the solution by stirring it at room temperature. After each addition, aliquots of 10 mL were evaporated, re-suspended in 5 mL methanol, and analyzed by HPLC-(DAD-UV)-MS. At the end, a 10 mL aliquot of the remaining hemin/aq. H_2O_2 solution was diluted with 4 volumes of water. This solution was extracted three consecutive times with dichloromethane (50 mL for each extraction). After each extraction, the organic phase was collected. After the three extractions, the organic phases were combined, dried over magnesium sulfate, and evaporated to dryness. The residue was re-suspended in methanol to make a 1 mg/mL solution and was analyzed by HPLC-(DAD-UV)-MS. The aqueous phase remaining after the last extraction was analyzed as well.

3.2.2. Oxidation under Alkaline Aqueous Conditions (Condition **B**, Table 1)

Hemin chloride (100 mg) was dissolved in 18 mL water containing 1% ammonia (pH 10.5). To this solution, 3 mL of 35% hydrogen peroxide (H_2O_2) solution was added (final concentration 5% H_2O_2 *w/v*). The mixture was heated for 1 h at 60 °C and then lyophilized. After resuspending the lyophilizate in methanol, the solution was diluted with 4 volumes of water and extracted three consecutive times with dichloromethane (50 mL for each extraction). After each extraction, the organic phase was collected. After the three extractions, the organic phases were combined, dried over magnesium sulfate, and evaporated to dryness. The residue was re-suspended in methanol to make a 1 mg/mL solution and was analyzed by HPLC-(DAD-UV)-MS.

3.2.3. Oxidation at Physiological pH Value (Condition **C**, Table 1)

A 1.3 mg/mL (2 mM) solution of hemin chloride in phosphate-buffered saline (PBS) was set to pH 7.4 (8.55 mL of PBS, 0.45 mL of 0.1 N HCl, and 1 mL of a 20 mM hemin in 0.1 N NaOH were added). This concentration was chosen because hemin was not soluble in PBS at the high concentrations used in the previous experiments (more soluble in alkaline conditions). Portions (5 drops or 0.25 mL) of 30% *w/v* H_2O_2 were added to 5 mL of 2 mM hemin in PBS to obtain the final concentration of 5% H_2O_2, and the reaction was monitored for 15 min., then left to stand. Aliquots were taken for measurement with HPLC-(DAD-UV)-MS after 5, 10, and 15 min. and after left standing for 4 and 8 h.

3.3. Thermal Degradation

3.3.1. Thermal Degradation at Physiological pH Value (Conditions **D**–**F**, Table 1)

A 1.3 mg/mL (2 mM) solution of hemin in PBS was set to pH 7.4 (8.55 mL of PBS, 0.45 mL of 0.1 N HCl, and 1 mL of a 20 mM hemin in 0.1 N NaOH were added) and heated to 75 °C (condition **D**, Table 1) or to 95 °C (condition **E**, Table 1) in a glass-stoppered flask, respectively. Aliquots were taken at 0, 2 h, 4 h, 6 h, 1 day, and then daily intervals for a total of 7 days (at 75 °C, condition **D**, Table 1) and for 3 days (95 °C, condition **E**, Table 1) and analyzed by HPLC-(DAD-UV)-MS. To study the effect of anoxic conditions, the same procedure at 75 °C was performed over 2 days under an argon atmosphere (condition **F**, Table 1). Aliquots were taken at 0, 2 h, 4 h, 6 h, 24 h, and 48 h and analyzed by HPLC-(DAD-UV)-MS.

3.3.2. Thermal Degradation at Alkaline pH under an Argon Atmosphere (Condition **G**, Table 1)

A 12 mg/mL solution of hemin in 0.1 N NaOH was set to pH 8 using 0.1 N HCl and heated to 70 °C under an argon atmosphere for a total of 12 days (condition **G**, Table 1). The solution was flushed with argon at the beginning of the experiment for at least 15 min, and then the vial remained closed for 12 days. Aliquots were taken at the start and afterward daily, lyophilized and re-dissolved in methanol to give a 1 mg/mL solution, or, if not soluble in methanol, in a mixture of methanol and Millipore water, and then analyzed by HPLC-

(DAD-UV)-MS. As control experiments, a 1.8 mg/mL solution of ferric mesoporphyrin IX chloride (pH 8) and a 12 mg/mL solution of protoporphyrin IX disodium salt were exposed to the same conditions for 12 days.

3.4. Reductive Conditions (Condition **H**, Table 1)

A 12 mg/mL solution of hemin in 0.1 N NaOH was set to pH 8 using 0.1 N HCl and heated to 70 °C in the presence of sodium dithionite (0.9% *w/v*) under an argon atmosphere for a total of 12 days (condition **H**, Table 1). Aliquots of 2 mL were taken at the start and daily, lyophilized and re-dissolved in methanol to give a 1 mg/mL solution, or, if not soluble in methanol, in a mixture of methanol and Millipore water, and then analyzed by HPLC-(DAD-UV)-MS.

3.5. Preparative Reversed-Phase HPLC for Isolation of Hematinic Acid

Isolation of hematinic acid by preparative HPLC was performed as follows: A portion of the lyophilized reaction mixture from condition A (1% NH_3 in methanol, pH 11.5, final conc. 5% aq. H_2O_2, RT) having a crude weight of 3.3 g was purified by preparative reversed-phase HPLC. The method consisted of the following parameters: flow rate was 25 mL/min, mobile phase A consisted of acetonitrile + 0.05% trifluoroacetic acid (TFA), and mobile phase B consisted of water + 0.05% TFA. The run started as follows: 20% A (0–1 min), followed by a gradient that reached 100% A (1–8 min), followed by flushing with 100% A (8–16 min). This produced 41.3 mg (1.3% yield) of hematinic acid, having 93.6% purity. The structure was confirmed by high-resolution electrospray mass spectrometry (Orbitrap XL, Thermo Fisher Scientific) and by nuclear magnetic resonance spectroscopy (NMR; see Supplementary Figures S1–S4 for spectra).

3.6. Analysis by HPLC-(DAD-UV)-MS

Measurements were performed on an Agilent 1260 Infinity HPLC coupled to an Agilent Infinity Lab LC/MSD single-quadrupole mass spectrometer with an electrospray ion source and a DAD-UV detector (200–600 nm) (Agilent Technologies Germany GmbH & Co. KG, Waldbronn, Germany). Chromatographic separation was performed on an EC 50/3 Nucleodur C18 Gravity, 3 μm column (Macherey-Nagel, Düren, Germany) column. Mobile phase A consisted of methanol with 2 mmol/l ammonium acetate, and mobile phase B consisted of water with 0.1% formic acid. The run started with 10% A and 90% B, followed by a gradient that reached 100% of eluent A after 20 min. Then, the column was flushed for 5 min. with 100% of mobile phase A followed by 10% A and 90% B for 5 min. before starting the next run. Positive full-scan MS was obtained from 100 to 1500 *m/z*. The column temperature was set at 40 °C, the injection volume varied between 1 and 5 μL depending on the concentration of the sample, and the flow rate was adjusted to 0.5 mL/min. Data were collected and processed using the Data Analysis program on OpenLab CDS 2.6 software (Agilent Technologies Germany GmbH & Co. KG, Waldbronn, Germany). The extracted ion chromatogram (EIC) was used to identify known degradation products using their masses, and the DAD total wavelength chromatogram was used to calculate yields of the different degradation products at each time point. Sample concentration was approximately 1 mg/mL in methanol or a mixture of methanol and Millipore water.

3.7. Analysis by HPLC-Coupled High-Resolution Mass Spectrometry

Measurements were performed on a Bruker micrOTOF-Q quadrupole/time-of-flight mass spectrometer equipped with an electrospray ion source. The mass spectrometer was coupled with an Agilent HPLC 1200 Series with a UV variable wavelength detector set to 450 nm. A reversed-phase Eurospher II 100-5 C18 column (150 × 2 mm) from Knauer was used with a flow rate of 0.2 mL/min. Mobile phases A and B were used as described in Section 3.6. The run started with 10% A and 90% B for 2 min, followed by a gradient that reached 100% of eluent A after 22 min. Then, the column was flushed for 5 min with 100% of mobile phase A followed by 10% A and 90% B for 20 min before starting the next run.

ESI mass spectra were recorded in positive mode in a mass range from m/z 150 to 2000 and externally calibrated with the LC-MS calibration standard Tuning Mix from Agilent. Collision-induced dissociation (CID) spectra were measured in MRM mode with a collision energy of 30–50 eV. Data were collected and processed using the Compass software package (Compass 1.3—SR1, Data Analysis 4.0—SR5, HyStar 3.2 SR4) from Bruker Daltonik GmbH, Bremen, Germany.

3.8. Analysis of Hematinic Acid by Nuclear Magnetic Resonance Spectroscopy (NMR)

Proton NMR (^{1}H NMR) and attached proton test (APT)-carbon NMR (^{13}C NMR) spectra were recorded at room temperature on a Bruker-500 spectrometer (at 500 MHz and 126 MHz, respectively) using tetramethylsilane as internal standard. Chemical shifts are reported in δ (parts per million: ppm). The following abbreviation is used for multiplicity of NMR signals: (s) singlet. For hematinic acid, the spectra were determined in $(CD_3)_2SO$ (DMSO-d_6): ^{1}H NMR (500 MHz, DMSO-d_6): δ 1.86 (s, 3H, CH_3), 2.45 (s, 2H, CH_2), 2.51 (s, 2H, CH_2). The propionic acid and pyrrolic-NH protons were exchanged with deuterium in a D2O exchange experiment. ^{13}C APT-NMR (126 MHz, DMSO-d_6): δ 173, 31.8, 18.9, 8.3. Signals matched the chemical shifts reported in the literature for hematinic acid [18,24,48].

4. Conclusions

Heme, the prosthetic group of hemoglobin present in blood, was studied under a series of different, controlled conditions potentially present in the early stages of fossilization. Our aim was to simulate heme decay and identify potential degradation products formed during fossilization and preservation. The results obtained in the present study indicate that hemin, due to its central iron atom and reactive vinyl groups, has limited stability under conditions relevant for early-stage fossilization. The highest stability was observed under anaerobic reductive conditions.

Under strongly oxidative conditions, hemin is especially vulnerable and rapidly degraded. As a major degradation product of hemin, we identified hematinic acid (**15**). Under less harsh conditions, degradation of hemin is slower, and some intermediate oxidation products can be observed, i.e., ferric 2-formyl-8-vinylporphyrin IX (**20**), ferric 2,8-diformylporphyrin IX (**21**), and ferric 2-formylporphyrin IX-8-carboxylic acid, among others, including positional isomers and further oxidized products. Compounds **21** and **22** had been previously predicted but were identified now by mass spectrometry as degradation products of heme for the first time. Hematinic acid was formed only in the presence of air oxygen after heating at neutral pH or in the presence of the powerful oxidizing agent H_2O_2. DP-1 was formed after heating at neutral pH (7.4) or alkaline pH (8). DP-2 and DP-3 were only observed in the absence of air oxygen and at alkaline pH (8). Control experiments using mesohemin (**19**) and protoporphyrin IX (**17**) clearly showed that the vinyl groups are the site of degradation via the stepwise oxidation of the vinyl groups to formyl and further to the corresponding carboxylic acid functions and that iron plays a crucial role in these transformations. Thus, based on the findings from these experiments, the preservation of hemin in the fossil record is not unlikely, as the experiments were performed under presumed fossilization conditions, but the preservation of heme is more probable in the absence of air in a basic environment. To our knowledge, this is the first molecular taphonomy study on heme. The identification of degradation pathways and products under various conditions may be useful for further investigations on heme in fossils.

Supplementary Materials: The following Supporting Information can be downloaded at https://www.mdpi.com/article/10.3390/molecules28134887/s1: Figure S1: ^{1}H-NMR spectrum of the isolated hematinic acid, including signal assignments, determined in DMSO-d_6, Figure S2: [13]C attached proton test (APT) NMR spectrum of the isolated hematinic acid, including signal assignments, determined in DMSO-d_6, Figure S3: Orbitrap XL high-resolution mass spectra of the isolated hematinic acid, showing its molecular ions at m/z 184.06042 (calculated 184.06043 for [M + H]$^+$) and m/z 206.04239 (206.04238 calculated for [M + Na]$^+$), Figure S4: High-resolution collision-induced

dissociation mass spectra of the isolated hematinic acid, showing its fragmentation pattern to the major fragments 166.051, 138.056, and 84.045 *m/z*.

References

1. Giardina, B.; Messana, I.; Scatena, R.; Castagnola, M. The multiple functions of hemoglobin. *Crit. Rev. Biochem. Mol. Biol.* **1995**, *30*, 165–196. [CrossRef]
2. Tahoun, M.; Gee, C.T.; McCoy, V.E.; Sander, P.M.; Müller, C.E. Chemistry of porphyrins in fossil plants and animals. *RSC Adv.* **2021**, *11*, 7552–7563. [CrossRef]
3. Kundu, S.; Trent, J.T.; Hargrove, M.S. Plants, humans and hemoglobins. *Trends Plant Sci.* **2003**, *8*, 387–393. [CrossRef]
4. Yoshida, T.; Migita, C.T. Mechanism of heme degradation by heme oxygenase. *J. Inorg. Biochem.* **2000**, *82*, 33–41. [CrossRef]
5. Kikuchi, G.; Yoshida, T.; Noguchi, M. Heme oxygenase and heme degradation. *Biochem. Biophys. Res. Commun.* **2005**, *338*, 558–567. [CrossRef]
6. Terry, M.J.; Linley, P.J.; Kohchi, T. Making light of it: The role of plant haem oxygenases in phytochrome chromophore synthesis. *Biochem. Soc. Trans.* **2002**, *30*, 604–609. [CrossRef]
7. Cornejo, J.; Beale, S.I. Phycobilin biosynthetic reactions in extracts of cyanobacteria. *Photosynth. Res.* **1997**, *51*, 223–230. [CrossRef]
8. Beale, S.I. Biosynthesis of phycobilins. *Chem. Rev.* **1993**, *93*, 785–802. [CrossRef]
9. Pendrak, M.L.; Chao, M.P.; Yan, S.S.; Roberts, D.D. Heme oxygenase in *Candida albicans* is regulated by hemoglobin and is necessary for metabolism of exogenous heme and hemoglobin to α-biliverdin. *J. Biol. Chem.* **2004**, *279*, 3426–3433. [CrossRef]
10. Schmitt, M.P. Utilization of host iron sources by *Corynebacterium diphtheriae*: Identification of a gene whose product is homologous to eukaryotic heme oxygenases and is required for acquisition of iron from heme and hemoglobin. *J. Bacteriol.* **1997**, *179*, 838–845. [CrossRef]
11. Wilks, A.; Schmitt, M.P. Expression and characterization of a heme oxygenase (Hmu O) from *Corynebacterium diphtheriae*. *J. Biol. Chem.* **1998**, *273*, 837–841. [CrossRef] [PubMed]
12. Melanie, R.; Wenming, Z.; Rahul, D.; Angela, W.; Igor, S. Homologues of neisserial heme oxygenase in Gram-negative bacteria: Degradation of heme by the product of the *pigA* gene of *Pseudomonas aeruginosa*. *J. Bacteriol.* **2001**, *183*, 6394–6403. [CrossRef]
13. Zhu, W.; Wilks, A.; Stojiljkovic, I. Degradation of heme in Gram-negative bacteria: The product of the *hemO* gene of neisseriae is a heme oxygenase. *J. Bacteriol.* **2000**, *182*, 6783–6790. [CrossRef]
14. Zhu, W.; Hunt, D.J.; Richardson, A.R.; Stojiljkovic, I. Use of heme compounds as iron sources by pathogenic neisseriae requires the product of the *hemO* gene. *J. Bacteriol.* **2000**, *182*, 439–447. [CrossRef]
15. Tenhunen, R.; Marver, H.S.; Schmid, R. The enzymatic conversion of heme to bilirubin by microsomal heme oxygenase. *Proc. Natl. Acad. Sci. USA* **1968**, *61*, 748–755. [CrossRef]
16. Bonnett, R.; McDonagh, A.F. The meso-reactivity of porphyrins and related compounds. Part VI. Oxidative cleavage of the haem system. The four isomeric biliverdins of the IX series. *J. Chem. Soc. Perkin Trans. 1* **1973**, 881–888. [CrossRef] [PubMed]

17. Giulivi, C.; Cadenas, E. The reaction of ascorbic acid with different heme iron redox states of myoglobin. *FEBS Lett.* **1993**, *332*, 287–290. [CrossRef]

18. Schaefer, W.H.; Harris, T.M.; Guengerich, F.P. Characterization of the enzymic and nonenzymic peroxidative degradation of iron porphyrins and cytochrome P-450 heme. *Biochemistry* **1985**, *24*, 3254–3263. [CrossRef] [PubMed]

19. Guengerich, F.P. Destruction of heme and hemoproteins mediated by liver microsomal reduced nicotinamide adenine dinucleotide phosphate-cytochrome P-450 reductase. *Biochemistry* **1978**, *17*, 3633–3639. [CrossRef]

20. Ouellet, Y.H.; Ndiaye, C.T.; Gagné, S.M.; Sebilo, A.; Suits, M.D.L.; Jubinville, É.; Jia, Z.; Ivancich, A.; Couture, M. An alternative reaction for heme degradation catalyzed by the *Escherichia coli* O157:H7 ChuS protein: Release of hematinic acid, tripyrrole and Fe(III). *J. Inorg. Biochem.* **2016**, *154*, 103–113. [CrossRef]

21. Groves, J.T.; Haushalter, R.C.; Nakamura, M.; Nemo, T.E.; Evans, B.J. High-valent iron-porphyrin complexes related to peroxidase and cytochrome P-450. *J. Am. Chem. Soc.* **1981**, *103*, 2884–2886. [CrossRef]

22. Takahashi, A.; Kurahashi, T.; Fujii, H. Redox potentials of oxoiron(IV) porphyrin π-cation radical complexes: Participation of electron transfer process in oxygenation reactions. *Inorg. Chem.* **2011**, *50*, 6922–6928. [CrossRef]

23. Ritter, M.; Oetama, V.S.P.; Schulze, D.; Muetzlaff, K.; Meents, A.K.; Seidel, R.A.; Görls, H.; Westerhausen, M.; Boland, W.; Pohnert, G. Pyrrolic and dipyrrolic chlorophyll degradation products in plants and herbivores. *Chem.-Eur. J.* **2020**, *26*, 6205–6213. [CrossRef] [PubMed]

24. Lightner, D.A.; Quistad, G.B. Hematinic acid and propentdyopents from bilirubin photo-oxidation in vitro. *FEBS Lett.* **1972**, *25*, 94–96. [CrossRef] [PubMed]

25. Lightner, D.A.; Linnane, W.P.; Ahlfors, C.E. Bilirubin photooxidation products in the urine of jaundiced neonates receiving phototherapy. *Pediatr. Res.* **1984**, *18*, 696–700. [CrossRef]

26. Rüdiger, W. Recent chemistry and biochemistry of bile pigments. *Angew. Chem. Int. Ed. Engl.* **1970**, *9*, 473–480. [CrossRef]

27. Muir, H.M.; Neuberger, A. The biogenesis of porphyrins. 2. The origin of the methyne carbon atoms. *Biochem. J.* **1950**, *47*, 97–104. [CrossRef] [PubMed]

28. Hirota, K.; Sasaki, K. Production of hematinic acid by the reaction of hemoglobin with phenylhydrazine: Evidence for the oxidative cleavage of heme. *Biol. Pharm. Bull.* **1994**, *17*, 856–858. [CrossRef] [PubMed]

29. Suzuki, Y.; Shioi, Y. Detection of chlorophyll breakdown products in the senescent leaves of higher plants. *Plant Cell Physiol.* **1999**, *40*, 909–915. [CrossRef]

30. Schweitzer, M.H.; Marshall, M.; Carron, K.; Bohle, D.S.; Busse, S.C.; Arnold, E.V.; Barnard, D.; Horner, J.R.; Starkey, J.R. Heme compounds in dinosaur trabecular bone. *Proc. Natl. Acad. Sci. USA* **1997**, *94*, 6291–6296. [CrossRef]

31. Greenwalt, D.E.; Goreva, Y.S.; Siljeström, S.M.; Rose, T.; Harbach, R.E. Hemoglobin-derived porphyrins preserved in a Middle Eocene blood-engorged mosquito. *Proc. Natl. Acad. Sci. USA* **2013**, *110*, 18496–18500. [CrossRef] [PubMed]

32. Lindgren, J.; Kuriyama, T.; Madsen, H.; Sjövall, P.; Zheng, W.; Uvdal, P.; Engdahl, A.; Moyer, A.E.; Gren, J.A.; Kamezaki, N.; et al. Biochemistry and adaptive colouration of an exceptionally preserved juvenile fossil sea turtle. *Sci. Rep.* **2017**, *7*, 13324. [CrossRef]

33. Wiemann, J.; Yang, T.R.; Sander, P.N.; Schneider, M.; Engeser, M.; Kath-Schorr, S.; Müller, C.E.; Sander, P.M. Dinosaur origin of egg color: Oviraptors laid blue-green eggs. *PeerJ* **2017**, *5*, e3706. [CrossRef] [PubMed]

34. Wiersma, K.; Läbe, S.; Sander, P.M. Organic phase preservation in fossil dinosaur and other tetrapod bone from deep time. In *Fossilization: Understanding the Material Nature of Ancient Plants and Animals*; Gee, C.T., McCoy, V.E., Sander, P.M., Eds.; Johns Hopkins University Press: Baltimore, MD, USA, 2021; pp. 16–45. ISBN 9781421440217.

35. Schweitzer, M.H.; Wittmeyer, J.L.; Horner, J.R. Soft tissue and cellular preservation in vertebrate skeletal elements from the Cretaceous to the present. *Proc. R. Soc. B Biol. Sci.* **2007**, *274*, 183–197. [CrossRef]

36. Schweitzer, M.H. Soft tissue preservation in terrestrial Mesozoic vertebrates. *Annu. Rev. Earth Planet. Sci.* **2011**, *39*, 187–216. [CrossRef]

37. Tahoun, M.; Engeser, M.; Namasivayam, V.; Sander, P.M.; Müller, C.E. Chemistry and analysis of organic compounds in dinosaurs. *Biology* **2022**, *11*, 670. [CrossRef]

38. Behrensmeyer, A.K.; Kidwell, S.M. Taphonomy's contributions to paleobiology. *Paleobiology* **1985**, *11*, 105–119. [CrossRef]

39. Behrensmeyer, A.K.; Kidwell, S.M.; Gastaldo, R.A. Taphonomy and paleobiology. *Paleobiology* **2000**, *26*, 103–147. [CrossRef]

40. Gifford, D.P. Taphonomy and paleoecology: A critical review of archaeology's sister disciplines. In *Advances in Archaeological Method and Theory*; Academic Press: New York, NY, USA, 1981; pp. 365–438.

41. Schweitzer, M.H.; Zheng, W.; Cleland, T.P.; Goodwin, M.B.; Boatman, E.; Theil, E.; Marcus, M.A.; Fakra, S.C. A role for iron and oxygen chemistry in preserving soft tissues, cells and molecules from deep time. *Proc. R. Soc. B Biol. Sci.* **2014**, *281*, 20132741. [CrossRef] [PubMed]

42. Eglinton, G.; Logan, G.A. Molecular preservation. *Philos. Trans. R. Soc. Lond. B Biol. Sci.* **1991**, *333*, 315–328. [CrossRef]

43. Latham, K.E.; Miller, J.J. DNA recovery and analysis from skeletal material in modern forensic contexts. *Forensic Sci. Res.* **2019**, *4*, 51–59. [CrossRef]

44. Retallack, G.J. Organisms. In *Soils of the Past: An Introduction to Paleopedology*, 2nd ed.; Blackwell Science Ltd.: Oxford, UK, 2001; pp. 128–159.

45. Pfretzschner, H.-U. Fossilization of Haversian bone in aquatic environments. *Comptes Rendus Palevol* **2004**, *3*, 605–616. [CrossRef]

46. Von Endt, D.W.; Ortner, D.J. Experimental effects of bone size and temperature on bone diagenesis. *J. Archaeol. Sci.* **1984**, *11*, 247–253. [CrossRef]

47. Briggs, D.E.G.; McMahon, S. The role of experiments in investigating the taphonomy of exceptional preservation. *Palaeontology* **2016**, *59*, 1–11. [CrossRef]

48. Brynjelsen, S.E.; Doty, M.; Poss, M.J. Facile synthesis of hematinic acid. *Synth. Commun.* **1998**, *28*, 1885–1889. [CrossRef]

49. Tomat, E. Propentdyopents: Brief history of a family of dipyrrolic pigments. *J. Porphyr. Phthalocyanines* **2019**, *23*, 1265–1272. [CrossRef]

50. Charkin, O.P.; Klimenko, N.M.; Nguyen, P.T.; Charkin, D.O.; Mebel, A.M.; Lin, S.H.; Wang, Y.-S.; Wei, S.-C.; Chang, H.-C. Fragmentation of heme and hemin+ with sequential loss of carboxymethyl groups: A DFT and mass-spectrometry study. *Chem. Phys. Lett.* **2005**, *415*, 362–369. [CrossRef]

51. Siegert, S.W.K.; Holt, R.J. Physicochemical properties, pharmacokinetics, and pharmacodynamics of intravenous hematin: A literature review. *Adv. Ther.* **2008**, *25*, 842–857. [CrossRef]

52. Rothschild, M.-L.; Cosi, L.; Myers, L.S. Effect of gamma-radiation on ferriprotoporphyrin. *Nature* **1958**, *182*, 316. [CrossRef] [PubMed]

53. Jackson, A.H.; Kenner, G.W.; Wass, J. Pyrroles and related compounds. Part XXV. Pemptoporphyrin, isopemptoporphyrin, and chlorocruoroporphyrin (*Spirographis* porphyrin). *J. Chem. Soc. Perkin Trans. 1* **1974**, 480–490. [CrossRef]

54. Inhoffen, H.H.; Bliesener, C.; Brockmann, H. Zur weiteren Kenntnis des Chlorophylls und des Hämins, VIII.: Umwandlung von Protoporphyrin IX über Photoprotoporphyrin in Spirographis- und Isospirographisporphyrin. *Tetrahedron Lett.* **1966**, *7*, 3779–3783. [CrossRef]

55. Fischer, H.; Wecker, G. Synthese des Spirographisporphyrins. *Hoppe. Seylers. Z. Physiol. Chem.* **1942**, *272*, 1–22. [CrossRef]

56. Fischer, H.; Deilmann, K.-O. Überführung von Hämin IX in Spirographisporphyrin und über einige Derivate des Deuteroporphyrins. *Hoppe. Seylers. Z. Physiol. Chem.* **1944**, *280*, 186–216. [CrossRef]

57. Tsubaki, M.; Nagai, K.; Kitagawa, T. Resonance Raman spectra of myoglobins reconstituted with spirographis and isospirographis hemes and iron 2, 4-diformylprotoporphyrin. *Biochemistry* **1980**, *19*, 379–385. [CrossRef]

58. Sono, M.; Asakura, T. Separation and properties of spirographis and isospirographis porphyrin dimethyl esters. *Biochemistry* **1974**, *13*, 4386–4394. [CrossRef]

59. Inhoffen, H.H.; Brockmann, H., Jr.; Bliesener, K.-M. Zur weiteren Kenntnis des Chlorophylls und des Hämins, XXX Photoprotoporphyrine und ihre Umwandlung in Spirographis-sowie Isospirographis-porphyrin). *Justus Liebigs Ann. Chem.* **1969**, *730*, 173–185. [CrossRef]

60. Horsey, B.E.; Whitten, D.G. Photochemical reactions in organized monolayer assemblies. 8. Environmental effects on photochemical reactions: Contrasts in the photooxidation behavior of protoporphyrin IX in solution, monolayer films, organized monolayer assemblies, and micelles. *J. Am. Chem. Soc.* **1978**, *100*, 1293–1295. [CrossRef]

61. Drabkin, D.L. Spectrophotometric studies: X. Structural interpretation of the spectra of cyanide, pyridine, and carbon monoxide derivatives of cytochrome *c* and hemoglobin. *J. Biol. Chem.* **1942**, *146*, 605–617. [CrossRef]

62. Rothschild, M.-L.; Myers, L.S. The spontaneous change of ferriprotoporphyrin in alkaline solution. *Nature* **1958**, *182*, 1671–1672. [CrossRef] [PubMed]

63. Rothschild, M.-L. The reaction of ferriprotoporphyrin with hydrogen peroxide in alkaline solutions. *Arch. Biochem. Biophys.* **1960**, *90*, 229–233. [CrossRef] [PubMed]

64. Fischer, H.; Deilmann, K.-O. Überführung von Hämin in Deuteroporphyrin-2,4-dicarbonsäure-tetramethylester und von Hämatoporphyrin in Diacetyl-deuteroporphyrin. *Justus Liebigs Ann. Chem.* **1940**, *545*, 22–27. [CrossRef]

65. Cox, G.S.; Whitten, D.G. Mechanisms for the photooxidation of protoporphyrin IX in solution. *J. Am. Chem. Soc.* **1982**, *104*, 516–521. [CrossRef]

66. Gonzalez-de-Castro, A.; Xiao, J. Green and efficient: Iron-catalyzed selective oxidation of olefins to carbonyls with O_2. *J. Am. Chem. Soc.* **2015**, *137*, 8206–8218. [CrossRef]

67. Li, X.; Liu, T.; Li, F.; Zhang, W.; Zhou, S.; Li, Y. Reduction of structural Fe(III) in oxyhydroxides by *Shewanella decolorationis* S12 and characterization of the surface properties of iron minerals. *J. Soils Sediments* **2012**, *12*, 217–227. [CrossRef]

68. Yan, B.; Wrenn, B.A.; Basak, S.; Biswas, P.; Giammar, D.E. Microbial reduction of Fe(III) in hematite nanoparticles by *Geobacter sulfurreducens*. *Environ. Sci. Technol.* **2008**, *42*, 6526–6531. [CrossRef] [PubMed]

Supporting Information

Molecular taphonomy of heme: Chemical degradation of hemin under presumed fossilization conditions

Mariam Tahoun [1], Marianne Engeser [2] *, Luca Svolacchia [1], Paul Martin Sander [3] and Christa E. Müller [1], *

[1] PharmaCenter Bonn & Pharmaceutical Institute, Department of Pharmaceutical and Medicinal Chemistry, University of Bonn, An der Immenburg 4, D-53121 Bonn, Germany; mtahoun@uni-bonn.de; s6lusvol@uni-bonn.de; christa.mueller@uni-bonn.de

[2] Kekulé Institute for Organic Chemistry and Biochemistry, University of Bonn, D-53121 Bonn, Germany; marianne.engeser@uni-bonn.de

[3] Institute of Geosciences, Department of Paleontology, University of Bonn, D-53113 Bonn, Germany; paulmartinsander@gmail.com

* Correspondence: christa.mueller@uni-bonn.de; marianne.engeser@uni-bonn.de

Table of Contents

I. ^{1}H-NMR and ^{13}C-NMR spectra of isolated hematinic acid
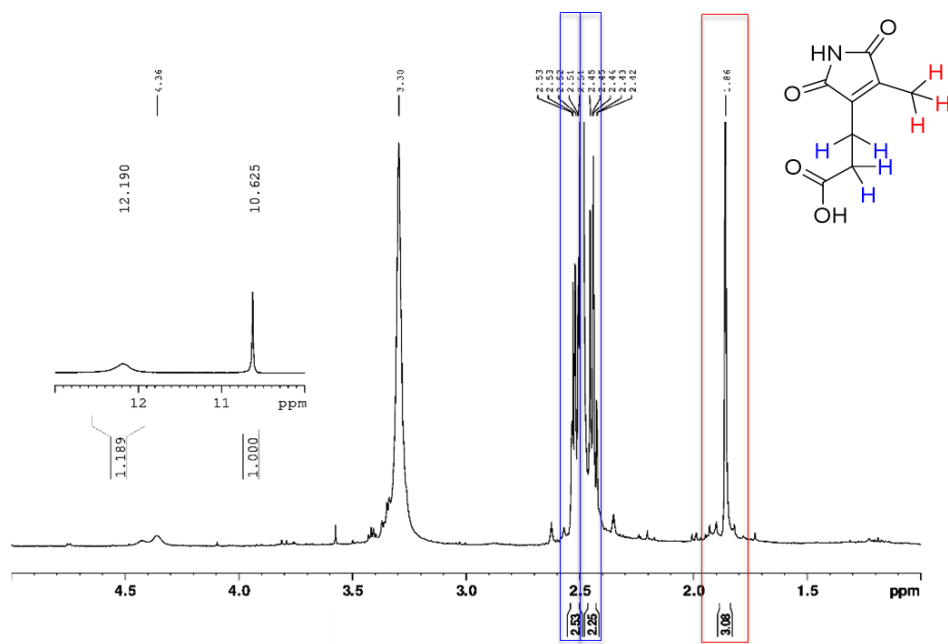
Figure S1. ^{1}H NMR spectrum of isolated hematinic acid determined in DMSO-d_6.
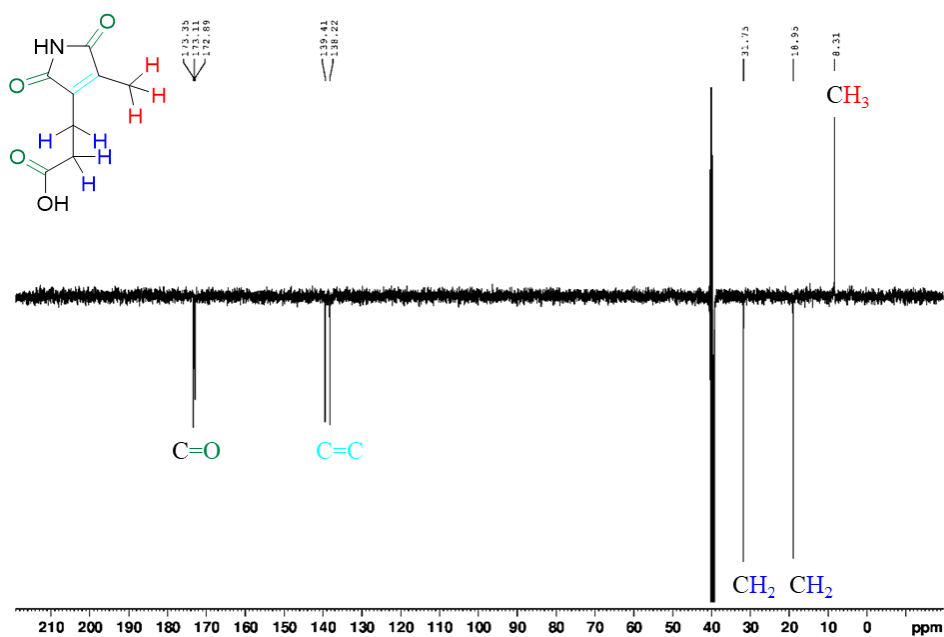
Figure S2. ^{13}C NMR spectrum (attached proton test, APT) of isolated hematinic acid determined in DMSO-d_6.

183

2

II.   High-resolution mass spectra of isolated hematinic acid
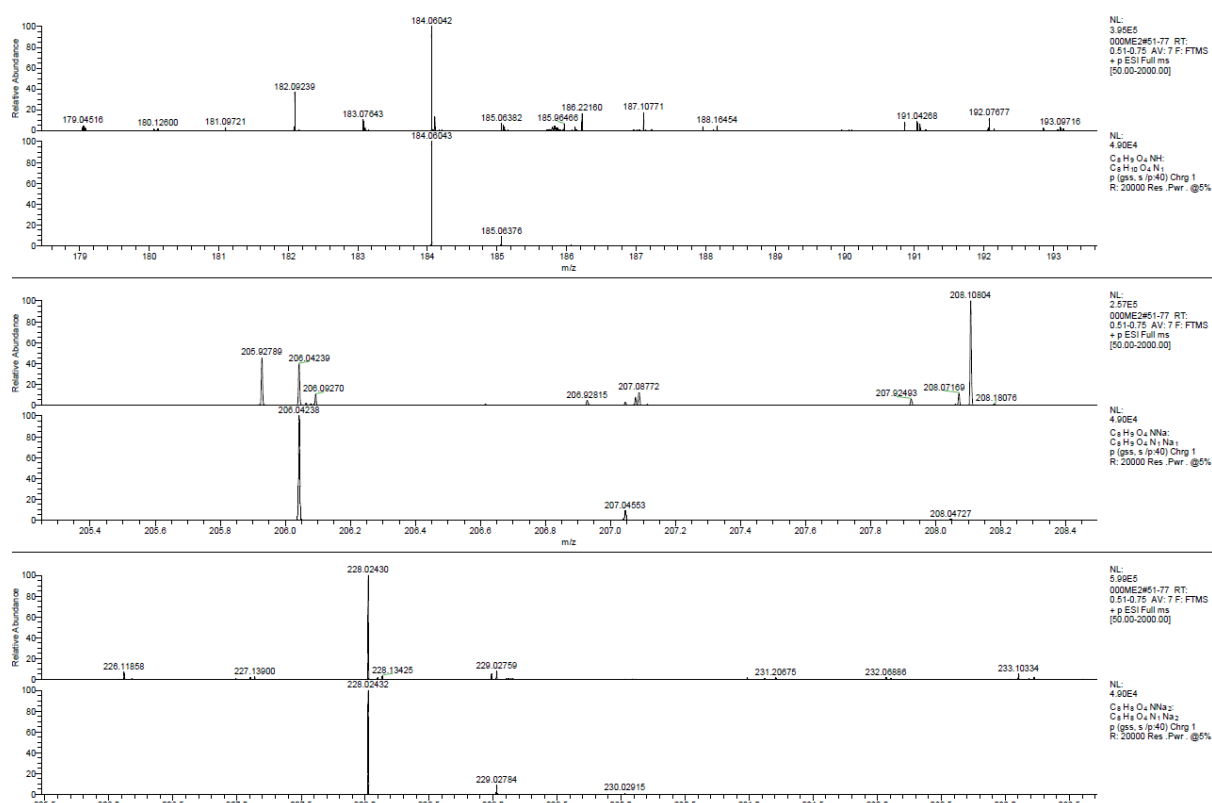
Figure S3. High resolution direct infusion electrospray mass spectra (Orbitrap XL) of isolated hematinic acid showing its molecular ions [M+H]$^+$ at *m/z* 184.06043 (top), [M+Na]$^+$ at *m/z* 206.04239 (top),   and [M+2Na-H]$^+$ at *m/z* 228.02430 (bottom). In each case, the measured spectrum is shown above, the calculated one below for comparison.

3
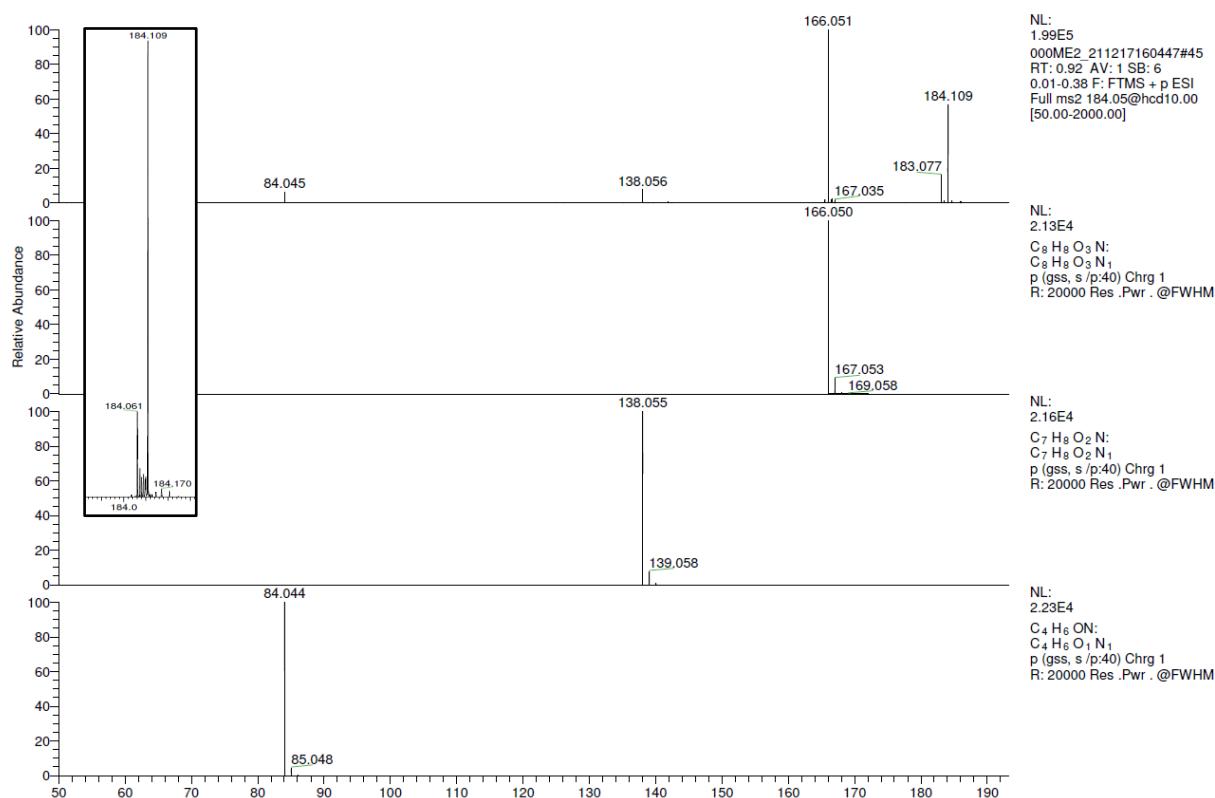
Figure S4. Collision-induced dissociation (CID) high resolution mass spectrum of mass-selected protonated hematinic acid showing its fragmentation pattern starting with consecutive losses of H$_2$O and CO, calculated spectra for the fragments below for comparison. The inset on the top left shows a zoom into the mass-selected region in the measured CID spectrum. Two signals with *m/z* 184 were present in the original spectrum (see Figure S3 top row), most of the molecular ion of hematinic acid (*m/z* 184.061) was fragmented by CID.

4

16.4. Appendix D – Macrocyclic Gq protein inhibitors FR900359 and/or YM-254890 – fit for translation?

This section contains the article "Macrocyclic Gq protein inhibitors FR900359 and/or YM-254890 – fit for translation?" and its supporting information as it appears in the journal *ACS Pharmacology and Translational Science* by American Society of Chemistry (ACS). According to ACS, the re-use of this article for a thesis or dissertation is allowed, and a legal note from the Copyright Clearance Center is presented below. The article is reprinted with permission from *ACS Pharmacol. Transl. Sci.* **2021**, 4(2), 888-897.

Article

Macrocyclic Gq Protein Inhibitors FR900359 and/or YM-254890−Fit for Translation?

Jonathan G. Schlegel,[⊥] Mariam Tahoun,[⊥] Alexander Seidinger, Jan H. Voss, Markus Kuschak, Stefan Kehraus, Marion Schneider, Michaela Matthey, Bernd K. Fleischmann, Gabriele M. König, Daniela Wenzel, and Christa E. Müller*

Cite This: *ACS Pharmacol. Transl. Sci.* 2021, 4, 888−897

Read Online

ACCESS | Metrics & More | Article Recommendations | Supporting Information

ABSTRACT: Guanine nucleotide-binding proteins (G proteins) transduce extracellular signals received by G protein-coupled receptors (GPCRs) to intracellular signaling cascades. While GPCRs represent the largest class of drug targets, G protein inhibition has only recently been recognized as a novel strategy for treating complex diseases such as asthma, inflammation, and cancer. The structurally similar macrocyclic depsipeptides FR900359 (FR) and YM-254890 (YM) are potent selective inhibitors of the Gq subfamily of G proteins. FR and YM differ in two positions, FR being more lipophilic than YM. Both compounds are utilized as pharmacological tools to block Gq proteins in vitro and in vivo. However, no detailed characterization of FR and YM has been performed, which is a prerequisite for the compounds' translation into clinical application. Here, we performed a thorough study of both compounds' physicochemical, pharmacokinetic, and pharmacological properties. Chemical stability was high across a large range of pH values, with FR being somewhat more stable than YM. Oral bioavailability and brain penetration of both depsipeptides were low. FR showed lower plasma protein binding and was metabolized significantly faster than YM by human and mouse liver microsomes. FR accumulated in lung after chronic intratracheal or intraperitoneal application, while YM was more distributed to other organs. Most strikingly, the previously observed longer residence time of FR resulted in a significantly prolonged pharmacologic effect as compared to YM in a methacholine-induced bronchoconstriction mouse model. These results prove that changes within a molecule which seem marginal compared to its structural complexity can lead to crucial pharmacological differences.

KEYWORDS: FR900359, Gq inhibitor, metabolic stability, physicochemical properties, pharmacokinetic behavior, YM-254890

1. INTRODUCTION

The macrocyclic depsipeptide FR900359 (FR, **1**) isolated from the higher plant *Ardisia crenata*,[1] in the leaves of which it is produced by the bacterial endophyte *Candidatus Burkholderia crenata*,[2] acts as a selective Gq protein inhibitor.[3] The structurally closely related natural product YM-254890 (YM, **2**), which had been isolated from a culture broth of *Chromobacterium* sp. QS3666 during the search for novel platelet aggregation inhibitors,[4] was reported to block Gq proteins with similar potency as **1**. These Gq protein inhibitors have become indispensable tool compounds to study Gq protein-mediated signaling induced by G protein-coupled receptors (GPCRs).[5−12] In contrast to the Gi protein inhibitor pertussis toxin and the Gs protein activator choleratoxin, proteins which have been essential tools for studying GPCR signaling for decades, FR and YM are small, macrocyclic, druglike molecules. Several studies provided strong evidence for the potential of Gq protein inhibitors as novel pharmacological agents to treat complex diseases, such as
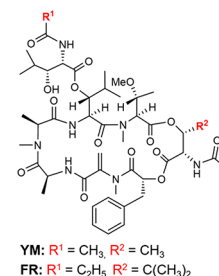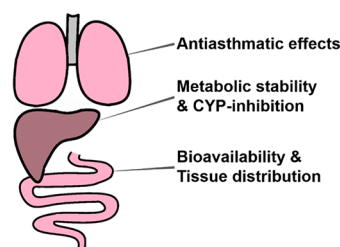
obesity,[13] asthma,[14] and cancer.[17−20] Analogs have been isolated from bacteria[21−23] or prepared by chemical synthesis,[12,24−26] but none of them were significantly more potent than the natural products; in fact, most of them displayed much lower Gq-inhibitory potency or were even inactive.

FR and YM differ only in two residues (see Figure 1), and both inhibitors have been generally regarded as exchangeable due to their almost identical structures. However, in a recent study, we observed that tritiated FR binding to Gq proteins displayed a significantly longer residence time than radiolabeled YM suggesting pseudoirreversible binding of FR but

16. Appendix

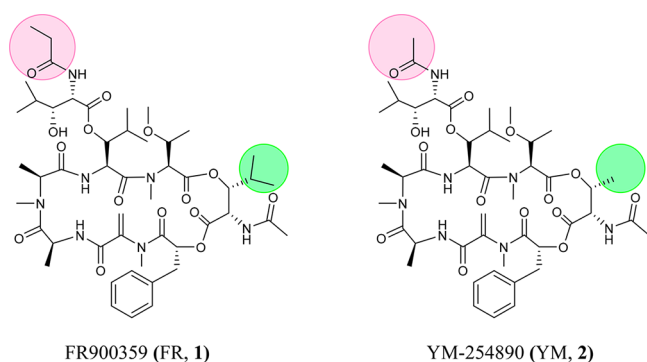FR900359 (FR, **1**)   YM-254890 (YM, **2**)

Figure 1. Chemical structures of the macrocyclic depsipeptidic Gq protein inhibitors FR (**1**) and YM (**2**).

not of YM.[27] Thus, despite their striking structural similarity, these results indicated that both compounds may, in fact, behave differently. However, not much is known about FR's and YM's physicochemical and pharmacokinetic properties, and whether these might result in pharmacodynamic consequences. Such information would be important for guiding biological experiments including preclinical studies and for translation of this class of compounds into the clinics. In the present study, we present essential data providing a basis for future in vivo investigations utilizing FR and YM as tool compounds and promising therapeutic drugs.

2. RESULTS AND DISCUSSION

In a first step, we collected, calculated, and/or determined the physicochemical properties of FR and YM, which are relevant for their application as drug molecules (see Table 1).

Table 1. Physicochemical and Druglike Properties of FR and YM

		FR	YM
exact mass (Da)		1001.53	959.49
heavy atom[a] count		71	68
number of defined stereocenters		11	11
specific rotation[b] ($[\alpha]_D^{20}$)		−54.8	−64.5
rotatable bond count		15	13
polar surface area		285 Å^2	285 Å^2
calculated logP value[c]		1.86	1.37
number of hydrogen bond donors		5	5
number of hydrogen bond acceptors		22	22
solubility in phosphate-buffered saline containing 1% dimethyl sulfoxide (DMSO)[d]		189 ± 17 μM	88 ± 12 μM
plasma protein binding		35%	79%
residence time of tritiated derivative at human platelet membranes[e]	at 37 °C	92.1 min	3.8 min
	at 21 °C	343.3 min	13.4 min

[a]Non-hydrogen atoms [b]Synthetic compounds, measured in methanol, *c* (FR) 0.073 g/mL, *c* (YM) 0.11 g/mL.[24] [c]Calculated logP values were obtained using the StarDrop program. [d]Values represent means ± SD (*n* = 3). [e]Reference 27.

2.1. Physicochemical and Druglike Properties.
Macrocyclic compounds have recently gained much attention in drug development due to their favorable pharmacokinetic properties despite their large molecular weight, which does not conform to Lipinsky's rule of 5.[28] The macrocyclic Gq protein inhibitors FR and YM, which are depsipeptides, differ only in two

substituents: FR contains a propionyl instead of an acetyl group and an isopropyl instead of a methyl group (see Figure 1). FR is therefore larger (exact mass: 1001.53 Da) than YM (959.49 Da) and somewhat more lipophilic. Calculated logP values are 1.37 for YM-254890 compared to 1.86 for FR900359 (Table 1). FR and YM are highly complex molecules containing 11 stereocenters and 15 (FR) or 13 (YM) rotatable bonds, respectively. Both compounds were predicted not to be brain-permeable due to their high polar surface area (285 Å^2) and their large number of hydrogen bond donors (5) and acceptors (22). N-Methylation of three of the peptide bonds increases their lipophilicity, which is, however, altogether moderate. The compounds are sufficiently and similarly water-soluble (FR, 189 μM; YM, 88 μM; kinetic solubility). Both display low to moderate plasma protein binding; interestingly, the bound proportion of the more lipophilic FR was significantly lower (35%) compared to that of the more polar analog YM (79%). This property of FR and its relatively high water solubility may be due to the bulky isopropyl substituent, which likely affects the molecule's conformation, crystal packing, and interactions.

One striking difference between FR and YM is their residence time at Gq proteins (Table 1). FR binds pseudoirreversibly to Gq proteins and displays a residence time of 92.1 min at 37 °C compared to 3.8 min for YM.[27] This finding was the first indication that FR and YM are not exchangeable with respect to therapeutic applications despite their high degree of structural similarity.

Thus, FR and YM are macrocyclic molecules with very similar physicochemical properties. The main differences are their lipophilicity, percentage of plasma protein binding, and target residence time.

2.2. Caco-2 Cell Permeation.
To experimentally assess the potential of the two Gq protein inhibitors for oral bioavailability, Caco-2 cell permeability assays were performed.[29,30] Caco-2 cells, a human colon adenocarcinoma cell line, are cultured on transwell cell culture plates. After differentiation, they resemble intestinal epithelial cells characterized by the formation of a polarized monolayer with a well-defined brush border on the apical surface expressing various transporters and enzymes as well as intercellular junctions. Results of Caco-2 permeability tests are used to predict intestinal absorption and consequently the bioavailability of a drug when orally administered. Both FR and YM possessed a low apparent permeability coefficient (P_{app}) of 0.4 × 10^{-6} cm/s and 0.1 × 10^{-6} cm/s, respectively (see Table 2). Apical to basolateral transport rates for both compounds were found to be well below the transport rate of the well-penetrating reference drug testosterone and in a similar range as those for the control drugs atenolol and erythromycin, both of which display low peroral absorption. Perhaps due to its higher lipophilicity, Caco-2 cell permeation was somewhat higher for FR as compared to YM. Interestingly, YM showed a P_{app} of 20.9 × 10^{-6} cm/s for basolateral to apical transport resulting in a ratio of 182, indicating very high efflux. This ratio was even higher than that determined for erythromycin included as a reference compound for drugs that are substrates of P-glycoprotein 1 (Pgp, multidrug resistance protein MDR1). In general, a ratio of >2 indicates Pgp transport.[31] The determined ratio shows that YM is indeed a substrate of an efflux transporter such as Pgp. The more lipophilic FR displayed an efflux/influx ratio of 29 indicating that it possesses Pgp substrate properties too, although not as strong as

Table 2. Apparent Transport Rates (P_{app}) of YM-254890, FR900359, and Control Compounds in Caco-2 Cells

compound	direction	$P_{app} \cdot 10^{-6}$ (cm/s)[a]	ratio (b-a/a-b)[b]	permeability
YM-254890	a-b	0.1 ± 0.0	182	low
	b-a	20.9 ± 2.8		
FR900359	a-b	0.4 ± 0.0	29	low
	b-a	11.5 ± 0.4		
testosterone	a-b	19.2 ± 1.0	2	high
	b-a	39.7 ± 5.2		
erythromycin	a-b	0.1 ± 0.1	106	low
	b-a	11.2 ± 0.4		
atenolol	a-b	0.4 ± 0.0	7	low
	b-a	2.8 ± 0.4		

[a]Apparent permeability (values represent means ± SD, n = 3). [b]High ratio indicates efflux by transporter proteins.

observed for YM. Lacking or low permeation could be advantageous to avoid intoxication upon local, e.g., inhalative treatment. Thus, low absorption combined with high efflux will result in very low oral bioavailability.

2.3. Chemical Stability. Next, we studied the Gq protein inhibitors' chemical stability at different pH values including simulated gastric fluid[32] (pH 1), weakly basic (pH 9), and more strongly basic conditions (pH 11, see Figure 2). The chemical stability of both compounds, FR and YM, was assessed in aqueous solution at 37 °C. A straightforward high-performance liquid chromatography−mass spectrometry (HPLC-MS) method was developed to detect and quantify both compounds and their potential degradation products. In short, HPLC on a reversed-phase column coupled to a single-quadrupole mass spectrometer equipped with an electrospray ionization source was applied for chromatographic separation, and the extract ion chromatograms (EICs) of both compounds

were used for identification and quantification (for details see Methods).

We did not observe significant degradation of FR and YM in simulated gastric fluid containing hydrochloric acid (pH 1) and the peptidase pepsin indicating high stability in acid and toward proteolytic cleavage. Both compounds were also stable in an aqueous solution of pH 9. While FR appeared to be completely stable, a slight degradation of YM could be observed (see Figure 2). These results show that both Gq inhibitors would likely survive peroral application. In contrast, at a strongly basic pH value of 11, both compounds were degraded, the more lipophilic FR being significantly more stable than YM. YM decomposed rapidly and completely within 20 min, whereas more than 75% of FR was still present after 4 h of incubation. Interestingly, under all conditions, both depsipeptides formed a small amount of an isomer with equal mass as the parent compound. The isomer could be separated by analytical HPLC from the parent compound, but its structure remains unknown. We propose that the formed isomer constitutes a rearrangement product caused by intramolecular transesterification involving the secondary alcoholic function of the compounds (see Figure 3), a hypothesis that needs to be tested in future studies.

Apart from the mass peaks of the parent compounds and the rearrangement products, a rising number and amount of degradation products were observed with an increased incubation time. Under all conditions, but predominantly at pH 11, hydrated products (FR/YM+H_2O; 1020.19 g/mol; 978.11 g/mol) and the FR/YM "core" structure, lacking the 3-hydroxy-4-methylpentanoate side chain, were detected (816.95 g/mol and 788.9 g/mol, respectively; see Figure 3). The hydrated compounds (FR/YM+H_2O) are likely the result of ester hydrolysis; alternatively, Michael addition reaction to the α,β-unsaturated ketone might occur. These results show that
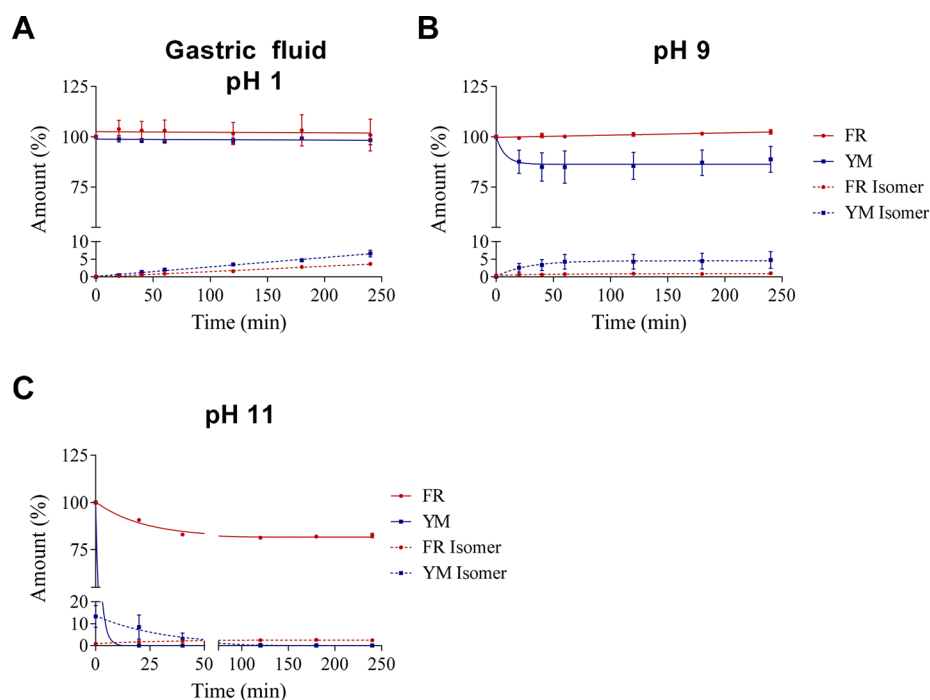

Figure 2. Chemical stability of FR and YM **A**. in simulated gastric fluid, pH 1, **B**. at pH 9, and **C**. at pH 11 (100 μM starting concentration). Solutions were prepared by adding 50 μL of a 1 mM stock solution in DMSO of FR or YM to 450 μL of an aqueous solution A, B, or C. Values represent means ± SEM from three independent experiments. For details, see Methods.
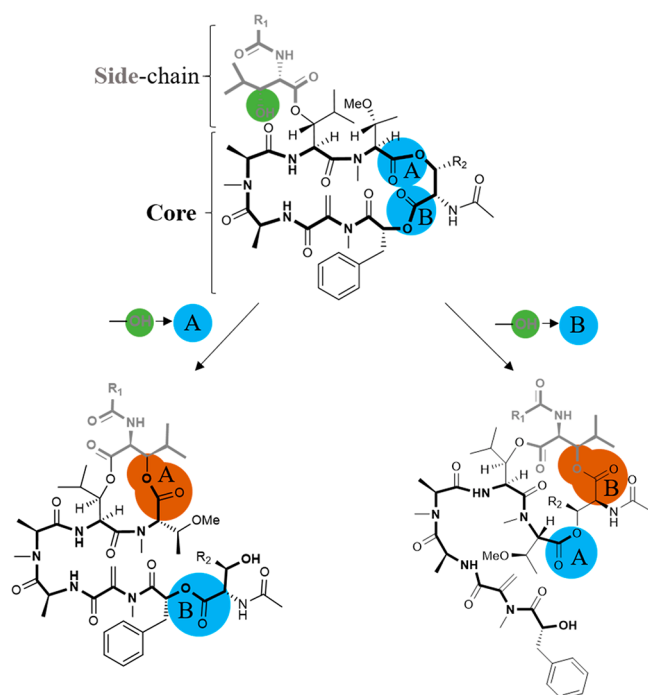
16. Appendix

Figure 3. Proposed isomerization reactions (FR: R_1 = CH_2CH_3, R_2 = $CH(CH_3)_2$; YM: R_1 = CH_3, R_2 = CH_3). The secondary alcohol is displayed in green. Esters which possibly take part in the isomerization reaction are highlighted in blue and labeled A or B. Ester bonds newly formed after the reaction are highlighted in dark orange.

the ester functions of YM and FR are reactive toward nucleophiles, and they support the proposed mechanism for the formation of the observed isomers by intramolecular transesterification. Our results indicate that the chemical stability of both FR and YM under physiological conditions is high. Degradation was mainly observed at strongly basic pH values, and the more lipophilic FR was found to be more stable than YM.

2.4. Metabolic Stability. *2.4.1. Stability in Liver Microsomes and Cytochrome P450 Enzyme Inhibition.* Next, we studied the metabolic stability of the compounds in liver microsomal preparations; results are summarized in Table 3.

Table 3. Metabolic Stability of FR and YM in Human and Mouse Liver Microsomes

	$CL_{int,app}$ ($\mu L/min/mg$ protein)		$t_{1/2}$ (min)	
	human	mouse	human	mouse
FR900359	171.0	237.4	8.1	5.8
YM-254890	50.8	82.2	27.3	16.9
verapamil (control)	134.6	335.7	10.3	4.1

Incubation of FR or YM with human (Figure 4A) and mouse (Figure 4B) liver microsomes resulted in degradation of both compounds, which was more pronounced in mouse as compared to human liver. FR revealed a higher apparent intrinsic clearance ($CL_{int, app}$) as compared to YM. Because of its low half-life of only 5.8 min in mouse and 8.1 min in human liver microsomes, FR was completely metabolized within 60 min in both preparations. YM was more stable with $CL_{int, app}$ values of 82.2 $\mu L/min/mg$ protein in mouse and 50.8 $\mu L/min/$

mg protein in human liver microsomes translating into half-lives of 16.9 min (mouse) and 27.3 min (human). There was approximately one-quarter of YM left after 60 min of incubation in human liver microsomes. The apparent intrinsic clearance of verapamil, which is known to be rapidly metabolized[33] and was therefore included as a positive control, was in a similar range as that of FR. Based on the measured $CL_{int, app}$ value, an in vivo CL_{int} can be estimated using suitable scaling factors, i.e., microsomal protein content per gram of liver to be 45 mg of microsomal protein per gram of liver tissue and 26 g (human) or 87 g (mouse) of liver tissue per kilogram of body weight.[34,35] CL_{int} values of FR and YM in humans were determined to be 200.1 mL/min/kg and 59.4 mL/min/kg, respectively. Typically, a CL_{int} (human) below 15 mL/min/kg, between 15−45 mL/min/kg, and above 45 mL/min/kg can be classified as low, intermediate, and high metabolic degradation, respectively.[34,36] Thus, YM and FR were found to be high clearance compounds and do not appear to be suitable for systemic application based on their short half-lives. Due to its somewhat slower metabolic clearance, YM would be preferred for systemic treatment; however, a very short duration of action has to be expected.

Subsequent metabolite identification studies revealed that N/O-dealkylation at various positions of the depsipetides, as well as hydroxylation (observed only for FR), constituted the main metabolic pathways. Structures of specific metabolites have not been identified due to the structural complexity of the compounds which feature many functional groups that may be susceptible to metabolism.

Subsequently, we investigated potential inhibition of cytochrome P450 (CYP enzymes) that is important for drug metabolism by FR and YM. At a concentration of 1 μM, both compounds exhibited only negligible effects on the investigated CYP enzymes. At a very high concentration of 10 μM, inhibition was still negligible to low (Figure S1 of the Supporting Information), except for CYP3A4, which was inhibited by about 50% (FR: 50%, YM: 56%). FR at 10 μM also displayed moderate inhibition of CYP2C8 (30%) and CYP2C19 (38%), whereas inhibition by 10 μM of YM was below 25%. These results indicate that both Gq inhibitors are not expected to interfere with hepatic metabolism of other molecules.

2.4.2. Stability in Lung Tissue and Blood Plasma. FR, which had been found to be less metabolically stable in liver microsomes than YM, was selected for stability testing in lung tissue and blood plasma of mice. The compound was found to be highly stable in both matrices, with more than 90% of the unaltered compound still present after 4 h of incubation in mouse plasma or lung tissue, respectively. A very small amount was converted to its isomer with equal mass (for the presumed structure see Figure 3). This clearly shows that FR is well suited for local, bronchial application.

2.5. In Vivo Bioavailability and Organ Distribution. Next, we studied the concentrations of intact FR and YM in vivo after different application schemes in mice utilizing a recently developed sensitive LC-MS/MS method combined with an optimized extraction procedure.[37]

2.5.1. Intratracheal Application. FR or YM (5 μg) was intratracheally (i.t.) applied to mice on 7 consecutive days. The organs were harvested approximately 45 min after the last FR/YM application, subsequently extracted, and analyzed for FR or YM concentration. High levels of both Gq protein inhibitors were detected in lung and kidney (Figure 5A,B). Only low
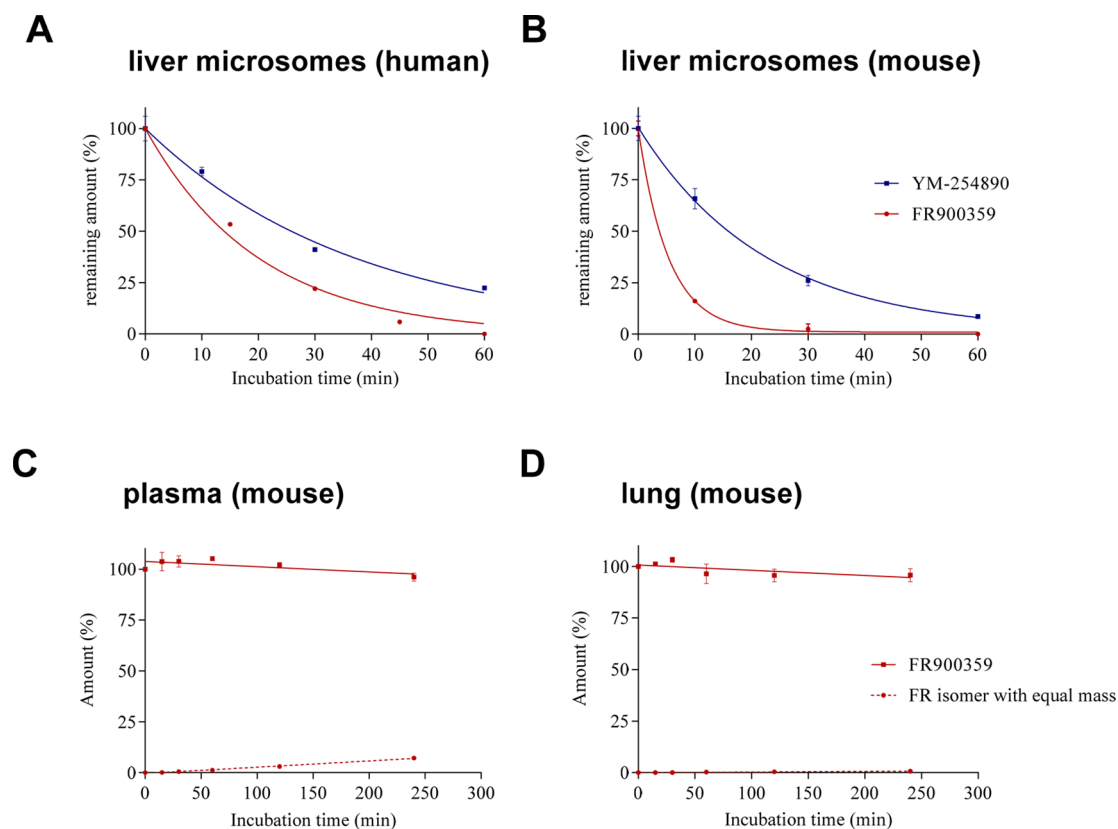
Figure 4. Stability of G protein inhibitors under various conditions: **A.** human liver microsomes (FR, YM); **B.** mouse liver microsomes (FR, YM); **C.** stability in mouse plasma (FR); and **D.** mouse lung tissue (FR). Data represent means $\pm$ SEM (n = 3).
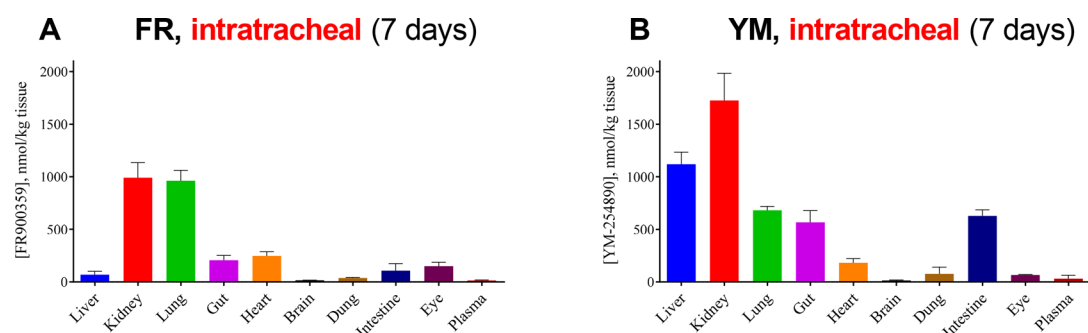

Figure 5. A. Concentration of FR $\pm$ SEM and **B.** concentration of YM $\pm$ SEM in mouse tissues after intratracheal application of 5 μg of drug on 7 consecutive days. FR and YM levels in organs from three mice were determined.
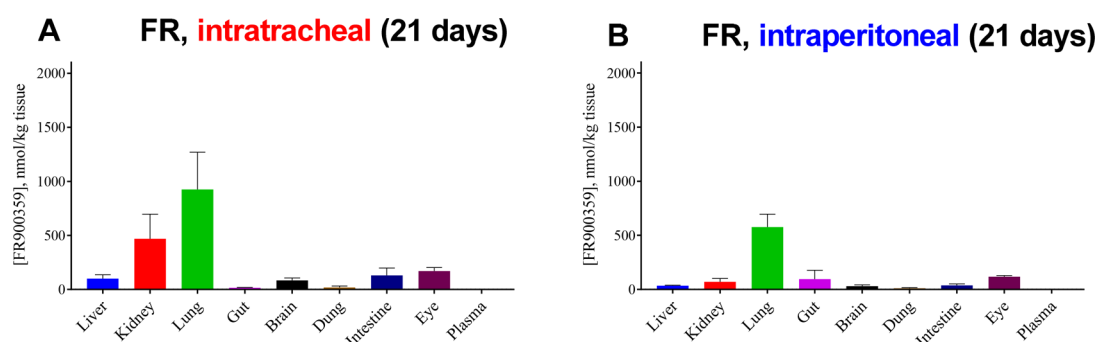
Figure 6. A. Concentration of FR $\pm$ SEM in various mouse tissues after intratracheal application of 2.5 μg of FR twice a day for 3 weeks. **B.** Concentration of FR $\pm$ SEM in mouse tissues after intraperitoneal application of 10 μg of FR for 3 weeks (administration from Monday to Friday). FR levels in organs from three mice were determined.
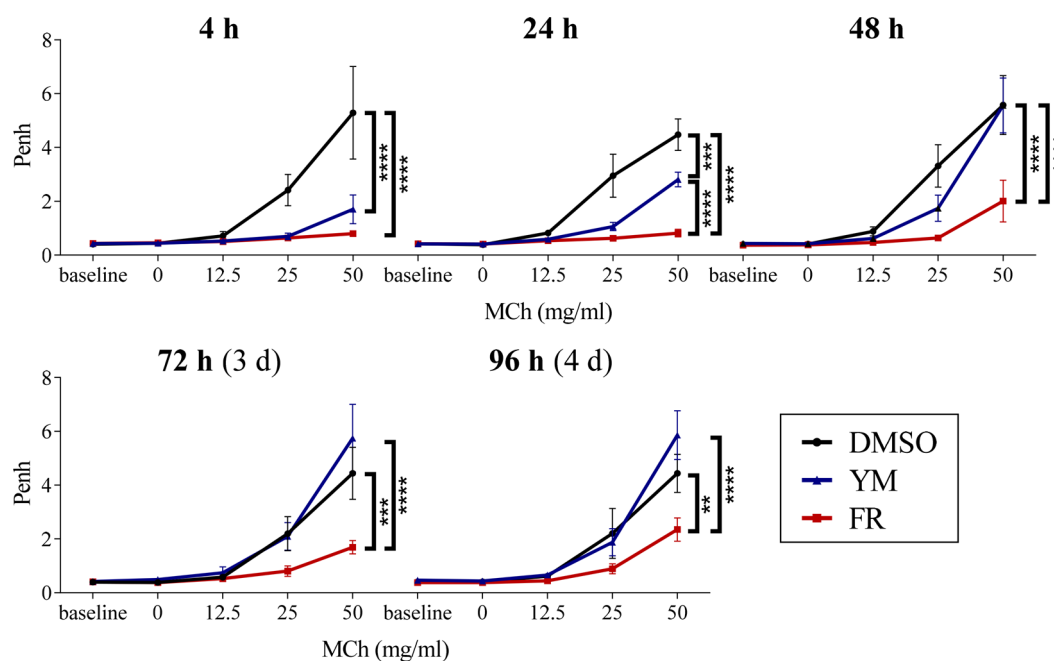
Figure 7. Repeated enhanced pause (Penh) measurements after intratracheal application of FR and YM. Bronchoconstriction was induced by application of methacholine (MCh). FR/YM (2.5 μg) or DMSO was administered intratracheally on day 0. Whole-body plethysmography was carried out after 4 h, 24 h, 48 h, 72 h, and 96 h in the presence of increasing concentrations of MCh which was applied as an aerosol by a nebulizer in the plethysmograph. Data represent means ± SEM (FR, DMSO $n = 5$; YM $n = 4$). Statistical significance was assessed by two-way repeated measures ANOVA with Bonferroni's post hoc test. ****, ***, and ** represent a p value < 0.0001, 0.001, and 0.01, respectively.

concentrations of YM and FR were found in brain and blood plasma. Liver, intestine, and lung showed significantly different drug levels of FR as compared to YM. While YM concentrations in liver and kidney were significantly higher than those of FR, the opposite was true for lung, in which higher FR levels than YM levels were detected. These differences are likely due to the different metabolic stabilities of the compounds in liver (compare Figure 4B), FR being less metabolically stable than YM. Moreover, different lipophilicities and different residence times may contribute. FR, which displays a very slow dissociation kinetic,[27] shows higher accumulation in lung as compared to YM likely because it displays pseudoirreversible binding to the Gq proteins and therefore sticks to its targets at the point of entry. Both compounds are preferentially eliminated via the kidneys and, to a smaller but still measurable extent, through feces.

We subsequently studied FR, the preferred Gq inhibitor for intratracheal application, for 21 days. Even after a 3-week treatment, FR levels in lung remained high and were at about the same level as those measured after 1 week (see Figure 6A). These results show that long-term treatment in lung, e.g., for antiasthmatic therapy, is feasible resulting in constantly high drug levels.

2.5.2. Intraperitoneal Application. In further in vivo studies, FR was administered intraperitoneally for 3 weeks. Subsequent extraction and analysis showed that the highest concentrations of FR were again found in the lung (Figure 6B). Direct comparison of i.p. versus i.t. application of FR is shown in Figure 6. In general, FR displayed a similar distribution in the body after both routes of application, but FR levels were overall slightly higher after intratracheal as compared to i.p. application despite slightly lower applied doses. Interestingly, systemic i.p. application resulted in FR levels in the lung comparable to those after local i.t. application. This may be

due to high Gq expression in the lung combined with pseudoirreversible binding of FR. FR concentrations determined in the kidneys were significantly higher after intratracheal application, whereas moderate amounts of FR in the gut could only be measured after i.p. application. Independent of the way of application, FR could also be found in the eyes, liver, and intestine. Again, only low to marginal concentrations were found in the brain.

Both in vivo studies showed that FR and YM are not or only marginally able to cross the blood-brain barrier but can be detected in other vital organs, partly in relatively high concentrations in organs which most likely take part in their metabolism or excretion (liver, kidney). Because FR and YM possess low nanomolar IC_{50}/K_i values at their target protein,[22,27] the determined drug concentrations can be expected to be sufficient for pharmacological activity. Besides lung, eye diseases, e.g., uveal melanoma,[16−18] would be the primary targets for local or systemic FR treatment.

2.6. Pharmacological Effects of FR and YM in Mouse Lung Determined by Plethysmography. The results obtained so far in in vitro and in vivo studies indicated that FR and YM may be particularly suited for treating lung disease, since both drugs accumulate in this organ (see Figures 5 and 6). To find out whether the structurally similar Gq inhibitors FR and YM display the same pharmacological properties in vivo, we studied and compared their effect on airways in mice by plethysmography.

Enhanced pause (Penh) displays an index which indicates changes of the airflow waveform in a whole-body plethysmograph that can be correlated with pulmonary reactivity.[38] This noninvasive method enables long-term measurements in vivo in specific individuals and allows assessment of kinetic profiles over a long time course. Previous studies had demonstrated that FR is able to potently induce airway relaxation in mice.[14]

Since radiolabeled FR was recently shown to have a much longer residence time than radiolabeled YM[27] (also see Table 1), we wanted to compare the effects of both Gq protein inhibitors on bronchial function. Figure 7 shows the results of repeated Penh measurements with increasing concentrations of methacholine (MCh), a muscarinic acetylcholine receptor agonist inducing bronchoconstriction, after a one-time intra-tracheal application (i.t.) of FR or YM, respectively. Both Gq protein inhibitors were able to reduce a methacholine-induced Penh increase 4 h after application. However, 48 h after application, mice that had been treated with YM showed a similar reaction as control mice treated with dimethyl sulfoxide (DMSO), in which the Gq protein inhibitors had been dissolved. This indicates, that after 48 h, the antiasthmatic effects of YM were terminated. Interestingly, the effect of FR persisted much longer and could be observed even 96 h after FR application.

These data demonstrate that the significantly longer residence time of the Gq inhibitor FR as compared to YM translates into much longer persistence of the antiasthmatic action.

3. CONCLUSION

Until now, great efforts have been made to evaluate the biochemical and pharmacological profiles of the Gq protein inhibitors FR and YM in order to fully understand their effects on a molecular level.[5,39−41,25,42] The current project focused on a comparison between both compounds and provides first insights into their pharmacokinetic behavior which is a prerequisite for their translational development as therapeutic drugs. Both compounds are Pgp substrates. Interestingly, we found that FR was metabolized significantly faster than YM in human and mouse liver microsomal preparations, which correlated with higher YM levels in vital organs after intratracheal application (Figure 5A,B). Another striking difference was the effect of FR on methacholine-induced bronchoconstriction upon Penh measurements which clearly lasted significantly longer than the effect of YM. This can be explained by the slower dissociation kinetic of FR. These data, along with the determined high FR levels in the lung after local and systemic applications, imply that FR is a prime compound for targeting Gq-based signaling in the respiratory system. However, local administration of the Gq protein inhibitor will be preferred since systemic application can be expected to block Gq signaling throughout the body and is therefore not suitable for use in the clinic. In addition, our results prove that changes within a molecule which seem marginal compared to its structural complexity can lead to crucial pharmacological differences. Additionally, our work demonstrates that differences which were identified by utilizing an artificial and simplified test system like measurement of target residence time of drugs can be transferred to and confirmed in more complex models.

4. METHODS

4.1. Caco-2 Permeability. Caco-2 permeability assays were performed by Pharmacelsus GmbH (Saarbruecken, Germany) in a differentiated Caco-2 cell monolayer-based test system.[15] Transport rates of FR and YM were determined at 10 μM and at a pH of 6.5 (apical, A) and 7.4 (basolateral, B). As reference compounds, testosterone (high transport rates, high bioavailability), atenolol (low transport rates, low

bioavailability) and erythromycin (Pgp substrate) were included. Measurements were made at the following time points: 0, 15, 45, and 90 min. Caco-2 cells were differentiated for 21 days in Transwell plates. Bidirectional permeation experiments were performed according to Pharmacelsus in-house protocols. Data represent means ± SEM from three experiments.

4.2. Stability in Simulated Gastric Fluid. Artificial gastric fluid (450 μL, prepared according to the European Pharmacopoeia (Ph. Eur. 10) consisting of 0.32 g of pig pepsin, 0.2 g of NaCl, 8 mL of 1 M HCl, and 100 mL of H_2O) was spiked with 50 μL of FR or YM (1 mM stock solution prepared in DMSO). The mixture was subsequently incubated at 37 °C. Samples (50 μL each) were drawn after 0, 20, 40, 60, 120, 180, and 240 min, treated with ice-cold acetonitrile (1:1), vortexed, and centrifuged for 3 min at 15,000 g. An aliquot (50 μL) of the supernatant was transferred to a vial and subjected to LC-MS/MS analysis (see Section Quantitative Analysis of FR and YM by LC-MS/MS for in Vitro Stability Studies). Each experiment was repeated 3 times for each compound.

4.3. Stability in Alkaline Solutions. Alkaline aqueous solutions were prepared by adjusting the pH value of deionized water with NaOH until a pH of 9.0 or 11.0, respectively, was reached. To the alkaline solutions (450 μL) was added 50 μL of FR or YM (1 mM stock solution in DMSO), and the mixtures were incubated at 37 °C. Samples (50 μL each) were drawn after 0, 20, 40, 60, 80, 120, 180, and 240 min. Samples were treated with ice-cold acetonitrile (1:1), vortexed, and centrifuged for 3 min at 15,000 g. Aliquots (50 μL) of the supernatant were transferred to a vial and subjected to LC-MS/MS analysis (see Section Quantitative Analysis of FR and YM by LC-MS/MS for in Vitro Stability Studies). Each experiment was repeated 3 times for each compound.

4.4. Quantitative Analysis of FR and YM by LC-MS/MS for in Vitro Stability Studies. Measurements were performed on an Agilent 1260 Infinity HPLC coupled to an Agilent Infinity Lab LC/MSD Single Quadrupole mass spectrometer with an electrospray ion source. Chromato-graphic separation was performed on an EC 50/3 Nucleodur C18 Gravity, 3 μm (Macherey-Nagel, Dueren, Germany). Mobile phase A consisted of methanol containing 2 mM ammonium acetate and 0.1% formic acid, and mobile phase B consisted of water with 2 mM ammonium acetate and 0.1% formic acid. The run started with 60% A and 40% B for 1 min, followed by a gradient that reached 100% of eluent A after 9 min. Then, the column was flushed for 5 min with 100% of mobile phase A. The flow rate was adjusted to 0.4 mL/min. Positive full scan MS was observed from 200 to 1500 m/z. The peak appeared at 5.7 min for YM-254890 and at 7.4 min for FR900359. For identification and quantification using the Data Analysis program on OpenLab CDS software 2.4, the extracted ion chromatogram (EIC) of 960.5 ± 0.7 m/z was used for YM, and the EIC of 1002.5 ± 0.7 m/z was used for FR. This method was used for the stability studies. Peak areas were evaluated from the EICs and normalized to the FR and YM areas at zero time, and the percentage of remaining compound was calculated. Three independent experiments were performed.

4.5. Metabolic Stability in Human and Mouse Liver Microsomes. Metabolic stability of FR and YM in human and mouse liver microsomes was assessed by Pharmacelsus GmbH (Saarbruecken, Germany). FR or YM (1 μM) was incubated with pooled human or mouse liver microsomes (0.5 mg/mL)

16. Appendix

in phosphate buffer pH 7.4 in the presence of NADPH and $MgCl_2$. Samples were drawn after 0, 10, 30, and 60 min. The percentage loss of the parent compound was determined by LC-MS analysis. Subsequent metabolite identification in mouse liver microsomes was carried out using HPLC-HRMS by determining accurate masses and fragmentation patterns.

4.6. Metabolic Stability in Mouse Lung Tissue. For stability testing in lung tissue, lungs from four CD1 wild-type mice were pooled, weighed, and subsequently homogenized in a TissueLyzer (Qiagen, Venlo, Netherlands) for 8 min at 50 strokes/min in a precooled tube holder. HEPES buffer, 50 mM, pH 7.4, was added to the homogenate (1 mL of buffer was added to 300 mg of tissue), and the mixture was transferred to a reagent tube. Then, 50 μL of FR solution (1 mM dissolved in DMSO) was added to 450 μL of the lung homogenate and incubated at 37 °C. Samples (6 samples, 80 μL each) were drawn after 0, 15, 30, 60, 120, and 240 min, mixed with ice-cold acetonitrile (1:1), vortexed, and centrifuged for 3 min at 15,000 g. An aliquot of 50 μL of the supernatant was transferred to a suitable vial and subjected to LC-MS/MS analysis.

4.7. Stability in Mouse Blood Plasma. Blood plasma of three wild-type CD1 mice was pooled, and 90 μL of the plasma was mixed with 10 μL of FR solution (1 mM in DMSO) and incubated at 37 °C. Samples (6 samples, 10 μL each) were drawn at 0, 15, 30, 60, 120, and 240 min, mixed with ice-cold acetonitrile (1:1), vortexed, and centrifuged for 3 min at 15,000 g. Aliquots of 10 μL of the supernatant were transferred to a suitable vial and subjected to LC-MS/MS analysis.

4.8. In Vivo Experiments. Animal experiments were approved by the local ethics committee and carried out in accordance to the guidelines of the German law of protection of animal life with approval by the local government authorities (Landesamt für Natur, Umwelt und Verbraucherschutz Nordrhein-Westfalen, NRW, Germany).

4.8.1. Quantification of FR and YM in Mouse Tissues. In an initial in vivo study, FR or YM (5 μg) was administered intratracheally on 7 consecutive days. In further studies, 10 μg and 2.5 μg of FR, respectively, were administered intra-peritoneally (Monday to Friday) and intratracheally (twice a day, Monday to Sunday), respectively, for 3 weeks. In each study, organs from three different mice were harvested and snap-frozen approximately 45 min after the last FR or YM application. FR and YM were extracted by a three-step liquid–liquid extraction method and quantified as previously described by HPLC-ESI-MS/MS.[37] Chromatographic separation was performed using a Dionex Ultimate 3000 (Thermo Fisher Scientific, MA, USA) equipped with an integrated variable wavelength detector coupled to a micrOTOF-Q mass spectrometer (Bruker, MA, USA) with an electrospray ion source. An EC50/2 Nucleodur C18 Gravity 3 μm column (Macherey-Nagel, Dueren, Germany) was used for chromatographic separation. The two mobile phases were A (40% aq. methanol containing 2 mM ammonium acetate and 0.1% formic acid) and B (methanol, 2 mM ammonium acetate, 0.1% formic acid). The run started with 100% A. After 1 min, a gradient was started reaching 100% eluent B within 9 min. Then, the column was flushed for 5 min with solvent B. Positive full scan MS was recorded from 200 to 1500 m/z. The extract ion chromatogram (EIC) of 1002.54 ± 0.01 m/z was used for the identification and quantification of FR by the QuantAnalysis program (Bruker, MA, USA). An EIC of 960.49

± 0.01 m/z was employed for the identification and quantification of YM.

4.8.2. Whole Body Plethysmography. For i.t. drug application, mice were anaesthetized with isoflurane (5%) and orotracheally intubated using an i.v. cannula (22 G, Vasofix Safely, B. Braun, Melsungen, Germany). The correct positioning of the endotracheal tube was checked under mechanical ventilation with 1.5% isoflurane via a small animal ventilator (MiniVent, Hugo Sachs, Germany). Then, the tube was disconnected from the ventilator, and Gq inhibitors FR or YM (2.5 μg, 1% DMSO in 0.9% NaCl, 50 μL) or the solvent (1% DMSO in 0.9% NaCl, 50 μL) was applied into the tube by a pipet. Thereafter, mechanical ventilation was continued for about 30 s to allow uptake of the liquid. Whole body plethysmography was performed at 4, 24, 48, 72, and 96 h after extubation. Therefore, the awake and unrestrained mice were placed into cylindrical Plexiglas chambers of the whole body plethysmograph (emka Technologies, France). Penh was recorded for 40 s under resting conditions (baseline) and after nebulization of increasing concentrations of methacholine (0, 12.5, 25, and 50 mg/mL).

4.9. Calculation of Compound Properties. LogP, PSA, and peroral and CNS bioavailability were calculated using StarDrop (Optibrium, Cambridge, UK, 2013).

4.10. Data Analysis. *4.10.1. Statistical Analysis.* Statistical significance was determined using a two-way repeated measures ANOVA with a subsequent Bonferroni's post hoc test. Data analysis and plotting were performed using GraphPad PRISM, Version 7.0 (GraphPad, San Diego, CA, USA).

4.10.2. Metabolic Stability. The metabolic degradation process was defined as a first-order decay (eq 1). To obtain a straight line, the natural log of the remaining compound (%) was plotted against time (min). The slope was used to calculate half-lives (eq 2), and $CL_{int,app}$ was determined by using eq 3.[35] Subsequently, eq 4 was applied to obtain $CL_{int,app}$ based on 45 mg of microsomal protein per g of liver tissue and 87 g (mouse) or 26 g (human) of liver tissue per kg body mass.

$$[A]_t = [A]_0 \times e^{-kt} \tag{1}$$

$$t_{1/2} = \frac{\ln(2)}{k} \tag{2}$$

$$CL_{int,app} = \frac{\ln(2)}{t_{1/2}\,[\text{min}]} \times \frac{\text{incubation volume}\,[\mu L]}{\text{protein amount}\,[\text{mg}]} \tag{3}$$

$$CL_{int} = CL_{int,app}\,[\mu L/\text{min}\,/\text{mg}]$$
$$\times \frac{\text{microsomal protein}\,[\text{mg}]}{\text{liver mass}\,[\text{g}]} \times \frac{\text{liver mass}\,[\text{g}]}{\text{body weight}\,[\text{kg}]} \tag{4}$$

■ ASSOCIATED CONTENT

● Supporting Information

The Supporting Information is available free of charge at https://pubs.acs.org/doi/10.1021/acsptsci.1c00021.

Inhibition of CYP450 enzymes by FR and YM (PDF)

■ AUTHOR INFORMATION

Corresponding Author

Christa E. Müller − *PharmaCenter Bonn, Pharmaceutical Institute, Pharmaceutical & Medicinal Chemistry, University of Bonn, 53121 Bonn, Germany;* ⊙ orcid.org/0000-0002-0013-6624; Phone: +49 228 73 2301; Email: christa.mueller@uni-bonn.de

Authors

Jonathan G. Schlegel − *PharmaCenter Bonn, Pharmaceutical Institute, Pharmaceutical & Medicinal Chemistry, University of Bonn, 53121 Bonn, Germany;* ⊙ orcid.org/0000-0002-6337-0872

Mariam Tahoun − *PharmaCenter Bonn, Pharmaceutical Institute, Pharmaceutical & Medicinal Chemistry, University of Bonn, 53121 Bonn, Germany*

Alexander Seidinger − *Department of Systems Physiology, Medical Faculty, Ruhr University Bochum, 44801 Bochum, Germany*

Jan H. Voss − *PharmaCenter Bonn, Pharmaceutical Institute, Pharmaceutical & Medicinal Chemistry, University of Bonn, 53121 Bonn, Germany*

Markus Kuschak − *PharmaCenter Bonn, Pharmaceutical Institute, Pharmaceutical & Medicinal Chemistry, University of Bonn, 53121 Bonn, Germany*

Stefan Kehraus − *Institute for Pharmaceutical Biology, University of Bonn, 53115 Bonn, Germany*

Marion Schneider − *PharmaCenter Bonn, Pharmaceutical Institute, Pharmaceutical & Medicinal Chemistry, University of Bonn, 53121 Bonn, Germany*

Michaela Matthey − *Department of Systems Physiology, Medical Faculty, Ruhr University Bochum, 44801 Bochum, Germany*

Bernd K. Fleischmann − *Institute of Physiology I, Life & Brain Center, Medical Faculty, University of Bonn, 53105 Bonn, Germany*

Gabriele M. König − *Institute for Pharmaceutical Biology, University of Bonn, 53115 Bonn, Germany;* ⊙ orcid.org/0000-0003-0003-4916

Daniela Wenzel − *Department of Systems Physiology, Medical Faculty, Ruhr University Bochum, 44801 Bochum, Germany; Institute of Physiology I, Life & Brain Center, Medical Faculty, University of Bonn, 53105 Bonn, Germany*

Complete contact information is available at:
https://pubs.acs.org/10.1021/acsptsci.1c00021

Author Contributions

[⊥]J.G.S. and M.T. contributed equally.

Notes

The authors declare no competing financial interest.

■ ACKNOWLEDGMENTS

■ REFERENCES

(1) Fujioka, M., Koda, S., Morimoto, Y., and Biemann, K. (1988) Structure of FR900359, a cyclic depsipeptide from *Ardisia crenata Sims. J. Org. Chem.* 53, 2820−2825.

(2) Carlier, A., Fehr, L., Pinto-Carbó, M., Schäberle, T., Reher, R., Dessein, S., König, G., and Eberl, L. (2016) The genome analysis of *Candidatus* Burkholderia crenata reveals that secondary metabolism may be a key function of the *Ardisia crenata* leaf nodule symbiosis. *Environ. Microbiol.* 18, 2507−2522.

(3) Takasaki, J., Saito, T., Taniguchi, M., Kawasaki, T., Moritani, Y., Hayashi, K., and Kobori, M. (2004) A novel Gα$_{q/11}$-selective inhibitor. *J. Biol. Chem.* 279, 47438−47445.

(4) Taniguchi, M., Nagai, K., Arao, N., Kawasaki, T., Saito, T., Moritani, Y., Takasaki, J., Hayashi, K., Fujita, S., Suzuki, K.-i., and Tsukamoto, S.-i. (2003) YM-254890, a novel platelet aggregation inhibitor produced by *Chromobacterium* sp. QS3666. *J. Antibiot.* 56, 358−363.

(5) Schrage, R., Schmitz, A.-L., Gaffal, E., Annala, S., Kehraus, S., Wenzel, D., Büllesbach, K. M., Bald, T., Inoue, A., Shinjo, Y., Galandrin, S., Shridhar, N., Hesse, M., Grundmann, M., Merten, N., Charpentier, T. H., Martz, M., Butcher, A. J., Slodczyk, T., Armando, S., Effern, M., Namkung, Y., Jenkins, L., Horn, V., Stößel, A., Dargatz, H., Tietze, D., Imhof, D., Galés, C., Drewke, C., Müller, C. E., Hölzel, M., Milligan, G., Tobin, A. B., Gomeza, J., Dohlman, H. G., Sondek, J., Harden, T. K., Bouvier, M., Laporte, S. A., Aoki, J., Fleischmann, B. K., Mohr, K., König, G. M., Tüting, T., and Kostenis, E. (2015) The experimental power of FR900359 to study G$_q$-regulated biological processes. *Nat. Commun.* 6, 10156.

(6) Bolognini, D., Moss, C. E., Nilsson, K., Petersson, A. U., Donnelly, I., Sergeev, E., König, G. M., Kostenis, E., Kurowska-Stolarska, M., Miller, A., Dekker, N., Tobin, A. B., and Milligan, G. (2016) A novel allosteric activator of free fatty acid 2 receptor displays unique G$_i$-functional bias. *J. Biol. Chem.* 291, 18915−18931.

(7) Carr, R., Koziol-White, C., Zhang, J., Lam, H., An, S. S., Tall, G. G., Panettieri, R. A., and Benovic, J. L. (2016) Interdicting G$_q$ activation in airway disease by receptor-dependent and receptor-independent mechanisms. *Mol. Pharmacol.* 89, 94−104.

(8) Kim, S. H., MacIntyre, D. A., Hanyaloglu, A. C., Blanks, A. M., Thornton, S., Bennett, P. R., and Terzidou, V. (2016) The oxytocin receptor antagonist, Atosiban, activates pro-inflammatory pathways in human amnion via G$_{\alpha i}$ signalling. *Mol. Cell. Endocrinol.* 420, 11−23.

(9) Liao, Y., Lu, B., Ma, Q., Wu, G., Lai, X., Zang, J., Shi, Y., Liu, D., Han, F., and Zhou, N. (2016) Human neuropeptide S receptor is activated via a Gα$_q$ protein-biased signaling cascade by a human neuropeptide S analog lacking the C-terminal 10 residues. *J. Biol. Chem.* 291, 7505−7516.

(10) Badolia, R., Inamdar, V., Manne, B. K., Dangelmaier, C., Eble, J. A., and Kunapuli, S. P. (2017) G$_q$ pathway regulates proximal C-type lectin-like receptor-2 (CLEC-2) signaling in platelets. *J. Biol. Chem.* 292, 14516−14531.

(11) Pfeil, E. M., Brands, J., Merten, N., Vögtle, T., Vescovo, M., Rick, U., Albrecht, I.-M., Heycke, N., Kawakami, K., Ono, Y., Ngako Kadji, F. M., Hiratsuka, S., Aoki, J., Häberlein, F., Matthey, M., Garg, J., Hennen, S., Jobin, M.-L., Seier, K., Calebiro, D., Pfeifer, A., Heinemann, A., Wenzel, D., König, G. M., Nieswandt, B., Fleischmann, B. K., Inoue, A., Simon, K., and Kostenis, E. (2020) Heterotrimeric G protein subunit Gα$_q$ is a master switch for Gβγ-mediated calcium mobilization by Gi-coupled GPCRs. *Mol. Cell* 80, 940.

(12) Zhang, H., Nielsen, A. L., and Strømgaard, K. (2020) Recent achievements in developing selective G$_q$ inhibitors. *Med. Res. Rev.* 40, 135−157.

(13) Klepac, K., Kilić, A., Gnad, T., Brown, L. M., Herrmann, B., Wilderman, A., Balkow, A., Glöde, A., Simon, K., Lidell, M. E., Betz, M. J., Enerbäck, S., Wess, J., Freichel, M., Blüher, M., König, G., Kostenis, E., Insel, P. A., and Pfeifer, A. (2016) The G$_q$ signalling pathway inhibits brown and beige adipose tissue. *Nat. Commun.* 7, 10895.

(14) Matthey, M., Roberts, R., Seidinger, A., Simon, A., Schröder, R., Kuschak, M., Annala, S., König, G. M., Müller, C. E., Hall, I. P., Kostenis, E., Fleischmann, B. K., and Wenzel, D. (2017) Targeted inhibition of G$_q$ signaling induces airway relaxation in mouse models of asthma. *Sci. Transl. Med.* 9, eaag2288.

(15) van Breemen, R. B., and Li, Y. (2005) Caco-2 cell permeability assays to measure drug absorption. *Expert Opin. Drug Metab. Toxicol.* 1, 175−185.

195

16. Appendix

(16) Sun, H., Chow, E. C., Liu, S., Du, Y., and Pang, K. S. (2008) The Caco-2 cell monolayer: usefulness and limitations. *Expert Opin. Drug Metab. Toxicol.* 4, 395−411.

(17) Onken, M. D., Makepeace, C. M., Kaltenbronn, K. M., Kanai, S. M., Todd, T. D., Wang, S., Broekelmann, T. J., Rao, P. K., Cooper, J. A., and Blumer, K. J. (2018) Targeting nucleotide exchange to inhibit constitutively active G protein α subunits in cancer cells. *Sci. Signaling* 11, eaao6852.

(18) Annala, S., Feng, X., Shridhar, N., Eryilmaz, F., Patt, J., Yang, J., Pfeil, E. M., Cervantes-Villagrana, R. D., Inoue, A., Häberlein, F., Slodczyk, T., Reher, R., Kehraus, S., Monteleone, S., Schrage, R., Heycke, N., Rick, U., Engel, S., Pfeifer, A., Kolb, P., König, G., Bünemann, M., Tüting, T., Vázquez-Prado, J., Gutkind, J. S., Gaffal, E., and Kostenis, E. (2019) Direct targeting of $G\alpha_q$ and $G\alpha_{11}$ oncoproteins in cancer cells. *Sci. Signal.* 12, eaau5948.

(19) Lapadula, D., Farias, E., Randolph, C. E., Purwin, T. J., McGrath, D., Charpentier, T. H., Zhang, L., Wu, S., Terai, M., Sato, T., Tall, G. G., Zhou, N., Wedegaertner, P. B., Aplin, A. E., Aguirre-Ghiso, J., and Benovic, J. L. (2019) Effects of oncogenic $G\alpha_q$ and $G\alpha_{11}$ inhibition by FR900359 in uveal melanoma. *Mol. Cancer Res.* 17, 963−973.

(20) Chua, V., Lapadula, D., Randolph, C., Benovic, J. L., Wedegaertner, P. B., and Aplin, A. E. (2017) Dysregulated GPCR signaling and therapeutic options in uveal melanoma. *Mol. Cancer Res.* 15, 501−506.

(21) Taniguchi, M., Suzumura, K.-i., Nagai, K., Kawasaki, T., Takasaki, J., Sekiguchi, M., Moritani, Y., Saito, T., Hayashi, K., Fujita, S., Tsukamoto, S.-i., and Suzuki, K.-i. (2004) YM-254890 analogues, novel cyclic depsipeptides with $G\alpha_{q/11}$ inhibitory activity from *Chromobacterium* sp. QS3666. *Bioorg. Med. Chem.* 12, 3125−3133.

(22) Reher, R., Kuschak, M., Heycke, N., Annala, S., Kehraus, S., Dai, H.-F., Müller, C. E., Kostenis, E., König, G. M., and Crüsemann, M. (2018) Applying molecular networking for the detection of natural sources and analogues of the selective Gq protein inhibitor FR900359. *J. Nat. Prod.* 81, 1628−1635.

(23) Hermes, C., Richarz, R., Wirtz, D. A., Patt, J., Hanke, W., Kehraus, S., Voß, J. H., Küppers, J., Ohbayashi, T., Namasivayam, V., Alenfelder, J., Inoue, A., Mergaert, P., Gütschow, M., Müller, C. E., Kostenis, E., König, G. M., and Crüsemann, M. (2021) Thioesterase-mediated side chain transesterification generates potent Gq signaling inhibitor FR900359. *Nat. Commun.* 12, 144.

(24) Xiong, X.-F., Zhang, H., Underwood, C. R., Harpsøe, K., Gardella, T. J., Wöldike, M. F., Mannstadt, M., Gloriam, D. E., Bräuner-Osborne, H., and Strømgaard, K. (2016) Total synthesis and structure-activity relationship studies of a series of selective G protein inhibitors. *Nat. Chem.* 8, 1035−1041.

(25) Xiong, X.-F., Zhang, H., Boesgaard, M. W., Underwood, C. R., Bräuner-Osborne, H., and Strømgaard, K. (2019) Structure-activity relationship studies of the natural product $G_{q/11}$ protein inhibitor YM-254890. *ChemMedChem* 14, 865−870.

(26) Rensing, D. T., Uppal, S., Blumer, K. J., and Moeller, K. D. (2015) Toward the selective inhibition of G proteins: Total synthesis of a simplified YM-254890 analog. *Org. Lett.* 17, 2270−2273.

(27) Kuschak, M., Namasivayam, V., Rafehi, M., Voss, J. H., Garg, J., Schlegel, J. G., Abdelrahman, A., Kehraus, S., Reher, R., Küppers, J., Sylvester, K., Hinz, S., Matthey, M., Wenzel, D., Fleischmann, B. K., Pfeifer, A., Inoue, A., Gütschow, M., König, G. M., and Müller, C. E. (2020) Cell-permeable high-affinity tracers for G_q proteins provide structural insights, reveal distinct binding kinetics and identify small molecule inhibitors. *Br. J. Pharmacol.* 177, 1898−1916.

(28) Lipinski, C. A., Lombardo, F., Dominy, B. W., and Feeney, P. J. (1997) Experimental and computational approaches to estimate solubility and permeability in drug discovery and development settings. *Adv. Drug Delivery Rev.* 23, 3−25.

(29) Lennernäs, H. (1997) Human jejunal effective permeability and its correlation with preclinical drug absorption models. *J. Pharm. Pharmacol.* 49, 627−638.

(30) Yee, S. (1997) In vitro permeability across Caco-2 cells (colonic) can predict in vivo (small intestinal) absorption in man–fact or myth. *Pharm. Res.* 14, 763−766.

(31) Faassen, F. (2003) Caco-2 permeability, P-glycoprotein transport ratios and brain penetration of heterocyclic drugs. *Int. J. Pharm.* 263, 113−122.

(32) Federal Institute of Drugs and Medical Devices. (2020). *European Pharmacopoeia*, 10th ed., Bonn, Germany.

(33) Hamann, S. R., Blouin, R. A., and McAllister, R. G. (1984) Clinical pharmacokinetics of verapamil. *Clin. Pharmacokinet.* 9, 26−41.

(34) Słoczyńska, K., Gunia-Krzyżak, A., Koczurkiewicz, P., Wójcik-Pszczoła, K., Żelaszczyk, D., Popiół, J., and Pękala, E. (2019) Metabolic stability and its role in the discovery of new chemical entities. *Acta Pharm.* 69, 345−361.

(35) Smith, D. A., Beaumont, K., Maurer, T. S., and Di, L. (2019) Clearance in drug design. *J. Med. Chem.* 62, 2245−2255.

(36) McNaney, C. A., Drexler, D. M., Hnatyshyn, S. Y., Zvyaga, T. A., Knipe, J. O., Belcastro, J. V., and Sanders, M. (2008) An automated liquid chromatography-mass spectrometry process to determine metabolic stability half-life and intrinsic clearance of drug candidates by substrate depletion. *Assay Drug Dev. Technol.* 6, 121−129.

(37) Kuschak, M., Schlegel, J. G., Schneider, M., Kehraus, S., Voss, J. H., Seidinger, A., Matthey, M., Wenzel, D., Fleischmann, B. K., König, G. M., and Müller, C. E. (2020) Sensitive LC-MS/MS method for the quantification of macrocyclic $G\alpha_q$ protein inhibitors in biological samples. *Front. Chem.* 8, 833.

(38) Hamelmann, E., Schwarze, J., Takeda, K., Oshiba, A., Larsen, G. L., Irvin, C. G., and Gelfand, E. W. (1997) Noninvasive measurement of airway responsiveness in allergic mice using barometric plethysmography. *Am. J. Respir. Crit. Care Med.* 156, 766−775.

(39) Inamdar, V., Patel, A., Manne, B. K., Dangelmaier, C., and Kunapuli, S. P. (2015) Characterization of UBO-QIC as a $G\alpha_q$ inhibitor in platelets. *Platelets* 26, 771.

(40) Roszko, K. L., Bi, R., Gorvin, C. M., Bräuner-Osborne, H., Xiong, X.-F., Inoue, A., Thakker, R. V., Strømgaard, K., Gardella, T., and Mannstadt, M. (2017) Knockin mouse with mutant $G\alpha_{11}$ mimics human inherited hypocalcemia and is rescued by pharmacologic inhibitors. *JCI Insight* 2, e91079.

(41) Tietze, D., Kaufmann, D., Tietze, A. A., Voll, A., Reher, R., König, G., and Hausch, F. (2019) Structural and dynamical basis of G protein inhibition by YM-254890 and FR900359: An inhibitor in action. *J. Chem. Inf. Model.* 59, 4361−4373.

(42) Boesgaard, M. W., Harpsøe, K., Malmberg, M., Underwood, C. R., Inoue, A., Mathiesen, J. M., König, G. M., Kostenis, E., Gloriam, D. E., and Bräuner-Osborne, H. (2020) Delineation of molecular determinants for FR900359 inhibition of $G_{q/11}$ unlocks inhibition of $G\alpha_s$. *J. Biol. Chem.* 295, 13850.

Supporting Information

Macrocyclic Gq protein inhibitors

FR900359 and/or YM-254890 – fit for translation?

Jonathan G. Schlegel,[1][§] Mariam Tahoun,[1][§] Alexander Seidinger,[2] Jan H. Voss,[1] Markus

Kuschak,[1] Stefan Kehraus,[3] Marion Schneider,[1] Michaela Matthey,[2] Bernd K. Fleischmann,[4]

Gabriele M. König,[3] Daniela Wenzel,[2,4] and Christa E. Müller[1]*

[1]PharmaCenter Bonn, Pharmaceutical Institute, Pharmaceutical & Medicinal Chemistry, University of Bonn, Bonn, Germany
[2]Department of Systems Physiology, Medical Faculty, Ruhr University Bochum, Bochum, Germany
[3]Institute for Pharmaceutical Biology, University of Bonn, Bonn, Germany
[4] Institute of Physiology I, Life & Brain Center, Medical Faculty, University of Bonn, Bonn, Germany

[§]Equal contribution

*Address correspondence to
Prof. Dr. Christa E. Müller
Pharmazeutisches Institut
Pharmazeutische & Medizinische Chemie
An der Immenburg 4
D-53121 Bonn, Germany
Email: christa.mueller@uni-bonn.de
Phone: +49 228 73 2301

Cytochrome P450 enzyme inhibition

Most drugs undergo first-phase biotransformation reactions in the human liver which is catalyzed by enzymes of the cytochrome P450 (CYP450) family. High-affinity interactions between a drug and CYP enzymes may interfere with the metabolism of other drugs or natural products present as food constituents. Experiments investigating potential inhibition of CYP enzymes that are known to be important for drug metabolism showed no critical CYP-inhibitory effects, neither by FR nor YM. Both compounds displayed a similar profile. At a concentration of 1 µM, they exhibited only negligible effects on the investigated CYP enzymes. At a very high concentration of 10 µM, inhibition was still negligible to low (Figure 6), except for CYP3A4, which was inhibited by about 50% (FR: 50%, YM:56%). FR at 10 µM also displayed moderate inhibition of CYP2C8 (30 %) and CYP2C19 (38 %), whereas inhibition by 10 µM of YM was below 25%. These results indicate that both Gq inhibitors are not expected to interfere with hepatic metabolism of other drug molecules.
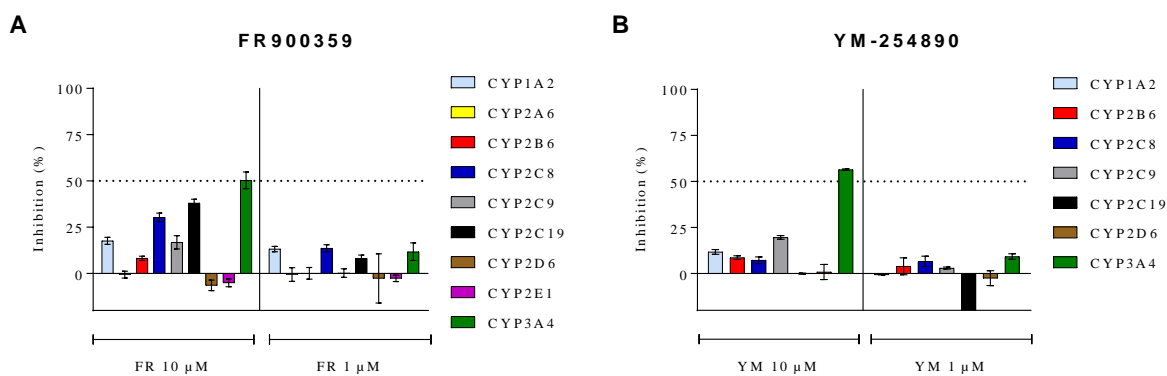
Figure S1. **A**. Percentage inhibition of CYP450 enzymes by FR at a concentration of 10 µM (left) and 1 µM (right). **B**. Percentage inhibition of CYP450 enzymes by YM at a concentration of 10 µM (left) and 1 µM (right).

CYP inhibition

The interactions of FR and YM with different recombinant human cytochrome P450 (CYP) enzymes were investigated by Pharmacelsus GmbH (Saarbrücken, Germany) using a fluorescence-based assay system. FR and YM were screened at 1 and 10 µM for inhibition of CYP1A2, CAP2B6, CYP2C8, CYP2C9, CYP2C19, CYP2D6 and CYP3A4. Additionally, FR was screened at 1 and 10 µM for inhibition of CYP2E and CYP2A6 enzymes. Assay was performed in a NADPH regenerating system containing 100 mM phosphate buffer and coumarine derivatives as substrates. Data represent means ± SEM (FR n=3; YM n=2).

16.5. Appendix E – Calcite precipitation forms crystal clusters and muscle mineralization during the decomposition of *Cambarellus diminutus* (Decapoda: Cambaridae) in freshwater

This section contains the article and supporting information of "Calcite precipitation forms crystal clusters and muscle mineralization during the decomposition of *Cambarellus diminutus* (Decapoda: Cambaridae) in freshwater" as it appears in the journal *Palaeontologia Electronica* by Palaeontological Association. Reprinted from *Palaeontologia Electronica* **2020**, 23(3):a55, copyright (2020), with permission from Palaeontological Association. This work is licensed under the Creative Commons Attribution-NonCommercial-ShareAlike 4.0 International (CC BY-NC-SA 4.0). To view a copy of this license, visit http://creativecommons.org/licenses/by-nc-sa/4.0/. As guaranteed by the author rights policy, copying and re-use of the article in any medium or format is allowed without permission or payment, as long as it is not used for commercial uses and the original article is fully acknowledged.
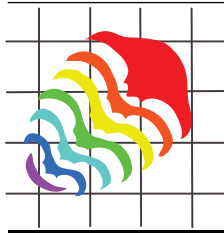
Palaeontologia Electronica
palaeo-electronica.org

Calcite precipitation forms crystal clusters and muscle mineralization during the decomposition of *Cambarellus diminutus* (Decapoda: Cambaridae) in freshwater

Bastian Mähler, Kathrin Janssen, Martina Menneken, Mariam Tahoun, Markus Lagos, Gabriele Bierbaum, Christa E. Müller, and Jes Rust

ABSTRACT

The fossilization of soft tissues is generally the replacement of organic structures by pseudomorphs in which muscle tissue is mostly replaced by minerals (i.e., phosphate, carbonate or pyrite). Micro-CT observations of decomposing crayfish in tank and distilled water, show a precipitation of crystal clusters over time. In addition, a mineralized muscle was found by SEM analyses. Raman spectroscopy (CRS) revealed that crystal clusters and the muscle consist of well-ordered calcite. Inductively coupled plasma mass spectrometry (ICPMS) of the distilled water showed a calcium content below the detection limit at the beginning of the experiments, which indicates that most of the calcium ions needed for the precipitation were provided by the decomposing carcasses themselves. Volume measurements of 3D-reconstructed calcite clusters and gastroliths showed a general increase of the volume of calcite clusters and simultaneously volume reduction of gastroliths with progressive decay. Specimens that were in the postmoult phase showed a smaller total volume of precipitated calcite, compared to specimens, which were in the intermoult or premoult phase. In addition, measurements of the total amount of body calcium of *Cambarellus diminutus* by atomic absorption spectrophotometry (AAS) revealed a higher amount of calcium in individuals without gastroliths than in individuals with gastroliths. It is assumed, that the higher the body size, the higher the volume of precipitated calcite, if the individuals were in the intermoult phase at the time of death. If the individuals were in the postmoult or premoult phase, the phase itself seems to be important.

Bastian Mähler. Section: Palaeontology, Institute of Geosciences, Rheinische Friedrich-Wilhelms-Universität Bonn, Nussallee 8, 53115 Bonn, Germany. Corresponding author. bastian.maehler@uni-bonn.de
Kathrin Janssen. Institute of Medical Microbiology, Immunology and Parasitology, Medical Faculty, Rheinische Friedrich-Wilhelms-Universität Bonn, Venusberg-Campus 1, 53127 Bonn, Germany. Kathrin.Janssen@ukbonn.de

Martina Menneken. Section Geochemistry, Institute of Geosciences, Rheinische Friedrich-Wilhelms-Universität Bonn, Meckenheimer Allee 169, 53115 Bonn, Germany. mmenneke@uni-bonn.de
Mariam Tahoun. Pharmazeutisches Institut, Pharmazeutische & Medizinische Chemie, Rheinische Friedrich-Wilhelms-Universität Bonn, An der Immenburg 4, 53121 Bonn, Germany. mtahoun@uni-bonn.de
Markus Lagos. Section Geochemistry, Institute of Geosciences, Rheinische Friedrich-Wilhelms-Universität Bonn, Meckenheimer Allee 169, 53115 Bonn, Germany. mlagos@uni-bonn.de
Gabriele Bierbaum. Institute of Medical Microbiology, Immunology and Parasitology, Medical Faculty, Rheinische Friedrich-Wilhelms-Universität Bonn, Venusberg-Campus 1, 53127 Bonn, Germany. g.bierbaum@uni-bonn.de
Christa E. Müller. Pharmazeutisches Institut, Pharmazeutische & Medizinische Chemie, Rheinische Friedrich-Wilhelms-Universität Bonn, An der Immenburg 4, 53121 Bonn, Germany. orcid.org/0000-0002-0013-6624 christa.mueller@uni-bonn.de
Jes Rust. Section: Palaeontology, Institute of Geosciences, Rheinische Friedrich-Wilhelms-Universität Bonn, Nussallee 8, 53115 Bonn, Germany. jrust@uni-bonn.de

INTRODUCTION

During the last 25 years, actuopaleontological studies of taphonomy have been performed by several scientists to shed light upon the conditions that are responsible for soft tissue preservation in the fossil record (Sansom, 2014; Briggs and McMahon, 2016). Soft tissues are not originally preserved, but occur as so called pseudomorphs that are generally formed by the replacement of the tissue by phosphates (e.g., Wilby and Whyte, 1995; Martill, 1988; Briggs et al., 2005; Briggs et al., 2011), carbonates (e.g., Wilby et al., 1996; Briggs et al., 1997; McCobb et al., 1998; Briggs et al., 2011), or pyrite (e.g., Wilby et al., 1996; Briggs, 2003; Schiffbauer et al., 2014; Farrell, 2014). In some cases, soft tissues can be organically preserved (Wiemann et al., 2018). Interactions between biotic and abiotic factors play an important role in these processes. For example, the pH value (abiotic factor) inside and around a carcass can be influenced by microbial activities (biotic factor) during decomposition (Berner, 1968; Vass, 2001). Fluctuations in the pH value caused by microbial activities can lead to the precipitation of crystal clusters composed of aragonite or calcite (pH increase) or soft tissue replacement by apatite (pH decrease) (Briggs and Kear, 1993; 1994; Briggs and Wilby, 1996; Sagemann et al., 1999; Raff et al., 2008).

Briggs and Kear (1993; 1994) reported that during their decomposition experiments with shrimps (*Crangon crangon*) and prawns (*Palaemon elegans*), in standard artificial seawater, muscle tissues were replaced by calcium phosphate in which the sole source of phosphate were the carcasses themselves. In addition, during their experiments precipitation of calcium carbonate clusters (aragonite) occurred within carcasses. Sagemann et al. (1999) also observed replacement of muscle tissue by calcium phosphate inside the shrimp *Crangon crangon* decaying in artificial seawater, but noticed precipitation of calcite crystal bundles as it is known from the fossil record (Briggs and Wilby, 1996). Klompmaker et al. (2019) published the first global data set of exceptionally preserved muscles in malacostracans in the fossil record and postulated that muscles are primarily preserved through phosphatization.

The results of this experimental approach demonstrate the possibility of muscle tissue mineralization only by calcite. The phenomenon of calcified muscles is very rare, but known in the fossil record (Jarzembowski, 1980; Wilby et al., 1996; McCobb et al., 1998; Selden, 2001; and Briggs et al., 2011).

MATERIAL AND METHODS

Individuals of the extant crayfish *Cambarellus diminutus* were taken from a settled tank community raised in our lab. The animals were kept in 54 L tanks of 60 x 30 cm in size, at a constant temperature of 26°C. Tanks were filled with pipe water and fortified with "Biotopol C" water conditioner (JBL, GmbH & Co. KG, Neuhofen, Germany) to neutralize zinc (Zn) and plumbum (Pb) and to remove chlorine (Cl) and bind copper (Cu). The crayfish were fed with nothing but "Crab Natural" (Sera, GmbH, Heinsberg, Germany), a main food

2

TABLE 1. Specimen sizes. C, crayfish; tank, tank water; dist, distilled water; ww, wet weight [g]; bs, body size [cm].

Sample	ww	bs	Sample	ww	bs	Sample	ww	bs
C1$_{tank}$	0.26	1.90	C1$_{dist.}$	0.39	2.10	C1$_{Ca}$	0.52	2.70
C2$_{tank}$	0.17	1.50	C2$_{dist.}$	0.19	1.70	C2$_{Ca}$	0.27	2.00
C3$_{tank}$	0.19	1.70	C3$_{dist.}$	0.21	1.70	C3$_{Ca}$	0.26	2.10
C4$_{tank}$	0.20	1.70	C4$_{dist.}$	0.25	1.90	C4$_{Ca}$	0.22	2.20
C5$_{tank}$	0.15	1.40	C5$_{dist.}$	0.23	1.80	C5$_{Ca}$	0.25	2.00
C6$_{tank}$	0.48	2.30	C6$_{dist.}$	0.52	2.50	C6$_{Ca}$	0.47	2.40
C7$_{tank}$	0.42	2.30	C7$_{dist.}$	0.24	1.70			
C8$_{tank}$	0.48	2.30	C8$_{dist.}$	0.36	2.10			
C9$_{tank}$	0.43	2.20	C9$_{dist.}$	0.34	1.90			
C10$_{tank}$	0.41	2.20	C10$_{dist.}$	0.31	2.00			

for crayfish (ingredients can be found in Appendix 1).

Twenty individuals (specimen C1$_{tank}$ to C10$_{tank}$ and C1$_{dist.}$ to C10$_{dist.}$), with partly filled guts, were sacrificed by placing them in an atmosphere of carbon dioxide (CO_2). Specimens were not dried before weighing on a micro scale. Lengths were measured from the anterior tip of the cephalothorax to the end of the abdomen without the telson (Table 1).

For the experiment, the 20 dead specimens (C1$_{tank}$ to C10$_{tank}$ / C1$_{dist.}$ to C10$_{dist.}$) were each placed in one sterile Falcon tube (50 mL) and fixed in place by synthetic filter floss (JBL GmbH & Co. KG, Neuhofen, Germany) in the middle of the test tube. Ten tubes were then filled with 50 mL of tank water (tank) and 10 tubes were filled with 50 mL of distilled water (dist.). Afterwards, tubes were sealed and stored in an incubator (Memmert GmbH & Co. KG, Schwabach, Germany) at a constant temperature of 30°C for 11 days.

Micro Computed Tomography (µ-CT)

During the first four days, samples were initially scanned once per day, followed by scans after seven and 11 days using a phoenix|x-ray v|tomex s 240 micro-computed-tomography (µ-CT) scanner (GE Measurement & Control, Wuntsdorf, Germany) located at the Institute of Geosciences of the University of Bonn. Each data set has a resolution of 30 µm; the scans were carried out at 120 kV and 120 µA. The CT data were processed using the software VGStudio Max 2.0 (Volume Graphics, Heidelberg, Germany) and Avizo 8.1 (FEI Visualization Sciences Group, Burlington, MA) to reconstruct and visualize the precipitated crystal clusters inside the specimens, and the gastroliths located inside the stomach. In addition, Avizo 8.1 was used for volume measurements of polygonal 3D-surface models.

Inductively Coupled Plasma Mass Spectrometry (ICPMS)

For water analyses, 4 mL of each test tube were taken and filled in a 5 mL tube, which had been previously cleaned twice by deionised water [MilliQ] (18.2 MΩ*cm at 25°C) and dried for two days. Afterwards, water samples in 5 mL tubes were acidified by 0.2 mL of concentrated nitric acid (HNO_3 [65 %]) and stored at 4°C. The calcium (Ca) content of the sample solutions were determined with an Element 2/XR Sector Field ICP-MS instrument (Thermo Fisher Scientific™) at medium resolution mode in order to avoid contributions from interfering species on the monitored Ca masses (^{43}Ca and ^{44}Ca). All solutions (including sample solutions, blank solutions, calibration solutions and reference materials) were measured twice and concentration data were derived from both signals, which were finally also compared for consistency. However, only concentrations based on ^{44}Ca signal intensities were eventually used because of generally higher precision. Prior to analysis all solutions were further diluted and adjusted to ~2 vol. % HNO_3. To correct for instrumental drift, rhodium (Rh) was added as an internal standard (all solutions were adjusted to a final Rh content of 1 µg/L). In addition to the internal standard, also drift monitors were repeatedly measured throughout the analytical sequence in order to allow, if necessary, for the correction of any additional drift that cannot be compensated by the internal standard. To evaluate the Ca content of the sample solutions, a 5-point linear calibration (covering the concentra-

3

TABLE 2. Concentration of calcium in tank water and distilled water. STD, standard; < DL, below detection limit.

Sample	Tank water	Distilled water
Concentration [µg/L]	56.52	< DL
	56.11	< DL
	55.88	< DL
	55.78	< DL
Mean concentration [µg/L]	56.07	< DL
STD [µg/L]	3.3	

tion range between 1 and 10 mg/L) was used with calibration solutions that were diluted from a Merck Certipur® VI certified multi element solution. The calibration was validated with SPS-SW2 (a certified reference material for element analysis in surface water). For this purpose, two different dilutions of SPS-SW2 that lie within the calibrated concentration range (a 2- fold and 4-fold diluted solution with Ca contents of 2.5 mg/L and 5.0 mg/L) were freshly prepared and analyzed.

ICPMS measurements revealed that at the beginning of the experiments an average of 56.07 µg/mL calcium was contained in tank water. The amount of calcium in distilled water was below the detection limit (Table 2).

Scanning Electron Microscope (SEM)

On day 11 the altered crayfish samples were removed from the test tubes. Crystal clusters and the mineralized muscle were dissected and coated by a thin layer of gold. Afterwards, samples were scanned with an 'environmental' scanning electron microscope (SEM) unit (TESCAN VEGA).

Confocal Raman Spectroscopy (CRS)

Crystal clusters and the mineralized muscle were embedded in epoxy resin (Araldite, Huntsman Advanced Materials (UK) Ltd.), ground with silicon carbide and polished with aluminium oxide for confocal Raman spectroscopy. Samples were analysed by a LabRam HR800 Raman spectrometer (Horiba Scientific) using a 784 nm laser as excitation source, a grating of 600 grooves/mm, and a 100 x objective with a numerical aperture of 0.9. The confocal hole size and the spectrometer entrance slit size was set to 1000 and 100 µm, respectively. With these settings the spectral resolution was 4.55 cm^{-1}. The total exposure time was 2 minutes with four accumulations of 30 s.

Atomic Absorption Spectrophotometry (AAS)

To analyse the complete amount of calcium inside *Cambarellus diminutus*, 6 individuals (C1$_{Ca}$ - C6$_{Ca}$) were taken from a settled tank community of our own breed and sacrificed by placing them in an atmosphere of CO_2. Afterwards crayfish were washed in MilliQ and weighed on a micro scale. Lengths were measured from the anterior tip of the cephalothorax to the end of the abdomen without the telson (Table 1). The individuals were then each dried in one ceramic bowl using an incubator (Memmert GmbH & Co. KG, Schwabach, Germany) at a constant temperature of 105°C for 24 hours and afterwards weighed on a micro scale. Each individual was finely ground by using a porcelain mortar and pestle and weighed again. Thereafter, powdered dry crayfish samples were ashed in a porcelain dish for 1 hour at 450°C using a muffle oven. Ashes were subsequently dissolved in 2 mL of 0.5 N aqueous hydrochloric acid solution, filtered and diluted to 25 mL with deionized water. A 1:10 dilution was made for each sample and analysed by using a Shimadzu AA-7000 Atomic Absorption Spectrophotometer (Shimadzu Deutschland GmbH). Calcium chloride solutions in a concentration range of 0.005-0.03 g/L were prepared for constructing a calibration curve (Appendix 2). Measurements were evaluated using the WizAArd Software (Shimadzu Deutschland GmbH).

RESULTS

General Observations

On day 2 carapaces changed their colouration from greenish-brown to red. On day 3 muscles began to shrink, becoming soft and crumbling by physical contact. On day 6 all carapaces appeared soft, jellylike and translucent. The crayfish specimens were fully articulated to day 11 (end of experiment), if not touched and kept in water.

Micro Computed Tomography (µ-CT)

µ-CT images revealed a precipitation of crystal clusters inside the chelipeds of sample C3$_{tank}$ after two days already. As the decay proceeded, crystalline structures were observed at the ventral side of the cephalothorax, inside the pereiopods, inside the coxa of the pleopods, along the ventro-lateral side of the tergites, in the telson, and the uropods (Figure 1.1 - 4). Specimens C4$_{tank}$, C6$_{tank}$, C9$_{tank}$ and C10$_{tank}$ as well as C1$_{dist.}$, C3$_{dist.}$, C4$_{dist.}$, C8$_{dist.}$, C9$_{dist.}$ and C10$_{dist.}$ contained one pair of gastroliths inside their stomach. Volume
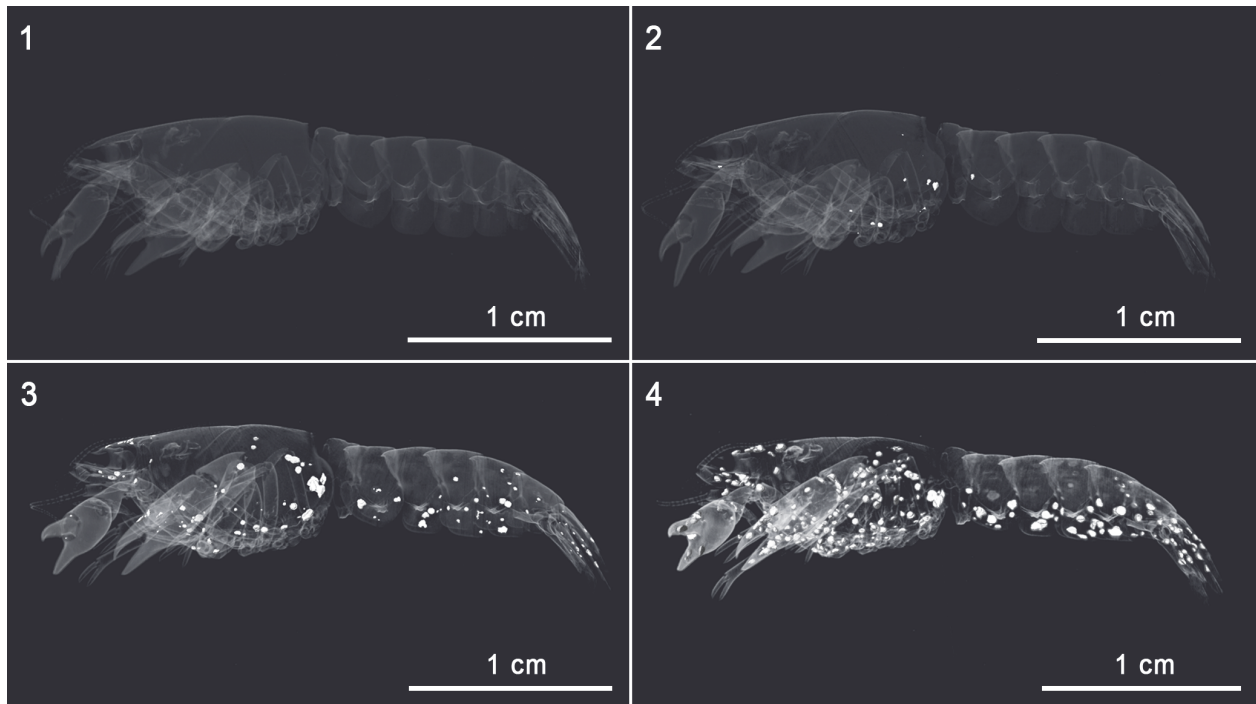
4

FIGURE 1. Translucent 3D-models of *Cambarellus diminutus* sample C7$_{tank}$ in combination with 3D-models of calcite clusters, which precipitated inside the carcass during its decomposition in freshwater. **1.1** 3D-model without calcite clusters on day 1. **1.2** 3D-model on day 2 showing a small amount of calcite clusters inside the cephalothorax and the first tergite. **1.3** 3D-model on day 4 showing a lot of calcite clusters inside the antennules, the left major propodus, the rostrum, the cephalothorax, the tergites, the uropods, and the telson. **1.4** 3D-model on day 7, showing widespread calcite clusters at the inner side of the carapace of the carcass except the dorsal side of the cephalothorax and the tergites (see also Figure.4.1). 3D-models were reconstructed based on µ-CT data.

measurements of polygonal 3D-surface models of gastroliths in tank and in distilled water showed an increase of the volume of the crystal clusters and a simultaneous volume reduction of gastroliths with progressive decay (Figure 2; see also Appendices 3-10). Further on, most specimens that contained gastroliths showed a smaller total volume of crystal clusters (TVC) compared to specimens without these structures (Figure 3). In addition, µ-CT images revealed that these crystal clusters only precipitated at the inner side of the carapaces (Figure 4.1).

Scanning Electron Microscope (SEM)

SEM-images show several structures of precipitated crystal clusters (Figure 5.1 – 5.6) varying in sizes from 260 µm to 470 µm at the end of the experiment. Most of these structures are spherical (Figure 5.2 and 5.3) or bispherical with mineralized cuticle and plumose setae (Figure 5.1 and 5.6). In addition, some crystal clusters are elliptical and tapering at one side as shown in Figure 5.4. Furthermore, a complete muscle in sample C3$_{tank}$ was mineralized (Figure 6). It was detected inside the

dactyl of the chela of the first left pereiopod. The muscle is 700 µm in length, slightly bent, thicker at the base and slightly tapering with a slightly rounded top. The muscle fibres are clearly visible. In addition, bacteria, which display rod-shaped structures, were detected on some precipitated clusters (Figure 4.2 – 4.3; Figure 5.6).

Confocal Raman Spectroscopy (CRS)

Raman analyses clearly revealed that the crystal clusters (Figure 5) and the mineralized muscle of sample C3$_{tank}$ (Figure 6.2 – 6.3) consist of well-ordered calcite (Figure 7), which can be identified by a sharp band near 1085 cm^{-1}, as well as the presence of lattice vibrations near 154 and 281 cm^{-1}, with the latter being absent in amorphous calcium carbonate (ACC).

Atomic Absorption Spectrophotometry (AAS)

AAS measurements of calcium content of six individuals of *Cambarellus diminutus* (C1$_{Ca}$ – C3$_{Ca}$ [containing gastroliths] and C4$_{Ca}$ – C6$_{Ca}$ [without gastroliths]) revealed that specimens without gas-
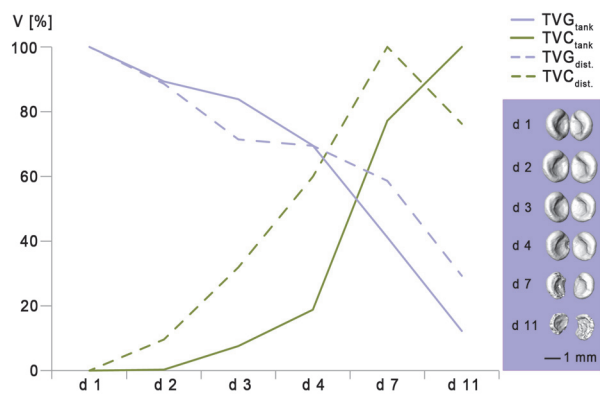
5

FIGURE 2. Median values of percentage decrease in the total volume of gastroliths (TVG_{tank} and $TVG_{dist.}$) in comparison to the percentage increase in the total volume of calcite clusters (TVC_{tank} and $TVC_{dist.}$) of sample $C4_{tank}$, $C6_{tank}$, $C9_{tank}$, $C10_{tank}$ and $C1_{dist.}$, $C3_{dist.}$, $C4_{dist.}$, $C8_{dist.}$, $C9_{dist.}$ and $C10_{dist.}$ for the duration of 11 days (Data set can be found in the supplement [Appendix 7– 10]). 100 % in $TVG_{tank/dist}$ represents the starting volume of gastroliths at the beginning of the experiments. 100 % in $TVC_{tank/dist}$ represents the maximum volume of calcite precipitation achieved during the experimental period. 3D-models in violet box show the reduction of gastroliths for the duration of 11 days. V, Volume; d, day; TVG, total volume of gastroliths; TVC, total volume of calcite; tank, tank water; dist., distilled water. 3D-models were reconstructed based on µ-CT data.

FIGURE 3. Comparison of the maximum volume of precipitated calcite of samples $C1_{tank}$ to $C10_{tank}$ and $C1_{dist.}$ to $C10_{dist.}$ in dependence of the body size. Specimens without gastroliths (which were in the intermoult phase) are marked with a circle. Specimens with gastroliths are marked by using a filled triangle (early premoult phase), filled squares (late premoult phase) and filled circles (postmoult phase). Also shown are regression lines for individuals without gastroliths ($R^2 = 0.39$) and with gastroliths ($R^2 = 0.08$).

troliths contain a higher amount of calcium than individuals with gastroliths (Appendix 7). Specimens $C1_{Ca}$ and $C3_{Ca}$ contain both ~1.9 µmol/mg with a gastrolith volume of 7.72 mm^3 and 2.12 mm^3. Specimen $C2_{Ca}$ showed a gastrolith volume of 0.2 mm^3 and a calcium content of 2.82 µmol/mg. Specimens without gastroliths ($C4_{Ca}$ - $C6_{Ca}$) showed a calcium content of 2.94 µmol/mg, 3.94 µmol/mg and 3.12 µmol/mg (Appendix 11).

DISCUSSION

In the exoskeleton (i.e., carapace) of crustaceans, calcium carbonate ($CaCO_3$) occurs in two forms: As (i) calcite and/or (ii) amorphous calcium carbonate (ACC) (Luquet and Marin, 2004), which both mainly provide the mechanical stability of the carapace (Nagasawa, 2012).

Results of the decomposition experiments employing the freshwater crayfish *Cambarellus diminutus*, in tank and distilled water, revealed that carapaces so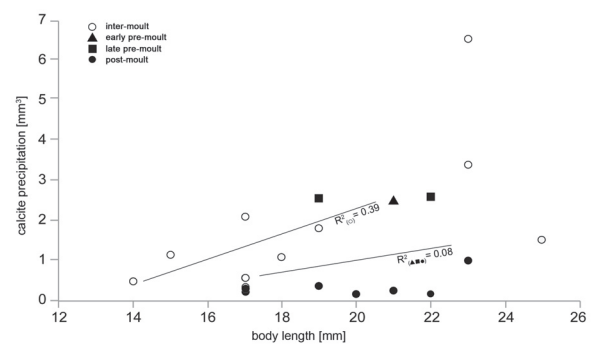ftened and continuously thinned out with progressive decay. This likely reflects the acidification of the body fluids inside the carcasses and their immediate surrounding environment, which usually occurs rapidly post mortem (Skopp, 2010; Mähler et al., 2015). The acidification is caused by an enzyme-controlled process called autolysis (Vass, 2001) and by bacterial activity (Skopp, 2010). During the decomposition, bacteria metabolize sugars, which may be derived from chitin (poly-β-1,4-N-acetyl-D-glucosamine) into organic acids and carbon dioxide. These compounds are water soluble and will dissolve in water as carbonic acid (Schoenen, 2013) and lead to a decrease of the pH value. Under such acidic conditions ACC and calcite inside the cuticle layers dissolve and release calcium ions (Ca^{2+}) into the body fluid and the surrounding medium resulting in a softened and thinned carapace.

Simultaneously with the degradation of the exoskeleton, crystal clusters of well-ordered calcite precipitated at the inner side of the carapaces of the carcasses (Figure 4.1), as in the experiments conducted by Briggs and Kear (1994) in which crystal bundles were formed by aragonite. A general increase of these calcite clusters in time can be deduced from polygonal 3D-surface models (Figure 1 and 2). Therefore, the local pH value at the inner side of the cuticle had to be increased during decay, because $CaCO_3$ will only precipitate by a change of the pH to more alkaline conditions. It is known that with progressive decay bacteria
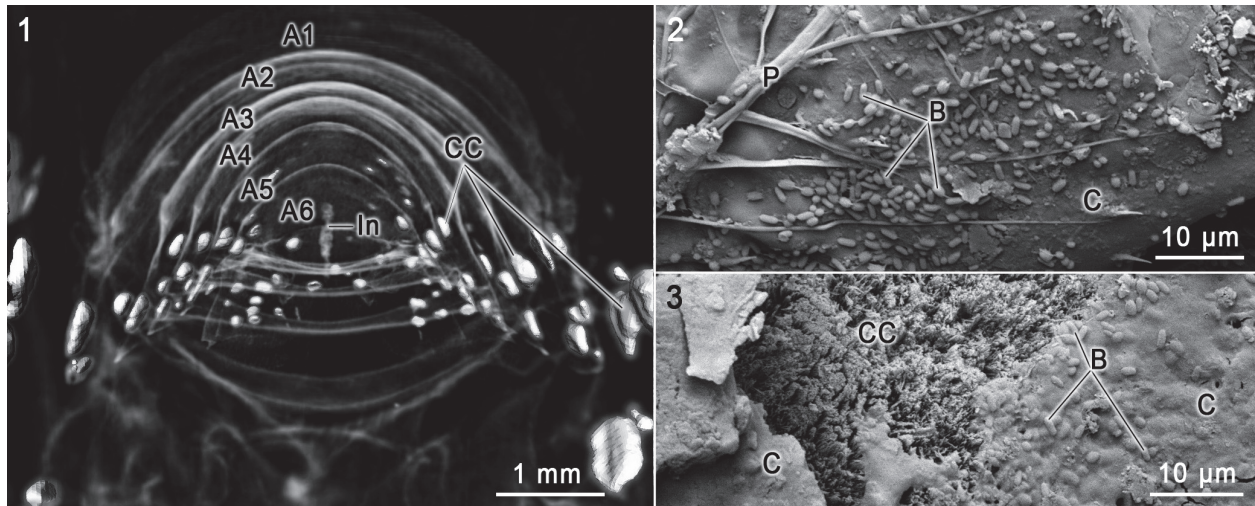
6

206

FIGURE 4. 4.1 Anterior view from the cephalothorax into the abdominal region of a translucent 3D model of *Cambarellus diminutus* sample C7$_{tank}$ in combination with 3D models of calcite clusters on day 7). **4.2** SEM image of the carapace surface with a plumose seta and some kind of bacteria. **4.3** SEM image of the surface of a calcite cluster with parts of the cuticle layers and bacteria. Abbreviations: A, abdominal segment; B, bacteria; C, cuticle; CC, calcite cluster; In, intestine; P, plumose seta. 3D-models were reconstructed based on µ-CT data.

start to degrade soft tissues and produce microbial enzymes, such as ureases and proteases and the bacterial metabolism switches to decomposition of amino acids and urea, leading to an increase of the pH value and an alkalization of the carcass (Skopp, 2010; Socks-Fischer et al., 1999). Urea is present in the haemolymph of crayfish as a detoxification product (Sharma, 1969) and is hydrolysed to ammonia and carbamate, which spontaneously decompose into a second molecule of ammonia and carbonic acid. In water, the products react to bicarbonate, ammonium and hydroxide ions, which results in an increase of the pH value. This alkalization of the surrounding area leads to the formation of $CaCO_3$ if soluble calcium ions are present (Hammes et al., 2003; Mobley and Hausinger, 1989). As the bacterial cell wall is negatively charged, it serves as a nucleation site for the mineralization process (Hammes et al., 2003; Stocks-Fischer et al., 1999). This observation is supported by descriptions of crystallized bacteria in the fossil record (Trewin and Knoll, 1999; Westall, 1999) and, likewise, growth of crystalline bacterial biofilms that occlude urinary catheters is a well-known problem in intensive care (Stickler, 2008).

It is thus conceivable, that because of autolytic processes, acidic conditions prevailed around and inside the carcasses. Under such acidic conditions calcium ions could be dissolved out of the cuticle layers (Figure 8.1 and 8.3). Due to the microbial activity inside the biofilm at the carcasses the pH increases with progressive decay, resulting in a recrystallization of calcium ions as calcite clusters at the inner side of the carapaces (Figure 8.2 and 8.4). This phenomenon of concentrated calcite clusters at the marginal areas of the carapaces were found in fossils like *Mesolimulus* and *Eryma fuciformes* from the Solnhofen limestone (Briggs and Wilby, 1996) and *Palaeobenthesicymus libanensis* from the Sahel Alma Lagerstätte of Lebanon (Audo and Charbonnier, 2011). As in our experiments, calcite clusters have not been observed in the centre of these fossil bodies (Briggs and Wilby, 1996; Audo and Charbonnier, 2011).

In decapods, gastroliths are $CaCO_3$ storages inside the cardiac stomach wall and consist of a network of protein-chitin fibres within calcium precipitated as ACC (Shechter et al., 2008; Luquet, 2013). Among other functions they are important for the restabilization of the carapace after ecdysis. In the moulting cycle crustaceans pass the four stages premoult, moult (ecdysis), postmoult and intermoult (Drach and Tchernigovtzeff, 1967). Initially to each premoult phase, calcium ions are dissolved out of the cuticle layers of the carapace and transported via the haemolymphatic circulatory system to the stomach (Ahearn et al., 2004). Inside the gastrolith cavity located inside the cardiac stomach wall (two anterior lateral specific discoid areas of the monolayered epithelium) (Shechter et al., 2008), $CaCO_3$ solidifies as amorphous calcium carbonate (ACC) under basic conditions to form gastroliths (Travis, 1960; Travis, 1963; Luquet,
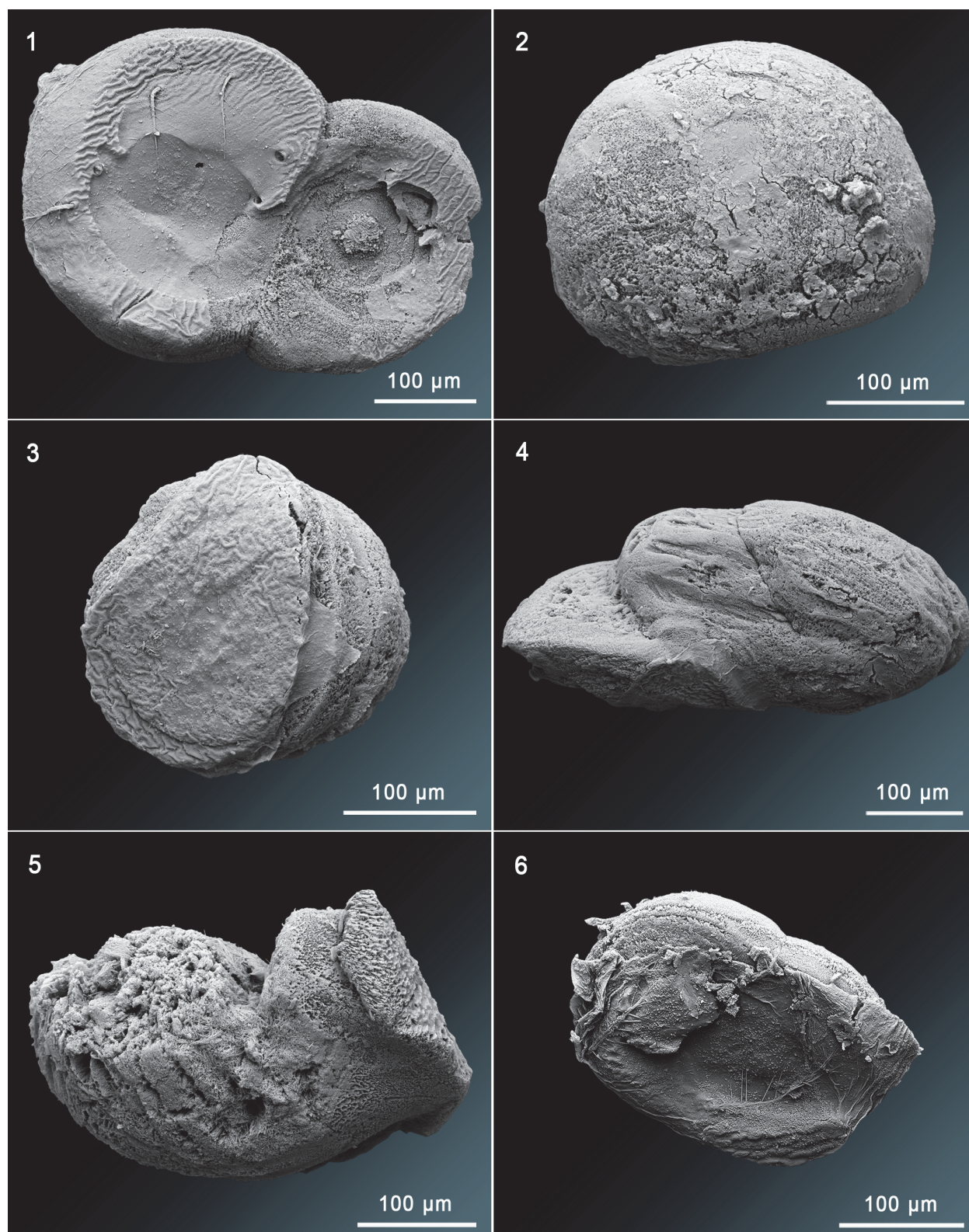
7

FIGURE 5. SEM-images of several diverse calcite structures which precipitated inside the carcasses. **5.1** Bispherical structure with mineralized setae and a part of the cuticle layers. **5.2** and **5.3** Spherical structures. **5.4** Elliptical structure which is tapering at the left side. **5.5** Complex structure. **5.6** Bispherical structure with mineralized setae and a part of the cuticle layers.
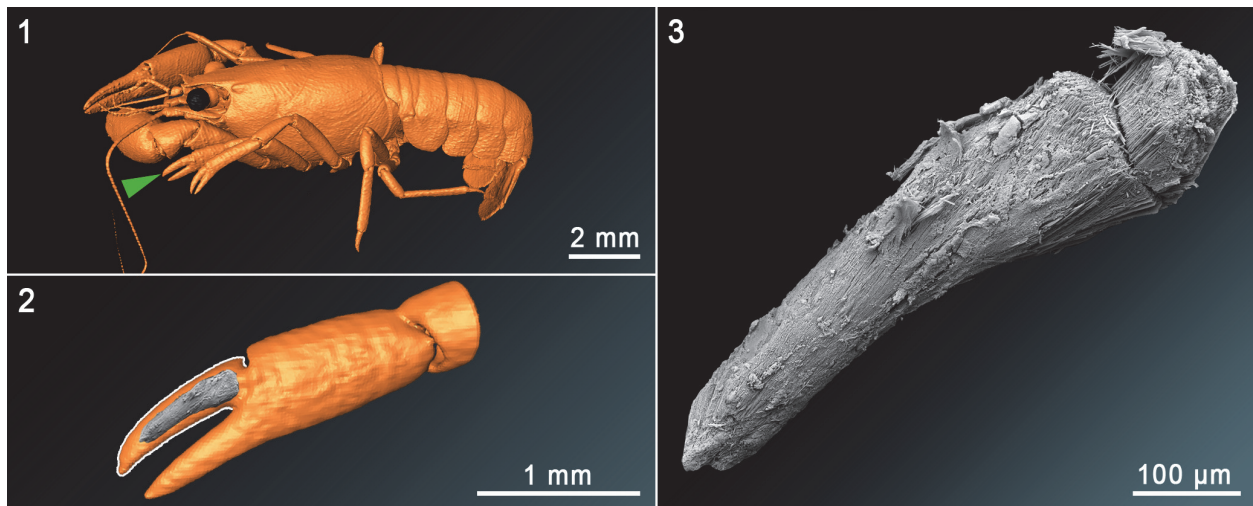
8

FIGURE 6. 3D-models and SEM-images of sample C3$_{tank}$. **6.1** 3D-model of the whole crayfish in dorso-lateral view. **6.2** 3D-model of the chela of the first left pereiopod in combination with a SEM-image of the calcified muscle of the dactyl. **6.3** SEM-image of a calcified muscle from the inside of the dactyl of the chela of the first left pereiopod. 3D-models were reconstructed based on μ-CT data.

2013), which are separated from digestive secretions by a cuticular lining (Ueno and Mizuhira, 1983). After the moulting gastroliths drop into the gastric lumen where they are digested and calcium ions can be reabsorbed (Ueno and Mizuhira, 1983). However, substantial quantities of calcium

FIGURE 7. Representative Raman spectra of a mineralized muscle of *Cambarellus diminutus* (sample C3$_{tank}$) and observed crystal clusters compared to Raman reference spectra of crystalline calcite and apatite, taken from the RRUFF Raman data base (*R040170, #R060070, Laetsch and Downs, 2006). Raman spectra of the mineralized muscle as well as of the crystal cluster exhibit all main Raman bands typically observed in well crystallized calcite, including the lattice modes, which are absent in amorphous calcium carbonate (Wang et al., 2011).

are released to the environment during the moulting phase.

Based on the presence of gastroliths, in individuals used in the decomposition experiments, there were 10 specimens in one of the two moulting phases, premoult or postmoult. In contrast, there were 10 individuals in the intermoult phase because of the absence of gastroliths.

Volume measurements of 3D-reconstructed gastroliths and calcite clusters revealed a volume reduction of gastroliths and simultaneously a general increase of the volume of calcite clusters with on-going decomposition (Figure 2). Consequently, two different pH values during the decomposition must have occurred inside the carcasses. On the one hand high pH values on the inner side of the cuticle, because of the precipitation of calcite clusters and on the other hand lower pH values inside the stomach, because of the continuous volume reduction of the gastroliths. In addition, gastrolith reduction in the experiment is a hint for an intact stomach wall during the decay for a duration of 11 days at 30°C.
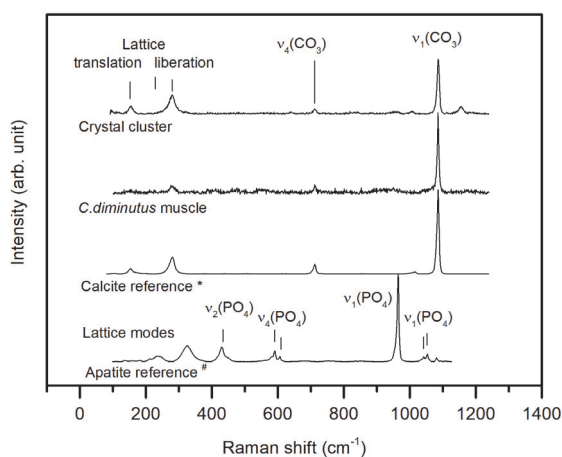
Because of the dissolving of the gastroliths, calcium ions necessary for the precipitation of calcite clusters could be provided (i) by dissolving ACC and calcite out of the cuticle layers, (ii) by free calcium ions inside the haemolymphatic circulatory system and (iii) by dissolving ACC of gastroliths inside the stomach (Figure 8.4). However, volume measurements of polygonal 3D surface models of calcite clusters of crayfish samples, which were in the postmoult phase, showed a smaller total vol-
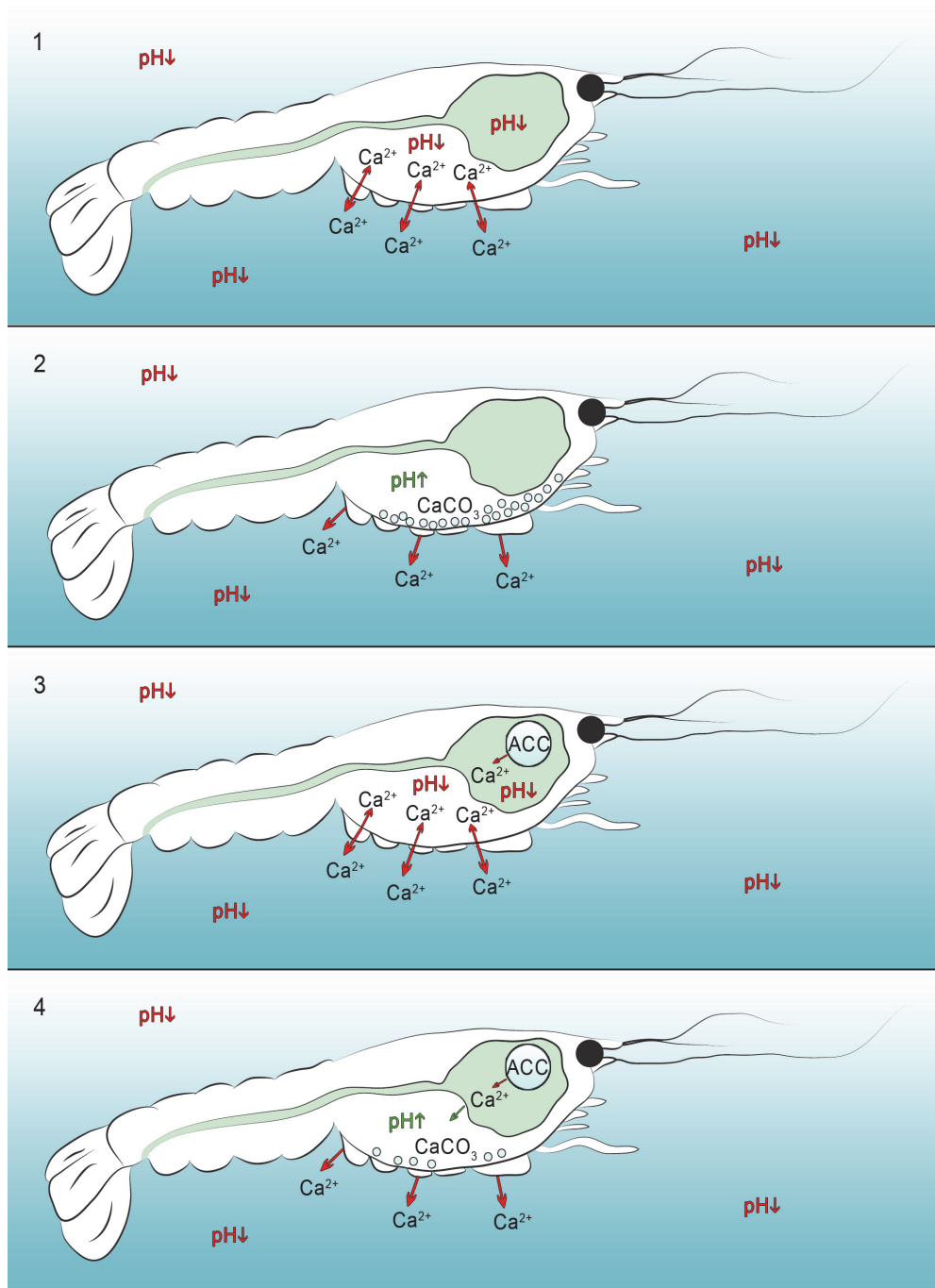
9

209

FIGURE 8. Hypothetical scenarios of calcium dissolution and precipitation of calcite clusters inside decomposing crayfish without (8.1-2) and with gastroliths in tank water (8.3-4). **8.1** Low pH-values around and inside the carcass caused by an enzymatic self-digestion (autolysis) and bacterial activity release dissolved calcium ions which migrate out of the carapace into the body cavity and into the environment (red arrows). **8.2** Increase of the pH-value inside the carcass caused by microbial activities during the putrefaction result in a precipitation of calcite clusters at the inner side of the carapace, consisting of previously dissolved calcium ions out of the cuticle layers. **8.3** Low pH-values around and inside the carcass caused by enzymatic self-digestion (autolysis) and bacterial activity resulted in an accumulation of dissolved calcium ions (red arrows). In addition, low pH conditions inside the stomach and decay of the "gastrolith-cavity-membrane" resulted in dissolving calcium ions from the gastroliths. **8.4** An increase of the pH-value inside the carcass, along the inner side of the carapace, caused by microbial activities during the putrefaction resulted in a precipitation of calcite clusters by previously dissolved calcium ions out of the cuticle layers and gastroliths.

10

ume of precipitated calcite (TVC) compared to specimens which were in the intermoult or premoult phase (Figure 3). In addition, calcium measurements of six crayfish individuals ($C1_{Ca} - C6_{Ca}$) by AAS showed a higher amount of calcium in individuals without gastroliths than in individuals containing big gastroliths like $C1_{Ca}$ (7.72 mm^3) and $C3_{Ca}$ (2.11 mm^3) (Appendix 11). It is assumed that the individuals $C1_{Ca}$ and $C3_{Ca}$ were in the early postmoult phase and lost most of their calcium ions during the moulting process. After moulting not enough calcium ions had been taken up by nutrition till the moment of death. However, individual $C2_{Ca}$ (containing gastroliths) showed a higher amount of calcium (2.82 µmol/mg) than $C1_{Ca}$ and $C3_{Ca}$ (1.91 µmol/mg and 1.92 µmol/mg). It is assumed that this individual was in the early premoult phase, at the time of death, where calcium ions were still inside the cuticle and the haemolymphatic circulatory system. In addition, only a small amount was inside the stomach where gastroliths are normally formed (TVG$_{Ca}$ of $C2_{Ca}$ = 0.195mm^3). The same is assumed for sample $C1_{dist}$ (decomposing in distilled water) in which the volume of gastroliths was quite small (0.077 mm^3), but the volume of precipitated calcite on day 7 was as high as in samples without gastroliths (2.52 mm^3) (marked in Figure 3 with a triangle; see also Appendix 4 and 6). Individuals like $C9_{tank}$ and $C9_{dist.}$ (marked in Figure 3 with squares) showed relatively high volumes of precipitated calcite (2.6 mm^3 and 2.58 mm^3) and high volumes of gastroliths (5.08 mm^3 and 3.44 mm^3), because both specimens might be in the late premoult phase, shortly before moulting in which one part of calcium was still bound in the old cuticle, and the other part was bound inside the stomach wall. For individuals which were in the intermoult phase at the time of death, it is assumed that the higher the body size, the higher the maximum of the total volume of precipitated calcite (Figure 3 and Appendix 12). But if the individuals were in the premoult or postmoult phase, only the moulting phase seems to be important for the amount of calcite precipitation and not the body size (Figure 3 and Appendix 12). Therefore, the moulting phase and/or the body size at the time of death might have an impact on the calcite precipitation and maybe on the fossilization process.

As shown by this preliminary study, variations in the precipitated calcite might cause by different body sizes (only in the intermoult phase) and might be influenced by the phase of moulting at the time of death. But variations of precipitated calcite in different individuals might also be caused by different intakes of calcium from the food, because the individuals were taken from a settled tank community where they were fed together. Whether the sex of the crayfish plays an important role in the precipitation of calcite is not known but possible. Sourie and Chaisemartin (1961) found a higher concentration of calcium in the haemolymph of crayfish males than in females. On the other hand, Greenway (1974) found no significant differences in his experiments with the same species.

A precipitation of calcite was noticed in individuals which decomposed in distilled water in which no relevant quantities of calcium were measured at the beginning of the experiment (Table 2). Consequently, calcium ions, which are needed for the precipitation of calcite clusters, were mostly provided from the crayfish individuals themselves.

Wilby et al. (1996) published a digenetic sequence in which soft tissues of *Dollocaris ingens*, discovered from the marine Konservat-Lagerstätte of La Voulte-sur-Rhône, were first stabilized by apatite, later replaced by calcite and afterwards coated or replaced by pyrite. Jauvion et al. (2019) investigated the fossil of *Dollocaris ingens* again, along with another specimen of *D. ingens* discovered from the same locality and presented the thesis that an early precipitation of fluorapatite and pyrite was responsible for the exceptional preservation of soft tissues and anatomical details. They suspect further that Mg-calcite precipitated afterwards, while the sediment was still soft, and protected the individuals and formed the concretions (Jauvion et al., 2019). Klompmaker et al. (2019) postulated that muscle tissues in malacostracans are primarily preserved through phosphatization, and because of taphonomic experiments conducted by Briggs and Kear (1993 and 1994) or Sagemann et al. (1999), phosphatization (apatite) seems to be the natural way of muscle tissue preservation. However, nearly most of the experiments conducted before were carried out with marine and/or artificial seawater to simulate marine conditions. In our experiments fresh water was used, and it could be shown that the muscle tissue of sample $C3_{tank}$ (Figure 6) was only replaced by calcite (Figure 7). Even if it could only be proven in one individual, we demonstrate that under freshwater conditions muscle tissue can be stabilized by calcium carbonate early in the decomposition process. This phenomenon of muscle preservation by calcite in the fossil record is very

rare but known from invertebrate fossils discovered from the lacustrine limestones of the insect bed of Bembridge Marls in England (McCobb et al., 1998). Jarzembowski (1980) found in this locality calcified muscle tissue inside the abdomen of a butterfly and McCobb et al. (1998) found calcified muscle fibres and sarcolemma in two of fifteen examined insect fossils. Based on the results of Jarzembowski (1980) and McCobb et al. (1998), Selden (2001) assumed that the muscle fibres of an Eocene spider (*Vectaraneus yulei*) from Bembridge Marls are also calcified. But muscle tissue preservation by calcite is also known from the Jurassic marine biota of La Voulte-sur-Rhône in France (Wilby et al., 1996) or from *Montecaris gogensis* discovered from the Upper Devonian Gogo Formation in Western Australia (Briggs et al., 2011).

CONCLUSIONS

The precipitation of calcite clusters and the mineralization of muscle tissue in crayfish carcasses under freshwater conditions at 30°C occur early in the decomposition process. In addition, the difference in the total volume of calcite clusters in different individuals is due to the amount of calcium ions inside the cuticle layers, the haemolymphatic circulatory system and the gastroliths at the time of death, and the chemical conditions of the surrounding medium. It seems that the precipitation of diverse, calcified structures during the decomposition of *Cambarellus diminutus* in tank (freshwater) and distilled water depends on the body size when individuals are in the intermoult phase at the time of death. But in individuals which were in the pre-

moult or postmoult phase, the body size plays a subordinate role. In this case the phases of the moulting cycle might have a higher impact on the precipitation of calcite. In addition, the absence of gastroliths might favour the precipitation of calcite. Whether the absence of gastroliths favours the mineralization of muscle tissue (like in sample $C3_{tank}$) has to be proved in further experiments. To validate the results of this experimental approach, an experimental setup with a larger number of individuals and a permanent measurement of the pH values inside and outside the specimens will be conducted.

REFERENCES

Ahearn, G.A., Mandal, P.K., and Mandal, A. 2004. Calcium regulation in crustaceans during the molt cycle: a review and update. Comparitive Biochemistry and Physiology Part A: Molecular & Integrative Physiology, 137(2):247-257. https://doi.org/10.1016/j.cbpb.2003.10.012

Audo, D. and Charbonnier, S. 2011. The crest-bearing shrimps from the Sahel Alma Lagerstätte (Late Cretaceous, Lebanon). Acta Palaeontologica Polonica 58(2):335-349. https://doi.org/10.4202/app.2011.0056

Berner, R.A. 1968. Calcium carbonate concentrations formed by the decomposition of organic matter. Science, 159(3811):195-197. https://doi.org/10.1126/science.159.3811.195

Briggs, D.E.G. 2003. The role of decay and mineralization in the preservation of soft-bodied fossils. Annual Review of Earth and Planetary Sciences, 31:275-301. https://doi.org/10.1146/annurev.earth.31.100901.144746

Briggs, D.E.G. and Kear, A.J. 1993. Decay and preservation of polychaetes: taphonomic thresholds in soft-bodied organisms. Paleobiology, 19(1):107-135. https://doi.org/10.1017/S0094837300012343

Briggs, D.E.G. and Kear, A.J. 1993. Fossilization of soft tissue in the laboratory. Science, 259(5100):1439-1442. https://doi.org/10.1126/science.259.5100.1439

Briggs, D.E.G. and Kear, A.J. 1994. Decay and mineralization of shrimps. Palaios, 9:431-456. https://doi.org/10.2307/3515135

Briggs, D.E.G. and McMahon, S. 2016. The role of experiments in investigating the taphonomy of exceptional preservation. Palaeontology, 59(1):1-11. https://doi.org/10.1111/pala.12219

Briggs, D.E.G., Moore, R.A., Shultz, J.W., and Schweigert, G. 2005. Mineralization of soft-part anatomy and invading microbes in the horseshoe crab *Mesolimulus* from the Upper Jurassic Lagerstätte of Nusplingen, Germany. Proceedings of the Royal Society B, 272:627-632. https://doi./10.1098/rspb.2004.3006

Briggs, D.E.G., Rolfe, W.D.I., Butler, P.D., Liston, J.J., and Ingham, J.K. 2011. Phyllocarid crustaceans from the Upper Devonian Gogo Formation, Western Australia. Journal of Systematic Palaeontology 9(3):399-424. https://doi.org/10.1080/14772019.2010.493050

Briggs, D.E.G. and Wilby, P.R., 1996. The role of the calcium carbonate-calcium phosphate switch in the mineralization of soft- bodied fossils. Journal of the Geological Society, 153:665-668. htt s://doi.org/10.1144/gsjgs.153.5.0665

Briggs, D.E.G., Wilby, P.R., Pérez-Moreno, B.P., Luis Sanz, J., and Fregenal-Martínez, M. 1997. The mineralization of dinosaur soft tissue in the Lower Cretaceous of Las Hoyas, Spain. Journal of the Geological Society, 154:587-588. https://doi.org/10.1144/gsjgs.154.4.0587

Drach, P. and Tchernigovtzeff, C. 1967. Sur la method de determination des stades d'intermue et son application générale aux crustacés. Vie et Milieu Serie A: Biologie Marine, 18(3A):595-610.

Farrell, Ù.C. 2014. Pyritization of soft tissues in the fossil record: an overview. The Paleontological Society Papers, 20:35-58. https://doi.org/10.1017/S1089332600002795

Greenaway, P. 1974. Total body calcium and haemolymph calcium concentrations in the crayfish *Austropotamobius pallipes* (Lereboullet). Journal of Experimental Biology, 61:19-26.

Hammes, F., Boon, N., Villiers, J. de, Verstraete, W., and Siciliano, S.D. 2003. Strain-specific ureolytic microbial calcium carbonate precipitation. Applied and Environmental Microbiology, 69(8):4901-4909. https://doi.org/10.1128/aem.69.8.4901-4909.2003

Jarzembowski, E.A. 1980. Fossil insects from the Bembridge Marls, Palaeogene of the Isle of Wight, southern England. Bulletin of the British Museum of Natural History (Geology), 4:237-293.

Jauvion, C., Bernard, S., Gueriau, P., Mocuta, C., Pont, S., Benzerara, K., and Charbonnier, S. 2019. Exceptional preservation requires fast biodegradation: thylacocephalan specimens from La Voulte-sur-Rhône (Callovian, Jurassic, France). Palaeontology, 63(3):395-413. https://doi.org/10.1111/pala.12456

Klompmaker, A.A., Hyžný, M., Portell, R.W., Jauvion, C., Charbonnier, S., Fussell, S.S., Klier, A.T., Tejera, R., and Jakobsen, S.L. 2019. Muscles and muscle scars in fossil malacostracan crustaceans. Earth-Science Reviews, 194:306-326. https://doi.org/10.1016/j.earscirev.2019.04.012

Laetsch T. and Downs, R.T. 2006. Software for identification and refinement of cell parameters from powder diffraction data of minerals using the RRUFF project and American mineralogist crystal structure databases. Abstracts from the 19th General Meeting of the International Mineralogical Association, Kobe, Japan, 23-28 July 2006.

Luquet, G. and Marin, F. 2004. Biomineralization in crustaceans: storage strategies. Comptes Rendus Palevol, 3(6-7):515-534. https://doi.org/10.1016/j.crpv.2004.07.015

Luquet, G., Fernández, M.S., Badou, A., Guichard, N., Le Roy, N., Corneillat, M., Alcaraz, G., and Arias, J.L. 2013. Comparative ultrastructure and carbohydrate composition of gastroliths from Astacidae, Cambaridae and Parastacidae freshwater crayfish (Crustacea, Decapoda). Biomolecules, 3:18-38. https://doi.org/10.3390/biom3010018

Martill, D.M. 1988. Preservation of fish in the Cretaceous Santana Formation of Brazil. Paleontology, 31(1):1-18.

Mähler, B., Schwermann, A.H., Wuttke, M., Schultz, J.A., and Martin, T. 2015. Four-dimensional virtopsy and the taphonomy of a mole from the Oligocene of Lake Enspel (Germany). Palaeobiodiversity and Palaeoenvironment, 95(1):115-131. https://doi.org/10.1007/s12549-014-0180-x

McCobb, L.M.E., Duncan, I.J., Jarzembowski, E.A., Stankiewicz, B.A., Wills, M.A., and Briggs, D.E.G. 1998. Taphonomy of the insects from the Insect Bed (Bembridge Marls), late Eocene, Isle of Wight, England. Geological Magazine, 135(4):553-563. https://doi.org/10.1017/s0016756898001204

McWhinnie, M.A. 1962. Gastrolith growth and calcium shifts in the freshwater crayfish, *Orconectes virilis*. Comparative Biochemistry and Physiology, 7:1-14. https://doi.org/10.1016/0010-406x(62)90021-x

Mobley, H.L.T. and Hausinger, R.P. 1989. Microbial ureases: significance, regulation, and molecular characterization. Microbiological Reviews, 53(1):85-108.

Nagasawa, H. 2012. The crustacean cuticle: structure, composition and mineralization. Frontiers in Bioscience, E4:711-720. https://doi.org/10.2741/e412

Pinheiro, F.L., Horn, B.L.D., Schultz, C.L., Andrade, J.A.F.G. de, and Sucerquia, P.A. 2012. Fossilized bacteria in a Cretaceous pterosaur headcrest. Lethaia, 45:495-499. https://doi.org/10.1111/j.1502-3931.2012.00309.x

Raff, E.C., Schollaert, K.L., Nelson, D.E., Donoghue, P.C.J., Thomas, C.-W., Turner, F.R., Stein, B.D., Dong, X., Bengtson, S., Huldtgren, T., Stampanoni, M., Chongyu, Y., and Raff, R.A. 2008. Embryo fossilization is a biological process mediated by microbial biofilms. Proceedings of the National Academy of Sciences, 105(49):19360-19365. https://doi.org/10.1073/pnas.0810106105

Sagemann, J., Bale, S.J., Briggs, D.E.G., and Parkes, R.J. 1999. Controls of the formation of authigenic minerals in association with decaying organic matter: an experimental approach. Geochimica et Cosmochimica Acta, 63(7/8):1083-1095. https://doi.org/10.1016/S0016-7037(99)00087-3

Sansom, R.S. 2014. Experimental decay of soft tissues. The Paleontological Society Papers, 20:259-274. https://doi.org/10.1017/S1089332600002886

Schiffbauer, J.D., Xiao, S., Cai, Y., Wallace, A.F., Hua, H., Hunter, J., Xu, H., Peng, Y., and Kaufman, A.J. 2014. A unifying model for Neoproterozoic-Palaeozoic exceptional fossil preservation through pyritization and carbonaceous compression. Nature Communications, 5:5754. https://doi.org/10.1038/ncomms6754

Schoenen, D. 2013. Verwesung, der mikrobielle Abbauprozess menschlicher Leichen und seine Bedeutung für den öffentlichen Gesundheitsdienst, Hygiene, Friedhofswesen, Bodenkunde, Rechtsmedizin und Kriminologie. Shaker Verlag, Aachen.

Selden, P.A. 2001. Eocene spiders from the Isle of Wight with preserved respiratory structures. Palaeontology, 44(4):695-729. https://doi.org/10.1111/1475-4983.00199

Sharma, M.L. 1969. Trigger mechanism of increased urea production by the crayfish, *Orconectes rusticus* under osmotic stress. Comparative Biochemistry and Physiology, 30(2):309-321. https://doi.org/10.1016/0010-406X(69)90813-5

Shechter, A., Berman, A., Singer, A., Freiman, A., Grinstein, M., Erez, J., Aflalo, E.D., and Sagi, A. 2008. Reciprocal changes in calcification of the gastrolith and cuticle during the molt cycle of the red claw crayfish *Cherax quadricarinatus*. The Biological Bulletin, 214:122-134. https://doi.org/10.2307/25066669

Skopp, G. 2010. Postmortem toxicology. Forensic Science Medicine and Pathology, 6:314-325. https://doi.org/10.1007/s12024-010-9150-4

Sourie, R. and Chaisemartin, C. 1961. Les variations de la teneur en calcium de l'hémolymphe chez Astacus pallipes Lereboullet. Vie Milieu, 12:605-613.

Stickler DJ. 2008. Bacterial biofilms in patients with indwelling urinary catheters. Nature Clinical Practice Urology, 5:598-608. https://doi.org/10.1038/ncpuro1231

Stocks-Fischer, S., Galinat, J.K., and Bang, S.S. 1999. Microbiological precipitation of $CaCO_3$. Soil Biology and Biochemistry, 31:1563-1571. https://doi.org/10.1016/s0038-0717(99)00082-6

Travis, D.F. 1960. The deposition of skeletal structures in the Crustacea. I. The histology of the gastrolith skeletal tissue complex and the gastrolith in the crayfish, *Orconectes (Cambarus) virilis* Hagen - Decapoda. The Biological Bulletin, 118(1):137-149. https://doi.org/10.2307/1539064

Travis, D.F. 1963. Structural features of mineralization from tissue to macromolecular levels of organization in the decapod Crustacea. Annals of the New York Academy of Science, 109(1):177-245. https://doi.org/10.1111/j.1749-6632.1963.tb13467.x

Trewin, N.H. and Knoll, A.H. 1999. Preservation of Devonian chemotrophic filamentous bacteria in calcite veins. Palaios, 14:288-294. https://doi.org/10.2307/3515441

14

Ueno, M. and Mizuhira, V. 1983. Calcium transport mechanism in crayfish gastrolith epithelium correlated with the molting cycle. II. Cytochemical demonstration of Ca^{2+}-ATPase and Mg^{2+}-ATPase. Histochemistry, 80:231-217. https://doi.org/10.1007/bf00495768

Vass, A.A. 2001. Beyond the grave-understanding human decomposition. Microbiology Today, 28:190-192

Wang, D., Hamm, L.M., Bodnar, R.J., and Dove, P.M. 2011. Raman spectroscopic characterization of the magnesium content in amorphous calcium carbonates. Journal of Raman Spectroscopy, 43(4):543-548. https://doi.org/10.1002/jrs.3057

Westall, F. 1999. The nature of fossil bacteria: a guide to the search for extraterrestrial life. Journal of Geophysical Research, 104(E7):16437-16451. https://doi.org/10.1029/1998JE900051

Wiemann, J., Fabbri, M., Yang, T.-R., Stein, K., Sander, P.M., Norell, M.A., and Briggs, D.E.G. 2018. Fossilization transforms vertebrate hard tissue proteins into N-heterocyclic polymers. Nature Communications, 9:4741. https://doi.org/10.1038/s41467-018-07013-3

Wilby, P.R., Briggs, D.E.G., and Riou, B. 1996. Mineralization of soft-bodied invertebrates in a Jurassic metalliferous deposit. Geology, 24(9):847-850. https://doi.org/10.1130/0091-7613(1996)024<0847:mosbii>2.3.co;2

Wilby, P.R. and Whyte, M.A. 1995. Phosphatized soft tissue in bivalves from the Portland Roach of Dorset (Upper Jurassic). Geological Magazine, 132(1):117-120. https://doi.org/10.1017/S001675680001147X

15

16. Appendix

APPENDICES

All appendices are available as PDF files for download at
https://palaeo-electronica.org/content/2020/2893-decomposing-crayfish

APPENDIX 1.

Contents of the feed.

APPENDIX 2.

Data set and calibration curve for calcium chloride.

APPENDIX 3.

Total volume of calcite precipitation in crayfish in tank water on day 1 to 4 and day 7 and 11.

APPENDIX 4.

Total volume of calcite precipitation in crayfish in distilled water on day 1 to 4 and day 7 and 11.

APPENDIX 5.

Total volume of gastroliths of crayfish in tank water $C4_{tank}$, $C6_{tank}$, $C9_{tank}$ and $C10_{tank}$ on day 1 to 4 and day 7 and 11.

APPENDIX 6.

Total volume of gastroliths of crayfish in distilled water $C1_{dist.}$, $C3_{dist.}$, $C4_{dist.}$, $C8_{dist.}$, $C9_{dist.}$ and $C10_{dist.}$ on day 1 to 4 and day 7 and 11.

APPENDIX 7.

Total volume of gastroliths in percent (%) for day 1 to 4 and day 7 and 11 of crayfish sample $C4_{tank}$, $C6t_{ank}$, $C9_{tank}$ and $C10_{tank}$ in tank water.

APPENDIX 8.

Total volume of gastroliths in percent (%) for day 1 to 4 and day 7 and 11 of crayfish sample $C1_{dist.}$, $C3_{dist.}$, $C4_{dist.}$, $C8_{dist.}$, $C9_{dist.}$, and $C10_{dist.}$ in distilled water.

APPENDIX 9.

Total volume of gastroliths in percent [%] for day 1 to 4 and day 7 and 11 of crayfish sample $C4_{tank}$, $C6_{tank}$, $C9_{tank}$ and $C10_{tank}$ in tank water.

16

APPENDIX 10.

Total volume of gastroliths in percent [%] for day 1 to 4 and day 7 and 11 of crayfish sample $C1_{dist.}$, $C3_{dist.}$, $C4_{dist.}$, $C8_{dist.}$, $C9_{dist.}$, and $C10_{dist.}$ in distilled water.

APPENDIX 11.

Additional information on the crayfish samples used for AAS.

APPENDIX 12.

Relationship between body size and maximum volume of precipitated calcite.

Product information

Complete feed for all crustaceans

Ingredients

fish meal, corn starch, wheat flour, spirulina, brewers yeast, wheat germ, gammarus, Ca-caseinate, sea algae, stinging nettle, willow bark, alder cones, fish oil (containing 49% omega fatty acids), mannan oligosaccharides, herbs, alfalfa, parsley, paprika, green-lipped mussel, spinach, carrots, Haematococcus algae, garlic.

Analytical constituents

Crude Protein 36.7%, Crude Fat 11.1%, Crude Fiber 4.5%, Moisture 5.2%, Crude Ash 8.6%, Ca 1.9%, P 1.0%.

Additives

Vitamins and provitamins: Vit. A 37,000 IU/kg, Vit. D_3 1,800 IU/kg, Vit. E (D, L-α-tocopheryl acetate) 120 mg/kg, Vit. B_1 35 mg/kg, Vit. B_2 90 mg/kg, stab. Vit. C (L-ascorbyl monophosphate) 550 mg/kg.

TableS1 Data set of calibration curve for calcium chloride

Concentration [g/L]	0.00549	0.01098	0.01647	0.02196	0.02745	0.03294
	0.1033	0.2344	0.3728	0.4936	0.6371	0.7297
	0.1036	0.2324	0.3615	0.496	0.6148	0.7336
	0.1083	0.2342	0.3759	0.5057	0.622	0.726
Mean Absorbance	**0.1051**	**0.2337**	**0.3701**	**0.4984**	**0.6246**	**0.7298**
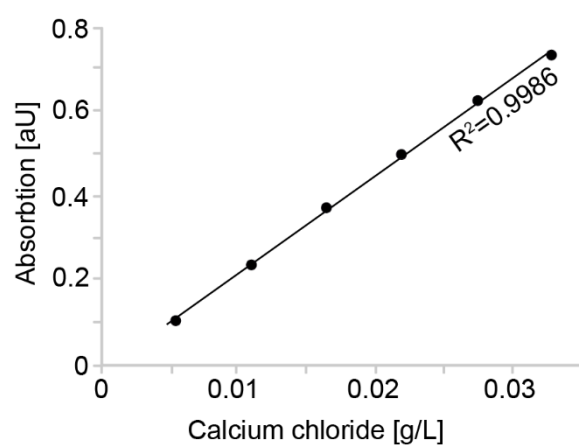
16. Appendix

Table S2 Total Volume of Calcite (TVC_{tank}) [mm^3]

Sample	day 1	day 2	day 3	day 4	day 7	day 11
$C1_{tank}$	0.000	0.007	0.494	0.818	1.044	1.825
$C2_{tank}$	0.000	0.009	0.018	0.199	1.156	0.626
$C3_{tank}$	0.000	0.017	0.122	0.604	1.772	2.107
$C4_{tank}$	0.000	0.000	0.001	0.009	0.210	0.285
$C5_{tank}$	0.000	0.029	0.039	0.375	0.485	0.418
$C6_{tank}$	0.000	0.006	0.147	0.322	0.813	1.007
$C7_{tank}$	0.000	0.035	0.621	1.165	2.304	3.401
$C8_{tank}$	0.000	0.000	0.759	1.894	3.292	6.544
$C9_{tank}$	0.000	0.000	0.015	0.147	1.017	2.604
$C10_{tank}$	0.000	0.020	0.043	0.119	0.177	0.193

Table S3 Total Volume of Calcite (TVC$_{dist}$) [mm^3]

Sample	day 1	day 2	day 3	day 4	day 7	day 11
C1$_{dist}$	0.000	0.484	1.695	1.849	2.520	1.460
C2$_{dist}$	0.000	0.000	0.023	0.026	0.195	0.350
C3$_{dist}$	0.000	0.082	0.120	0.205	0.241	0.101
C4$_{dist}$	0.000	0.000	0.000	0.122	0.369	0.349
C5$_{dist}$	0.000	0.000	0.254	0.528	1.086	0.762
C6$_{dist}$	0.000	0.369	1.237	1.131	1.530	0.746
C7$_{dist}$	0.000	0.007	0.027	0.028	0.295	0.588
C8$_{dist}$	0.000	0.000	0.001	0.124	0.230	0.267
C9$_{dist}$	0.000	0.979	2.044	2.275	2.584	2.513
C10$_{dist}$	0.000	0.000	0.024	0.027	0.171	0.088

Table S4 Total Volume of Gastroliths (TVG$_{tank}$) [mm^3]

Sample	day 1	day 2	day 3	day 4	day 7	day 11
C4$_{tank}$	0.802	0.797	0.793	0.642	0.509	0.045
C6$_{tank}$	3.396	2.863	2.325	1.949	1.429	0.641
C9$_{tank}$	5.079	4.341	3.837	3.368	2.046	0.000
C10$_{tank}$	1.615	1.505	1.488	1.175	0.575	0.415

Table S4 Total Volume of Gastroliths (TVG$_{tank}$) [mm^3]

Table S5 Total Volume of Gastroliths (TVG$_{dist}$) [mm^3]

Sample	day 1	day 2	day 3	day 4	day 7	day 11
C1$_{dist}$	0.077	0.068	0.044	0.041	0.040	0.031
C3$_{dist}$	1.638	1.515	1.507	1.151	1.037	0.920
C4$_{dist}$	0.188	0.130	0.094	0.072	0.029	0.000
C8$_{dist}$	1.420	1.263	1.008	0.975	0.766	0.260
C9$_{dist}$	3.442	3.397	3.016	2.921	2.837	2.479
C10$_{dist}$	0.675	0.577	0.485	0.484	0.480	0.109

Table S6 Total Volume of Gastrolith (TVG_{tank}) [%]

Sample	day 1	day 2	day 3	day 4	day 7	day 11
$C4_{tank}$	100	99.38	98.88	80.05	63.47	5.61
$C6_{tank}$	100	84.31	68.46	57.39	42.08	18.88
$C9_{tank}$	100	85.47	75.54	66.31	40.28	0
$C10_{tank}$	100	93.19	92.14	72.76	35.60	25.7
median	**100**	**89.33**	**83.84**	**69.54**	**41.18**	**12.25**

100 % represents the starting volume of gastroliths at the beginning of the experiments.

Table S7 Total Volume of Gastrolith (TVG$_{dist}$) [%]

Sample	day 1	day 2	day 3	day 4	day 7	day 11
C1$_{dist}$	100	88.31	57.14	53.25	51.95	40.26
C3$_{dist}$	100	92.49	92	70.27	63.31	56.17
C4$_{dist}$	100	69.15	50	38.3	15.43	0
C8$_{dist}$	100	88.94	70.99	68.66	53.94	18.31
C9$_{dist}$	100	98.69	87.62	84.86	82.42	72.02
C10$_{dist}$	100	85.48	71.85	71.7	71.11	16.15
median	**100**	**88.63**	**71.42**	**69.47**	**58.63**	**29.29**

100 % represents the starting volume of gastroliths at the beginning of the experiments.

Table S8 Total Volume of Calcite (TVC$_{tank}$) [%]

Sample	day 1	day 2	day 3	day 4	day 7	day 11
C4$_{tank}$	0	0	0.35	3.15	73.68	100
C6$_{tank}$	0	0.6	14.6	31.98	80.73	100
C9$_{tank}$	0	0	0.58	5.65	39.06	100
C10$_{tank}$	0	10.36	22.28	61.66	91.71	100
median	**0**	**0.3**	**7.59**	**18.82**	**77.21**	**100**

100 % represents the maximum volume of calcite precipitation achieved during the experimental period.

Table S9 Total Volume of Calcite (TVC_{dist}) [%]

Sample	day 1	day 2	day 3	day 4	day 7	day 11
$C1_{dist}$	0	19.21	67.26	73.37	100	57.94
$C3_{dist}$	0	34.02	49.79	85.06	100	41.91
$C4_{dist}$	0	0	0	33.06	100	94.58
$C8_{dist}$	0	0	0.37	46.44	86.14	100
$C9_{dist}$	0	37.89	79.1	88.04	100	97.25
$C10_{dist}$	0	0	14.04	15.79	100	51.46
median	**0**	**9.61**	**31.92**	**59.91**	**100**	**76.26**

100 % represents the maximum volume of calcite precipitation achieved during the experimental period.

Table S10 Additional information of individuals of AAS

Sample	Dry weight [g]	powder weight [g]	TVG_{Ca} [mm^3]	Mean concentration of Ca [µmol/mg]
$C1_{Ca}$	0.11	0.09	7.719	1.91
$C2_{Ca}$	0.05	0.04	0.195	2.82
$C3_{Ca}$	0.08	0.05	2.107	1.92
$C4_{Ca}$	0.05	0.03	-	2.94
$C5_{Ca}$	0.02	0.01	-	3.94
$C6_{Ca}$	0.05	0.02	-	3.12

Table S11 Body size and maximum volume of prsipitated calcite in crayfish samples without and with gastroliths. C, crayfish; tank, tankwater; dist, distilled water; TVC, total volume of calcite; GL, gastrolith; PCC, Pearson correlation coefficient

Sample	body size	TVC	$Sample_{GL}$	body size	TVC
$C1_{tank}$	1.90	1.825	$C4_{tank}$	1.70	0.285
$C2_{tank}$	1.50	1.156	$C6_{tank}$	2.30	1.007
$C3_{tank}$	1.70	2.107	$C9_{tank}$	2.20	2.604
$C5_{tank}$	1.40	0.485	$C10_{tank}$	2.20	0.193
$C7_{tank}$	2.30	3.401	$C1_{dist}$	2.10	2.52
$C8_{tank}$	2.30	6.544	$C3_{dist}$	1.70	0.241
$C2_{dist}$	1.70	0.35	$C4_{dist}$	1.90	0.369
$C5_{dist}$	1.80	1.086	$C8_{dist}$	2.10	0.267
$C6_{dist}$	2.50	1.53	$C9_{dist}$	1.90	2.584
$C7_{dist}$	1.70	0.588	$C10_{dist}$	2.00	0.171
PCC	**0.624387605**		**PCC_{GL}**	**0.28595119**	
PCC_{tank}	**0.859432014**		**$PCC_{GL-tank}$**	**0.405063566**	
PCC_{dist}	**0.874055133**		**$PCC_{GL-dist}$**	**0.243503552**	

16.6. Appendix F – Adipocere formation in biofilms as a first step in soft tissue preservation

This section contains the article and supporting information of "Adipocere formation in biofilms as a first step in soft tissue preservation" as it appears in the journal *Scientific Reports* by Springer Nature. Reprinted from *Sci. Rep.* **2022**, 12(1):10122, copyright (2020), with permission from Springer Nature. This work is licensed under the Creative Commons Attribution 4.0 International License (CC-BY). To view a copy of this license, visit http://creativecommons.org/licenses/by/4.0/. As guaranteed by the author rights policy, copying and re-use of the article in any medium or format is allowed without permission or payment, as long as the original article is fully acknowledged.

scientific reports

Check for updates

OPEN

Adipocere formation in biofilms as a first step in soft tissue preservation

Bastian Mähler[1✉], Kathrin Janssen[2], Mariam Tahoun[3], Frank Tomaschek[4], Rico Schellhorn[1], Christa E. Müller[3], Gabriele Bierbaum[2] & Jes Rust[1]

The preservation of soft tissue in the fossil record is mostly due to the replacement of organic structures by minerals (e.g. calcite, aragonite or apatite) called pseudomorphs. In rare cases soft tissues were preserved by pyrite. We assume that adipocere, as the shaping component, might be a preliminary stage in the pyritisation of soft tissues under anaerobic conditions. Using high-performance liquid chromatography coupled to ultraviolet and mass spectrometric detection (HPLC–UV/MS) and confocal Raman spectroscopy (CRS) we were able to demonstrate the transformation of the hepatopancreas (digestive gland) of the crayfish *Cambarellus diminutus* [Hobbs 1945] into adipocere within only 9 days, just inside a biofilm. Microorganisms (bacteria and fungi) which were responsible for the biofilm (*Sphaerotilus* [Kutzig 1833] and *Pluteus* [Fries 1857]) and maybe the adipocere formation (*Clostridium* [Prazmowski 1880]) were detected by 16S rRNA gene amplicon sequencing. Furthermore, micro-computed tomography (μ-CT) analyses revealed a precipitation of calcite and further showed that in animals with biofilm formation calcite precipitates in finer grained crystals than in individuals without biofilm formation, and that the precipitates were denser and replicated the structures of the cuticles better than the coarse precipitates.

In aquatic environments, dead organisms are often covered by biofilms[1]. The effects of microbial activity on fossilisation processes are still being investigated. Taphonomic studies under laboratory conditions revealed various pathways how bacteria can influence the decomposition and lead to preservation[2,3]. The preservation of soft tissues (e.g. muscles) occurs in form of pseudomorphs, in which the original muscle tissue is replaced by calcium phosphate ($CaPO_4$)[2–5], or calcite[6]. In a recent experiment, the midbrain of a frog, that had been placed on a microbial mat was replaced by calcium carbonate ($CaCO_3$) after 1.5 years[7]. In other studies, the hepatopancreases (digestive glands) of the shrimps *Crangon crangon* [Linnaeus 1758] and *Neogonodactylus oerstedii* [Hansen 1895] were mineralised by $CaPO_4$[2,4,5]. Briggs and Kear[4] even assumed that the mineralisation was initiated in the hepatopancreas. Taphonomic experiments have shown that these mineralisation processes are early diagenetic and dynamic, because tissue mineralised by $CaPO_4$ can be covered by $CaCO_3$ crystals if the pH switches to more alkaline conditions[2,8]. In addition, the pH in a decaying carcass might vary in different parts of the organism and result in the precipitation of various minerals (e.g. apatite, calcite, aragonite) in the same carcass[8] or lead to the dissolution of minerals (e.g. amorphous calcium carbonate)[6]. For example, the fossils of the crustacean-like specimen *Dollocaris ingens* [Van Straelen 1924] from the Jurassic Konservat-Lagerstätte of La Voulte-sur-Rhône in France show a variation of different minerals inside the body cavity[9].

In this study we describe the transformation of the hepatopancreas of *Cambarellus diminutus* [Hobbs 1945] into adipocere inside a biofilm. Adipocere is the result of incomplete hydrolysis of fat in animal tissue by bacteria under mainly anaerobic conditions[10]. Caused by the ability of adipocere to slow down or inhibit decay processes[11] it has been suggested as a key component in the outstanding preservation of fossils in Konservat-Lagerstätten like Messel, Holzmaden[12] or Solnhofen[13]. It is also assumed, that adipocere formation preceded the phosphatization of insects discovered at Quercy (France) as a shaping component[14]. Berner[15] as well hypothesized, that well-preserved fossils in calcium carbonate ($CaCO_3$) concretions may have formed originally as adipocere, which was later converted into $CaCO_3$.

[1]Section Palaeontology, Institute of Geosciences, Rheinische Friedrich-Wilhelms Universität Bonn, 53115 Bonn, Germany. [2]Institute of Medical Microbiology, Immunology and Parasitology, Medical Faculty, Rheinische Friedrich-Wilhelms Universität, 53127 Bonn, Germany. [3]Pharmazeutisches Institut, Pharmazeutische und Medizinische Chemie, Rheinische Friedrich-Wilhelms-Universität Bonn, 53121 Bonn, Germany. [4]Section Geochemistry/Petrology, Institute of Geosciences, Rheinische Friedrich-Wilhelms-Universität Bonn, 53115 Bonn, Germany. ✉email: bastian.maehler@uni-bonn.de

nature portfolio 1

16. Appendix

	Experiment 1.1	Experiment 1.2	Experiment 2	Experiment 3
Type of water	Pipe water	Pipe water	Pipe water	Pipe water
Amount of water	54 L	54 L	54 L	54 L
Water conditioner	Biotopol C	Biotopol C	Biotopol C	Biotopol C
pH-value	8	8	8	8
Temperature	28 °C	28 °C	28 °C	28 °C
Oxygen saturation	8 mg/L	8 mg/L	8 mg/L	8 mg/L
Special ingredients	Food ring	Food ring	Ostracods	–
Sediment type	Artificial	Artificial	Artificial	Artificial
Conducted in:	Tank 1	Tank 1	Tank 1	Tank 2
Number of individuals	3	4	3	3

Table 1. Setups of three different experiments.

Materials and methods

Individuals of the extant crayfish *Cambarellus diminutus* [Hobbs 1945] were taken from a breeding tank community raised in our lab. The animals were kept in 54 L tanks of $60 \times 30 \times 30$ cm in size, at a constant water temperature of 28 °C. Tanks were filled with pipe water and fortified with "Biotopol C" water conditioner (JBL, GmbH & Co. KG, Neuhofen, Germany) to neutralise zinc (Zn) and lead (Pb) and to remove chlorine (Cl) and bind copper (Cu). The crayfish were fed with nothing but "Crab Natural" (Sera, GmbH, Heinsberg, Germany), a main food for crayfish (ingredients can be found in Supplement 1).

Thirteen individuals with partly filled guts, were sacrificed by placing them in an atmosphere of carbon dioxide (CO_2). Specimens were not dried before weighing them on a micro scale. Lengths were measured from the anterior tip of the cephalothorax to the end of the pleon without the telson (Supplementary Table S1). At the beginning of each experiment oxygen saturation and pH-value were measured with an oxygen probe, OXPB-11 and pH-meter, PCE-PHD 1 (both PCE Deutschland GmbH, Meschede, Germany). Images of decomposing crayfish were taken by an i-Phone 12 mini. Images have 4032×3024 pixel and 24 bit with an exposure time of 1/50 s. The hepatopancreases (digestive glands) of C4 and C8 were lying in tank water at room temperature and were photographed by using a stereomicroscope (Stemi 2000, Carl Zeiss Microscopy Deutschland GmbH, Oberkochen, Germany) combined with an iPhone 12 mini holding by a Gosky Universal Digiscoping Smartphone Adapter, FBA_QHAPO21 (Gosky-optics, USA). The image of the calcite conglomerate in Fig. 3 was photographed with a stereo-zoom-microscope (Axio Zoom. V16, Carl Zeiss Microscopy Deutschland, Oberkochen, Germany). Final figures were created by using Adobe Photoshop CS5 (Adobe, Dublin, Republic of Ireland) with 300 dpi.

Experiment 1. The first experiment was conducted twice with first 3 and secondly 4 dead crayfish specimens (C1 to C7) that were placed on artificial sediment inside a 54 L tank (tank 1) filled with pipe water and fortified with "Biotopol C" water conditioner, under a constant water temperature of 28 °C for a duration of 9 days. The pH of the water was 8 and had an oxygen saturation of 8 mg/L. In order to obtain a suitable biofilm, a piece of the crab food "Crab Natural" was placed next to the dead individuals (Table 1). This was done because it was observed that food rings have the potential to induce biofilms. Individuals were photographed once per day.

After 9 days, crayfish remains were removed from the tank and analysed by using a stereomicroscope. In addition, crayfish remains were scanned by using a micro-CT device, if possible.

Experiment 2. The second experiment was conducted with 3 crayfish individuals (C8 to C10) after experiment 1 inside the same tank (tank 1) and water under a constant water temperature of 28 °C, for a duration of 8 days. The pH of the water was 8 with an oxygen saturation of 8 mg/L (Table 1). The individuals were photographed once per day and after 8 days, crayfish remains were analysed by using a stereomicroscope. Contrary to experiment 1, the water was colonized by a large number of ostracods (Supplementary Fig. S1a,b), which had been introduced by the crab food used in experiment 1.

Experiment 3. In the third experiment crayfish individuals C11 to C13 were placed inside another tank (tank 2) filled with pipe water, which was also fortified with "Biotopol C" water conditioner. The experiment was conducted under a constant water temperature of 28 °C for a duration of 7 days. The pH of the water was 8 with an oxygen saturation of 8 mg/L. The water was free from ostracods and no crab food was add to the experiment (Table 1). Afterwards, the crayfish remains were removed from the tank and analysed by stereomicroscopy.

At the beginning of each experiment carcasses were fully articulated and blue in colour. In addition, no symbiotic, parasitic or commensally organisms were found on the carcasses.

DNA extraction. DNA was extracted from the biofilm with the ZymoBIOMICS DNA/RNA Miniprep Kit (Zymo Research, Irvine, USA). Biofilm samples of C1, C2 and C4 were transferred into ZR BashingBead™ Lysis Tubes (0.1 and 0.5 mm) with 750 µl ZymoBIOMICS Lysis solution. Bead beating was performed with a Precellys® homogenizer (Bertin Technologies S.A.S., Montigny Le Bretonneux, FR), 6000×*g* for 30 s. Samples were sub-

sequently processed according to the manufacturer's instructions. DNA was eluted in 50 µl DNase/RNase-free water and DNA concentration and quality was checked using a NanoDrop One/OneC Microvolume-UV/VIS-spectrophotometer (Thermo Fisher Scientific, Waltham, Massachusetts, USA).

16S rRNA gene amplicon sequencing. For 16S rRNA gene sequencing, the V4 variable region of the 16S rRNA gene sequence was amplified with the specific 16S primers of 16S-515F (GTG CCA GCM GCC GCG GTA A) and 16S-806R (GGA CTA CVS GGG TAT CTA AT)[16]. Fungal ITS-region was amplified with specific ITS-primers (for: CTT GGT CAT TTA GAG GAA GTA A rev: GCT GCG TTC TTC ATC GAT GC). The PCR reaction was performed as a single-step PCR with the HotStarTaq Plus Master Mix Kit (Qiagen, USA) including an initial denaturation at 95 °C for 5 min, followed by 30–35 cycles of 95 °C for 30 s, 53 °C for 40 s, and 72 °C for 1 min, with a final elongation step at 72 °C for 10 min. Paired end sequencing (bTEFAP®) was performed by MR DNA (http://www.mrdnalab.com, Shallowater, TX, USA) on a MiSeq following the manufacturer's guidelines[17]. Raw sequence data was processed via the QIIME2 pipeline[18] with default parameters unless otherwise noted. DADA2 pipeline was used for sequence quality control, denoising and chimeric filtering[19]. Taxonomy classification of the final bacterial ASVs (amplicon sequencing variant), clustered at 99% identity, was performed with a naive Bayesian classifier which was trained against SILVA database release 138 especially for 515F/806R rRNA region[20,21]. ASVs of fungal composition analysis were aligned to a curated database derived from NCBI which was performed by the sequencing facility. For prediction of metabolic characteristics of the bacteria, the sequences were taxonomically classified with the Greengenes database[22]. The allocation of the phenotypes was then performed with BugBase[23].

All raw sequence data related to this study are deposited in the European Nucleotide Archive (ENA) (European Bioinformatics Institute, EMBL-EBI) database a collaboration partner of the International Nucleotide Sequence Database (INSDC), [Study-Accession Number: PRJEB43756].

Micro-computed tomography (µ-CT). The propodus of the right chela of sample C4 and the complete carcasses of sample C1, C2 and C6 were removed from the tank and were scanned by using a phoenix|x-ray v|tomex s 240 micro-computed-tomography (µ-CT) scanner (GE Measurement and Control, Wunstorf, Germany) located at the Institute of Geosciences of the University of Bonn. The data set has a resolution of 12.66 µm; the scans were carried out at 80 kV and 100 µA. Three frames per projection were acquired by a timing of 500 ms for a total of 1000 projections. The CT data were processed using the software VG Studio Max 3.2 (Volume Graphics, Heidelberg, Germany) and Avizo 8.1 (Thermo Fisher Scientific, Schwerte, Germany) to reconstruct and visualize the precipitated crystal clusters inside the specimens and specimen remains.

Confocal Raman spectroscopy (CRS). *Cambarellus diminutus* [Hobbs 1945] hepatopancreas samples and reference materials as well as crystal clusters were analysed using a Horiba Scientific LabRam HR800 (located at the Institute of Geosciences, University of Bonn). Raman scattering was excited with a 784 nm diode laser as excitation source. The spectrometer was calibrated with the first-order Si Raman band at 520.7 cm^{-1}. Data in the spectral region of 300 to 1800 cm^{-1} (hepatopancreas) and 100 to 1800 cm^{-1} (crystal clusters) were collected with a 100×long working distance objective, a confocal hole size set to 1000 µm, spectrometer entrance slit size of 100 µm, and a grating of 600 grooves/mm. The exposure time was 42 min per window with 50 accumulations of 50 s for the hepatopancreas samples, and 4.2 min with 50 accumulations of 5 s for saturated fatty acid reference materials, respectively. The exposure time for crystal clusters was 2 min with 4 accumulations of 30 s.

Scanning electron microscopy (SEM). The right propodus and the dactylus, as well as a part of the hepatopancreas of sample C4 and crystal clusters were dissected and coated by a thin layer of gold with a cool sputter coater (Cressington Sputter Coater 108 manual, Tescan GmbH, Dortmund, Germany). Samples were subsequently scanned with an 'environmental' scanning electron microscope (SEM) unit (TESCAN VEGA 4 LMU) by using the SE detector at 20 keV. Images have 1536×1331 pixel and 16 bit. The working distance of each SEM-image can be found in the figure captions.

High performance liquid chromatography coupled to ultraviolet and mass spectrometry detection (HPLC–UV/MS). *Materials and analytical conditions.* Measurements were performed on an Agilent 1260 Infinity HPLC coupled to an Agilent Infinity Lab LC/MSD single quadrupole mass spectrometer with an electrospray ion (ESI) source and a diode array UV detector (DAD-UV, 200–600 nm, Agilent Technologies Germany GmbH & Co. KG, Waldbronn, Germany). Chromatographic separation was performed on an EC 50/3 Nucleodur C18 Gravity column, 3 µm (Macherey–Nagel, Dueren, Germany). Standard solutions of palmitic acid, oleic acid, and stearic acid (Sigma Aldrich Chemie GmbH, Taufkirchen, Germany) were prepared in a 1:1 solution of dichloromethane/acetonitrile, and known amounts were added to a sample for confirmation of retention times. A triglyceride mixture containing glyceryl trimyristate as the main component (Sigma Aldrich Chemie GmbH, Taufkirchen, Germany) was employed as a further standard. All solvents used were HPLC grade. Mobile phase A consisted of methanol with 2 mmol/l ammonium acetate, and mobile phase B consisted of water with 2 mmol/l ammonium acetate. The run started with 50% A and 50% B for 1 min, followed by a gradient that reached 100% of eluent A after 15 min. Then, the column was flushed for 10 min with 100% of mobile phase A followed by 50% A and 50% B for 5 min before starting the next run. Positive and negative full scan MS was obtained from 100 to 1000 m/z. The column temperature was set at 40 °C, the injection volume was 5 µl, and the flow rate was adjusted to 0.5 ml/min. Identification of the peaks was performed using the data analysis program of the OpenLab CDS 2.5 software (Agilent Technologies Germany GmbH & Co. KG, Waldbronn, Germany).

233

16. Appendix

The extracted ion chromatogram (EIC) was used to evaluate peak areas and to provide a semi-quantitative estimate of the detected compounds.

Extraction of adipocere components. A part of the hepatopancreas of sample C4, taken approximately 9 days post-mortem and hypothesised to be adipocere based on its visual appearance, was extracted and analysed by HPLC-(DAD-UV)-ESI-MS with the aim to identify the different fatty acid components of adipocere from the resulting chromatographic peaks and mass spectra. A 0.9 mg sample was extracted with 5 ml of dichloromethane to obtain the lipophilic constituents present. Then, aliquots were diluted 1:1 with acetonitrile and subsequently analysed by HPLC-(DAD-UV)-ESI-MS. Equal volumes of sample were measured with and without adding a mixture of palmitic acid, stearic acid and oleic acid as reference compounds (final concentration of each fatty acid was 1 μmol/l). This standard addition technique was used for confirmation of the presence of the individual fatty acids and to identify possible matrix effects affecting their retention times.

Results

General observations.

Experiment 1. On day 1, specimens C1 to C7 were blue in colour and articulated, lying with the lateral bodyside on the sediment (Fig. 1a–d). The cephalothorax of each individual had changed its colouration from blue to dark red-brown on day 2. In addition, a translucent to milky translucent biofilm had formed on the carcasses and the carcasses C1, C3, C5 and C6 were twisted by about 90 degrees due to the formation of the biofilm (Fig. 1a,c). On day 3 the specimens were completely covered by the biofilm (Fig. 1a–d). An accumulation of putrefaction gas could be noticed around the branchial area of specimens C1 and C5, which resulted in a floating of the carcasses inside the biofilm, however, the biofilms held the carcasses to the ground (Fig. 1a). A gas accumulation could also be noticed in specimens C2, C6 and C7 but was not sufficient to let the carcasses "float" inside the biofilm. On day 4 the carcasses C1 and C5 had risen further within the biofilm, but were still fixed to the sediment. From day 5 to day 7 the gas accumulation increased and, in all specimens, the abdominal muscles had changed their colouration from white to pink. On day 7, ostracods had populated the carcasses and had started to degrade the biofilms. Most of the biofilms were degraded on day 8 and ostracods started to feed on the carcasses. On day 9 nearly the complete inner organs of the carcasses had been consumed by the ostracods. In all specimens the complete hepatopancreases remained, which were hard and crumbly (Fig. 2a). In addition, crystal clusters were found in all carcasses (Fig. 3).

Experiment 2. On day 1, specimens C8 to C10 were blue in colour and articulated, with the left half of the body lying on the sediment. The cephalothorax of the individuals had changed their colour from blue to red on day 2, and specimen C9 was floating at the water surface, this was probably caused by putrefaction gas, which accumulated at the branchial area. On day 3, a light white biofilm could be noticed around the cephalothorax of specimen C8 (Fig. 1e) and around the pleon of specimens C9 and C10, both lying on the ground. The abdominal muscles of each specimen had changed their colouration from white to pink. Cuticles of all individuals were completely red in colour and ostracods had populated the carcasses. On day 4 organs inside the cephalothorax of specimen C8 had been consumed up by the ostracods, except the hepatopancreas and the biofilms had been completely degraded (Fig. 1e). On day 5 nearly the whole carcass of specimen C8 had been consumed by the ostracods and only the chelipeds without any tissue inside as well as the hepatopancreas were left over (Fig. 1e). The anterior part of the cephalothorax of specimens C9 and C10 were degraded and gastroliths of specimen C9 were exposed. On day 8 nearly the complete carcasses of specimens C9 and C10 had been consumed the ostracods and only the hepatopancreases of both specimens and the gastroliths of specimen C9 remained. The hepatopancreas of all specimens were slightly yellow, soft and fragile.

Experiment 3. On day 1, specimens C11 to C13 were blue in colour and articulated, with the left half of the body lying on the sediment. With progressive decay cuticles became translucent, reddish and the muscles were pink (Fig. 1f). On day 7 internal organs had been mostly decomposed except the intestine and ganglia. Hepatopancreases could not be detected. In addition, muscles were pulpy and the cuticles of the cephalothorax and pleon were soft and jellylike. The chelipeds were still solid after 7 days. During the whole time, biofilm formation could not be detected and no gas accumulation occurred at the branchial area. The individuals were still articulated at the end of the experiment but ruptured at the transition from the cephalothorax to the pleon and the legs disarticulated quickly during the attempt to move them out of the tank. In addition, a precipitation of crystal clusters was noticed in all carcasses.

16S rRNA gene amplicon sequencing.

The 16S rRNA and ITS amplicon analyses of C1, C2 and C4 revealed that bacteria of the phyla γ-Proteobacteria, α-Proteobacteria, Bacteroidetes, and the class Clostridia were present in the biofilm. In particular, the samples were mainly composed of Gram-negative genera, such as *Sphaerotilus* [Kutzig 1833]*, Azospirillum, Hydrogenophaga,* or *Novispirillum* (Fig. 4a). In addition, the fungal colonisation was almost completely dominated by species of the genus *Pluteus* [Fries 1857] (Fig. 4b). Further on, almost all bacterial individuals exhibited biofilm forming ability in a bioinformatic analysis with the prediction tool BugBase (Fig. 4c).

Micro-computed tomography (μ-CT).

In contrast to coarse-grained calcite precipitations which occur in decomposing crayfish without a biofilm, μ-CT observations of the chela of specimen C4 and the complete carcasses of specimens C1, C2 and C6 revealed a precipitation of fine-grained crystal structures mostly inside the cuticle but also inside the pereiopods and chelipeds (Fig. 5a–e).

234

Figure 1. Decomposing crayfish individuals of three different experimental setups lying on artificial sediment at a constant water temperature of 28 °C. (**a**) Day 1 Dead articulated crayfish specimen C1, lying on its right body side in tank water. Day 2 Dead crayfish was moved by the development of a biofilm and the cephalothorax had changed its colouration from blue to red-brown. Day 3–7 Envelopment of the carcass by a biofilm and gas accumulation at the branchial area (green arrows), resulting in a "floating" carcass inside the biofilm. (**b**) Day 1 Dead articulated crayfish specimen C2, lying on its right body side in tank water. Day 2 Development of a biofilm around the cephalothorax, which had changed its colouration from blue to red-brown. Days 3–7 Envelopment of the carcass by a biofilm and gas accumulation at the branchial area (green arrow), resulting in a light "floating" carcass inside the biofilm. (**c**) Crayfish specimen C3 lying in tank water for a duration of nine days. Day 1 Dead articulated, blue crayfish lying on its right body side. Day 2 Cephalothorax had changed its colouration from blue to red-brown and is covered by a light, white biofilm. Day 3 The complete carcass was covered by a white biofilm and abdominal muscles had changed their colouration from white to pink. Days 6–9 Biofilm population by ostracods and its complete degradation. Day 9 Degraded cuticle of the pleon and some remains of the branchiae. (**d**) Crayfish specimen C4 in tank water for a duration of nine days. Day 1 Dead articulated, blue crayfish lying on its left body side. Day 2 Cephalothorax had changed its colouration from blue to red-brown and is covered by a light, white biofilm. Day 3 The complete carcass was covered by a white biofilm and abdominal muscles had changed their colouration from white to pink. Days 6–9 Biofilm population by ostracods and its degradation. Day 9 Remains of the biofilm and degraded cuticle. Chelipeds still intact and filled with pulpy muscles. (**e**) Crayfish specimen C8 in tank water for a duration of five days. Day 1 Dead articulated, blue crayfish lying on its left body side. Day 2 Cephalothorax had changed its colouration from blue to red. Day 3 The cephalothorax was covered by a white biofilm and abdominal muscles had changed their colouration form white to pink. Day 4 Carcass was populated by ostracods and the biofilm was completely degraded. Day 5 Only empty chelipeds and the hepatopancreas were left. (**f**) Crayfish specimen C11 lying in tank water for a duration of seven days. Days 1–7 Decomposing crayfish lying on its left bodyside. Cuticles of the cephalothorax and the pleon became light red and translucent. Muscles were pink in colour. Individuals were still articulated at day 7. All scale bars: 1 cm except the scale bars of the last two pictures in (**e**) which is 0.5 cm.
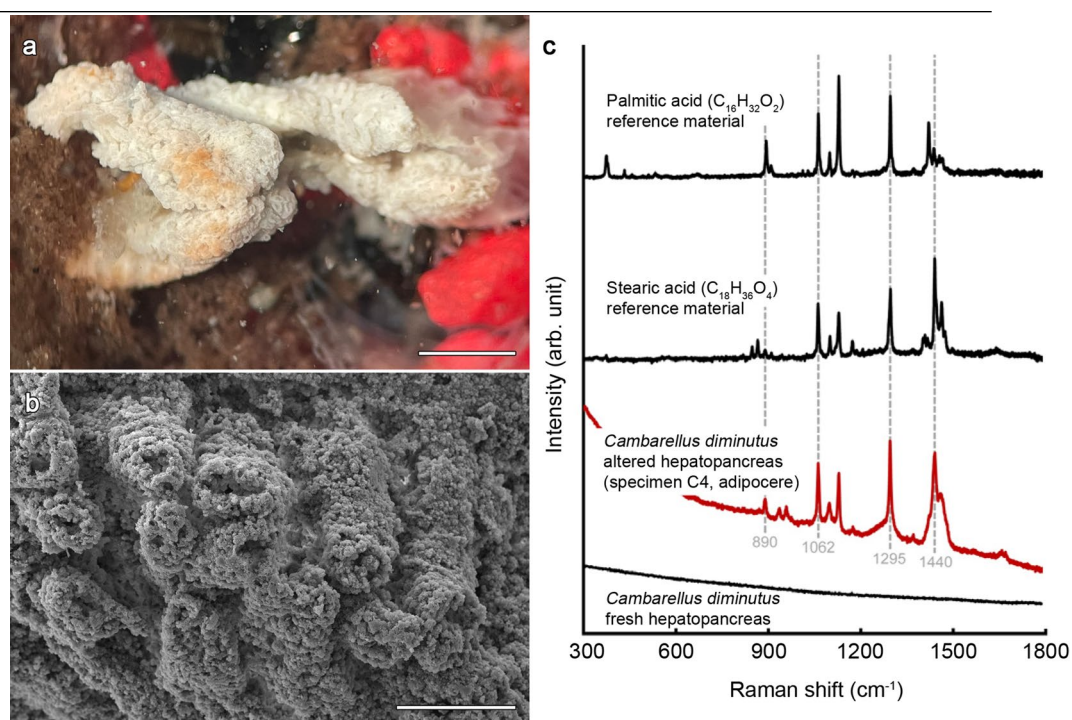
235

16. Appendix

Figure 2. Images of the hepatopancreas (digestive gland) of crayfish specimen C4 after nine days in tank water covered by a biofilm and Raman spectra. (**a**) Stereomicroscopic image of the hepatopancreas in water. Scale bar 1 mm. (**b**) SEM-image of an enhanced part of the dried hepatopancreas [WD: 22.01 mm]. Scale bar 200 μm. (**c**) Representative Raman spectra of an altered *Cambarellus diminutus* hepatopancreas (specimen C4, adipocere), reference data for saturated fatty acids (stearic and palmitic acids), and the hepatopancreas of a freshly killed *C. diminutus*. Raman bands typical for saturated fatty acids have developed post-mortem. *WD* working distance.

Confocal Raman spectroscopy (CRS).   Raman spectra were obtained for an altered *C. diminutus* [Hobbs 1945] hepatopancreas (specimen C4, adipocere) and saturated fatty acid reference materials (solid stearic and palmitic acids). All strong Raman bands obtained for specimen C4 (at 890, 1062, 1098, 1128, 1295, 1440, and 1460 cm^{-1}) are typical for Raman spectra of saturated fatty acids[25,26] (Fig. 2c). In addition, there are unassigned bands at 935 and 958 cm^{-1}, and a broad shoulder around ~ 1250 cm^{-1}, which may point to the presence of some additional compound(s). We also observed, that none of the Raman-active bands could be detected in a fresh hepatopancreas, indicating that saturated fatty acids must have formed post mortem.

Raman analyses clearly revealed that the crystal clusters consist of well-ordered calcite (Fig. 3a), which can be identified by the fully symmetric $v_1(CO_3)$ carbonate band near 1085 cm^{-1}, as well as the presence of lattice vibrations near 154 and 281 cm^{-1}, with the latter being absent in amorphous calcium carbonate (ACC). A mixed spectrum of crystalline calcite and the β-carotene, astaxanthin (AXT) could be identified at calcified cuticle remains on the clusters (Fig. 3a) by the typical high intensity modes at ~ 1157 and ~ 1517 cm^{-1} that are assigned to the C=C and C–C stretching vibrations of the polyene chain bonds, respectively[27–29]. In comparison to the spectrum obtained from the AXT standard, a small derivation in the frequency of the ~ 1517 cm^{-1} signal was observed. Such a shift can presumably be linked to the structural differences of AXT.

Scanning electron microscopy (SEM).   SEM analyses of the thoracic skeleton reveal the presence of fungi inside the biofilm (Supplementary Fig. S2). Crystal clusters of C1 to C7 varying in size from ~ 100 to ~ 200 μm with the largest conglomerate measuring 1200 μm (Fig. 3b,c) at the end of the experiment. Most of the structures were spherical or bispherical (Supplementary Fig. S3a). The largest structure presented a conglomerate of layered calcite structures combined with calcite bundles and two perfectly mineralised setae found between the pulpy remains of specimen C4 (Fig. 3b,c). The dactylus of the right chela of specimen C4 showed a lot of calcite clusters instead of the original cuticle (Supplementary Fig. S4). SEM images of the hepatopancreas of specimen C4 showed in contrast to crystalline structures a pattern resembling to cauliflower (Fig. 2b).

High performance liquid chromatography coupled to ultraviolet and mass spectrometric detection (HPLC–UV/MS).   *Identification of free fatty acids.*   HPLC–MS analysis of the untreated hepatopancreas extract of specimen C4 detected six of the free fatty acids typically found in adipocere, namely palmitic acid, stearic acid, oleic acid, myristic acid, linoleic acid, and palmitoleic acid. Peaks corresponding to each of the six fatty acids were visible in the extracted ion chromatograms (EIC) at the respective mass-to-charge ratio (Fig. 6a). To confirm their identity, a standard method, also known as spiking, was used in case of oleic acid, palmitic acid and stearic acid. Here, a defined amount of the fatty acid standard was added to the sample. An in-
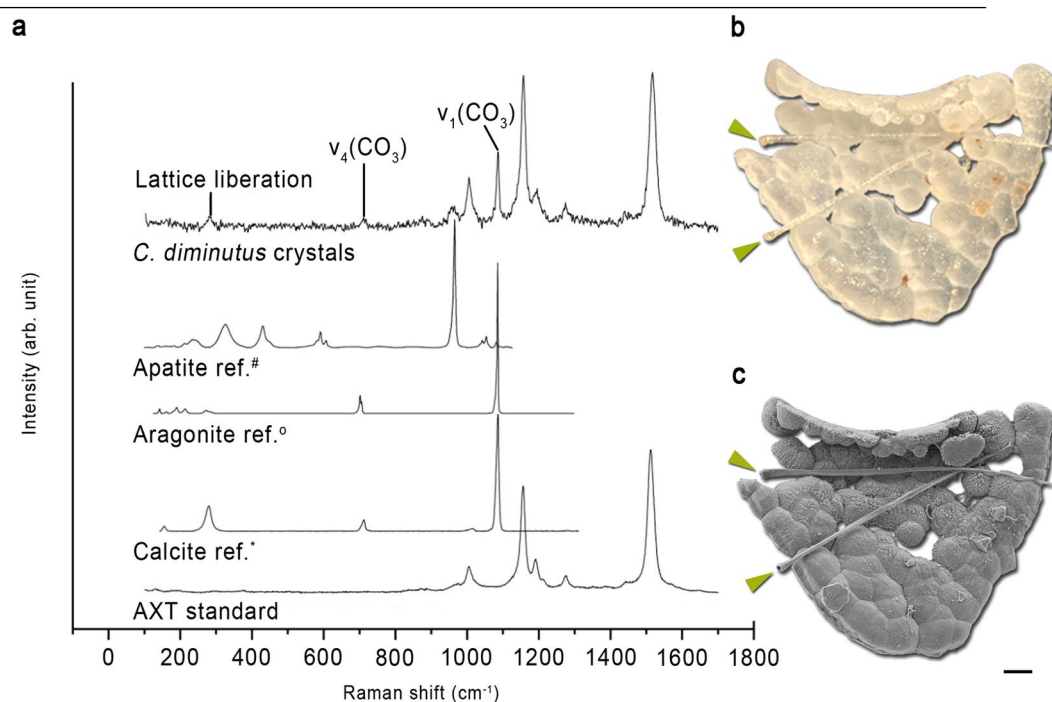
236

Figure 3. (**a**) Representative Raman spectra of observed crystal clusters compared to Raman reference spectra of crystalline apatite, aragonite and calcite, taken from the RRUFF Raman data base (#R060070, °R060070, *R040170[24]). Raman spectra of the crystal clusters exhibit main Raman bands typically for crystallized calcite and the β-carotene, astaxanthin. (**b**) A stereomicroscopic image of a calcite conglomerate of crayfish specimen C4 with two calcified setae (green arrows). (**c**) SEM-image of the cluster with two complete calcified seta (green arrows) [WD: 22.11 mm]. Scale bar 100 μm. *WD* working distance.

crease in the peak area was observed in the extracted ion chromatograms corresponding to the spiked fatty acids (Supplementary Table S2). Furthermore, there were no new peaks detected in the extracted ion chromatograms after spiking, confirming that the increase in peak area was due to the added free fatty acid standard.

Moreover, free fatty acids originally present in the sample could be readily detected in the negative ion mode of the mass spectrometer as deprotonated ions with a mass-to-charge ratio of $[M–H]^-$, where M is the monoisotopic mass of the acid (for details, see Supplementary Fig. S5 and Supplementary Fig.S6). Observation of the full scan electrospray ion (ESI)-mass spectra of the peaks (Fig. 6a) further confirmed the presence of palmitic acid, stearic acid and oleic acid in the sample. Although standard compounds for further fatty acids were not studied, myristic acid, palmitoleic acid and linoleic acid could be identified based on their mass (Fig. 6a,b).

Analysis of triglycerides. Since myristic acid was present in the sample, glycerol trimyristate (M = 721.6) was studied as a standard compound potentially present in the living crayfish. Mass spectra of triglycerides, determined under the applied conditions, show the ammonium adduct of the intact triglyceride in highest abundance, corresponding to M + 18 in the positive ion mode, where M is the monoisotopic mass of the triglyceride. Glyceryl trimyristate was not detected in the hepatopancreas sample, as shown in Fig. 7a–d. We only observed an unknown mass of 900.8 ± 0.3 m/z (Fig. 7c,d). The inability to detect glyceryl trimyristate or closely related triglycerides in the sample indicates that these must have been degraded. The lack of triglycerides, and the detection of free fatty acids expected to be present in adipocere confirms that the analysed hepatopancreas sample is indeed adipocere.

Discussion

The results of our study show, the fragility of the conditions that lead to a preservation of soft tissues or their complete decomposition. Experiment 1 and 3 were conducted under the same abiotic water conditions (temperature [28 °C]; pH [8]; oxygen saturation [8 mg/L]) and the same aquatic sediment (Dehner GmbH & CoKG, 86641 Rain, Germany), and water type. However, the course of decomposition of crayfish individuals of the same species, which had been raised in the same tank community, was completely different. While in tank 1 of experiment 1 biofilm formation with an envelopment of the whole carcass occurred and gas accumulation in the branchial area could be detected, none of these occurrences could be observed in any other crayfish, which decomposed in tank 2 during experiment 3. In addition, the tissue transformation of the hepatopancreases into adipocere occurred only in individuals which were covered by a biofilm. We assume that the microbial composition inside the tanks was different and therefore extrinsic bacteria were responsible for the significant differences in decay. We assume further, that inside the biofilm oxygen was metabolised by microbial activity, resulting in anaerobic
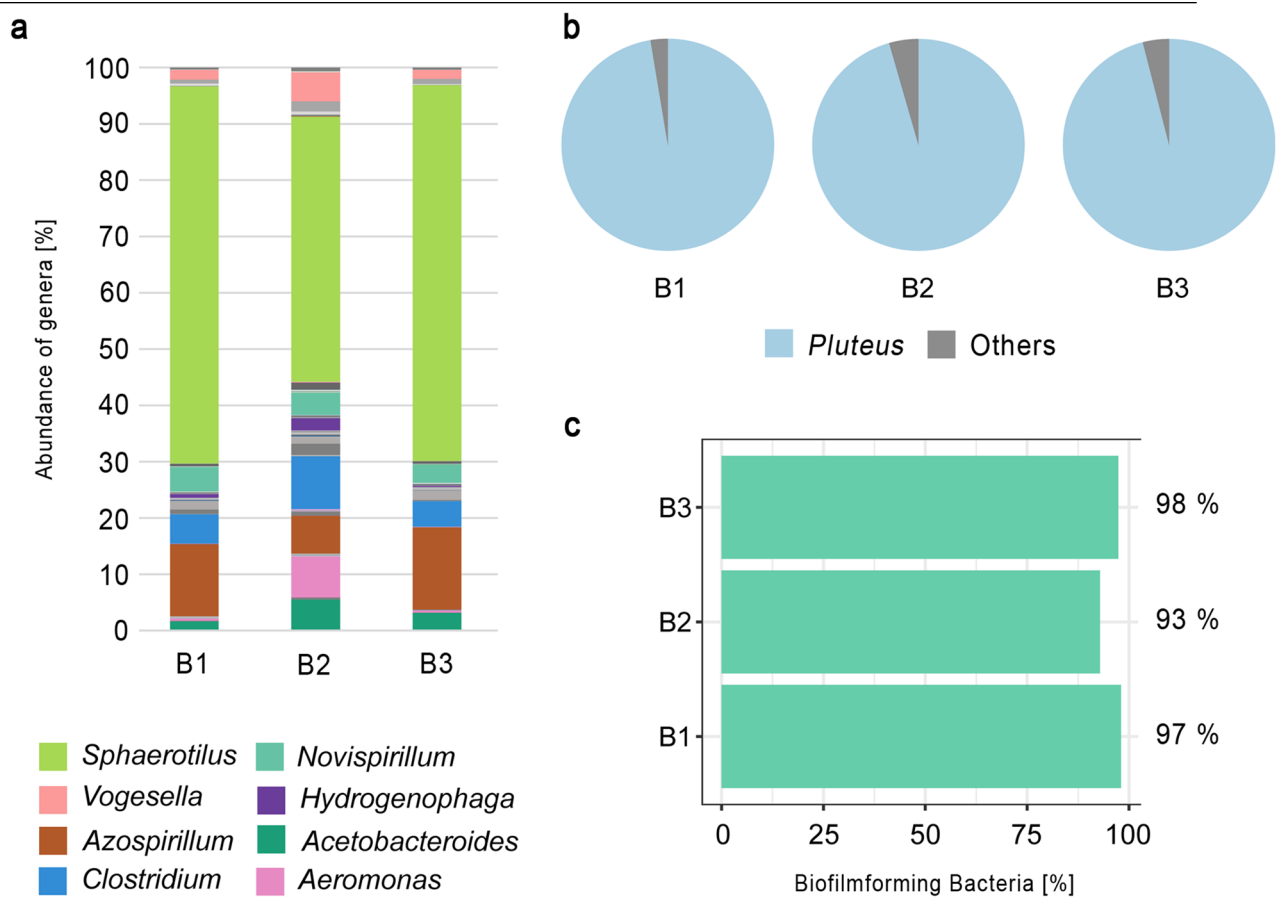
16. Appendix

Figure 4. Microbial community composition of three biofilm samples taken from experiment 1 (B1 = C1; B2 = C2 and B3 = C4). (**a**) Abundance of bacterial genera (%). (**b**) Composition of fungal genera, which was dominated by the genus *Pluteus*. (**c**) Comparison of predicted biofilm forming ability of the bacteria detected in the three biofilm samples.

conditions which favoured the adipocere formation, since fatty acids are stabilized by these conditions[30]. Other requirements, e.g., high temperatures (28 °C) and a wet environment (tank water) were also fulfilled[31,32]. Further- more, the genus *Clostridium* [Prazmowski 1880] was detected inside the biofilm, which is commonly associated with the formation of adipocere[33], since these bacteria are strong hydrolysers of triglycerides. It is assumed, that the initial formation of adipocere is mainly driven by Gram-positive bacteria, whereas it is important that in the final stages Gram-negative bacteria dominate due to adipocere degradation[34,35]. The bacterial composition in and on the biofilm of individuals of experiment 1, was dominated by Gram-negative organisms and some of these might be involved in biofilm formation, e.g. *Sphaerotilus* [Kutzig 1833]. This genus contains species which settle on surfaces and form filaments that are covered by a sheath and slime[36] (Fig. 1a, day 5). SEM-images of crayfish remains from experiment 1, that was enveloped by a biofilm show the presence of fungi that form branched mycelia (Supplementary Fig. S1) and 16S rRNA analyses of the biofilm show that the fungi genus *Pluteus* [Fries 1857] was the most abundant genus. Therefore, we assume that *Pluteus* [Fries 1857] might play an important role in our biofilm environment in experiment 1.

The genus *Pluteus* [Fries 1857] is mostly known from wood remains and food, but was also first identified by Niu[37] as the most abundant genus in activated sludge of eastern waste water treatment plants in China. But its metabolic activity was still unknown. In 2019, Booth[38] investigated the role of fungi in heterogenous sediment microbial networks in Mangrove sediments and found out that fungi play the major role in all microbial network interactions. They further showed, that the genus *Pluteus* [Fries 1857] [as a saprophyte (= heterotrophic organism that live in decomposing organic substances)] formed significant keystone nodes in the subsurface sediments and was one of the most important fungi genera in the microbial network[38]. Booth[38] assumed that the fungi acting synergistically with other environmental variables and determine the overall microbial community structure. If the genus *Pluteus* [Fries 1857] was important for the biofilm formation and/or the adipocere occurrence will be investigated in further studies.

Adipocere is the result of the incomplete hydrolysis of fat in animal tissue by bacteria under mainly anaerobic conditions, because the degradation of fatty acids is restricted to respiratory processes[10]. Under anaerobic condi- tions fatty acids cannot undergo β-oxidation and are degraded only very slowly.

Caused by the ability of adipocere to slow down or inhibit decay processes[11] it has been suggested as a key component in the outstanding preservation of fossils in Konservat-Lagerstätten like Messel, Holzmaden[12], or
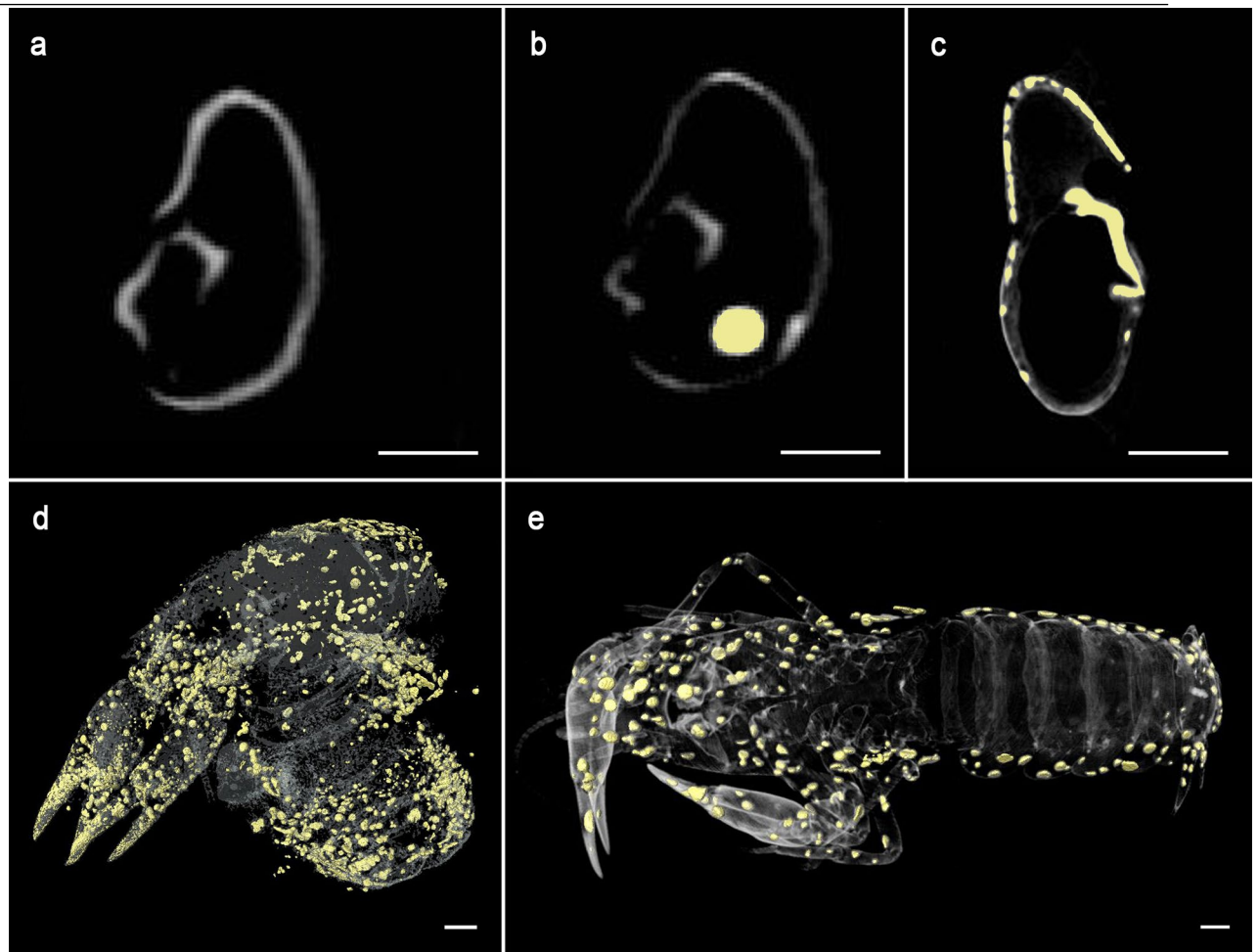
Figure 5. µ-CT images and 3D models of crayfish individuals and precipitated crystal clusters. (**a**) µ-CT image of a cross section of the right chela of an individual of *Cambarellus diminutus* (C7$_{tank}$) in tank water of an experiment described in Mähler[6] on day 1, with calcified cuticle. (**b**) The same chela as in (a) on day 7 with less calcified cuticle and a crystal cluster (yellow spot). (**c**) µ-CT image of a cross section of the left chela of C4 on day 9 with recrystallised cuticle (yellow structures). (**d**) Translucent 3D-model of C6 on day 9 with 3D-models of precipitated clusters (yellow spots). (**e**) Translucent 3D-model of an individual of *C. diminutus* (C7$_{tank}$) in tank water of an experiment described in Mähler[6] on day 7 with 3D-models of precipitated clusters (yellow spots). All scale bars 1 mm. µ-CT images were processed with VG Studio Max 3.2 (https://volumegraphics.com) and 3D models were reconstructed with Avizo 8.1 (https://thermofischer.com).

Solnhofen[13]. It is also assumed, that adipocere preceded the phosphatization of insects discovered from Quercy (France), as a shaping component[14].

In 2020, the crustacean-like specimens of the arthropod *Dollocaris ingens* [Van Straelen 1924], found in the Jurassic Konservat-Lagerstätte of La Voulte-sur-Rhône (France), were reinvestigated to clarify their preservation pathway[9]. These fossils show an exceptional morphological preservation of inner structures (e.g., muscles and hepatopancreas), which were preserved by fluorapatite and pyrite. Here, the transformation of the inner structures must have happened rapidly post mortem, when the sediment was still moist, loose and not complete anaerobic[9]. Jauvion[9], as well as Wilby[39] state, that the fossilisation process occurred simultaneously with the biodegradation and was influenced by the tissue type and local microenvironments. This assumption is supported by the results of Grimes[40], which show that the pyritisation of plant cells depends on the plant type and the specific conditions. In addition, Jauvion[9] did not exclude the possibility of a precipitation of pyrite and/or fluorapatite due to a biofilm.

In view of the fact, that the anatomical structure of the hepatopancreas of *Dollocaris ingens* [Van Straelen 1924] was very similar to that of modern crustaceans[41], and based on the fast transformation of the hepatopancreas into adipocere (only in 9 days) in experiment 1 of this study, we assume that the hepatopancreases of *Dollocaris ingens* [Van Straelen 1924] might also first have been stabilised by adipocere before they were preserved in pyrite. We are aware that the here presented results are based on freshwater processes, but the formation of adipocere is also known from decomposing human bodies or pigs in marine environments[42,43]. Further on, Grimes[40] published that the pyritisation did not directly replace the original tissue. The fossilisation was a result of precipitation of crystals on and between cells resulting in filling out of extracellular spaces. Grimes[40]

239

16. Appendix

a

b

240
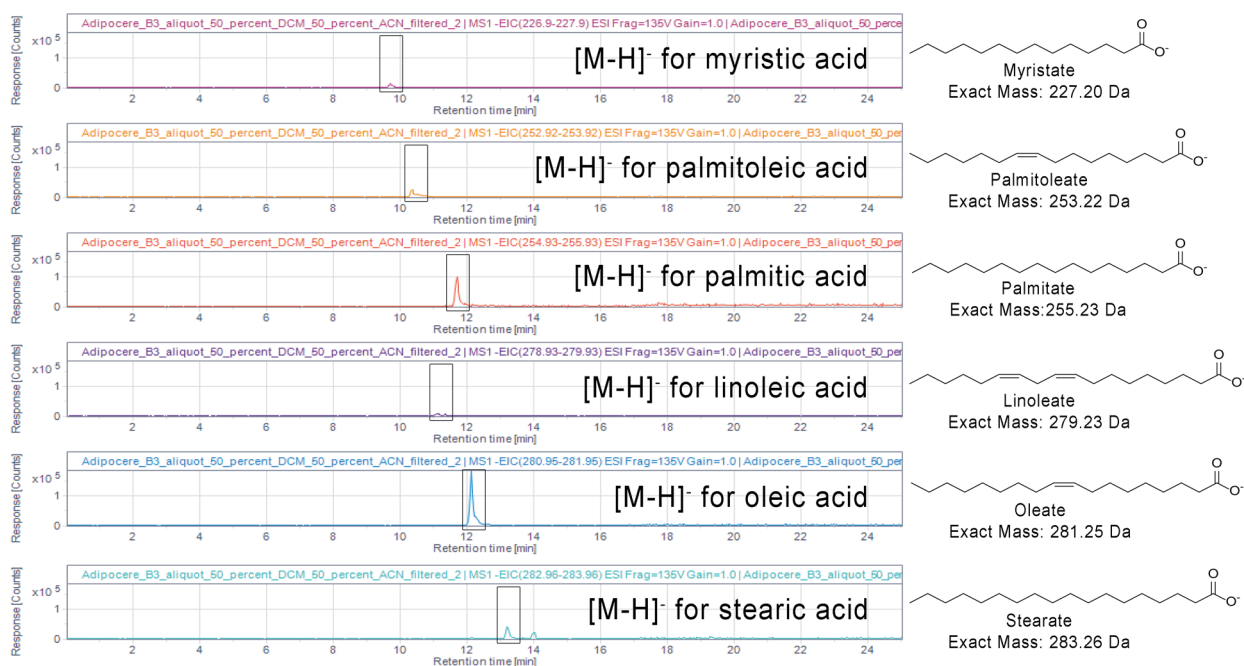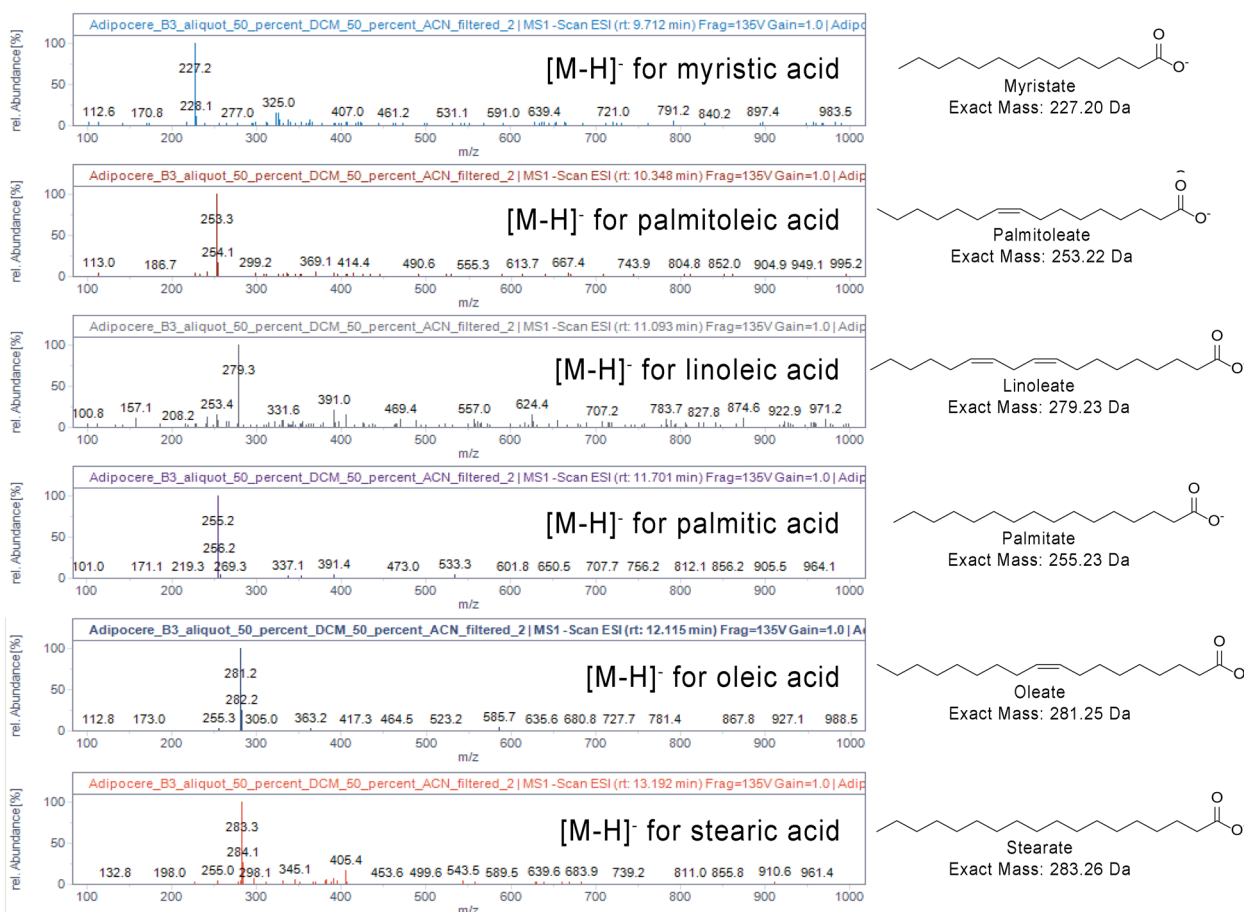
◄**Figure 6.** (**a**) Extracted ion chromatograms (EIC) showing the deprotonated ion of myristic acid (myristate, 227.2 ± 0.7 m/z), palmitoleic acid (palmitoleate, 253.2 ± 0.7 m/z), palmitic acid (palmitate, 255.2 ± 0.7 m/z), linoleic acid (linoleate, 279.2 ± 0.7 m/z), oleic acid (oleate, 281.3 ± 0.7 m/z) and stearic acid (stearate, 283.3 ± 0.7 m/z) in the adipocere extract, proving the presence of all of these free fatty acids in the adipocere extract. The peak areas observed in the chromatograms are shown indicating the relative amounts of acids present in the sample. (**b**) Electrospray negative ion mass spectra (ESI–MS) showing the deprotonated ions of myristic acid (myristate, 227.2 ± 0.3 m/z), palmitoleic acid (palmitoleate, 253.2 ± 0.3 m/z), palmitic acid (palmitate, 255.2 ± 0.3 m/z), linoleic acid (linoleate, 279.2 ± 0.3 m/z), oleic acid (oleate, 281.3 ± 0.3 m/z) and stearic acid (stearate, 283.3 ± 0.3 m/z) in the adipocere extract, proving the presence of these free fatty acids in the extract. The mass-to-charge ratios (m/z) are shown in relative abundance.

hypothesized that, as microbial decay continued, more space would become available for pyrite crystals resulting in a cast of the original material. For *Dollocaris ingens* [Van Straelen 1924] it is conceivable that during the decay under partly aerobic conditions triglycerides were hydrolytically split into glycerol and fatty acids and the sulfur-containing amino acids (cysteine and methionine) were degraded, whereby sulfur of the sulfide group was oxidised to sulfate or released as hydrogen sulfide deeper in the tissue[44]. In the anaerobic environment the fatty acids were degraded very slowly resulting in the formation of adipocere. However, over the years, bacterial syntrophic communities or bacterial species that are able to perform both reactions, use sulfate as alternative electron acceptors and degrade fatty acids (*Desulfobacteriaceae*, *Desulfarculaceae*, *Desulfohalobiaceae*, *Syntrophobacteraceae*, and *Peptococcaceae*)[45–47], degraded the adipocere and released hydrogen sulfide. From the field of forensic science, it is known that hydrogen sulfide is able to react abiotically with iron from the haemoglobin to form iron sulfide[48], which might later react to pyrite[49]. In *Dollocaris ingens* [Van Straelen 1924] hydrogen sulfide might have reacted with the iron from the haemolymph and/or the surrounding medium. It must be investigated, whether the increase of the iron content inside the haemolymph of decapods during the moulting process[50] might have a positive effect on the formation of iron sulfide and later the formation of pyrite.

The adipocere theory might also be interesting for the preservation of neural tissues in the arthropods of *Fuxianhuia* [Hou 1987] from the early Cambrian Chengjiang Lagerstätte in southwest China. We assume that the organic macromolecules of the central nerve system, where the tissue is enriched in lipids[51], were first stabilised by adipocere. Adipocere can be formed out of muscle tissue, fat and sphingosine[44]. Sphingosine is a carbon rich amino acid (C-18) which forms the primary part of sphingolipids in the membrane of myelin sheaths that surround nerve cell axons[52].

The results of our study further show a precipitation of calcite clusters inside the specimens. During the decomposition process calcium ions are dissolved out of the cuticle layers due to acidic conditions in and around a carcass caused by autolytic enzymes[6]. With progressive decay conditions become alkaline due to microbial activity and calcium ions together with carbonate ions precipitate as calcite at the inner side of the cuticles[6]. Our results show that a biofilm might influence the type of calcite precipitation. Calcite clusters appeared coarse-grained with a size of 260 to 470 μm in the absence of biofilms[6], and appeared fine grained (100–200 μm) if a biofilm was present (Fig. 4). Further on, the biofilms of our study were able to prevent the crayfish carcasses from floating if a gas accumulation occurred, but were not able to protect them against the degradation ability of ostracods.

Conclusions

It seems that the preservation of *Cambarellus diminutus* [Hobbs 1945] soft tissue or its complete decomposition was mainly influenced by the extrinsic microbial community of the tank water in our experiments. The hepatopancreas of our crayfish individuals were completely transformed into adipocere only in the presence of a biofilm. The biofilm was mainly composed of the bacterial genus *Sphaerotilus* [Kutzig 1833] and the fungi genus *Pluteus* [Fries 1857]. We assume that the combination of these microbial genera might play an important role in soft tissue preservation. The analyses of the altered hepatopancreas sample revealed that it contains a mixture of saturated (palmitic, stearic, and myristic acids) and unsaturated fatty acids (oleic, linoleic, and palmitoleic acids). The inability to detect glyceryl trimyristate or similar triglycerides in the sample indicates that most triglycerides have been degraded, which is typical for adipocere. We assume that, because of the early diagenetic transformation of soft tissue into adipocere (9 days) and the shape-retaining ability of this substance, adipocere might be a first step in soft tissue preservation under certain conditions.
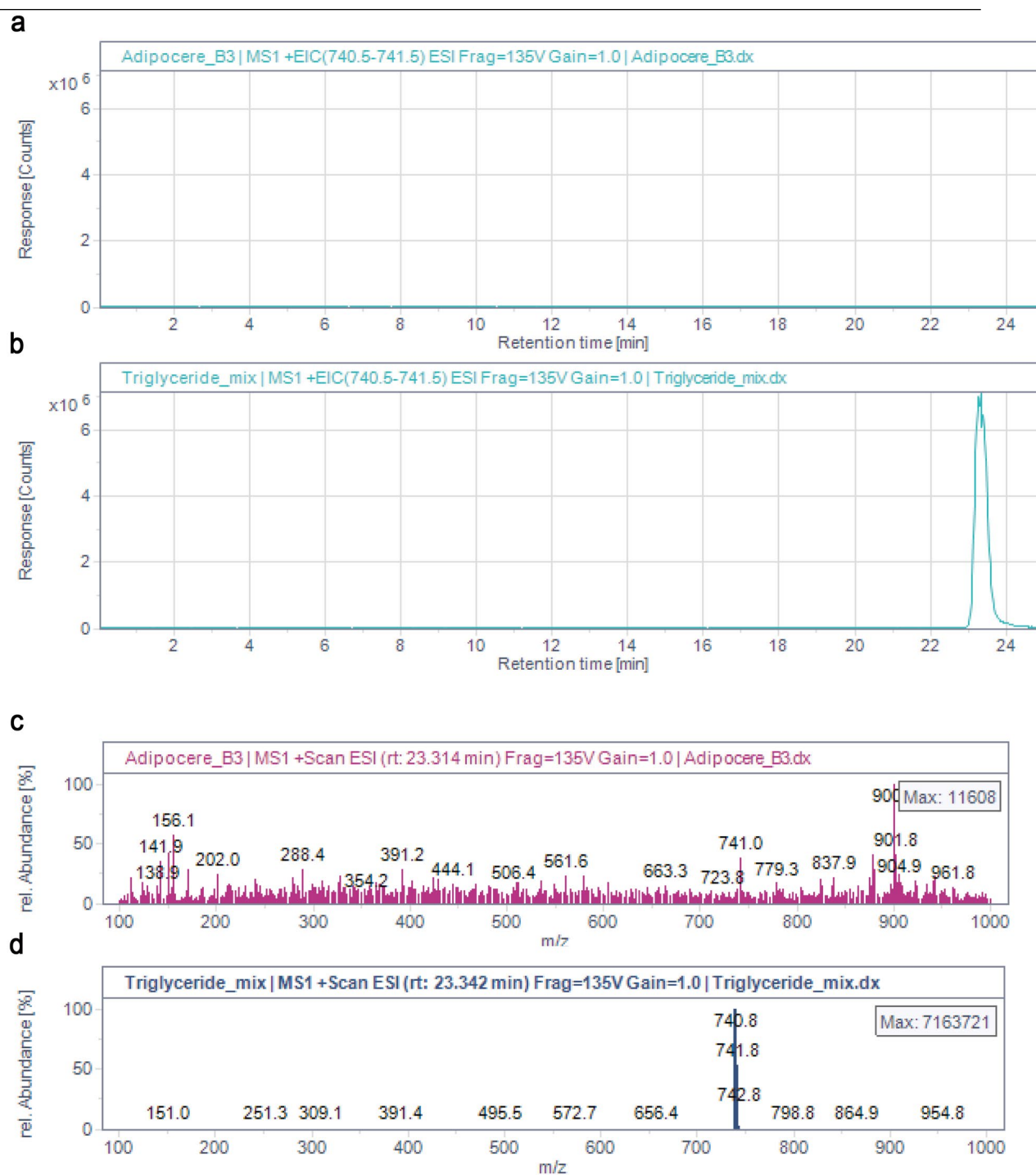
241

16. Appendix

a

b

c

d

Figure 7. (**a**,**b**) Extracted ion chromatograms (EIC) showing the ammonium adducts (M + 18) of the glyceryl trimyristate (722.6 + 18 = 740.6 ± 0.7 m/z), in the adipocere extract (**a**) and in the standard solution containing glyceryl trimyristate (**b**). (**c**,**d**) Electrospray positive ion mass spectra (ESI–MS) showing the ammonium adduct of glyceryl trimyristate (740.6 ± 0.3 m/z) indicated that the triglyceride was not present in the adipocere extract (**c**), but only in the standard solution (**d**). The mass-to-charge ratios (m/z) are shown in relative abundance.

Data availability

242

References

1. Briggs, D. E. G. The role of decay and mineralization in the preservation of soft-bodied fossils. *Annu. Rev. Earth Planet. Sci.* **31**, 275–301 (2003).
2. Briggs, D. E. G. & Kear, A. J. Decay and mineralization of shrimps. *Palaios* **9**, 431–456 (1994).
3. Sagemann, J., Bale, S. J., Briggs, D. E. G. & Parkes, R. J. Controls on the formation of authigenic minerals in association with decaying organic matter: An experimental approach. *Geochim. Cosmochim. Acta* **63**, 1083–1095 (1999).
4. Briggs, D. E. G. & Kear, A. J. Fossilization of soft tissue in the laboratory. *Science* **259**, 1439–1442 (1993).
5. Hoff, C. H. J. & Briggs, D. E. G. Decay and mineralization of mantis shrimp (Stomatopoda: Crustacea)—A key to their fossil record. *Palaios* **12**, 420–438 (1997).
6. Mähler, B. *et al.* Calcite precipitation forms crystal clusters and muscle mineralization during the decomposition of *Cambarellus diminutus* (Decapoda: Cambaridae) in freshwater. *Palaeontol. Electron.* **23**, 55. https://doi.org/10.26879/992 (2020).
7. Iniesto, M., Villalba, I., Buscalioni, A. D., Guerrero, M. C. & Lopez-Archilla, A. I. The effect of microbial mats in the decay of Anurans with implications for understanding taphonomic processes in the fossil record. *Sci. Rep.* **7**, 45160 (2017).
8. Wilby, P. R. & Briggs, D. E. G. Taxonomic trends in the resolution of detail preserved in fossil phosphatized soft tissues. *Geobios* **20**, 493–502 (1997).
9. Jauvion, C. *et al.* Exceptional preservation requires fast biodegradation: Thylacocephalan specimens from La Voulte-sur-Rhône (Callovian, Jurassic, France). *Palaeontology* **63**, 395–413 (2020).
10. Schoenen, D. & Schoenen, H. Adipocere formation – The result of insufficient microbial degradation. *Forensic Sci. Int.* **226**(301), e1-301.e6. https://doi.org/10.1016/j.forsciint.2013.01.023 (2013).
11. Forbes, S. L., Dent, B. B. & Stuart, B. H. The effect of soil type on adipocere formation. *Forensic Sci. Int.* **154**, 35–43 (2005).
12. Schwermann, A. H., Wuttke, M. & Schultz, J. A. Virtopsy of the controlled decomposition of a dormouse *Eliomys quercinus* as a tool to analyse the taphonomy of *Heterohyus nanus* from Messel (Eocene, Germany). *Palaeobiodivers. Palaeoenviron.* **92**, 29–43 (2012).
13. Reisdorf, A. G. & Wuttke, M. Re-evaluating moodie´s opisthotonic-posture hypothesis in fossil vertebrates part I: Reptiles—The taphonomy of the bipedal dinosaurs *Compsognathus longipes* and *Juravenator starki* from the Solnhofen Archipelago (Jurassic, Germany). *Palaeobiodivers. Palaeoenviron.* **92**, 119–168 (2012).
14. Flach, K. Über zwei fossile Silphiden (Coleoptera) aus den Phosphoriten von Caylux. *Deut. Entomol. Z.* **1**, 105–109 (1980).
15. Berner, R. A. Calcium carbonate concretions formed by the decomposition of organic matter. *Science* **159**, 195–197 (1968).
16. Caporaso, J. G. *et al.* Global patterns of 16S rRNA diversity at a depth of millions of sequences per sample. *PNAS* **108**, 4516–4522 (2011).
17. Dowd, S. E. *et al.* Survey of bacterial diversity in chronic wounds using pyrosequencing, DGGE, and full ribosome shotgun sequencing. *BMC Microbiol.* **8**, 1–15. https://doi.org/10.1186/1471-2180-8-43 (2018).
18. Boylen, E. *et al.* Reproducible, interactive, scalable and extensible microbiome data science using QIIME 2. *Nat. Biotechnol.* **37**, 848–857 (2019).
19. Callahan, B. J. *et al.* DADA2: High-resolution sample inference from Illumina amplicon data. *Nat. Methods* **13**, 581–587 (2016).
20. Bokulich, N. A. *et al.* Optimizing taxonomic classification of marker-gene amplicon sequences with QIIME 2's q2-feature-classifier plugin. *Microbiome* **6**, e3208v2. https://doi.org/10.1186/s40168-018-0470-z (2018).
21. Quast, C. *et al.* The SILVA ribosomal RNA gene database project: Improved data processing and web-based tools. *Nucleic Acids Res.* **41**, D590–D596. https://doi.org/10.1093/nar/gks1219 (2012).
22. McDonald, D. *et al.* An improved Greengenes taxonomy with explicit ranks for ecological and evolutionary analyses of bacteria and archaea. *ISME J.* **6**, 610–618 (2012).
23. Ward, T. *et al.* BugBase predicts organism-level microbiome phenotypes. *BioRxiv* 133462 (2017).
24. Laetsch T. & Downs, R. T. Software for identification and refinement of cell parameters from powder diffraction data of minerals using the RRUFF project and American mineralogist crystal structure databases. *Abstracts from the 19th General Meeting of the International Mineralogical Association*, Kobe, Japan (2006).
25. De Gelder, J., De Gussem, K., Vandenabeele, P. & Moens, L. Reference database of Raman spectra of biological molecules. *J. Raman Spectrosc.* **38**, 1133–1147 (2007).
26. Allen, A. L. C. *et al.* Detection of saturated fatty acids associated with a self-healing synthetic biological membrane using fiber-enhanced surface enhanced Raman scattering. *J. Phys. Chem. B* **122**, 8396–8403 (2018).
27. Kaczor, A. & Baranska, M. Structural changes of carotenoid astaxanthin in a single algal cell monitored in situ by Raman spectroscopy. *Anal. Chem.* **83**, 7763–7770 (2011).
28. Subramanian, B. *et al.* Investigantionns on the geometrical isomers of astaxanthin: Raman spectroscopy of conjugated polyene chain with electronic and mechanical confinement. *J. Raman Spectrosc.* **45**, 299–304 (2014).
29. Saito, S. & Tasumi, M. Normal-coordinate analysis of β-carotene isomers and assignments of the Raman and infrared bands. *J. Raman Spectrosc.* **14**, 310–321 (1983).
30. Mant, A. K. Knowledge acquired from post-war exhumations. In *Death, Decay and Reconstruction: Approaches to Archaeology and Forensic Science* (eds Boddington, A. *et al.*) 65–78 (Manchester University Press, 1987).
31. Prokop, O. & Göhler, W. *Forensische Medizin* (Verlag Volk und Gesundheit, 1975).
32. Penning, R. *Rechtsmedizin systematisch* (Uni Med-Verlag Bremen, 2006).
33. O'Brien, T. G. & Kuehner, A. C. Waxing grave about adipocere: Soft tissue change in an aquatic context. *J. Forensic Sci.* **52**, 294–301 (2007).
34. Pfeifer, S., Milne, S. & Stevenson, R. M. The natural decomposition of adipocere. *J. Forensic Sci.* **43**, 368–370 (1998).
35. Ueland, M., Breton, H. A. & Forbes, S. L. Bacterial populations associated with early-stage adipocere formation in lacustrine waters. *Int. J. Legal Med.* **128**, 379–387 (2014).
36. van Veen, W. L., Mulder, E. G. & Deinema, M. H. The Sphaerotilus-Leptothrix group of bacteria. *Microbiol. Rev.* **42**, 329–356 (1978).
37. Niu, L. *et al.* Ignored fungal community in activated sludge wastewater treatment plants: Diversity and altitudinal characteristics. *Environ. Sci. Pollut. Res.* **24**, 4185–4193 (2017).
38. Booth, J. M. *et al.* The role of fungi in heterogenous sediment microbial networks. *Sci. Rep.* **9**, 7537 (2019).
39. Wilby, P. R., Briggs, D. E. G., Bernier, P. & Gaillard, C. Role of microbial mats in the fossilization of soft tissues. *Geology* **24**, 787–790 (1996).
40. Grimes, S. T. *et al.* Understanding fossilization: Experimental pyritization of plants. *Geology* **29**, 123–126 (2001).
41. Esteve, M. & Herrera, F. C. Hepatopancreas alterations in *Litopenaeus vannamei* (Boone, 1939) (Crustacea: Decapoda: Penaeidae) experimentally infected with a *Vibrio alginolyticus* strain. *J. Invertebr. Pathol.* **76**, 1–5 (2000).
42. Anderson, G. S. & Hobischak, N. R. Decomposition of carrion in the marine environment in British Columbia, Canada. *Int. J. Legal Med.* **118**, 206–209 (2004).
43. Dumser, T. K. & Türkay, M. Postmortem changes of human bodies on the Bathyal Sea Floor-Two cases of aircraft accidents above the open sea. *J. Forensic Sci.* **53**, 1049–1052 (2008).
44. Schoenen, D. *Verwesung und Verwesungsstörungen-Entstehung von Eis- und Trockenmumien, Fettwachs-, Faul- und Moorleichen sowie fossilen Geweresten und lithifizierten Gewebeabdrucken* (Shaker Verlag GmbH, 2019).

243

16. Appendix

45. Rabus, R., Hansen, T. A. & Widdel, F. Dissimilatory sulfate- and sulfur-reducing prokaryotes. In *The Prokaryotes* (eds Dworkin, M. *et al.*) 659–768 (Springer, 2006).
46. Sousa, D. Z., Alves, J. I., Alves, M. M., Smidt, H. & Stams, A. J. M. Effect of sulfate on methanogenic communities that degrade unsaturated and saturated long-chain fatty acids (LCFA). *Environ. Microbiol.* **11**, 68–80 (2009).
47. Sousa, D. Z. *et al.* Degradation of long-chain fatty acids by sulfate-reducing and methanogenic communities. In *Handbook of Hydrocarbon and Lipid Microbiology* (eds Timmis, K. N. *et al.*) 963–980 (Springer, 2010).
48. Fiedler, S., Berns, A. E., Schwark, L., Woelk, A. T. & Graw, M. The chemistry of death—Adipocere degradation in modern graveyards. *Forensic Sci. Int.* **257**, 320–328 (2015).
49. Berner, R. A. Sedimentary pyrite formation. *Am. J. Sci.* **268**, 1–23 (1970).
50. Recio, J. M. & Léon, V. Hemolymph iron in Crustacea decapoda during the intermolt cycle. *Rev. Esp. Fisiol.* **32**, 307–311 (1976).
51. Ma, X., Edgecombe, G. D., Hou, X., Goral, T. & Strausfeld, N. J. Preservational pathways of corresponding brains of a Cambrian euarthropod. *Curr. Biol.* **25**, 2969–2975 (2015).
52. Kolter, T. & Sandhoff, K. Sphingolipide-Ihre Stoffwechselwege und die Pathobiochemie neurodegenerativer Erkrankungen. *Angew. Chem. Ger. Ed.* **111**, 1632–1670 (1999).

Author contributions

B.M. designed the study. Figures 1, 2a,b, 3, 5; Supplementary Figs. S1, S2, S3 and S4 were created by B.M., Fig. 2c was created by F.T., Fig. 4 was created by K.J. and Figs. 6, 7; Supplementary Figs. S5 and S6 were created by M.T. Table 1 and Supplementary Table S1 were created by B.M., Supplementary Table S2 was created by M.T. B.M. did μ-CT analysis, SEM, virtual reconstruction and took the photos for the general observation. K.J. extracted the DNA and did 16S rRNA gene amplicon sequencing. M.T. did HPLC–UV/MS analysis and F.T. did CRS. B.M. wrote the main part of the paper with contributions from K.J., M.T., F.T. and the remaining authors.

Competing interests

The authors declare no competing interests.

Additional information

Supplementary Information The online version contains supplementary material available at https://doi.org/10.1038/s41598-022-14119-8.

Correspondence and requests for materials should be addressed to B.M.

Reprints and permissions information is available at www.nature.com/reprints.

Publisher's note Springer Nature remains neutral with regard to jurisdictional claims in published maps and institutional affiliations.

244

Supplementary Information:

Adipocere formation in biofilms as a first step in soft tissue preservation

Bastian Mähler[1*], Kathrin Janssen[2], Mariam Tahoun[3], Frank Tomaschek[4], Rico Schellhorn[1], Christa E. Müller[3], Gabriele Bierbaum[2] & Jes Rust[1]

[1]Section Palaeontology, Institute of Geosciences, Rheinische Friedrich-Wilhelms Universität Bonn, 53115 Bonn, Germany

[2]Institute of Medical Microbiology, Immunology and Parasitology, Medical Faculty, Rheinische Friedrich-Wilhelms Universität, 53127 Bonn, Germany

[3]Pharmazeutisches Institut, Pharmazeutische & Medizinische Chemie, Rheinische Friedrich-Wilhelms-Universität Bonn, 53121 Bonn, Germany

[4]Section Geochemistry, Institute of Geosciences, Rheinische Friedrich-Wilhelms-Universität Bonn, 53115 Bonn, Germany

* Corresponding author: bastian.maehler@uni-bonn.de

Supplement

Product information "Crab Natural" (Sera, GmbH, Heinsberg, Germany)

Complete feed for all crustaceans

Ingredients

fish meal, corn starch, wheat flour, spirulina, brewers yeast, wheat germ, gammarus, Ca-caseinate, sea algae, stinging nettle, willow bark, alder cones, fish oil (containing 49% omega fatty acids), mannan oligosaccharides, herbs, alfalfa, parsley, paprika, green-lipped mussel, spinach, carrots, *Haematococcus* algae, garlic.

Analytical constituents

Crude Protein 36.7%, Crude Fat 11.1%, Crude Fiber 4.5%, Moisture 5.2%, Crude Ash 8.6%, Ca 1.9%, P 1.0%.

Additives

Vitamins and provitamins: Vit. A 37,000 IU/kg, Vit. D3 1,800 IU/kg, Vit. E (D, L-α-tocopheryl acetate) 120 mg/kg, Vit. B1 35 mg/kg, Vit. B2 90 mg/kg, stab. Vit. C (L-ascorbyl monophosphate) 550 mg/kg.

Supplementary Table S1 Information on the crayfish specimens used in the study

sample	wet weight	body size	sample	wet weight	body size
C1	0.26 g	2.50 cm	C8	0.28 g	1.80 cm
C2	0.17 g	1.80 cm	C9	0.22 g	1.80 cm
C3	0.42 g	2.10 cm	C10	0.13 g	1.70 cm
C4	0.37 g	1.90 cm	C11	0.43 g	2.40 cm
C5	0.32 g	2.10 cm	C12	0.34 g	2.00 cm
C6	0.34 g	2.10 cm	C13	0.32 g	2.10 cm
C7	0.30 g	2.30 cm	-	-	-

Supplementary Table S2 Mass-to-charge ratios (m/z) of the analysed fatty acids (Mr). In bold are the m/z values used for identification of the acids as their deprotonated ions ([M-H]).

Fatty acid	M_r	$[M–H]^-$
Myristic acid	228.2 Da	**227.2 Da**
Palmitoleic acid	254.2 Da	**253.2 Da**
Palmetic acid	256.2 Da	**255.2 Da**
Linoleic acid	280.2 Da	**279.2 Da**
Oleic acid	282.3 Da	**281.3 Da**
Stearic acid	284.3 Da	**283.3 Da**
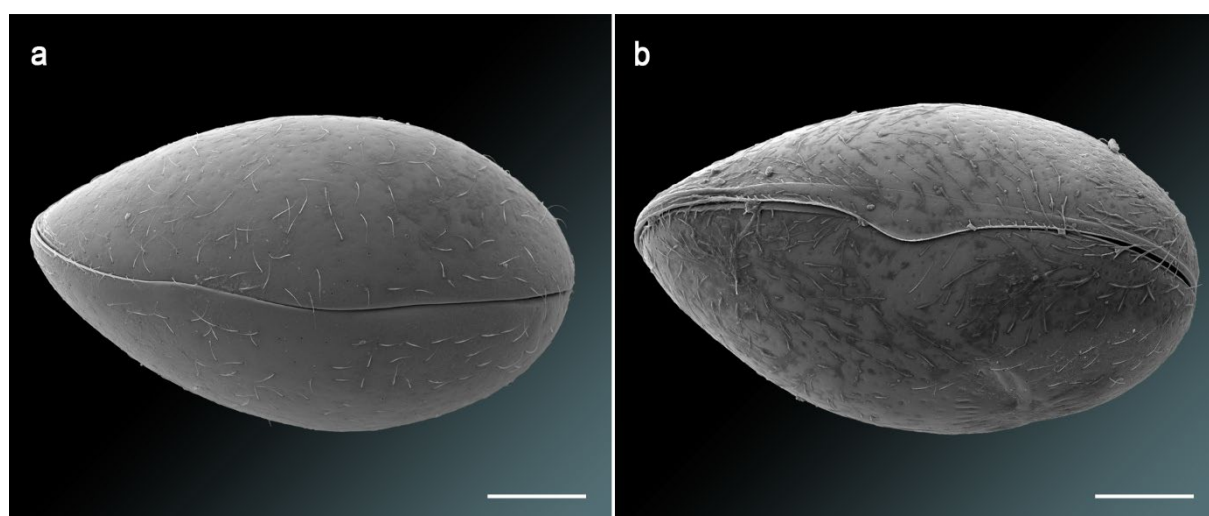
Supplementary Figure S1. (a-b) SEM-images of ostracods found on decomposing crayfish samples and biofilms [WD: 21.91 mm; 21.99 mm]. Scale bar 100 μm. **WD** working distance.
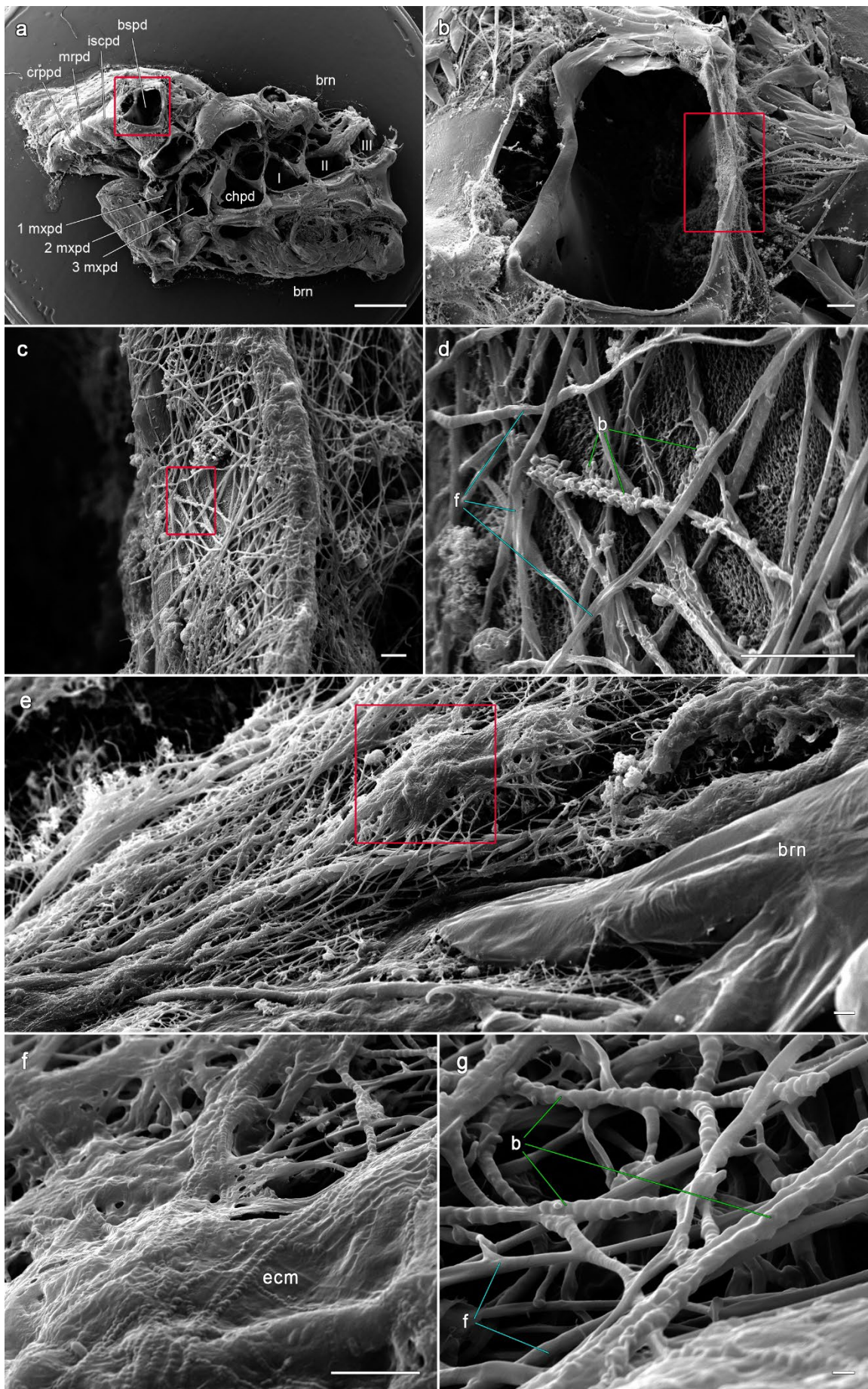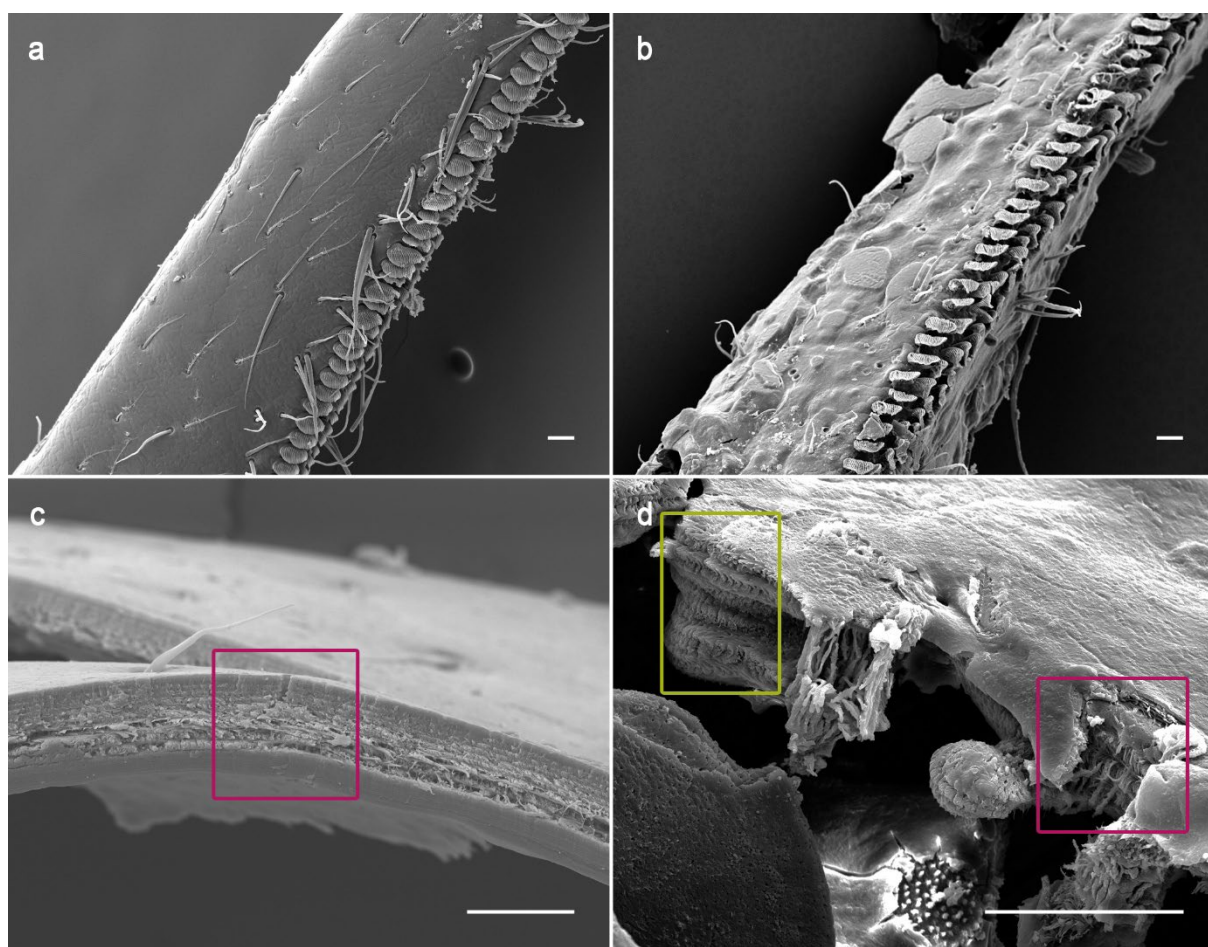
Supplementary Figure S2. SEM-images of the thoracic skeleton of a crayfish with fungal infestation. (**a**) Remains of the thoracic skeleton [WD: 9.49 mm]. Scale bar 1 mm. (**b**) Enlargement of the red box from 1a showing the right basipod [WD: 8.64 mm]. Scale bar 100 μm. (**c**) Enlargement of the red box from 1b showing the fungal infestation of the cuticle [WD: 8.62 mm]. Scale bar 10 μm. (**d**) Enlargement of the red box of 1c showing the fungal infestation with some kind of bacteria [WD: 9.63 mm]. Scale bar 10 μm. (**e**) Fungal biofilm around the branchiae. *Scale bar* 10 μm. (**f**) Enlargement of the red box from 1e showing the increase of the extracellular matrix. *Scale bar* 10 μm. (**g**) Enlargement of the fungal branches in combination of bacteria. *Scale bar* 1 μm. **WD** working distance **b** bacteria; **brn** branchia; **bspd** basipodite; **chpd** cheliped; **crppd** carpopodite; **ecm** extracellular matrix; **f** fungi **iscpd** ischiopodite; **mrpd** meropodite; **mxpd** maxilliped; **I-III** pereiopods.
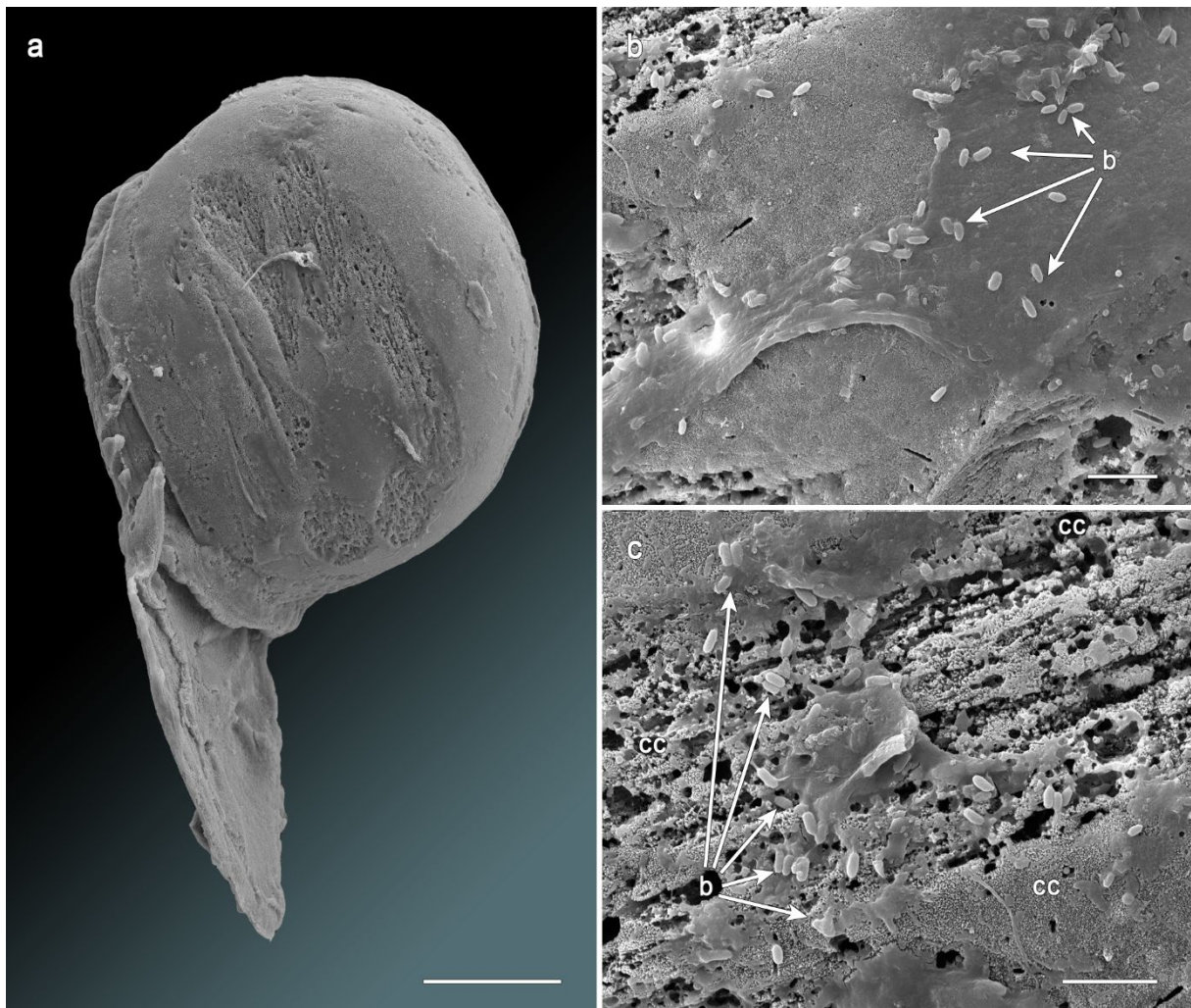
Supplementary Figure S3. SEM-images of a spherical calcite cluster. (**a**) Calcite cluster of C4 [WD: 22.14 mm]. Scale bar 100 μm (**b,c**) SEM-images of an enhanced part of the cluster with parts of a biofilm and bacteria [WD: 22.11 mm]. Scale bar 10μm. **WD** working distance.

Supplementary Figure S4. SEM-images of fresh and decomposed crayfish structures. (**a**) Middle section of a fresh crayfish dactylus [WD: 21.69 mm]. (**b**) Middle section of the decomposed crayfish dactylus of sample C4 after nine days covered by a biofilm in tank water [WD: 21.03 mm]. (**c**) Cross section of a fresh crayfish cuticle [WD: 21.61 mm]. (**d**) Cross section of the cuticle of the dactylus of sample C4 showing a recrystalized part of the cuticle by calcite clusters (green box) and "unaltered" cuticle structures (pink box) [WD: 21.96 mm]. All scale bars 50 μm. **WD** working distance.
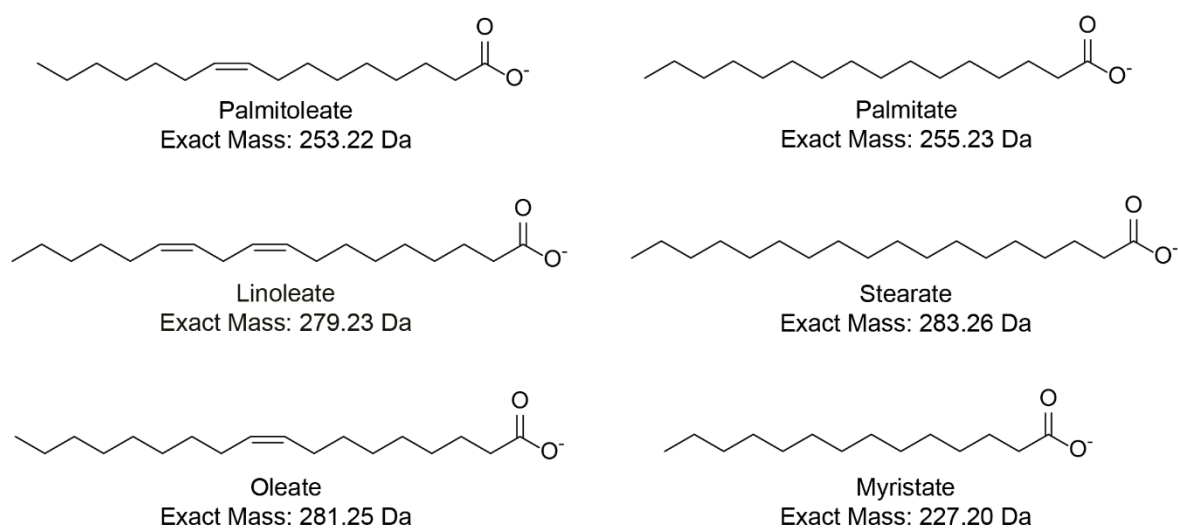
Supplementary Figure S5. Structures of the free fatty acids analysed as deprotonated species [M-H]⁻.
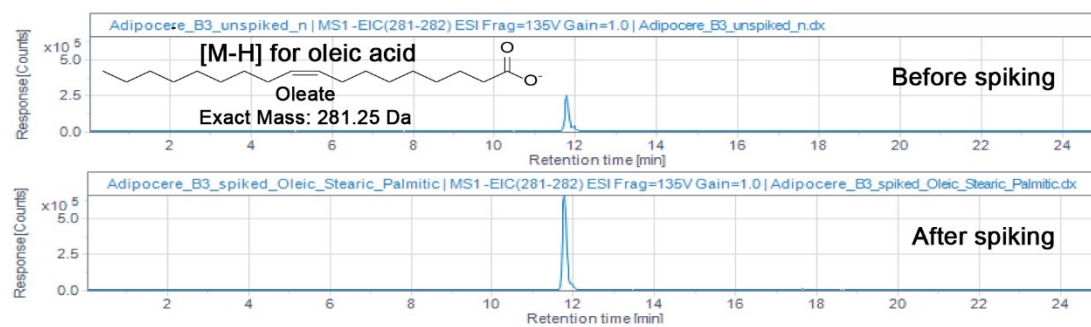
Supplementary Figure S6. Extracted ion chromatograms (EIC) showing the deprotonated ion of oleic acid (oleate, 281.3 ±0.7 m/z) in the adipocere extract, and the increase in its peak area following the addition of a known amount of oleic acid, confirming that oleic acid is present in the adipocere extract. Note that this standard addition experiment with oleic acid was performed in a different run and on a different day than the run shown in Figure 10, which explains the slight shift in retention time.